Spring 5-15-2019

Recent advances in low-cost particulate matter sensor: calibration and application

Jiayu Li
Washington University in St. Louis

WASHINGTON UNIVERSITY IN ST. LOUIS

School of Engineering and Applied Science
Department of Energy, Environmental and Chemical Engineering

Dissertation Examination Committee:
Pratim Biswas, Chair
Rajan Chakrabarty
Pramod Kulkarni
Chenyang Lu
Brent Williams

Recent Advances in Low-cost Particulate Matter Sensor: Calibration and Application

by

Jiayu Li

A dissertation presented to
The Graduate School
of Washington University in
partial fulfillment of the
requirements for the degree
of Doctor of Philosophy

May 2019

St. Louis, Missouri

Table of Contents

List of Figures

List of Tables

Acknowledgments

I would like to express my most sincere gratitude to Professor Pratim Biswas, my PhD advisor, for his wise guidance and continuous support during my time in Washington University in St. Louis. His endless support encouraged me to work on the projects I was interested in. From him, I learned *Stay Hungry. Stay Foolish.*

I thank Professors Rajan Chakrabarty, Brent Williams, Chengyang Lu, and Pramod Kulkarni for serving on my dissertation committee, and providing valuable suggestions to improve this dissertation and my career plan. I also want to thank Dr. Jingkun Jiang, who recommended me to Dr. Biswas and kept encouraging me during my PhD study. They are, and will always be, my career role models.

I also thank the colleagues in the Aerosol & Air Quality Research Laboratory for providing their help and assistance. We are a big family with a glorious history and bright future, and I have benefited so much from the collaboration and communication between us. Especially, I want to thank Yang Wang, Su Huang, Huang Zhang, Sameer Patel, Chun-Ying Chao, for their support in the sensor project. Ben Sumlin, Haoran Li, William Heinson, Yuli Heinson for their fabulous advice on sensor optical and electrical design. I also want to thank my peers Nathan Reed, Zhichao Li, Claire Fortenberry, Apoorva Pandey, Nan Hu, Yining Ou, Wei Bai, Yang Yu, Yi Li, Wei Yang for the memorable time in class. Also, friends in EECE: Yuanzi Sun, Xiangfeng Niu, Yi Jiang, Qinyi Chen, Yunzhu Zhang, Chen Chong, Pradeep Prathibha, Necip Under Becker, Trey Oldham. Many thanks also go to the staff in the EECE

department and the engineering school. I thank Mr. Ballard from the Engineering Communication Center for helping me with my manuscript and dissertation editing.

I also want to thank McDonnell International Scholar Academy for their endless support during my five years. Special thanks to James V. Wertsch, Mark S. Wrighton, John F. McDonnell, Kurt T. Dirks, Sarai, Teresa, Laura Benoist, Carla F. Koberna, Angie L. Rahaman, Kristin L. Williams for their guidance, support, and kindness.

Finally, I do want to express my special gratitude to my lovely husband and lab mate, Yang Wang. Many thanks also go to my parents and parents-in-law Dacun Li, and Yuxia Sun, Hongbin Wang, Xiuxia Ma, for their tremendous support and endless encouragement for my PhD studies.

Jiayu Li

Washington University in St. Louis

May 2019

ABSTRACT OF THE DISSERTATION

Characterization and application of low-cost particulate matter sensors

by

Jiayu Li

Doctor of Philosophy in School of Engineering and Applied Science

Department of Energy, Environmental and Chemical Engineering

Washington University in St. Louis, 2019

Particulate matter (PM) has been monitored routinely due to its negative effects on human health and atmospheric visibility. Standard gravimetric measurements and current commercial instruments for field measurements are still expensive and laborious. The high cost of conventional instruments typically limits the number of monitoring sites, which in turn undermines the accuracy of real-time mapping of sources and hotspots of air pollutants with insufficient spatial resolution. The new trends of PM concentration measurement are personalized portable devices for individual customers and networking of large quantity sensors to meet the demand of Big Data. Therefore, low-cost PM sensors have been studied extensively due to their price advantage and compact size. These sensors have been considered as a good supplement of current monitoring sites for high spatial-temporal PM mapping. However, a large concern is the accuracy of these low-cost PM sensors.

Multiple types of low-cost PM sensors and monitors were calibrated against reference instruments. All these units demonstrated high linearity against reference instruments with high R^2 values for different types of aerosols over a wide range of concentration levels. The question of whether low-cost PM monitors can be considered as a substituent of conventional instruments was discussed, together with how to qualitatively describe the improvement of data quality due to calibrations. A limitation of these sensors and monitors is that their outputs depended highly on particle composition and size, resulting in as high as 10 times difference in the sensor outputs.

Optical characterization of low-cost PM sensors (ensemble measurement) was conducted by combining experimental results with Mie scattering theory. The reasons for their dependence on the PM composition and size distribution were studied. To improve accuracy in estimation of mass concentration, an expression for K as a function of the geometric mean diameter, geometric standard deviation, and refractive index is proposed. To get rid of the influence of the refractive index, we propose a new design of a multi-wavelength sensor with a robust data inversion routine to estimate the PM size distribution and refractive index simultaneously.

The utility of the networked system with improved sensitivity was demonstrated by deploying it in a woodworking shop. Data collected by the networked system was utilized to construct spatiotemporal PM concentration distributions using an ordinary Kriging method and an Artificial Neural Network model to elucidate particle generation and ventilation processes. Furthermore, for the outdoor environment, data reported by low-cost sensors were

compared against satellite data. The remote sensing data could provide a daily calibration of these low-cost sensors. On the other hand, low-cost PM sensors could provide a better accuracy to demonstrate the microenvironment.

Chapter 1: Introduction: Calibration and Applications of Low-cost Particle Sensors – a Review of Recent Advances

1.1 Introduction

New designs for low-cost particulate matter (PM) sensors, new commercial products, and an accompanying number of new publications all show the trending interest in this top. The deployment of low-cost PM sensor networks, together with their pros and cons, has also been discussed in recent works[1-3]. Compared to conventional particulate matter (PM) monitoring techniques, the price advantage and minimal maintenance of low-cost PM sensors make them a promising supplement to current monitoring methods. They can enhance the spatiotemporal resolution of pollution mapping, improving the accuracy of personal exposure estimation and validation of the PM transport models. Estimating personal PM exposure accurately can benefit epidemiologic studies by identifying the adverse health effects of PM. Improving and understanding PM transport models can effectively control and even prevent pollution events. These promising applications explain the recent extensive studies of low-cost PM sensors. As shown in Figure 1, publications related to low-cost air quality sensors were almost nil before 2011, but have steadily increased since then.

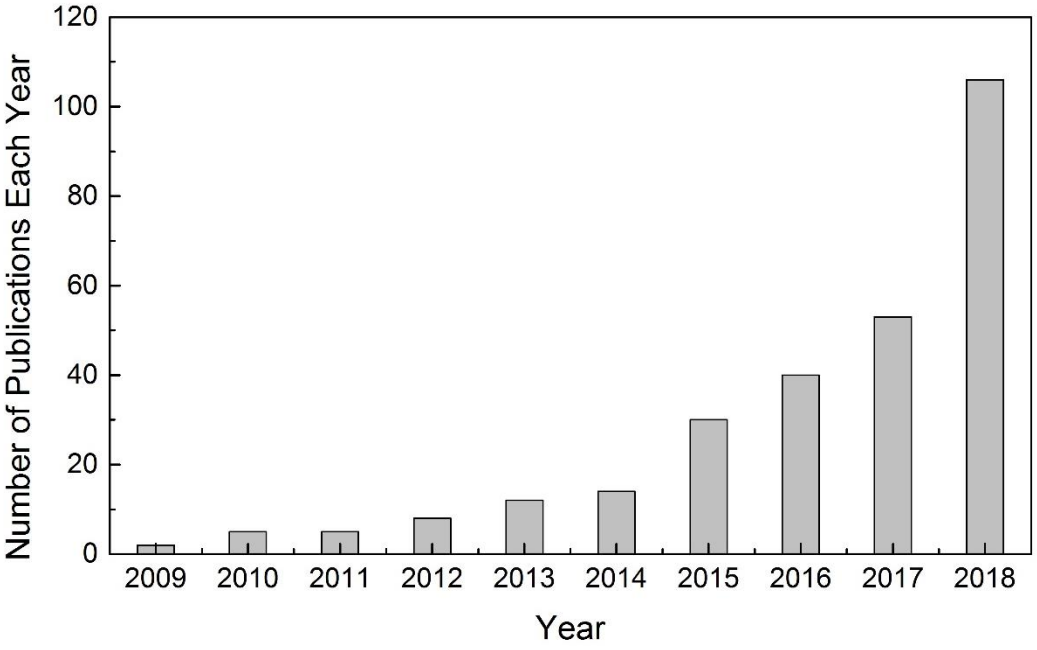

Figure 1.1 (a) The number of papers published each year related to "low-cost air quality sensors". Data from Web of Science Core Collection 1900 – 2019.

Studies related to low-cost sensors basically focus on their calibration and application. The calibration studies evaluate sensors' performance by comparing them with reference instruments, while the application studies focus on pollution mapping and personal exposure estimation. Several reviewers have summarized studies related to low-cost PM sensors[4-7]. Kumar et al. (2015) generally explained the motivations for the rising topic, and reviewed concerns of the reliability, sensitivity, selectivity, and durability of low-cost sensors[4]. Rai et al. (2017) concretely summarized literature on the performance of several different types of low-cost PM sensors, and also analyzed possible environmental factors and aerosol properties that could bias their performance[5]. Morawska et al. (2018) analyzed 17 large on-going funded research studies on low-cost PM sensors, and summarized the major concerns regarding sensor calibration and application[6]. Synder et al. (2013) highlighted that low-cost sensors can

improve existing air pollution monitoring capabilities and inspire innovative applications[7]. Several other reviews illustrate the current limitations and future of low-cost air quality sensors[8-10].

In this chapter, we further review the studies of low-cost PM sensors, and focus in detail on their working principles, calibration methods, calibration metrics, and application scenarios. The working principles of several low-cost PM sensors are demonstrated, using schematics from previous studies. Sensors measuring PM with other techniques are also briefly discussed. Calibration methods and metrics are summarized and compared. Calibration methods and tools include regression or correlation, the non-parametric Wilcoxon signed-rank test, the ranking method, the Bayesian information criterion, average slope and individual slope methods, and the machine learning method. Calibration metrics, parameters for evaluating the performance of low-cost PM sensors, include the limit of detection (LOD), the correlation coefficient of linear regression, bias and precision, the coefficient of variation (CV), and the detection efficiency. Finally, innovative applications of low-cost PM sensors in field measurements or personal exposure estimation are discussed. We also introduce several spatial analysis methods with corresponding cases, illustrating the use of the coefficient of divergence (COD), land use regression, and several spatial interpolation methods. One thing worth noting is that the term "low-cost PM sensor" generally refers to the both electrical sensing modules (e.g., popular models from Sharp, Shinyei, Samyoung, Oneair, and Plantower), together with low-cost PM monitors based on sensing modules. To make the sensing module functional, circuit board design, programming, and calibration are necessary

to establish the relationship between electrical signals (current, voltage, or pulse width) and PM concentrations. For low-cost PM monitors, electrical sensing modules have been integrated with data acquisition and storage systems before being distributed to users, and they have been calibrated and tested. Compared to the PM sensing module alone, the assembled monitors' prices are higher, but these monitors are advertised with enhanced data quality and stability due to improved algorithms and advanced factory calibration. Occasionally, these monitors have even been chosen as reference instruments to calibrate low-cost sensors. For convenience, here we still use the general term "low-cost PM sensors" for both sensing modules and low-cost PM monitors.

1.2 The working principles of low-cost PM sensors

Low-cost PM sensors, operating on basic optical principles, determine the PM concentration level by measuring the intensity of light scattered by particles. Basically, there are two types of these sensors, nephelometer type sensors and optical particle counter (OPC) type sensors. In a nephelometer type sensor, particles pass through the sensing volume almost simultaneously in a cloud, and the particle concentration is determined by the total scattered light intensity registered by a photodetector. In an OPC type sensor, when a single particle passes the sensing volume, the scattered light generates a pulse on the photodetector. The number and the intensity of pulses are proportional to PM's number concentration and size, respectively. The working principles of several popular types of low-cost PM sensors are

shown in Figure 2. Only the Plantower sensors in Figure 2(g) and Figure 2(h) are OPC type sensors; the rest are nephelometer type sensors. Apart from the commercial designs shown in Figure 2, several studies have proposed new designs for low-cost PM sensors, focusing on eliminating the effect of the particles' refractive index or enhancing the sensors' accuracy[11-14].

Low-cost optical PM sensors that light scattering techniques are often considered capable of measuring only particles larger than 0.3 μm. This conclusion is accurate for OPC type sensors, since the pulse signal generated by a very small particle will be buried in the noise. But for nephelometer type sensors, although individual small particles cannot generate intensive signals, if their number concentration is high enough, they can still generate a detectable response, since the totally scattered light intensity is also related to the number concentration.

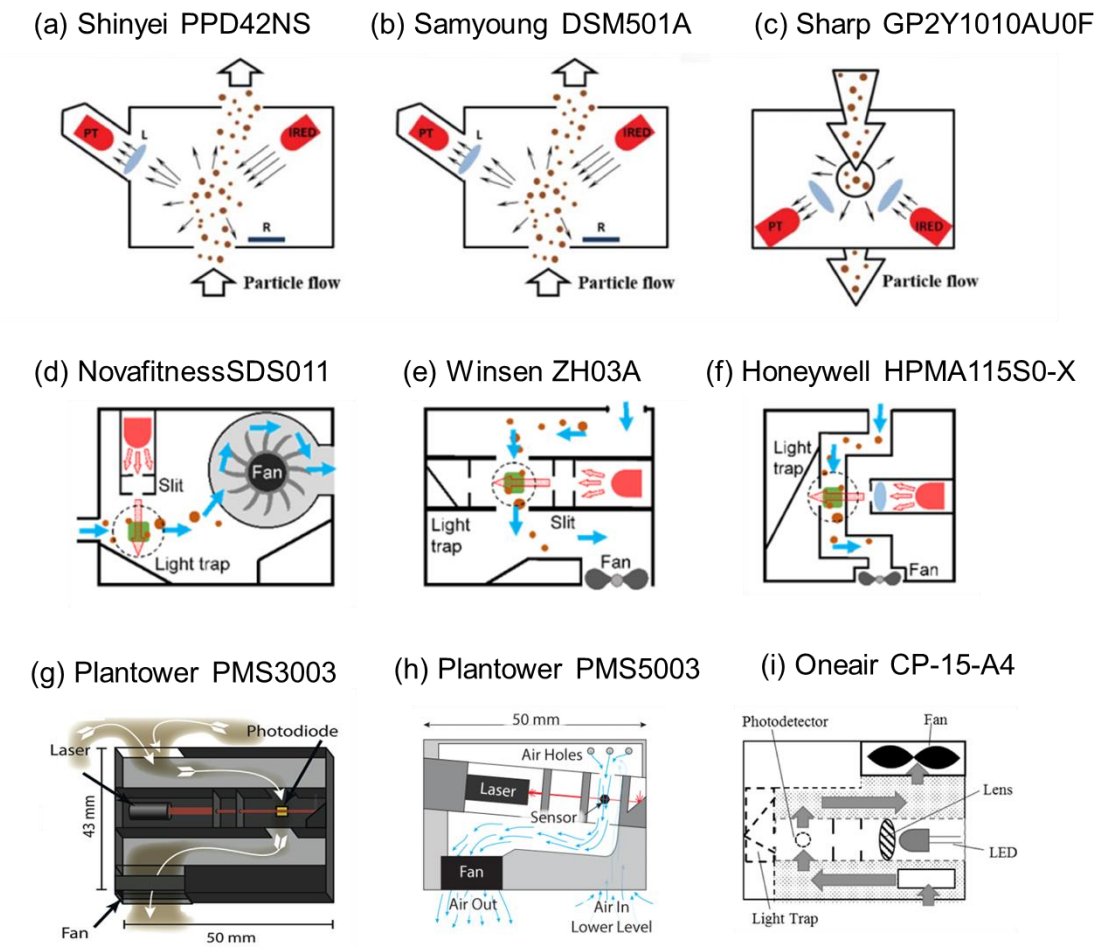

Figure 1.2 Working principles of (a) Shinyei PPD42NS, (b) Samyoung DSM501A, (c) Sharp GP2Y1010AU0F, (d) NovafitnessSDS011, (e) Winsen ZH03A, (f) Honeywell HPMA115S0-X, (g) Plantower PMS3003, (h) Plantower PMS5003, and (i) Oneair CP-15-A4. The figures are from the following studies – (a-c): Wang et al. (2015), (d-f): Hapidin et al. (2019), (g): Kelly et al. (2017), (h): Sayahi et al. (2019), and (i): Liu et al. (2017). The light sources in (a-c) and (i) are light emitting diode (LED), and (d-h) are lasers.

Apart from optical sensors, other types of low-cost PM sensors are receiving attention. Intra et al. (2013) presented a design based on unipolar corona charging and electrostatic detection of charged particles[15]. Volckens et al. (2016) designed a time-integrated filter sampler with an ultrasonic piezoelectric pump to drive flow, together with a cyclone to select particles of a certain size range[16]. Surface acoustic wave sensors can detect PM concentration by

measuring the resonant frequency change after particles deposit on the sensing area, which interferes with the propagation of acoustic waves[2, 17-19]. Budde et al. (2013) designed an add-on PM detector component for smart phones, using the flashlight and camera as the light source and photo detector[20]. Snik et al. (2014) also designed an attachable component that assists smart phones for aerosol optical thickness measurement[21]. Du et al. (2018) designed a PM sensor based on a CMOS (complementary metal oxide semiconductor) imager and an electrostatic particle collector[22]. A similar design was also reported by Carminati et al. (2017)[23]. Yang et al. (2018) synthesized a layer of polypyrrole sensing nanofilm on a photonic crystal fiber[24]. Particles deposited on the sensing nanofilm change its refractive index, indicating a PM concentration level change[24]. The feasibility of using photonic and microelectromechanical resonators for detecting particles or viruses has also been discussed[25]. Recently, a piezoelectric microelectromechanical resonator, together with a low-cost circuit, was proposed as a new low-cost PM sensor[26]. A quartz crystal microbalance (QCM) has been used to measure PM mass concentration, based on the frequency shift caused by particle deposition, and miniaturized devices based on QCM have been developed recently[27, 28].

Although these new innovative designs have an intriguing future, low-cost PM sensors operating on optical principles are still the dominant type, for several reasons. First, optical sensors are easy to use with a lower price compared to other type of sensors. Second, theories of the interactions between light and particles are maturely developed. At the same time, many research-grade PM measurement instruments are also based on optical principles, and

researchers are familiar with these instruments. Therefore, it is easy for them to shift from using conventional instruments to low-cost PM sensors operating on a similar principle. To prove the reliability and stability of the innovative designs, further effort is still needed. Third, their cost and fabrication procedures are also concerns. For some innovative design, although the sensing unit is low-cost, the signal processing and detection components are expensive. In summary, nephelometer type and OPC type designs still are the most widely used because they are compact, easily integrated with other systems, operate on familiar principles, and are conveniently deployed.

1.3 Calibration methods overview

Laboratory calibrations and field calibrations are the foundations of low-cost PM sensors' applications[29-35]. In a laboratory calibration, environmental factors and aerosol properties can be controlled. Environmental factors include the temperature, relative humidity, and ventilation rate. For aerosols, ultrafine particles can be generated from atomizers, and micron-sized particles can be generated from dust dispensers. A few studies have also used common residential or industrial PM sources (e.g., cookstoves and cigarettes) to mimic practical situations in laboratories. Salt particles, sucrose particles, cigarette emissions, welding fumes, and Arizona road dust have been used in laboratory calibrations. The size distribution and composition of aerosols can be controlled fairly well in laboratory experiments, which benefits the analysis of low-cost PM sensors' dependence on these

variables. Sensors' response highly depend on PM sources and size distributions, therefore, choosing an appropriate PM source during calibration will enhance the accuracy in later deployment. For ambient application, Arizona road dust (ARD) can be a good choice. Incense particles can be chosen for sensors planning to deploy for biomass burning measurement. The choice of PM sources can change with the application requirements. Common reference instruments include research-grade instruments (e.g., scanning mobility particle sizer (SMPS), aerodynamic particle sizer (APS), and GRIMM dust monitor) and portable instruments (e.g., TSI SidePak and TSI PTrak). When choosing reference instruments, federal reference/equivalent methods and best available techniques should be the first choice. Other standards, for example the availability and convenience, also need to be taken into consideration.

Field calibration focuses more on the performance of low-cost PM sensors under uncontrolled and dynamic environments, and can be conducted in residential or outdoor environments. In a residential environment, the sensors' responses to routine PM emission events (e.g., cookstove emissions, woodworking shop operations, and incense burning) can be studied. Outdoor calibration focuses on agreement between low-cost PM sensors and federal reference methods, including the gravimetric method, the β-attenuation analyzer, and the tapered element oscillating microbalance (TEOM). Outdoor emissions, especially urban traffic emissions, have been characterized in several studies. In field calibrations, the PM composition and concentration levels can be highly dynamic. Thus, the time domain is usually longer than in laboratory calibrations in order to collect enough data over a whole

concentration range. Although the performance of low-cost PM sensors in field calibration may not be as good as that in laboratory calibration, the results from field calibrations are closer to the real situation, and field calibration is a good method to examine the reliability, durability, and longevity of low-cost PM sensors.

Here we first discuss several calibration methods that have been used in previous studies, including linear regression or correlation, the reduced major axis method, Bayesian information criterion, non-parametric Wilcoxon signed-rank test, the average slope and individual slope method, and machine learning method. Then, methods to correct sensors' performance for the effects of temperature and relative humidity are briefly discussed.

Linear regression is the most common method for calibrating low-cost PM sensors. The sensors' outputs are plotted against the outputs from reference instruments, and a fitted equation is used to optimize the accuracy of the sensors' outputs. The correlation coefficient, *R*, is a statistic measuring the degree or strength of linear correlation. In different studies on evaluating sensors' performance, *R* is referred as the *r* coefficient, Pearson's product-moment *r*, or Pearson's correlation coefficient. *R* values, typically given with two decimal places, range from -1 for a strong negative correlation, through 0 for a no or a weak correlation, to +1 for a strong positive correlation. The value of R^2 is re-scaled to 0 to 1, describing purely the strength of the correlation. Several authors have explained that combining the hypothesis test (*p*-value significance test) with the *r* or R^2 value is a more rigorous method for judging the relationship between two variables[36-38].

If not otherwise specified, linear regression or correlation is usually based on the least squares method. The reduced major axis method, in addition to the least squares method was used in several studies, to calculate the correlation coefficient, slope, and intercept[30, 32]. The assumption of the least squares method is that the independent variables are measured accurately[39, 40]. Therefore, if we are calibrating low-cost sensors against a reference instrument and are very confident about the results from the reference instrument, the least squares method is appropriate. However, in situations where the accuracy of the reference instrument is underdetermined, or when comparing a low-cost sensor against another low-cost sensor, the reduced major axis method is more applicable, because it considers the measurement error of both the dependent and independent variables[40, 41].

To improve sensors' performance by including more variables in the model, for example, relative humidity and temperature, linear correlation or regression may not be adequate. Gao et al. (2015) used both the Bayesian information criterion (BIC) and the standard error of regression to evaluate fitted models that included temperature and humidity as variables[42]. The BIC method can prevent overfitting by introducing a penalty term that reflects the number of free parameters in the model[43-46]. The standard error of regression, also known as the standard error of the estimation, evaluates the difference between observed and model-predicted values. For complicated models, increasing the number of free parameters, for example, by including more variables or fitting with higher orders, will reduce the standard error of regression. However, it will also lower the BIC number due to the penalty term[47]. By

combining these two methods, an optimal predictive model can be selected with minimal discrepancy from the observations, without overfitting.

The Non-parametric Wilcoxon signed-rank test was used by Zikova et al. (2017) in their evaluation of the performance of Speck sensors[48]. This method, also known as Mann-Whitney *U* test or Mann-Whitney-Wilcoxon test, can be used to examine whether the sensor data and the reference instrument data are from the same population. If they are from a same population, then the quality of the sensor is satisfactory and it can be a replacement for the reference instrument. Unlike the majority of statistical methods (e.g., student's *t*-test), which require the assumption of a normal distribution, the Wilcoxon signed-rank test is intuitive, simple, and does not require assumptions about the distribution of the data[49, 50]. However, it only qualitatively demonstrates whether a hypothesis can hold, and is inadequate to quantify the magnitude of any effect. Another rank order analysis method was used by L. R. Crilley for evaluating the variability of 14 Alphasense OPC-N2s over a period of time[51]. The PM measurements were ordered from the highest to the lowest, after being normalized to the median concentration at the start of the analysis. Compared to pair-wise correlation, this method can show the dynamics of the variation, such as offset, as a function of time. The offset drift, or the temporal consistency of each sensor, can also be demonstrated by this method. Ideally, sensors initially reporting higher PM concentrations than peer sensors are supposed to also report higher concentration at the end of the measurement period, representing no drift or the same degree of drift.

The average slope and individual slope method was used to guide the deployment of a low-cost sensor network in a heavy-manufacturing site, for convenience in calibrating multiple sensors[52]. A large concern in the deployment of low-cost sensors is their unpredictable data quality. Repeated calibration has been recommended to enhance the data quality, however, it is time consuming and inconvenient for tens of sensors in a field deployment. The study mentioned above used the average slope method to select sensors with similar slopes in the calibration stage. Then, in the field deployment, the reference instrument was collocated with only several of the selected sensors, and a universal field calibration factor was applied to all the selected sensors.

Machine learning, as a popular concept in computer science, has also been used for sensor calibration. A feedforward Neural Network has been used in the calibration of the Plantower PMS7003[53]. An artificial neural network has been used to predict the PM distribution in a woodworking shop[54]. Zimmerman et al. (2018) compared three calibration methods, including laboratory univariate linear regression, empirical multiple linear regression, and machine-learning method (random forest) to calibrate different gas sensors, and these methods should be considered in the calibration of low-cost PM sensors[55].

The influence of temperature and relative humidity on the performance of low-cost PM sensors have been studied in field and lab studies. Some studies have indicated that the influence of temperature was a negligible effect on sensors' performance[30, 56]. Several other studies have concluded that high RH may bias the performance of low-cost PM sensors in

both laboratory calibration and field evaluation[57, 58]. However, still other studies, especially in field evaluations, indicate that the influence of relative humidity is negligible[59]. There have been attempts to eliminate the influence of relative humidity and temperature by including empirical equations, fitted equations, or hygroscopic growth factors in a more complicated model to calibrate low-cost PM sensors[42, 60-65]. Compared to research grade instruments, low-cost PM sensors lack temperature and humidity control components, and thus changes of shape, size, phase (solid to liquid or liquid to solid), and optical properties of particles under high relative humidity may bias their performance[66, 67]. The influence of relative humidity has been extensively studied by atmospheric scientists[68-70]. The influence of relative humidity also depends on particles' surface properties and compositions, which may explain why, in several field studies, the relative humidity did not show a significant influence on sensors' performance[66]. Further study is needed to explore in detail how environmental factors can influence the sensors' performance and how to correct such bias.

As mentioned above, researchers have tried several different calibration methods to improve the performance of low-cost PM sensors. It has been very controversial whether all studies should follow the same calibration methods to calibrate different kinds of sensors, so that the results from different reports can be comparable. However, a concern here is that such a standard guideline might discourage exploring and applying new statistical methods for sensor calibration. In addition, other issues arise. First, current OPC type sensors and nephelometer type sensors follow the same procedures for calibration. Considering the differences in their working principles and measurement metrics, the calibration methods

may need re-evaluation and modification. Second, the criterion for calibrating low-cost sensing modules (solely electrical component) and low-cost PM monitors (calibrated and tested before being distributed to users) is worth further discussion. For low-cost sensing modules, the focus of calibration is whether good linearity can be established; however, for low-cost PM monitors, agreement with reference instruments might be more important. For sensing modules, calibration is necessary to establish the relationship between electrical signals with $PM_{2.5}$. For low-cost PM monitors, since they already report $PM_{2.5}$, the bias and deviation should be the focuses, instead of correlation. Therefore, it is necessary to distinguish between sensing modules and low-cost PM monitors, since their calibration metrics and methods are inherently different.

1.4 Calibration metrics

Calibration metrics are parameter whose values are calculated from the calibration procedures used to evaluate the performance of low-cost PM sensors. For example, the correlation coefficient from linear regression is a common parameter to evaluate the linearity of low-cost PM sensors. Similar metrics include the limit of detection (LOD), the bias and precision, and the coefficient of variation (COV).

The R^2 value, from linear regression, is a primary parameter to evaluate the linearity of low-cost PM sensors. Details related to linear regression have been mentioned in the last section. The R^2 values of low-cost PM sensors from previous studies, as summarized by Rai et al. (2017), are presented in Figure 3. In the literature, R^2 values are reported for different PM

sources under various test environments. The maximum and the minimum R^2 values for several types of low-cost PM personal monitors are summarized in Figure 4. The major components of several of low-cost PM monitors in Figure 4 are sensing modules mentioned in Figure 3. For example, the major component of the AirAsure is the Sharp GP2Y1010AU0F, and the major component of the PurpleAir is the Plantower PMS series low-cost sensing module. Since the tests in Figure 3 and Figure 4 were not conducted following the same methodology and guidelines, the reported R^2 values could vary with different test conditions, and results may not be directly comparable. However, the trend is basically the same: the R^2 value from the laboratory calibration ($R^2 > 0.6$) is better than that from field calibration ($R^2 > 0.4$).

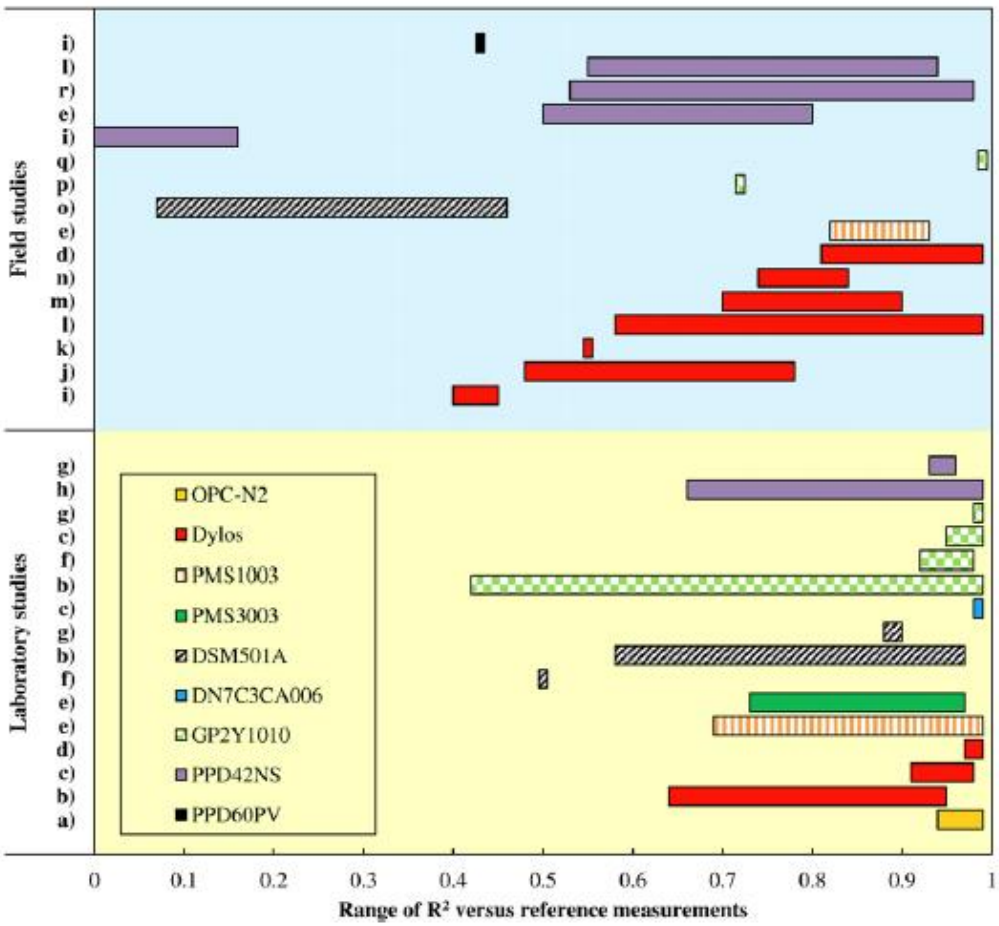

Figure 1.3 The R^2 values of low-cost PM sensors, summarized by Rai et al. (2017).

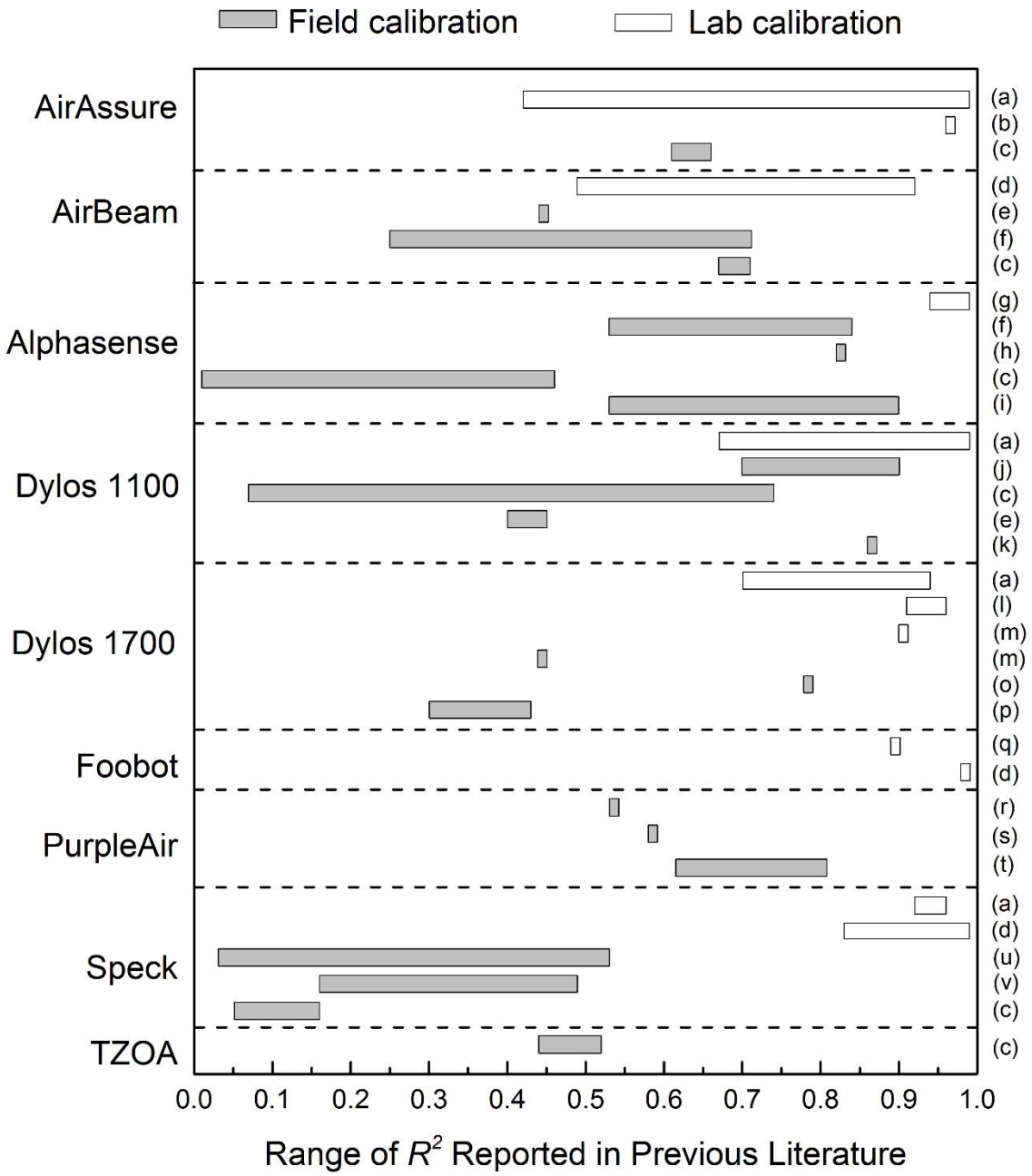

Figure 1.4 Reported R^2 values of low-cost PM personal monitors. The data are from the following studies – (a) Manikonda et al. (2016), (b) Wang et al. (2015), (c) Feinberg et al. (2018), (d) Sousan et al. (2017), (e) Jiao et al. (2016), (f) Mukherjee et al. (2017), (g) Sousan et al. (2016), (h) Gillooly et al. (2019), (i) Crilley et al. (2018), (j) Steinle et al. (2015), (k) Semple et al. (2015), (l) Sousan et al. (2016), (m) Semple et al. (2013), (n) Jovašević-Stojanović et al. (2015), (o) Han et al. (2017), (p) Franken et al. (2019), (q) Moreno-Range et al. (2018), (r) Sayahi et al. (2019), (s) Malings et al. (2018), (t) Malings et al. (2018), (u) Zikova et al. (2017), and (v) Zikova et al. (2017).

The limit of detection (LOD) is the lowest detectable concentration that significantly stands out from the background noise. Low-cost PM sensors are considered to report reliable and meaningful data, only when the concentration exceeds the LOD. Equation (1.1) for calculating the LOD is given below, where k and σ_{blk} represent the slope from the fitted model and the standard deviation of low-cost PM sensors under a particle-free background[30, 71]. Knowing the LOD before deployment is necessary to produce reliable data, especially for atmospheric measurement. However, LOD is for reference only and should not limit the application of low-cost PM sensors. According to the requirements of different applications, LOD is not the lower the better.

$$LOD = 3\sigma_{blk}/k \tag{1.1}$$

Equation (1.2a) shows the bias defined by the National Institute for Occupational Safety and Health (NIOSH), where C_{LS} and C_{rf} represent the concentrations measured by low-cost sensors and reference instruments[33, 72, 73]. NIOSH bias, also known as the percent difference, evaluates the percent of error of low-cost sensors' output compared to reference instruments. Zikova et al. (2017) and Sousan et al. (2018) have used this method to evaluate the performance of Speck monitors and Sharp sensors respectively[48, 52]. Kelly et al. (2019), used a similar definition, referred to as the normalized residual, to evaluate Plantower sensors[59]. The EPA specifies the bias of low-cost PM sensors by Equation (1.2b), which given the average of the percent difference in k different measurements[72]. Both NIOSH bias and EPA bias have been recommended to be within ± 10%.

$$NIOSH\ bias\ (d_i) = \frac{C_{LS} - C_{rf}}{C_{rf}} \times 100\% \quad (1.2a)$$

$$EPA\ bias\ (b_i) = \frac{1}{k}\sum_{i=1}^{k} \frac{C_{LS} - C_{rf}}{C_{rf}} \times 100\% = \frac{1}{k}\sum_{i=1}^{k} d_i \times 100\% \quad (1.2b)$$

The measurement precision parameter reflects the stability and repeatability of low-cost PM sensors at a certain concentration level. There are several different definitions of measurement precision. For evaluating the repeatability and stability of low-cost PM sensors for a fixed concentration level Long et al. (2016) defined measurement precision, as shown in Equation (1.3a), where P_1, P_2, and P_3 represent three individual measurements of low-cost PM sensors for the same concentration level[74]. Manikonda et al. (2016), Zikova et al. (2017), and Zamora et al. (2019) used a similar definition of precision that involved the difference and mean of the sensor's and reference instruments' outputs, as shown in Equation (1.3b and 1.3c)[48, 61, 75]. Manikonda et al. (2016) used the normalized root mean square error to quantify the difference of paired data, as shown in Equation (1.3b)[75]. In the equation, n is the number of data pairs in a period of measurement, and P_i and C_i represent the paired data from two low-cost PM sensors. Zikova et al. (2017) and Zamora et al. (2019) used the same definition (Equation (1.3c)) and referred to the method as "unbiased variance estimate" and "relative precision error" respectively in their papers[48, 61]. Compared to Equation (1.3a), Equations (1.3b and 1.3c) might be more practical for calibration since they do not require a fixed concentration level, and they consider the precision values with respect to concentration levels by normalizing them to average measurement results.

$$Precision = \sqrt{\frac{1}{2}\left[\sum_{i=1}^{3} P_i^2 - \frac{1}{3}\left(\sum_{i=1}^{3} P_i\right)^2\right]} \quad (1.3a)$$

$$Precision\ of\ measurement = \frac{\sqrt{\frac{1}{n}\sum_{i=1}^{n}(P_i - C_i)^2}}{\frac{1}{n}\sum_{i=1}^{n}(P_i + C_i)/2} \quad (1.3b)$$

$$Precision = \frac{|P_i - C_i|}{P_i + C_i} \times 100\% \quad (1.3c)$$

The coefficient of variation (CV), another parameter for evaluating the precision of low-cost PM sensors, is defined by Equation (1.4), where σ and μ represent the standard deviation and the mean of measurements. CV measures the degree of variation, indicating the dispersion of data points around the mean value. Sousan et al. (2016) and Zamora et al. (2018) have used this parameter to evaluate the performance of the Alphasense OPC-N2 and Plantower PMS A003 respectively[33, 61], and several other studies have also used CV to evaluate different types of sensors[76]. A CV value of less than 10% is considered to be a satisfactory performance.

$$CV = \frac{\sigma}{\mu} \quad (1.4)$$

Apart from the parameters mentioned above, other statistical measures can be used to evaluate the performance of low-cost sensors. Examples include, the median, mean, mode, the 25th and 75th percentile[51], and the mean relative standard deviation[57]. All these statistical measures quantify the accuracy and repeatability of low-cost sensors from different perspectives. However, current studies and guidelines have limitations. First, the criterion for "good" performance is vague. In the methods mentioned above, only reference values for CV and bias are given by NIOSH and EPA. More criteria are needed, for example, in what range the reference value of R^2 can be called a "good" PM sensor. Several guidebooks discuss

standard procedures and guidelines to calibrate low-cost sensors, led by the EPA and air quality sensor performance evaluation center (AQ-SPEC), and we expect more discussion on this subject[77-79]. Second, the performance of low-cost PM sensors varies with the particle size distribution, composition, and testing environment, which makes the results from different reports difficult to compare. A guideline for specifying test conditions would be helpful in the field. Third, several different parameters are reported by low-cost PM sensors, including the number concentration, mass concentration, and size distribution. Sensors reporting number concentration and mass concentration have been evaluated by the statistical methods mentioned in this section, however, there are limited options for quantifying the accuracy of the size distribution data. Normally, the size distributions from low-cost PM monitors are plotted together with those from reference monitors. Also, sometimes, detection efficiency has been calculated to quantify the performance. More discussion is needed to evaluate size distribution measurements from different perspectives.

1.5 Applications

The superiority of low-cost PM sensors, their price advantage, portable size, and moderate accuracy have made them a good supplement to current monitoring stations. Several studies have shown that spatial variation cannot be neglected, even over a kilometer scale[80, 81], and such small-scale heterogeneity is important for accurately quantifying the personal exposure level[82]. Here we present several examples of field deployment of low-cost PM sensors,

together with related spatial analysis methods. An important topic in sensor deployment is using interpolation method to predict the PM concentration at locations without measurements, known as pollution mapping. Common interpolation methods were also discussed in this section.

Low-cost PM sensors have been innovatively applied in industrial or daily life. Low-cost sensors have been used to examine the relationship between different sources and PM concentration levels[83]. Dylos sensors were used to evaluate the pesticide off-target drift of agricultural tower sprayers[84]. A Novafitness sensor was used to evaluate the emissions of a surface filter[85]. Other than estimating personal exposure[86] and mapping pollution distribution[87], applications also include characterizing households emissions[88, 89], cigarette emissions[90], and industrial factory emissions[54, 91]. Low-cost PM sensors can also contribute to the construction of smart cities that provide personal exposure estimation with better accuracy[92-94].

Apart from deploying fixed sensors to enhance spatial resolution, several studies have involved mobile sensing nodes. When combined with a data logging system (e.g., on a microSD card) or position logging system (e.g., GPS), low-cost sensors can be used to refine the assessment of personal exposure[20, 95-99]. At indoor scale, an ultrasonic indoor positioning system has been used to position mobile low-cost PM sensors for indoor exposure estimation[100]. These sensors have also been integrated with unmanned aerial vehicles (e.g.,

drones) for outdoor vertical measurement[101, 102]. Furthermore, a low-cost robot, carrying a low-cost PM sensor has been tested for remote sampling or autonomous sampling [Abhay].

The coefficient of divergence (COD), defined by Equation (1.5), quantifies the level of heterogeneity between two places, where $x_{i,j}$ and $x_{i,k}$ are the i^{th} measurement at location j and k respectively[103]. Normally, a COD value smaller than 0.2 represents no significant difference between the measurements at two different locations, indicating homogeneity. COD values larger than 0.2 represents increasing heterogeneity[103, 104]. Zikova et al. (2017) and Saha et al. (2019) had used this method to examine, respectively, the PM distribution with 25 Speck monitors in New York and 32 RAMP (real-time, affordable, multi-pollutant) monitors in Pittsburg respectively[48, 81]. Reece et al. (2018) also used this method in a field campaign in Puerto Rico to analyze spatiotemporal distribution of $PM_{2.5}$ and NO_2.[76] Using the COD of different species, Saha et al. (2019) found that ultrafine particles and $PM_{2.5}$ respectively demonstrated higher and lower heterogeneity[81].

$$COD_{j,k} = \sqrt{\frac{1}{p}\sum_{i=1}^{p}[(x_{ij} - x_{ik})/(x_{ij} + x_{ik})]^2} \quad (1.5)$$

Different types of interpolation methods have been used for indoor and outdoor pollution mapping employing low-cost sensors. Zikova et al. (2017) used the inverse squared-distance weighing interpolation (IDW) to predict outdoor PM distribution with 25 Speck monitors[48]. Li et al. (2018) mapped the spatiotemporal PM distribution in a woodworking shop with 8 Sharp GP2Y sensors by Kriging interpolation and an artificial neural network method[54]. In two consecutive studies, Rajasegarar et al. (2014) used a Bayesian maximum entropy (BEM)

method to map the PM distribution in a garage and city of Melbourne, Australia, with GP2Y sensors.[105, 106] There are around 30-40 types spatial interpolation methods, have been deployed in environmental studies, and several reviews have made high-quality summaries explaining the differences among these methods and how to quantify the accuracy of the interpolation results[107-110]. The major differences among various types of interpolation methods is the weight assigned to measured data for predicting the concentration at unsampled locations. Methods used to assess the accuracy of the measurement can also be used to optimize sampling locations.

Land use regression (LUR) is another important method used to interpret the results from low-cost PM sensors[111]. LUR also uses data at sampled locations to predict the PM values at unsampled locations. However, a major difference that distinguishes LUR from other interpolation methods is the involvement of additional predictor variables, for example, land use, traffic, population density, physical geography, and meteorology. Including these additional predictor variables shows that the PM concentration is not only a function of the location. Another large difference between the spatial interpolation methods discussed above and the LUR is the restriction of measured datasets. For Kriging interpolation, the highest PM concentration belongs the measured datasets. However, for LUR, the highest PM concentration may not be the highest measured value, because the results are influenced by multiple variables.

Several questions demand further attention. First, the differences between indoor and outdoor pollution mapping need to be highlighted. Indoor pollution events are highly dynamic, and can change within several seconds due to complicated ventilation conditions. How to adjust the sampling locations and intervals to meet the requirements of indoor and outdoor pollution mapping needs further exploration. A second question is related to the strategy of measurement. The majority of monitoring stations are heterogeneously located, concentrated in and around metropolitan areas or industrial areas. The question of how this sparseness may undermine the accuracy of pollution mapping should be answered in future studies. Optimizing the locations of low-cost PM sensors is another potential topic related to the efficiency and effectiveness of measurements. The third question is how best to connect the pollution mapping results with studies in other fields. The pollution mapping results from conventional methods have already been used in epidemiologic studies. Low-cost PM sensors can indeed provide data with better spatiotemporal resolution; however, the reliability and accuracy of the data remain as concerns.

1.6 Challenges

We have summarized the methods and metrics used in previous studies to evaluate the performance of low-cost PM sensors. These methods can demonstrate the advantages and limitations of each type of sensor. Characterizing these sensors thoroughly will benefit their deployment in field studies. Low-cost PM sensors have demonstrated acceptable accuracy

and stability in the calibration and characterization, which demonstrates great potentials in various applications for mapping pollution distribution and quantifying personal exposure. However, here are several challenges that may still a concern in current studies.

First, previous studies have concluded the parameters that may bias sensors' performance, leading to overestimating or underestimating in mass concentrations. We have also mentioned in the previous section, environmental parameters (e.g., relative humidity and temperature) and PM properties (e.g., size distribution and optical properties) may all challenge the accuracy of the low-cost PM sensors. Either establishing models with more parameters or improving sensor structures can achieve a better accuracy. Several studies mentioned above have built different models to correct the bias caused by relative humidity and temperature. However, a big concern is whether the models are universal, applicable to all or most of the scenarios. To establish a universal model, more fundamental studies are needed. At the same time, there are limited studies of improving sensors' structure for better performance. Therefore, how to improve sensors' performance for an accurate estimation of PM mass concentration needs further effort.

Second, the LOD was not always reported in literature as correlation coefficients. However, they are vital for judging whether a specific type of sensors is appropriate for deployment. Further lower the LOD with either advancing algorithms or sensor structure improvement will benefit sensors' deployment in field measurement. The cut-off size for OPC type sensors is approximately 300 nm, which does not include ultrafine particles yet. Furthermore, ultra-

fine particles have showed a stronger mobility and have demonstrated a more heterogeneous distribution than larger particles. Therefore, lower the cut-off size for both OPC type and nephelometer type PM sensors is necessary and practical.

Third, although the cost and maintenance of a single PM sensor is low, maintaining a sensor network will be a different story. Although the maintenance requirement for low-cost PM sensors is lower compared to conventional methods, but still cannot be ignored. Identifying malfunctioning sensors and repairing them will be difficult for a sensor network with more than a hundred units. How to enhance the stability and robustness of low-cost PM sensors to realize zero-effort maintenance will benefit field applications.

Fourth, the data from low-cost sensors have been used for pollution mapping and exposure estimation. A few studies have also used robot and drone with low-cost PM sensors to realize autonomous measurement. Some attempts have been made to combine low-cost PM sensor with remote sensing or ground measurement[112]. More studies are expected to explore the possibilities of using sensor data in different applications and different scenarios.

1.7 References

1. Amegah, A. K., Proliferation of low-cost sensors. What prospects for air pollution epidemiologic research in Sub-Saharan Africa? *Environmental Pollution* **2018,** *241*, 1132-1137.
2. Thomas, S.; Cole, M.; Villa-López, F. H.; Gardner, J. W., High frequency surface acoustic wave resonator-based sensor for particulate matter detection. *Sensors and Actuators A: Physical* **2016,** *244*, 138-145.
3. Castell, N.; Dauge, F. R.; Schneider, P.; Vogt, M.; Lerner, U.; Fishbain, B.; Broday, D.; Bartonova, A., Can commercial low-cost sensor platforms contribute to air quality monitoring and exposure estimates? *Environment international* **2017,** *99*, 293-302.
4. Kumar, P.; Morawska, L.; Martani, C.; Biskos, G.; Neophytou, M.; Di Sabatino, S.; Bell, M.; Norford, L.; Britter, R., The rise of low-cost sensing for managing air pollution in cities. *Environment international* **2015,** *75*, 199-205.
5. Rai, A. C.; Kumar, P.; Pilla, F.; Skouloudis, A. N.; Di Sabatino, S.; Ratti, C.; Yasar, A.; Rickerby, D., End-user perspective of low-cost sensors for outdoor air pollution monitoring. *Science of The Total Environment* **2017,** *607*, 691-705.
6. Morawska, L.; Thai, P. K.; Liu, X.; Asumadu-Sakyi, A.; Ayoko, G.; Bartonova, A.; Bedini, A.; Chai, F.; Christensen, B.; Dunbabin, M., Applications of low-cost sensing technologies for air quality monitoring and exposure assessment: How far have they gone? *Environment international* **2018,** *116*, 286-299.
7. Snyder, E. G.; Watkins, T. H.; Solomon, P. A.; Thoma, E. D.; Williams, R. W.; Hagler, G. S.; Shelow, D.; Hindin, D. A.; Kilaru, V. J.; Preuss, P. W., The changing paradigm of air pollution monitoring. In ACS Publications: 2013.
8. Koehler, K. A.; Peters, T. M., New methods for personal exposure monitoring for airborne particles. *Current environmental health reports* **2015,** *2*, (4), 399-411.
9. Thompson, J. E., Crowd-sourced air quality studies: A review of the literature & portable sensors. *Trends in Environmental Analytical Chemistry* **2016,** *11*, 23-34.
10. Kumar, P.; Skouloudis, A. N.; Bell, M.; Viana, M.; Carotta, M. C.; Biskos, G.; Morawska, L., Real-time sensors for indoor air monitoring and challenges ahead in deploying them to urban buildings. *Science of the Total Environment* **2016,** *560*, 150-159.
11. Njalsson, T.; Novosselov, I., Design and optimization of a compact low-cost optical particle sizer. *Journal of aerosol science* **2018,** *119*, 1-12.
12. Dong, M.; Iervolino, E.; Santagata, F.; Zhang, G.; Zhang, G., Silicon microfabrication based particulate matter sensor. *Sensors and Actuators A: Physical* **2016,** *247*, 115-124.
13. Qiao, Y.; Tao, J.; Zhang, Y.; Qiu, J.; Hong, X.; Wu, J.; Chen, C.-H., Sub-micro Particle Matter Detection for Metal Three Dimensional Printing Workshop. *IEEE Sensors Journal* **2019**.
14. Li, X.; Iervolino, E.; Santagata, F.; Wei, J.; Yuan, C.; Sarro, P.; Zhang, G. In *Miniaturized particulate matter sensor for portable air quality monitoring devices*, SENSORS, 2014 IEEE, 2014; IEEE: 2014; pp 2151-2154.

15. Intra, P.; Yawootti, A.; Tippayawong, N., An electrostatic sensor for the continuous monitoring of particulate air pollution. *Korean Journal of Chemical Engineering* **2013,** *30*, (12), 2205-2212.
16. Volckens, J.; Quinn, C.; Leith, D.; Mehaffy, J.; Henry, C. S.; Miller-Lionberg, D., Development and evaluation of an ultrasonic personal aerosol sampler. *Indoor air* **2017,** *27*, (2), 409-416.
17. Wang, Y.; Wang, Y.; Liu, X.; Liu, W.; Chen, D.; Changju, W.; Xie, J., An aerosol sensor for PM1 concentration detection based on 3D printed virtual impactor and SAW sensor. *Sensors and Actuators A: Physical* **2019**.
18. Chiriacò, M. S.; Rizzato, S.; Primiceri, E.; Spagnolo, S.; Monteduro, A. G.; Ferrara, F.; Maruccio, G., Optimization of SAW and EIS sensors suitable for environmental particulate monitoring. *Microelectronic Engineering* **2018,** *202*, 31-36.
19. Liu, J.; Hao, W.; Liu, M.; Liang, Y.; He, S., A novel particulate matter 2.5 sensor based on surface acoustic wave technology. *Applied Sciences* **2018,** *8*, (1), 82.
20. Budde, M.; El Masri, R.; Riedel, T.; Beigl, M. In *Enabling low-cost particulate matter measurement for participatory sensing scenarios*, Proceedings of the 12th international conference on mobile and ubiquitous multimedia, 2013; ACM: 2013; p 19.
21. Snik, F.; Rietjens, J. H.; Apituley, A.; Volten, H.; Mijling, B.; Di Noia, A.; Heikamp, S.; Heinsbroek, R. C.; Hasekamp, O. P.; Smit, J. M., Mapping atmospheric aerosols with a citizen science network of smartphone spectropolarimeters. *Geophysical Research Letters* **2014,** *41*, (20), 7351-7358.
22. Du, Z.; Tsow, F.; Wang, D.; Tao, N., A Miniaturized Particulate Matter Sensing Platform Based on CMOS Imager and Real-Time Image Processing. *IEEE sensors journal* **2018,** *18*, (18), 7421-7428.
23. Carminati, M.; Ferrari, G.; Sampietro, M., Emerging miniaturized technologies for airborne particulate matter pervasive monitoring. *Measurement* **2017,** *101*, 250-256.
24. Yang, J.; Shen, R.; Wang, C.; Li, X.; Liu, Y.; Xu, K.; Chen, W. In *A novel sensor for detecting PM 2.5 concentration based on refractive index sensing of a photonic crystal fiber*, Photonic and Phononic Properties of Engineered Nanostructures VIII, 2018; International Society for Optics and Photonics: 2018; p 105412K.
25. Zhu, J.; Özdemir, Ş. K.; He, L.; Chen, D.-R.; Yang, L., Single virus and nanoparticle size spectrometry by whispering-gallery-mode microcavities. *Optics express* **2011,** *19*, (17), 16195-16206.
26. Toledo, J.; Ruiz-Díez, V.; Bertke, M.; Suryo Wasisto, H.; Peiner, E.; Sánchez-Rojas, J. L., Piezoelectric MEMS Resonators for Cigarette Particle Detection. *Micromachines* **2019,** *10*, (2), 145.
27. Paprotny, I.; Doering, F.; Solomon, P. A.; White, R. M.; Gundel, L. A., Microfabricated air-microfluidic sensor for personal monitoring of airborne particulate matter: Design, fabrication, and experimental results. *Sensors and Actuators A: Physical* **2013,** *201*, 506-516.
28. Zhao, J.; Liu, M.; Liang, L.; Wang, W.; Xie, J., Airborne particulate matter classification and concentration detection based on 3D printed virtual impactor and quartz crystal microbalance sensor. *Sensors and Actuators A: Physical* **2016,** *238*, 379-388.

29. Austin, E.; Novosselov, I.; Seto, E.; Yost, M. G., Laboratory evaluation of the Shinyei PPD42NS low-cost particulate matter sensor. *PloS one* **2015,** *10*, (9), e0137789.
30. Wang, Y.; Li, J.; Jing, H.; Zhang, Q.; Jiang, J.; Biswas, P., Laboratory evaluation and calibration of three low-cost particle sensors for particulate matter measurement. *Aerosol Science and Technology* **2015,** *49*, (11), 1063-1077.
31. Liu, D.; Zhang, Q.; Jiang, J.; Chen, D.-R., Performance calibration of low-cost and portable particular matter (PM) sensors. *Journal of Aerosol Science* **2017,** *112*, 1-10.
32. Hapidin, D. A.; Saputra, C.; Maulana, D. S.; Munir, M. M.; Khairurrijal, K., Aerosol chamber characterization for commercial particulate matter (PM) sensor evaluation. *Aerosol and Air Quality Research* **2019,** *19*, (1), 181-194.
33. Sousan, S.; Koehler, K.; Thomas, G.; Park, J. H.; Hillman, M.; Halterman, A.; Peters, T. M., Inter-comparison of low-cost sensors for measuring the mass concentration of occupational aerosols. *Aerosol Science and Technology* **2016,** *50*, (5), 462-473.
34. Kelly, K.; Whitaker, J.; Petty, A.; Widmer, C.; Dybwad, A.; Sleeth, D.; Martin, R.; Butterfield, A., Ambient and laboratory evaluation of a low-cost particulate matter sensor. *Environmental Pollution* **2017,** *221*, 491-500.
35. Johnson, K. K.; Bergin, M. H.; Russell, A. G.; Hagler, G. S., Field test of several low-cost particulate matter sensors in high and low concentration urban environments. *Aerosol Air Qual. Res* **2018,** *18*, 565-578.
36. Bewick, V.; Cheek, L.; Ball, J., Statistics review 7: Correlation and regression. *Critical care* **2003,** *7*, (6), 451.
37. Taylor, R., Interpretation of the correlation coefficient: a basic review. *Journal of diagnostic medical sonography* **1990,** *6*, (1), 35-39.
38. Sedgwick, P., Pearson's correlation coefficient. *Bmj* **2012,** *345*, e4483.
39. Smith, R. J., Use and misuse of the reduced major axis for line-fitting. *American Journal of Physical Anthropology: The Official Publication of the American Association of Physical Anthropologists* **2009,** *140*, (3), 476-486.
40. Clarke, M., The reduced major axis of a bivariate sample. *Biometrika* **1980,** *67*, (2), 441-446.
41. Ayers, G., Comment on regression analysis of air quality data. *Atmospheric Environment* **2001,** *35*, (13), 2423-2425.
42. Gao, M.; Cao, J.; Seto, E., A distributed network of low-cost continuous reading sensors to measure spatiotemporal variations of PM2. 5 in Xi'an, China. *Environmental pollution* **2015,** *199*, 56-65.
43. Weakliem, D. L., A critique of the Bayesian information criterion for model selection. *Sociological Methods & Research* **1999,** *27*, (3), 359-397.
44. Watanabe, S., A widely applicable Bayesian information criterion. *Journal of Machine Learning Research* **2013,** *14*, (Mar), 867-897.
45. Neath, A. A.; Cavanaugh, J. E., The Bayesian information criterion: background, derivation, and applications. *Wiley Interdisciplinary Reviews: Computational Statistics* **2012,** *4*, (2), 199-203.
46. Schwarz, G., Estimating the dimension of a model. *The annals of statistics* **1978,** *6*, (2), 461-464.

47. Vrieze, S. I., Model selection and psychological theory: a discussion of the differences between the Akaike information criterion (AIC) and the Bayesian information criterion (BIC). *Psychological methods* **2012,** *17*, (2), 228.
48. Zikova, N.; Masiol, M.; Chalupa, D.; Rich, D.; Ferro, A.; Hopke, P., Estimating hourly concentrations of PM2. 5 across a metropolitan area using low-cost particle monitors. *Sensors* **2017,** *17*, (8), 1922.
49. Wilcoxon, F., Individual comparisons by ranking methods. *Biometrics bulletin* **1945,** *1*, (6), 80-83.
50. Whitley, E.; Ball, J., Statistics review 6: Nonparametric methods. *Critical care* **2002,** *6*, (6), 509.
51. Crilley, L. R.; Shaw, M.; Pound, R.; Kramer, L. J.; Price, R.; Young, S.; Lewis, A. C.; Pope, F. D., Evaluation of a low-cost optical particle counter (Alphasense OPC-N2) for ambient air monitoring. *Atmospheric Measurement Techniques* **2018**, 709-720.
52. Sousan, S.; Gray, A.; Zuidema, C.; Stebounova, L.; Thomas, G.; Koehler, K.; Peters, T., Sensor Selection to Improve Estimates of Particulate Matter Concentration from a Low-Cost Network. *Sensors* **2018,** *18*, (9), 3008.
53. Chen, C.-C.; Kuo, C.-T.; Chen, S.-Y.; Lin, C.-H.; Chue, J.-J.; Hsieh, Y.-J.; Cheng, C.-W.; Wu, C.-M.; Huang, C.-M. In *Calibration of Low-Cost Particle Sensors by Using Machine-Learning Method*, 2018 IEEE Asia Pacific Conference on Circuits and Systems (APCCAS), 2018; IEEE: 2018; pp 111-114.
54. Li, J.; Li, H.; Ma, Y.; Wang, Y.; Abokifa, A. A.; Lu, C.; Biswas, P., Spatiotemporal distribution of indoor particulate matter concentration with a low-cost sensor network. *Building and Environment* **2018,** *127*, 138-147.
55. Zimmerman, N.; Presto, A. A.; Kumar, S. P.; Gu, J.; Hauryliuk, A.; Robinson, E. S.; Robinson, A. L.; Subramanian, R., A machine learning calibration model using random forests to improve sensor performance for lower-cost air quality monitoring. *Atmospheric Measurement Techniques* **2018,** *11*, (1).
56. Li, C.-R.; Lin, Y.-C.; Hung, M.-W.; Yang, C.-C.; Tsai, H.-Y.; Chang, Y.-J.; Huang, K.-C.; Hsiao, W.-T. In *Integrating temperature, humidity, and optical aerosol sensors for a wireless module for three-dimensional space monitoring*, 2018 IEEE Sensors Applications Symposium (SAS), 2018; IEEE: 2018; pp 1-4.
57. Wang, K.; Chen, F.-e.; Au, W.; Zhao, Z.; Xia, Z.-l., Evaluating the feasibility of a personal particle exposure monitor in outdoor and indoor microenvironments in Shanghai, China. *International journal of environmental health research* **2019,** *29*, (2), 209-220.
58. Jayaratne, R.; Liu, X.; Thai, P.; Dunbabin, M.; Morawska, L., The influence of humidity on the performance of a low-cost air particle mass sensor and the effect of atmospheric fog. *Atmospheric Measurement Techniques* **2018,** *11*, (8), 4883-4890.
59. Sayahi, T.; Butterfield, A.; Kelly, K., Long-term field evaluation of the Plantower PMS low-cost particulate matter sensors. *Environmental Pollution* **2019,** *245*, 932-940.
60. Zheng, T.; Bergin, M. H.; Johnson, K. K.; Tripathi, S. N.; Shirodkar, S.; Landis, M. S.; Sutaria, R.; Carlson, D. E., Field evaluation of low-cost particulate matter sensors in high-and

low-concentration environments. *Atmospheric Measurement Techniques* **2018,** *11*, (8), 4823-4846.
61. Zamora, L. M.; Xiong, F.; Gentner, D.; Kerkez, B.; Kohrman-Glaser, J.; Koehler, K., Field and Laboratory Evaluations of the Low-Cost Plantower Particulate Matter Sensor. *Environmental science & technology* **2018,** *53*, (2), 838-849.
62. Di Antonio, A.; Popoola, O.; Ouyang, B.; Saffell, J.; Jones, R., Developing a relative humidity correction for low-cost sensors measuring ambient particulate matter. *Sensors* **2018,** *18*, (9), 2790.
63. N Genikomsakis, K.; Galatoulas, N.-F.; I Dallas, P.; Candanedo Ibarra, L.; Margaritis, D.; S Ioakimidis, C., Development and On-Field testing of Low-Cost portable system for monitoring PM2. 5 concentrations. *Sensors* **2018,** *18*, (4), 1056.
64. Malings, C.; Tanzer, R.; Hauryliuk, A.; Saha, P. K.; Robinson, A. L.; Presto, A. A.; Subramanian, R., Fine Particle Mass Monitoring with Low-Cost Sensors: Corrections and Long-Term Performance Evaluation. **2018**.
65. Malings, C.; Tanzer, R.; Hauryliuk, A.; Saha, P. K.; Robinson, A. L.; Subramanian, R.; Presto, A. A., Correction and Long-Term Performance Evaluation of Fine Particulate Mass Monitoring with Low-Cost Sensors. **2018**.
66. Waggoner, A. P.; Weiss, R. E.; Ahlquist, N. C.; Covert, D. S.; Will, S.; Charlson, R. J., Optical characteristics of atmospheric aerosols. *Atmospheric Environment (1967)* **1981,** *15*, (10-11), 1891-1909.
67. McMurry, P. H.; Stolzenburg, M. R., On the sensitivity of particle size to relative humidity for Los Angeles aerosols. *Atmospheric Environment (1967)* **1989,** *23*, (2), 497-507.
68. Hess, M.; Koepke, P.; Schult, I., Optical properties of aerosols and clouds: The software package OPAC. *Bulletin of the American meteorological society* **1998,** *79*, (5), 831-844.
69. Shettle, E. P.; Fenn, R. W. *Models for the aerosols of the lower atmosphere and the effects of humidity variations on their optical properties*; Air Force Geophysics Lab Hanscom Afb Ma: 1979.
70. Steele, H. M.; Hamill, P., Effects of temperature and humidity on the growth and optical properties of sulphuric acid—water droplets in the stratosphere. *Journal of aerosol science* **1981,** *12*, (6), 517-528.
71. Kaiser, H.; Specker, H., Bewertung und vergleich von analysenverfahren. *Fresenius' Journal of Analytical Chemistry* **1956,** *149*, (1), 46-66.
72. EPA, 40 CFR Parts 58-Ambient Air Quality Surveillance (Subchapter C). In Environmental Protection Agency Washington, DC: 2016.
73. Bartley, D. L.; Shulman, S. A.; Schlecht, P. C., Measurement uncertainty and NIOSH method accuracy range. *NIOSH manual of analytical methods* **2003**, 208-228.
74. Long, R.; Beaver, M.; Williams, R.; Kronmiller, K.; Garvey, S., Procedures and Concepts of EPA's Ongoing Sensor Evaluation Efforts. *EM (Air Waste Manage. Assoc.)* **2014,** *8*.
75. Manikonda, A.; Zíková, N.; Hopke, P. K.; Ferro, A. R., Laboratory assessment of low-cost PM monitors. *Journal of Aerosol Science* **2016,** *102*, 29-40.

76. Reece, S.; Williams, R.; Colón, M.; Southgate, D.; Huertas, E.; O'Shea, M.; Iglesias, A.; Sheridan, P., Spatial-Temporal Analysis of PM2. 5 and NO2 Concentrations Collected Using Low-Cost Sensors in Peñuelas, Puerto Rico. *Sensors* **2018,** *18*, (12), 4314.
77. Williams, R.; Kilaru, V.; Snyder, E.; Kaufman, A.; Dye, T.; Rutter, A.; Russell, A.; Hafner, H., Air sensor guidebook. *US Environmental Protection Agency* **2014**.
78. Clements, A. L.; Griswold, W. G.; Rs, A.; Johnston, J. E.; Herting, M. M.; Thorson, J.; Collier-Oxandale, A.; Hannigan, M., Low-cost air quality monitoring tools: from research to practice (a workshop summary). *Sensors* **2017,** *17*, (11), 2478.
79. Papapostolou, V.; Zhang, H.; Feenstra, B. J.; Polidori, A., Development of an environmental chamber for evaluating the performance of low-cost air quality sensors under controlled conditions. *Atmospheric environment* **2017,** *171*, 82-90.
80. Li, H. Z.; Gu, P.; Ye, Q.; Zimmerman, N.; Robinson, E. S.; Subramanian, R.; Apte, J. S.; Robinson, A. L.; Presto, A. A., Spatially dense air pollutant sampling: Implications of spatial variability on the representativeness of stationary air pollutant monitors. *Atmospheric Environment: X* **2019**, 100012.
81. Saha, P. K.; Zimmerman, N.; Malings, C.; Hauryliuk, A.; Li, Z.; Snell, L.; Subramanian, R.; Lipsky, E.; Apte, J. S.; Robinson, A. L., Quantifying high-resolution spatial variations and local source impacts of urban ultrafine particle concentrations. *Science of the Total Environment* **2019,** *655*, 473-481.
82. Steinle, S.; Reis, S.; Sabel, C. E., Quantifying human exposure to air pollution—Moving from static monitoring to spatio-temporally resolved personal exposure assessment. *Science of the Total Environment* **2013,** *443*, 184-193.
83. Ngo, N. S.; Asseko, S. V. J.; Ebanega, M. O.; Allo'o, S. M. A. o.; Hystad, P., The relationship among PM2. 5, traffic emissions, and socioeconomic status: Evidence from Gabon using low-cost, portable air quality monitors. *Transportation Research Part D: Transport and Environment* **2018**.
84. Blanco, M. N.; Fenske, R. A.; Kasner, E. J.; Yost, M. G.; Seto, E.; Austin, E., Real-time monitoring of spray drift from three different Orchard Sprayers. *Chemosphere* **2019**.
85. Schwarz, A. D.; Meyer, J.; Dittler, A., Opportunities for Low-Cost Particulate Matter Sensors in Filter Emission Measurements. *Chemical Engineering & Technology* **2018,** *41*, (9), 1826-1832.
86. Mazaheri, M.; Clifford, S.; Yeganeh, B.; Viana, M.; Rizza, V.; Flament, R.; Buonanno, G.; Morawska, L., Investigations into factors affecting personal exposure to particles in urban microenvironments using low-cost sensors. *Environment international* **2018,** *120*, 496-504.
87. Subramanian, R.; Ellis, A.; Torres-Delgado, E.; Tanzer, R.; Malings, C.; Rivera, F.; Morales, M.; Baumgardner, D.; Presto, A.; Mayol-Bracero, O. L., Air quality in Puerto Rico in the aftermath of hurricane Maria: a case study on the use of lower cost air quality monitors. *ACS Earth and Space Chemistry* **2018,** *2*, (11), 1179-1186.
88. Patel, S.; Li, J.; Pandey, A.; Pervez, S.; Chakrabarty, R. K.; Biswas, P., Spatio-temporal measurement of indoor particulate matter concentrations using a wireless network of low-cost sensors in households using solid fuels. *Environmental research* **2017,** *152*, 59-65.

89. Curto, A.; Donaire-Gonzalez, D.; Barrera-Gómez, J.; Marshall, J. D.; Nieuwenhuijsen, M. J.; Wellenius, G. A.; Tonne, C., Performance of low-cost monitors to assess household air pollution. *Environmental research* **2018,** *163*, 53-63.
90. Dobson, R.; Semple, S., "How do you know those particles are from cigarettes?": An algorithm to help differentiate second-hand tobacco smoke from background sources of household fine particulate matter. *Environmental research* **2018,** *166*, 344-347.
91. Thomas, G.; Sousan, S.; Tatum, M.; Liu, X.; Zuidema, C.; Fitzpatrick, M.; Koehler, K.; Peters, T., Low-cost, distributed environmental monitors for factory worker health. *Sensors* **2018,** *18*, (5), 1411.
92. Cheng, H.; Wang, L.; Wang, D.; Zhang, J.; Cheng, L.; Yao, P.; Zhang, Z.; Di Narzo, A.; Shen, Y.; Yu, J., Bio3Air, an integrative system for monitoring individual-level air pollutant exposure with high time and spatial resolution. *Ecotoxicology and environmental safety* **2019,** *169*, 756-763.
93. Rogulski, M., Using Low-Cost PM Monitors to Detect Local Changes of Air Quality. *Polish Journal of Environmental Studies* **2018,** *27*, (4).
94. Penza, M.; Suriano, D.; Villani, M. G.; Spinelle, L.; Gerboles, M. In *Towards air quality indices in smart cities by calibrated low-cost sensors applied to networks*, SENSORS, 2014 IEEE, 2014; IEEE: 2014; pp 2012-2017.
95. Steinle, S.; Reis, S.; Sabel, C. E.; Semple, S.; Twigg, M. M.; Braban, C. F.; Leeson, S. R.; Heal, M. R.; Harrison, D.; Lin, C., Personal exposure monitoring of PM2. 5 in indoor and outdoor microenvironments. *Science of the Total Environment* **2015,** *508*, 383-394.
96. Leaffer, D.; Wolfe, C.; Doroff, S.; Gute, D.; Wang, G.; Ryan, P., Wearable Ultrafine Particle and Noise Monitoring Sensors Jointly Measure Personal Co-Exposures in a Pediatric Population. *International journal of environmental research and public health* **2019,** *16*, (3), 308.
97. Hu, R.; Wang, S.; Aunan, K.; Zhao, M.; Chen, L.; Liu, Z.; Hansen, M. H., Personal Exposure to PM 2.5 in Chinese rural households in the Yangtze River Delta. *Indoor air* **2019**.
98. SM, S. N.; Yasa, P. R.; Narayana, M.; Khadirnaikar, S.; Rani, P., Mobile monitoring of air pollution using low cost sensors to visualize spatio-temporal variation of pollutants at urban hotspots. *Sustainable Cities and Society* **2019,** *44*, 520-535.
99. Yang, F.; Lau, C. F.; Tong, V. W. T.; Zhang, K. K.; Westerdahl, D.; Ng, S.; Ning, Z., Assessment of personal integrated exposure to fine particulate matter of urban residents in Hong Kong. *Journal of the Air & Waste Management Association* **2019,** *69*, (1), 47-57.
100. Cheng, K.-C.; Tseng, C.-H.; Hildemann, L. M., Using Indoor Positioning and Mobile Sensing for Spatial Exposure and Environmental Characterizations: Pilot Demonstration of PM2. 5 Mapping. *Environmental Science & Technology Letters* **2019**.
101. Gu, Q.; Jia, C. In *A Consumer UAV-based Air Quality Monitoring System for Smart Cities*, 2019 IEEE International Conference on Consumer Electronics (ICCE), 2019; IEEE: 2019; pp 1-6.
102. Mayuga, G. P.; Favila, C.; Oppus, C.; Macatulad, E.; Lim, L. H. In *Airborne Particulate Matter Monitoring Using UAVs for Smart Cities and Urban Areas*, TENCON 2018-2018 IEEE Region 10 Conference, 2018; IEEE: 2018; pp 1398-1402.

103. Wilson, J. G.; Kingham, S.; Pearce, J.; Sturman, A. P., A review of intraurban variations in particulate air pollution: Implications for epidemiological research. *Atmospheric Environment* **2005,** *39*, (34), 6444-6462.
104. Wongphatarakul, V.; Friedlander, S.; Pinto, J., A comparative study of PM2. 5 ambient aerosol chemical databases. *Environmental Science & Technology* **1998,** *32*, (24), 3926-3934.
105. Rajasegarar, S.; Zhang, P.; Zhou, Y.; Karunasekera, S.; Leckie, C.; Palaniswami, M. In *High resolution spatio-temporal monitoring of air pollutants using wireless sensor networks*, 2014 IEEE Ninth International Conference on Intelligent Sensors, Sensor Networks and Information Processing (ISSNIP), 2014; IEEE: 2014; pp 1-6.
106. Rajasegarar, S.; Havens, T. C.; Karunasekera, S.; Leckie, C.; Bezdek, J. C.; Jamriska, M.; Gunatilaka, A.; Skvortsov, A.; Palaniswami, M., High-resolution monitoring of atmospheric pollutants using a system of low-cost sensors. *IEEE transactions on geoscience and remote sensing* **2014,** *52*, (7), 3823-3832.
107. Lam, N. S.-N., Spatial interpolation methods: a review. *The American Cartographer* **1983,** *10*, (2), 129-150.
108. Li, J.; Heap, A. D., A review of spatial interpolation methods for environmental scientists. **2008**.
109. Li, J.; Heap, A. D., A review of comparative studies of spatial interpolation methods in environmental sciences: performance and impact factors. *Ecological Informatics* **2011,** *6*, (3-4), 228-241.
110. Mitas, L.; Mitasova, H., Spatial interpolation. *Geographical information systems: principles, techniques, management and applications* **1999,** *1*, (2).
111. Masiol, M.; Zíková, N.; Chalupa, D. C.; Rich, D. Q.; Ferro, A. R.; Hopke, P. K., Hourly land-use regression models based on low-cost PM monitor data. *Environmental research* **2018,** *167*, 7-14.
112. Gupta, P.; Doraiswamy, P.; Levy, R.; Pikelnaya, O.; Maibach, J.; Feenstra, B.; Polidori, A.; Kiros, F.; Mills, K., Impact of California Fires on Local and Regional Air Quality: The Role of a Low-Cost Sensor Network and Satellite Observations. *GeoHealth* **2018**.

Chapter 2: Laboratory evaluation and calibration of three low-cost particle sensors for particulate matter measurement

The results of this chapter have been published in Wang, Y., Li, J., Jing, H., Zhang, Q., Jiang, J., & Biswas, P. (2015). Laboratory evaluation and calibration of three low-cost particle sensors for particulate matter measurement. Aerosol Science and Technology, 49(11), 1063-1077.

Abstract

Particle sensors offer significant advantages of compact size and low cost, and have recently drawn great attention for usage as portable monitors measuring particulate matter mass concentrations. However, most sensor systems have not been thoroughly evaluated with standardized calibration protocols, and their data quality is not well documented. In this work, three low-cost particle sensors based on light scattering (Shinyei PPD42NS, Samyoung DSM501A, and Sharp GP2Y1010AU0F) were evaluated by calibration methods adapted from the US EPA 2013 Air Sensor Workshop recommendations. With a SidePak (TSI Inc.), a scanning mobility particle sizer (TSI Inc.), and an AirAssure^{TM} $PM_{2.5}$ Indoor Air Quality Monitor (TSI Inc.) which itself relies on a GP2Y1010AU0F sensor as reference instruments, six performance aspects were examined: linearity of response, precision of measurement, limit of detection, dependence on particle composition, dependence on particle size, and relative humidity and temperature influences. This work found that: a) All three sensors demonstrated high linearity against SidePak measured concentrations, with R^2 values higher than 0.8914 in the particle concentration range of 0 to 1000 $\mu g/m^3$, and the linearity depended on the studied range of particle concentrations; b) The standard deviations of the sensors varied from 15 to 90 $\mu g/m^3$ for a concentration range of 0 to 1000 $\mu g/m^3$; c) The outputs of all three sensors depended highly on particle composition and size, resulting in as high as 10 times difference in the sensor outputs; and d) Humidity affected the sensor response. This paper provides further recommendations for applications of the three tested sensors.

2.1 Introduction

Particulate matter (PM) is an important parameter in determining air quality, affecting visibility (Guo et al., 2014), human health (Biswas and Wu, 2005; Karlsson et al., 2009), and global climate (Stocker et al., 2013). The size of PM is closely related to the inhalation and deposition properties of particles in the human respiratory system (Phalen et al., 1991). PM concentration can be quantified as PM_{10}, $PM_{2.5}$, or PM_1, according to the mass concentrations of particles below the aerodynamic sizes of 10 μm, 2.5 μm, and 1 μm, respectively. The US EPA-approved instruments for measuring PM concentrations include impactors, cyclones, tapered element oscillating microbalances (TEOM), and beta attenuation monitors (BAM) (EPA, 2013). Other instruments, such as the DustTrak™ and SidePak™ (TSI Inc.) use light scattering to obtain particle mass concentrations, while scanning mobility particle sizers (SMPS) (Knutson and Whitby, 1975; Wang and Flagan, 1990) and aerodynamic particle sizer (APS) derive particle mass concentrations from measured particle size distributions.

Temporal and spatial PM aggregate concentrations may vary significantly in a region. The PM concentrations provided by a single monitoring site may not accurately represent the particle concentrations around people distributed in its vicinity, who may be concerned about the health effects of PM exposure. In recent years, this concern has become especially acute in developing countries that are industrializing (Huang et al., 2014; Cao et al., 2013; Tiwari et al., 2013). To keep the citizens updated on air quality information through additional sources, the US embassy and consulates have started to measure and post the real-time PM concentrations in these countries. However, the embassy websites also emphasize that,

"citywide analysis cannot be done, on data from a single machine (US Embassy, 2015)." In order to obtain accurate PM concentrations with good resolution, a high density of measurement sites is required, and the cost associated with the conventional instruments mentioned above makes this impractical. Based on techniques first developed for smoke detectors decades ago (Mulholland and Liu, 1980), portable PM monitors have become popular in recent years (Hagler et al., 2014), driven by their remarkably low price and the emerging need for real-time "big data" reporting of local air quality (Chong and Kumar, 2003; Leavey et al., 2015). These particle sensors can be used in locating pollution hotspots or generating coarse 3-D maps of PM concentrations (Rajasegarar et al., 2014). In a broader sense, the usage of low-cost particle sensors also raises social awareness of air quality.

Particle sensors using light scattering are cheaper and more compact than sensors using the single particle counting method or other mechanical methods, and hence have drawn more attention from researchers in recent years (Weekly et al., 2013; Holstius et al., 2014;). A light scattering PM sensor is typically composed of an infrared emitting diode (IRED), a phototransistor (PT), and focusing lenses. While passing through the sensor, particles scatter light, and the intensity of the light received by the phototransistor is directly correlated with the concentration of particles. The light scattering of particles falls into different regimes (Friedlander, 2000), and the Rayleigh regime and Mie regime are often encountered for particles in micrometer size or smaller. Compared to sensors using single particle counting techniques, light scattering PM sensors measures the optical properties of the particles as an

ensemble. This feature greatly reduces the cost and size of the sensors; however, at the same time, it limits their measurement accuracy (Holstius et al., 2014; Gao et al., 2015).

Three models of light scattering particle sensors, the PPD42NS (Shinyei Inc.), DSM501A (Samyoung Inc.), and GP2Y1010AU0F (Sharp Inc.) are currently available to customers as single modules, which are simple to assemble, install, and use. Each sensor has been evaluated separately in previous work, and a qualitative match was observed between their outputs and the total mass concentrations obtained by established instruments (Nafis, 2012; Gao et al., 2015; Holstius et al., 2014; Olivares et al., 2012; Weekly et al., 2013). Further experiments were conducted on deploying the particle sensors for correlation with gas sensors (Olivares et al., 2012), monitoring occupancy in public space (Weekly et al., 2013), and measuring particle concentrations in field tests (Gao et al., 2015; Holstius et al., 2014). The PPD42NS sensor and GP2Y1010AU0F sensor have also been packaged in commercialized particle monitors, such as the AirAssure $PM_{2.5}$ Indoor Air Quality Monitor (TSI Inc.), which was tested in this study, the Air Box™ (Haier Inc.), and the Pervasive Air-Quality Monitor (PAM, Air-Scientific). To fulfill the need for smaller, cheaper, and more accurate particle monitors, other sensors have also been designed (Litton et al., 2004; Chowdhury et al., 2007), calibrated (Edwards et al., 2006), and applied in field studies (Chowdhury et al., 2007; Sahu et al., 2011).

Up until now, no parallel comparison among these sensors has been conducted. At the same time, the lack of studies using a standard protocol assessing the particle sensors has hindered

a comprehensive understanding of their performance. Several calibration protocols have been designed and used to calibrate air quality sensors (Spinelle et al., 2013; Long et al., 2014). The 2013 US EPA Air Sensor Workshop recommended seven parameters to be investigated upon the receipt of a new air quality sensor device from its developer or manufacturer: (1) Linearity of response, (2) Precision of measurements, (3) Limit of detection, (4) Concentration resolution, (5) Response time, (6) Interference equivalents, and (7) Relative humidity (RH) and temperature influences. Among these parameters, concentration resolution is reflected in the precision of measurements, as introduced in the EPA workshop summary (Long et al., 2014). For particle sensors using light scattering method, the light transfer time in the sensors can be ignored, and their response time is mainly determined by the electron transport time in the circuits, which can also be neglected. The interference equivalent does not need to be considered, since, unlike gas sensors, for which equivalent species can cause similar responses, particle sensors are affected by concentrations and properties of particles only. Particle composition critically affects the performance of light scattering sensors. Light scattering depends on the refractive indices of materials, while the light absorption of materials may also affect the intensity of light received by the phototransistor. The size of particles also directly influences the light scattering coefficient and absorption coefficient. Previous analyses indicated that particle mass concentrations determined by nephelometry, which is also based on light scattering, have an irreducible uncertainty of approximately ± 30 to 40%, which is directly attributable to the natural variability of $PM_{2.5}$ aerosol parameters, including particle concentration, particle refractive

index, particle size, and particle morphology (Molenar, 2005). Therefore, for evaluating light scattering particle sensors, the original EPA list of seven parameters was altered. Concentration resolution, response time, and interference equivalents were dropped, and particle composition and size dependence were added.

In this study, the performance of three low-cost light scattering particle sensors was compared for the first time against commonly used instruments in air quality research, a SidePak and a SMPS. The laboratory evaluation and calibration used a revised protocol provided by the EPA 2013 Air Sensor Workshop to obtain a comprehensive understanding of sensor performance.

2.2 Calibration platform

A calibration platform was built for testing the performance of the sensors. Detailed descriptions of the sensors, the reference instruments, the chamber, and the operating principles for the measurement are as follows.

2.2.1 Particle sensors and reference instrument

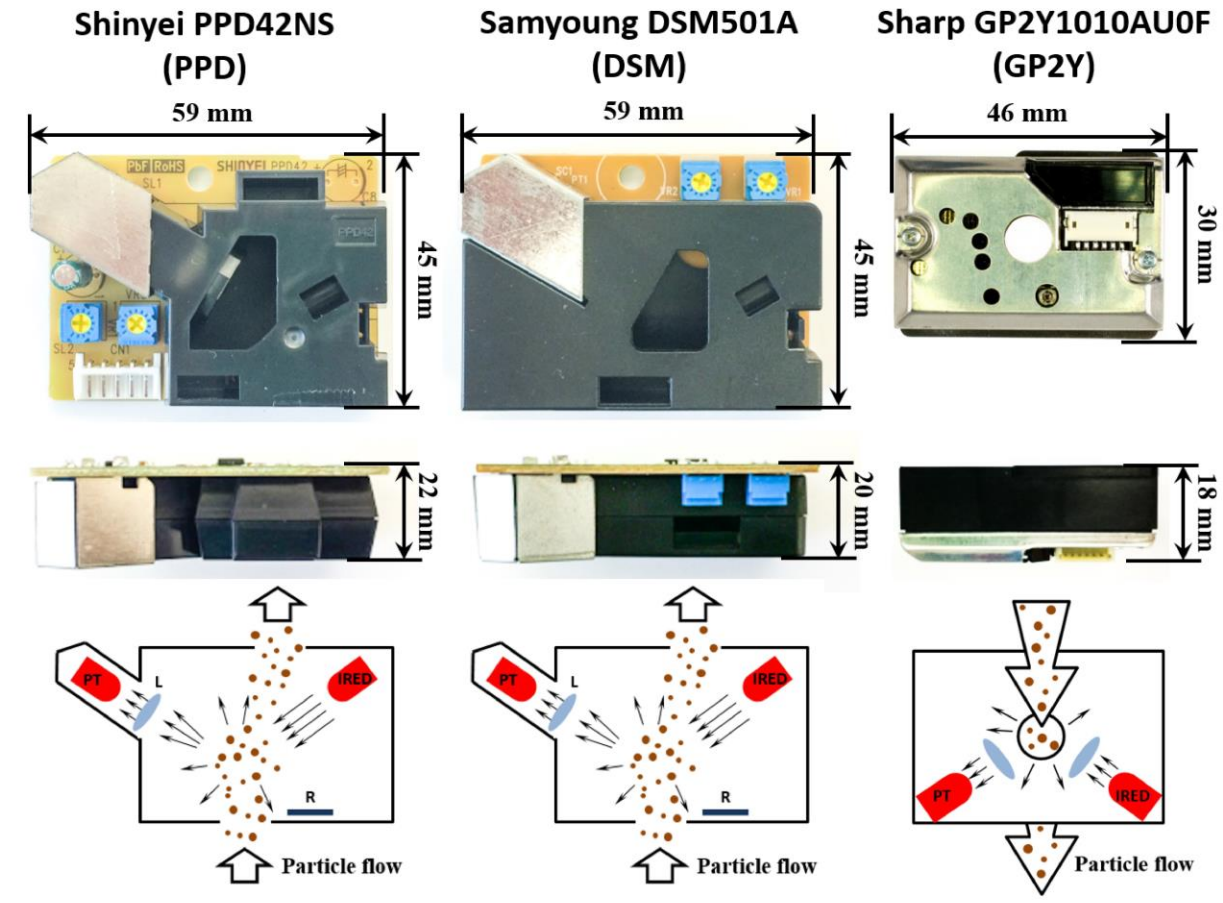

Figure 2.1 Dimensions, geometries and schematic diagrams of the sensors evaluated in this work. The sensors in the figure do not represent actual sizes. In the schematic diagrams shown in the third row, PT, IRED, and R stand for phototransistor, infrared emitting diode, and thermal resistor, respectively.

Table 2.1 Specifications of the tested sensors.

Model	**PPD42NS**	**DSM501A**	**GP2Y1010AU0F**
Abbreviation used in this work	PPD	DSM	GP2Y
Dimension W×H×D (mm)	59×45×22	59×45×20	46×30×18
Detectable PM size range	~1 μm	~1 μm	N/A
Operation voltage	5±0.5 V	5±0.5 V	5±0.5 V
Current consumption	<90mA	<90mA	<20mA
Maximum detectable concentration	28000 #/L	1400 μg /L	500 $\mu g/m^3$
Operation temperature	0 ~ +45 ºC	-10 ~ +65 ºC	-10 ~ +65 ºC
Operation humidity	<95%	<95%	N/A
Sensitivity	N/A	N/A	0.35-0.65V/(100μg/m3)
Output signal	Pulse width modulation	Pulse width modulation	Analog output
Cost (USD)	~$ 15.9	~$ 13.8	~$ 10.0

The Shinyei PPD42NS, Samyoung DSM501A, and Sharp GP2Y1010AU0F sensors were evaluated in this work. For simplification, the three sensors are named “PPD”, “DSM”, and “GP2Y” in the following, respectively. The geometries, schematic diagrams, and specifications of the three sensors are displayed in Figure 2.1 and Table 2.1. The PPD and DSM sensors share a similar geometry. Both use thermal resistors to generate heat so that natural convection creates an updraft of particles that flow through the light scattering region. The GP2Y sensor is smaller than the PPD and DSM sensors. Unlike the PPD and DSM sensors which are self-aspirated through the application of thermal resistors, the GP2Y sensor relies on a hole through the center of the body to allow for the convection of particles. The orientation of the GP2Y sensor is therefore different from the other two types of sensors, as discussed in the next section. Also, the GP2Y sensors with and without regulated external

convection may respond differently under the same particle concentrations. All the tested particle sensors use IREDs for light generation, and commonly used IREDs generate light with wavelengths between 870 to 980 nm (Schubert, 2005).

The PPD and DSM sensors were controlled by a LabVIEW program through a data acquisition system (NI 6008, National Instruments Inc.). Both sensors output modulated pulses, whose Lo Pulse Occupancy (LPO, percentage of time during which the sensors output a low voltage in a total sampling time of 30 seconds) was directly correlated with the particle concentrations. Due to the need for an external high frequency square wave to trigger the diode in the sensor, the GP2Y sensor was connected to a programmed Arduino data acquisition board (UNO Rev 3, Arduino Inc.). The particle concentration for the GP2Y was represented by the magnitude of the output voltage. While the GP2Y has a finer time resolution for data collection, to be consistent with the PPD and DSM which have a sampling resolution of 30 s, the data for all three sensors were collected by the computer every 30 seconds.

A SidePak Personal Aerosol Monitor AM510 (TSI Inc.), a scanning mobility particle sizer (SMPS, TSI Inc.), and an AirAssure $PM_{2.5}$ Indoor Air Quality Monitor (TSI Inc.) were used to provide reference measurement results to evaluate the performance of the sensors. Like the sensors, the SidePak also uses light scattering, while the flow of particles is regulated by a small built-in vacuum pump. A user-defined calibration factor was used to compensate for differences in the particulate materials' refractive indices. In the experiments, the calibration

factor of the SidePak was set to 1.0, because the study mainly focused on the linearity and precision of the measurements, while the calibration factor could be added in data processing.

The SMPS uses a differential mobility analyzer (DMA) to classify particles as a function of electrical mobility size, and a condensation particle counter (CPC) to measure particle concentrations. A continuous particle size distribution function is obtained through data inversion, which relates particle concentration to the charging efficiency of the neutralizer, the detection efficiency of the CPC, and the transfer function of the DMA (Stolzenburg and McMurry, 2008). The mass concentration is then calculated through the integration of the product of the size distribution function and particle mass of each size. If the particles follow lognormal distributions, the method of moments is a simple approach to calculate the mass concentrations (Hinds, 1982), as elaborated in Section 4.4.

The AirAssure $PM_{2.5}$ Indoor Air Quality Monitor utilizes a Sharp GP2Y sensor and regulates the flow through the sensor via a fan attached at one side of the sensor, so that particles pass through the sensor by convective flow instead of random diffusion. A specialized algorithm averages the particle concentrations over a period time to provide more accurate results. In order to study the effect of these modifications to the sensor prototype, a comparison between the GP2Y sensors without convective flow and the AirAssure monitor was conducted, focusing on the linearity of response and the precision of measurements.

2.2.2 Chamber for particle measurement

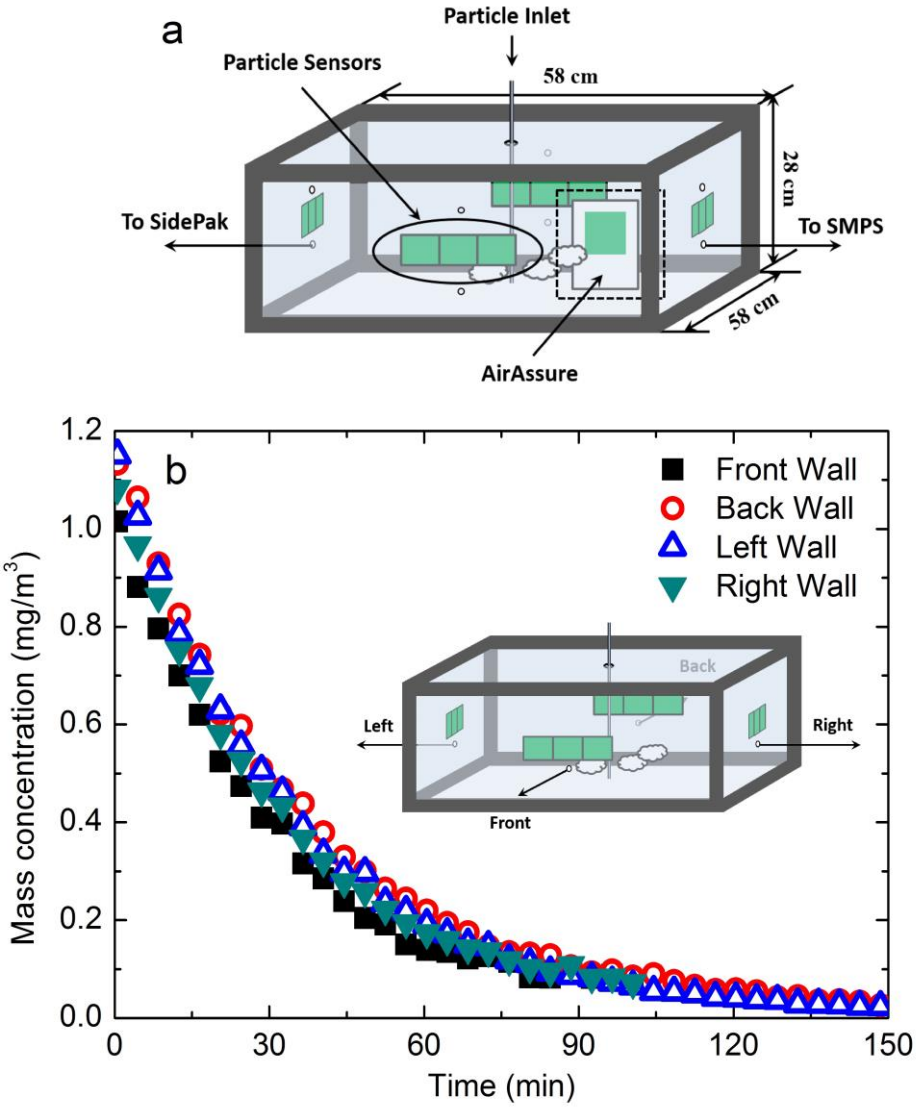

Figure 2.2 (a) Schematic diagram of the chamber for particle measurement and the arrangement of particle sensors. There are two ports on each vertical side of the chamber. The upper four ports were used for passing the electrical leads. The lower four ports allowed for particle sampling, including testing the sensor performance, where two ports were used by the SidePak and the SMPS; and testing the uniformity of the particle distribution, where all the four ports were used by the SidePak (Figure 2.2b). During the experiments, the unused ports were plugged. The AirAssure monitor (marked with a dashed box) was placed in the chamber only when comparing the performance with the GP2Y sensors without convective flow. (b) Particle mass concentrations measured from the four sides of the chamber. The results indicate that particles were uniformly distributed.

The evaluation of the particle sensors was conducted in a custom-built acrylic glass chamber with dimensions of 58×58×28 cm (Figure 2.2a). The edges of the chamber were sealed with rubber strips to prevent the leakage of particles and provide a uniform distribution of particles. Ports with a uniform diameter of 5 mm were drilled on the walls of the chamber to allow for sampling and passing electrical leads. During the experiments, the unused ports were snugly plugged. Generated particles were introduced into the center of the chamber via a stainless-steel tube. One sensor of each type was taped to each vertical side of the chamber, and the three tested sensors were attached as closely as possible to minimize the spatial differences in particle concentrations, although the concentration variance in the chamber was found to be small (Figure 2.2b). The PPD and DSM sensors were fixed with their backs facing the chamber wall, so that a vertical updraft of the particles could be generated. The GP2Y sensors were placed with the front panel facing the bottom of the chamber so that particles could pass through the hole in its center. In this study, due to the relatively large size of the test chamber and the limited air exchange rates, forced convection through mixing fans created an uneven distribution of particles. To maintain a uniform particle concentration at the four sides of the chamber walls, generated particles were transported mainly by random diffusion. As indicated in Figure 2.2b, the difference in particle concentrations at the four sides of the chamber was within 15%. This variation in particle concentration might result in different outputs of the four sensors of each type, but it was not the major reason for the deviation of the response of some sensors, as discussed in Section 4.1. The SidePak and SMPS were outside the chamber, and particle streams were sampled via tubes located 2 cm

below the sensors on two side walls of the chamber, at flow rates of 0.7 lpm and 0.3 lpm, respectively. The AirAssure monitor was not placed in the chamber until when conducting the comparison with the GP2Y sensors without regulated flows. Note that the convective flow regulated by the fan inside the AirAssure monitor might disturb the uniform distribution of particles in the chamber, possibly lead to some error in data analysis.

In the experiments, test particles were introduced into the chamber till the SidePak gave a mass concentration reading of around 5 mg/m^3, which is above the upper limit of the tested sensors as found in Section 4.1. The particle flow was discontinued and the system was allowed to equilibrate so that a uniform distribution of particle concentration and size distribution was obtained in the chamber. Due to particle precipitation and wall loss, the concentration of particles inside the chamber dropped gradually. Simultaneous measurements with the sensors, the SidePak, and the SMPS started when the mass concentration given by the SidePak was below 1 mg/m^3, which is slightly above the typical PM concentrations in highly polluted cities (Guo et al., 2014; Tiwari et al., 2013; Zhao et al., 2013). The whole process took approximately 2.5 hr (Figure 2.2b), which was close to the gravitational precipitation time for a 1 μm (aerodynamic size) particle to drop from the top to the bottom of the chamber (~ 2.4 hr). Hence, the evaluation results of the particle sensors were representative for PM_1 measurements.

2.3 Assessment aspects

Table 2.2 Experimental plan for the evaluation and calibration of the particle sensors PPD, DSM and GP2Y.

Test #	Assessment aspect	Source of Particles	Reference Instruments
1	**Linearity of response**	Incense burning	SidePak, AirAssure
2	**Concentration resolution**	Incense burning	SidePak, AirAssure
3	**Limit of Detection**	Incense burning	SidePak
4	**Dependence on composition**	Atomized NaCl, sucrose, and NH_4NO_3 particles	SidePak, SMPS
5	**Sensitivity to particle size**	Atomized PSL spheres with 300, 600, 900 nm	SidePak, SMPS
6	**RH and temperature influence**	Atomized NaCl particles	SidePak, SMPS

Six aspects of the sensor performance were studied in order to comprehensively understand their characteristics. Table 2 shows a brief summary of the experimental plan.

2.3.1 Linearity of response

The linearity of response was assessed using the least squares regression and Reduced Major Axis (RMA) regression after plotting the outputs of the sensors against the SidePak measured particle mass concentrations. Particles were generated by burning incense (Sandalum Agarbathi Cones, Cycle Brand), which is reported to be an important source of indoor aerosol in certain countries (Cheng, et al., 1995). The size distributions of the incense-generated particles as a function of time are displayed in Figure A1.1 in the supplemental information. Averaged outputs from the sensors on four sides of the chamber were used to evaluate their

linearity. In the study, the particle mass concentrations measured by the SidePak were used as the independent variable, while the sensor outputs were reported as the dependent variables. Due to the existing uncertainty of the SidePak measured particle concentrations, the least squares regression may not be an adequate method to evaluate linearity. The RMA regression is specifically formulated to consider the errors in both the dependent and independent variables (Sokal and Rohlf, 1981; McDonald, 2009). Linear correlations, together with R^2 values, via the RMA regression and least squares regression were calculated. The RMA regression analysis was conducted with software designed by Bohonak and Linde (2004).

2.3.2 Precision of measurements

The precision of the sensors was represented by their accuracy and repeatability of their measurements. The accuracy means the closeness between the measured results and the actual results, while the repeatability means the spread of the measured values (Petrozzi, 2012). Due to the lack of a universal calibration curve for the three tested sensors, the linear correlations derived as described in Section 3.1 were used to evaluate sensor accuracy. Therefore, the accuracies of the sensors with less linearity became lower. At the same time, the accuracies of all three particle sensors became dependent on the accuracy of the SidePak, which does not necessarily provide the actual particle concentration due to instrument errors and the missing of the calibration factors. The repeatability of the sensors was evaluated by the variation of sensor outputs at similar particle concentrations. In the experiments, due to

the difficulty in maintaining the particle concentrations at a constant level, different batches of measurements with the particle sensors were conducted, so that a series of sensor outputs was obtained corresponding to the same SidePak reported particle mass concentrations. The linear correlation derived in Section 4.1 was then applied to convert sensor outputs to particle concentrations. The standard deviations (σ) and the standard deviations relative to the SidePak measured particle concentrations were then calculated to evaluate the precision of measurements.

2.3.3 Limit of detection

The limit of detection (LOD) is defined as the lowest limit which deviates significantly from the signal obtained from blank measurements. Similar quantifications of detection limits also exist, such as the limit of determination, limit of quantitation (LOQ), and limit of blank. (Petrozzi, 2012). In this study, the LOD was obtained with the widely used Kaiser (1956) method,

$$LOD = 3\sigma_{blk} / k , \qquad [1]$$

where σ_{blk} is the standard deviation at blank conditions maintained by filling the chamber with air cleaned by HEPA filters. k is the slope of the fitted line obtained from linearity experiments described Section 4.1. Values of coefficients other than 3 before σ_{blk} / k were also used for other quantifications of detection limits: for example, the limit of determination

uses 6, and the LOQ uses 10. The σ_{blk} was calculated based on a measurement time of 60 min, meaning that 120 samples have been collected for each of the sensors.

2.3.4 Dependence on particle composition

A sensor's performance depends on particle composition, since light scattering is influenced by the refractive index. This study used three types of particles, produced by atomizing NaCl, sucrose ($C_{12}H_{22}O_{11}$), and NH_4NO_3 aqueous solutions. To exclude the effect of particle size on the performance of the particle sensors, the concentrations of the solutions were controlled to ensure that generated particles had similar normalized size distributions (Figure A1.2 in the supplemental information). After exiting the atomizer (Aerosol Generator 3076, TSI Inc.), particles passed through a custom-built diffusion dryer before entering the chamber. The different refractive indices of these three materials affected the performance of the particle sensors. The evolutions of particle size distributions during the measurements were found to be similar to that of the incense particles (Figure A1.1 in the supplemental information), i.e., the normalized size distributions remained the same, while the total particle concentration decreased. This property could exclude the effect of particle size change during the experiments. Due to the fact that the SidePak also measures particle concentrations with light scattering, reference concentrations were calculated from the size distributions obtained by the SMPS measurements. The outputs of the sensors, together with the readings of the SidePak were then compared with the mass concentrations calculated from size distributions.

2.3.5 Dependence on particle size

Light scattering is strongly dependent on particle size in both the Rayleigh regime and Mie regime. To assess this dependence, water solutions of polystyrene latex (PSL, Bangs Inc.) spheres were atomized to obtain particles with uniform diameters of 300 nm, 600 nm, and 900 nm, respectively. The mass concentrations of particles were calculated from the size distributions measured by the SMPS. The performance of the sensors and the SidePak were then evaluated by comparing the outputs with the mass concentrations calculated from the size distributions.

2.3.6 RH and temperature influence

RH values of 20%, 67%, 75% and 90%, and temperatures of 5 ^{o}C, 20 ^{o}C, and 32 ^{o}C were used to test the sensors. The RH and temperature were measured with a sensor probe (HMP60, Vaisala Inc., accuracy: ± 3% in 0 to 90% RH, ± 5% in 90 to 100% RH) and a type K thermocouple (OMEGA Inc., accuracy: ± 2.2 ^{o}C), respectively. The temperature was controlled by placing ice packs or heating tapes around the chamber. The RH was adjusted by flowing dry air through a deionized water bubbler and then into the chamber before the test. After the RH reached the set values, the feeding of water vapor was discontinued, and particles were introduced into the chamber. The decrease of RH was found to be less than 10% during the test. In this study, the particles were generated by atomizing NaCl aqueous

solution. Again, similar normalized particle size distributions as a function of time were observed in the experiments, and hence the effect of particle size change during the experiments could be excluded.

2.4 Results and discussion

This section discusses the experimental results on assessing the particle sensors using the revised protocol provided by EPA 2013 Air Sensor Workshop.

2.4.1 Linearity of response

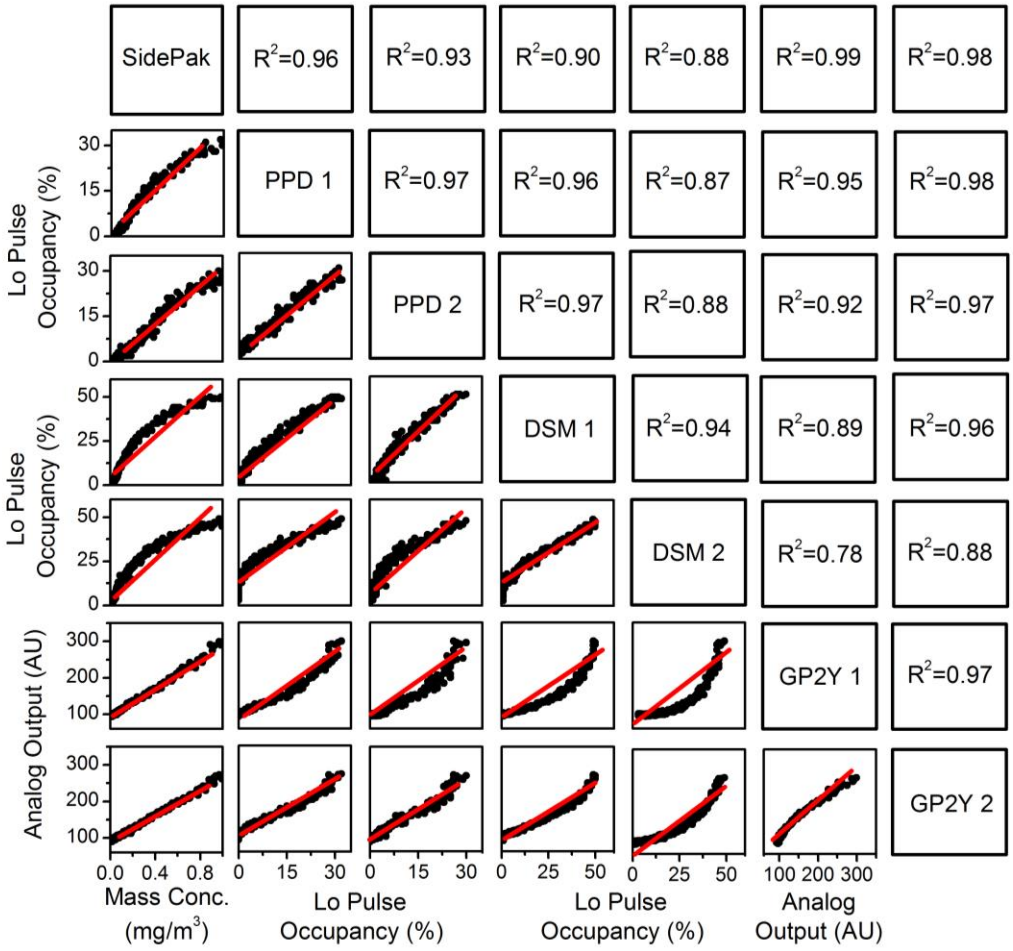

Figure 2.3 Pairwise correlation among the three sensors and the SidePak during the 2.5 hr measurement of the incense particles with a sampling interval of 30 s. Due to the limited space for plotting, two sensors of each type (PPD1, PPD2, DSM1, DSM2, GP2Y1, and GP2Y2) were chosen for comparison. The raw sensor outputs (Lo Pulse Occupancy and Analog Output) were used. R^2 values were calculated by the least squares regression.

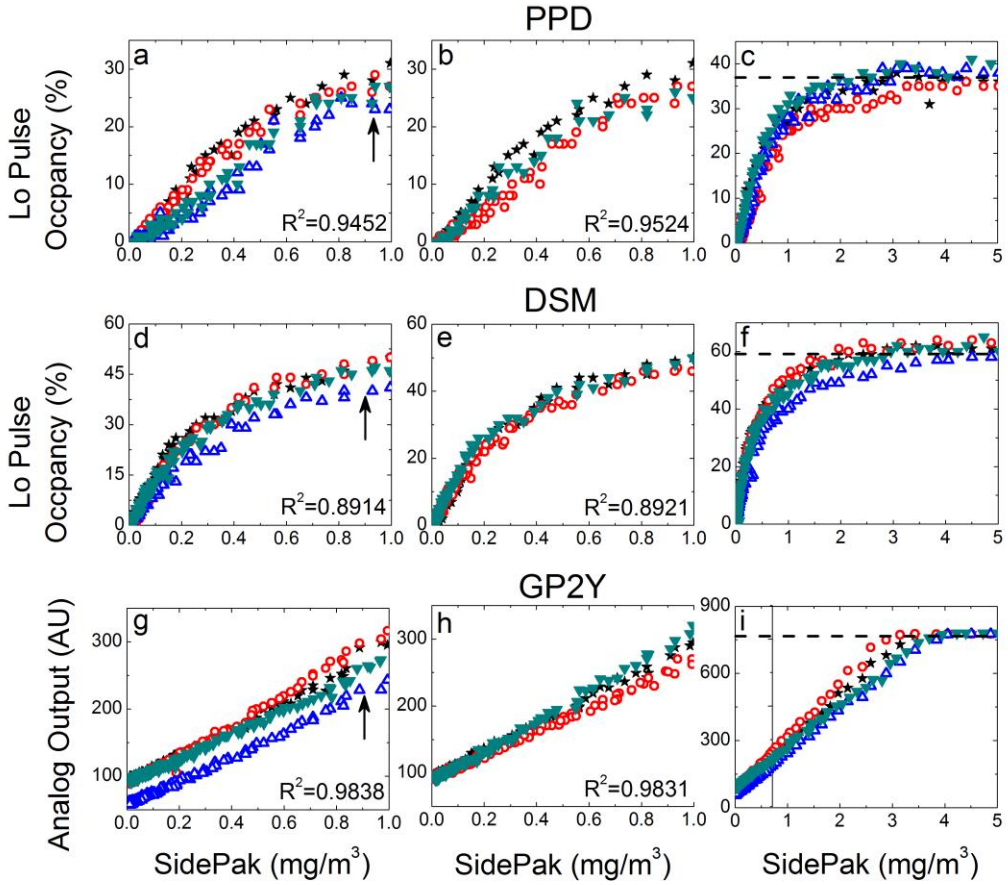

Figure 2.4 Pairwise correlation between the sensor outputs and the SidePak data during the 2.5 hr measurement of the incense particles with a sampling interval of 30 s: (a-c): PPD, (d-f): DSM, (g-i): GP2Y. (a), (d), (g): response of particle sensors of the same type in the concentration range of 0 – 1000 μg/m^3, different symbols represent the response of different sensors of the same type; (b), (e), (h): response of the same particle sensor in the particle concentration range of 0 – 1000 μg/m^3, different symbols represent the response of a same sensor for different batches of experiments; (c), (f), (i): response of particle sensors of the same type in the particle concentration range of 0 – 5000 μg/m^3. R^2 values were calculated by the least squares regression.

When using the incense as the particle source, the response of the three sensors and the SidePak agreed well in the particle mass concentration range of 0 – 1000 μg/m^3 (Figures 2.3 and 2.4). Pairwise correlations among the instruments were higher than 0.78 (DSM2 against GP2Y1). To further evaluate the properties of the three sensors, their responses were plotted

against the SidePak measured particle concentrations in Figure 2.4. Pairwise correlations between the outputs of the sensors and the SidePak measured particle concentrations were higher than 0.8914, as indicated by the R^2 values calculated by the least squares regression (Figures 2.4a, 2.4b, 2.4d, 2.4e, 2.4g, and 2.4h). Given the low cost of these particle sensors, it will be worthwhile to apply these sensors to obtain local and real-time PM concentrations in polluted cities, where the daily upper limit of particle concentrations is around 600 $\mu g/m^3$, and the hourly upper limit of particle concentrations is higher than 1 mg/m^3 (Guo et al., 2014; Tiwari et al., 2013; Zhao et al., 2013). Among the three sensors, the GP2Y sensor gave the highest linearity with an R^2 value of 0.9838 for sensors of the same type on four sides of the chamber wall in one measurement, and 0.9831 for the same sensor on one side of the chamber wall in several measurements. The DSM sensors provided the lowest values of R^2, with 0.8914 for sensors of the same type, and 0.8921 for the same sensor.

It should be noted that the lower R^2 values given by the PPD and DSM sensors were mainly caused by the "curvature" at higher particle concentrations shown in Figures 2.4a, 2.4b, 2.4d, and 2.4e. A substantial enhancement in the linearity of the PPD and DSM sensors can be expected in smaller particle concentration ranges. For example, the PPD and DSM sensors gave R^2 values of 0.9496 and 0.9506, respectively, in the particle concentration range of 0 to 100 $\mu g/m^3$. For practical applications or enacting regulations on atmospheric particulate matter, these lower particle concentration ranges may be used (EPA, 2013; MEP, 2013).

In testing particle sensors of the same type, some deviated significantly from the others, although the linearity was still high (Figures 2.4a, 2.4d, and 2.4g, as indicated by the arrows). This systematic deviation could not be explained by the concentration fluctuations at the four sides of the chamber, as shown in Figure 2.2b. This result suggests that each sensor should be calibrated separately before being used in commercialized particle monitors, since this existing systematic error may significantly affect the particle concentrations reported by the sensors (e.g., the same analog output of 200 from a GP2Y sensor corresponded to a particle concentration ranging from 600 to 900 μg/m^3 in Figure 2.4g). The linearity of the same sensor was similar in each test (Figures 2.4b, 2.4e, and 2.4h), demonstrating the reliability of the sensor for repeated measurements, as discussed in Section 4.2. Figures 2.4c, 2.4f, and 2.4i show the range of the particle concentrations in which sensors can be relied on. It was observed that the outputs of the three tested sensors became saturated at a concentration of around 4 mg/m^3 measured by the SidePak. Hence, the tested particle sensors are less applicable for measuring particle concentrations in highly polluted spaces, such as the outlet of stacks and construction sites.

Table 2.3 Linear correlations between particle sensor outputs and SidePak measured particle concentrations in different ranges of particle concentrations (0 – 1000 μg/ m^3, 0 – 100 μg/ m^3, and 0 – 300 μg/ m^3), calculated by the least squares and reduced major axis (RMA) regression methods.

Sensors	**Least squares (0 – 1000 μg/ m^3)**			**RMA (0 – 1000 μg/ m^3)**			**Least squares (0 – 100 μg/ m^3)**			**Least squares (0 – 300 μg/ m^3)**		
	intercept	**slope**	**R^2**	**intercept**	**slope**	**R^2**	**intercept**	**slope**	**R^2**	**intercept**	**slope**	**R^2**
PPD	-0.353	33.6	0.9452	-0.481	34.3	0.9558	-0.806	47.1	0.9496	-1.05	43.4	0.9525
DSM	3.93	59.7	0.8914	3.34	63.2	0.8924	-0.469	159	0.9506	-0.0469	119	0.9755
GP2Y	91.1	196	0.9838	90.8	198	0.9831	94.2	190	0.9332	94.2	189	0.9746

Table 3 gives the linear regression results of the three sensors using the least squares and RMA regression. The two regression methods yielded similar results, indicating a minimal influence of the variation of the SidePak measured particle concentrations. The least squares regression values in the particle concentration ranges of 0 to 100 $\mu g/m^3$ and 0 to 300 $\mu g/m^3$ were also tabulated, clearly showing the dependence of linearity on the choice of particle concentrations ranges. Note that the R^2 values obtained in this study are relatively larger than those calculated in previous studies on field calibration of the particle sensors (Gao et al., 2015; Holstius et al., 2014). This discrepancy may be due to variations in the material composition and size of the atmospheric particles in field calibrations, whereas the incense particles were the only particle source in the linearity test. Sections 4.4 and 4.5 elaborate the influence of particle composition and size on the performance of the particle sensors.

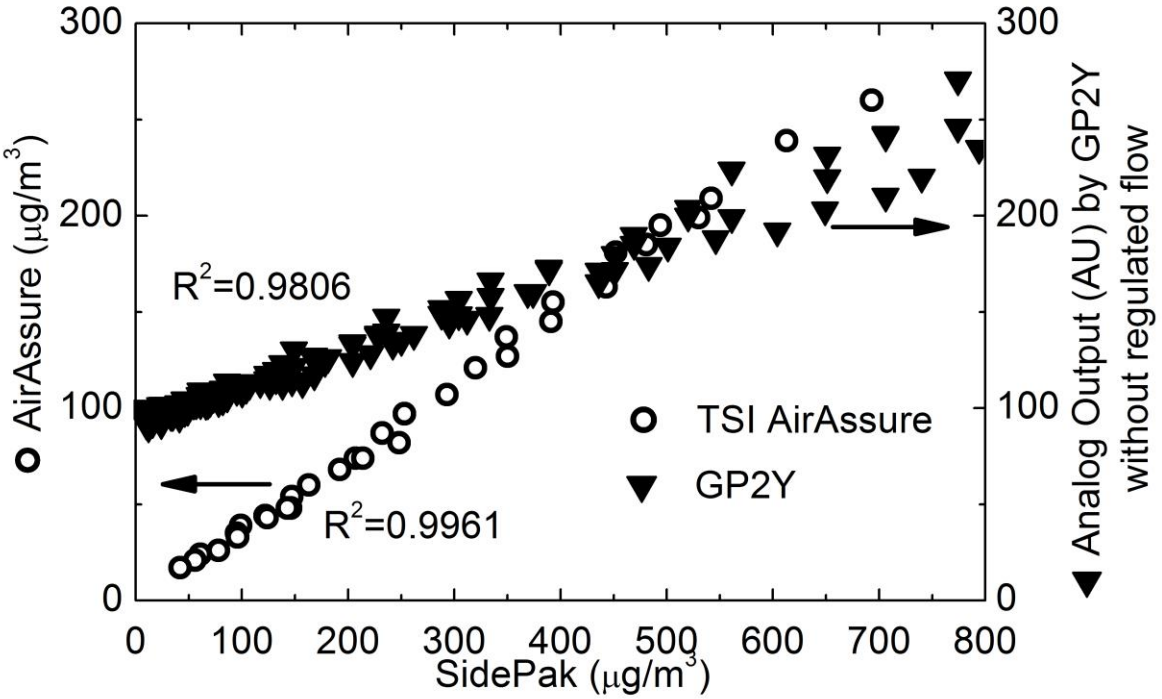

Figure 2.5 Mass concentrations measured by the AirAssure monitor and analog outputs reported by the GP2Y sensor without regulated convective flow in mass concentration range of 0 – 800 μg/m3. The experiment was conducted with the incense particles during a measurement time of around 2.5 hr with a sampling interval of 30 s. Mass concentrations on the x-axis were measured with the SidePak.

Making modifications to the GP2Y sensor prototype could further enhance the linearity of response, as shown in Figure 2.5. R^2 value calculated by the lease squares method increased to 0.9961 for the AirAssure monitor. This improvement might be brought by regulated flow, which decreased the amount of erratically distributed particles staying in the light scattering region of the particle sensor. The specialized algorithm of the AirAssure might also flatten the fluctuating sensor outputs and provided results with higher linearity.

2.4.2 Precision of measurements

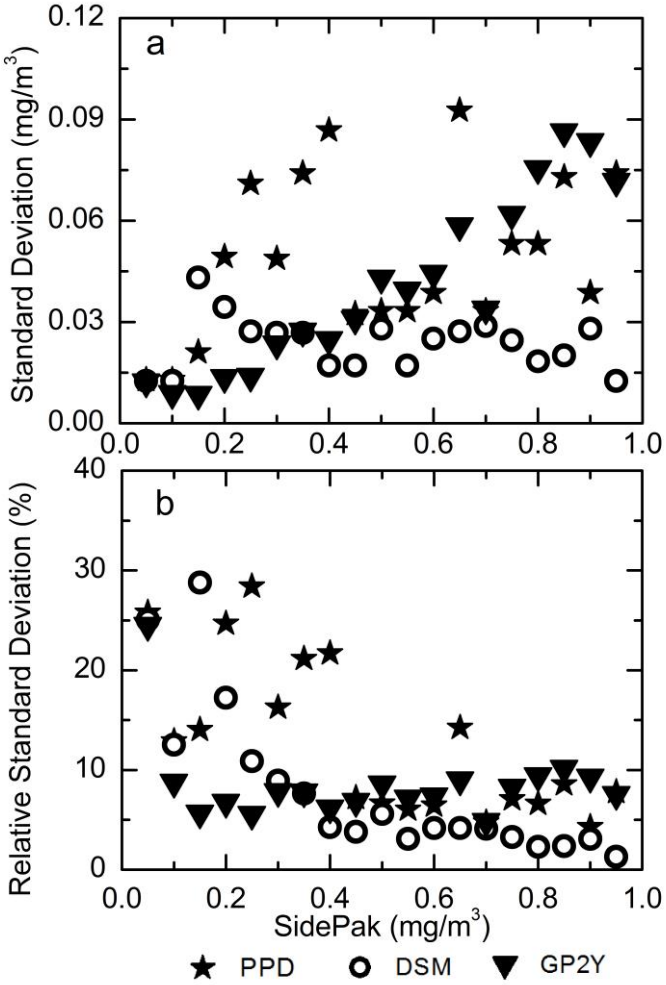

Figure 2.6 (a) Standard deviations and (b) relative standard deviations of the sensor-measured particle concentrations under different SidePak-measured particle concentrations. The GP2Y sensors were tested without regulated convective flow.

Experimental results on the repeatability of the three tested sensors as measured by the standard deviation and relative standard deviation are plotted as a function of SidePak concentration in Figure 2.6. The standard deviations of the sensors varied from 15 μg/m^3 to 90 μg/m^3 for a concentration range of 0 to 1000 μg/m^3 (Figure 2.6a). Although the

imprecision could also be partly attributed to the SidePak, the RMA regression calculated in Section 4.1 suggested a minimal influence of the SidePak's fluctuation. The DSM sensor demonstrated relatively constant and small values of standard deviation in the particle concentration range of 0 to 1000 $\mu g/m^3$, which can also be observed from the higher repeatability of the measurement in Figure 2.4e compared to other sensors. The PPD and the GP2Y sensors showed increased values of standard deviations at higher particle concentrations (Figure 2.6a), while the relative standard deviations of all the three tested sensors dropped as particle concentration increased (Figure 2.6b). The trend of increased relative standard deviation as concentration decreased, indicates that the sensors are not very accurate for low concentration measurements (<200 $\mu g/m^3$). It should be noted that these standard deviations were calculated based on approximately ten measurements due to constraints of the system used for the laboratory study. If the number of measurements were increased, it is anticipated that the uncertainty maybe lower. However, by averaging the data, the "real-time" information of the sensors may be lost. As in our system for testing incense combustion where the generated particle concentration decays rapidly in a sampling interval of 30 s, the averaged data over a longer period of time may not represent the actual particle concentration. Similar problems may be encountered when measuring fluctuating particle concentrations. In these situations, the high standard deviation of the sensor might cause a high uncertainty of the measurements. In this laboratory study, due to the considerable change of particle concentration in the sampling interval, the effect of averaging the measurements on the sensor performance was not investigated.

In the applications of real-time measurements, these sensors can be utilized to locate hotspots for particle emissions in the ambient conditions, and to measure PM concentrations in non-ambient environments of interest, such as indoor areas and industrial plants. Furthermore, these particle sensors could serve as preliminary substitutes for more accurate instruments in developing countries, where the atmospheric PM concentrations are high, and the commonly used accurate instruments are unaffordable. The AirAssure monitor reported particle mass concentrations with relatively higher repeatability, as shown in Figure 2.5, indicating the improvement of data quality after modifying the GP2Y sensor prototypes. Calculated standard deviations of the AirAssure monitor were below 10 $\mu g/m^3$ in the range of measurement between 0 – 300 $\mu g/m^3$. Note that the standard deviations of the particle sensors reflect the repeatability of the measurements, while precision is also described by the accuracy of the correlation between sensor outputs and particle concentrations. Since linear correlations of the three sensors in the particle concentration range of 0 to 1000 $\mu g/m^3$ were used in calculating particle concentrations, due to the low linearity of the DSM and PPD sensors as discussed above, the accuracy of the measurement was also negatively affected. Hence, depending on the specific properties of each type and model of the sensor, nonlinear correlations between the sensor output and the particle concentration are suggested to be calibrated to obtain more precise measurement results. For this study, simple second-order polynomial fittings could predict the response of the PPD and DSM sensors with much higher R^2 values. In the particle range of 0 to 1000 $\mu g/m^3$, the Lo Pulse Occupancy (LPO, %) of the PPD and DSM sensors could be fitted with equations:

$LPO_{PPD} = -17.8m^2 + 47.7m - 1.39$ and [2]

$LPO_{DSM} = -75.3m^2 + 118m + 0.544$, [3]

with R^2 values of 0.9651 and 0.9798, respectively, where m is the mass concentration (μg/m^3) measured by the SidePak. The calculated R^2 values were much higher than those obtained from the linear regressions and can be further improved by fitting the sensor outputs with higher orders of polynomial equations.

2.4.3 Limit of detection

Table 2.4 Limits of detection of the three tested sensors using *k* values in different mass concentration ranges (0 to 1000μg/m^3 and 0 to 100μg/m^3). The GP2Y sensors were tested without regulated convective flow.

Sensors	**PPD**	**DSM**	**GP2Y**
$3\sigma_{blk}$	0.216 (%)	0.680 (%)	5.11
k (0 to 1000 μg/m^3)	0.0336 (%×m^3/μg)	0.0597 (%×m^3/μg)	0.196 (m^3/μg)
LOD (0 to 1000 μg/m^3)	6.44 (μg/m^3)	11.4 (μg/m^3)	26.1 (μg/m^3)
k (0 to 100 μg/m^3)	0.0471 (%×m^3/μg)	0.159 (%×m^3/μg)	0.190 (m^3/μg)
LOD (0 to 100 μg/m^3)	4.59 (μg/m^3)	4.28 (μg/m^3)	26.9 (μg/m^3)

Table 4 lists the limits of detection (LOD), together with the values of σ_{blk} and k of the three tested sensors according to the calculation method introduced in Section 3.3. By using the k values obtained from the linear correlation in the concentration range of 0 to 1000 μg/m^3, the GP2Y sensor gave the highest LOD value of 30.2 μg/m^3. The LOD values of the PPD and the DSM sensors were relatively lower, with the PPD sensor showing the lowest

LOD of 6.44 μg/m^3. Accordingly, the LOQ for the GP2Y sensor and the PPD sensor were 101 and 21.5 μg/m^3, respectively. Considering the higher gradient of the response of the PPD and DSM sensors in the lower particle concentration range, the LOD values of the two types of sensors would become smaller if linear correlations in lower particle concentration ranges were used. Table 4 also lists the LOD values of the PPD and DSM sensors using the *k* values calculated from the least squares regression in the particle concentration range of 0 to 100 μg/m^3, where lower LOD values of 4.59 μg/m^3 and 4.28 μg/m^3 were obtained.

2.4.4 Dependence on particle composition

The SidePak also uses light scattering to measure particle mass concentrations, which are affected by the particle composition and sizes. Hence, particle mass concentrations calculated from the size distributions of particles can provide higher accuracy for evaluating the sensor performance. As indicated in Figure A1.2 in the supplemental information, the size distributions of the three types of generated particles were similar, and could be fitted by lognormal functions. The total mass concentration of the measured particles (m) can be calculated by using the method of moments (Hinds, 1982):

$$m = \frac{\pi}{6} M_0 \exp\left(3\ln d_{pg} + \frac{9}{2}\ln^2(\sigma_g)\right), \qquad [4]$$

where M_0, d_{pg}, and σ_g stand for the total number concentration, the geometric mean particle size, and the geometric standard deviation, which could be obtained through the curve fitting process.

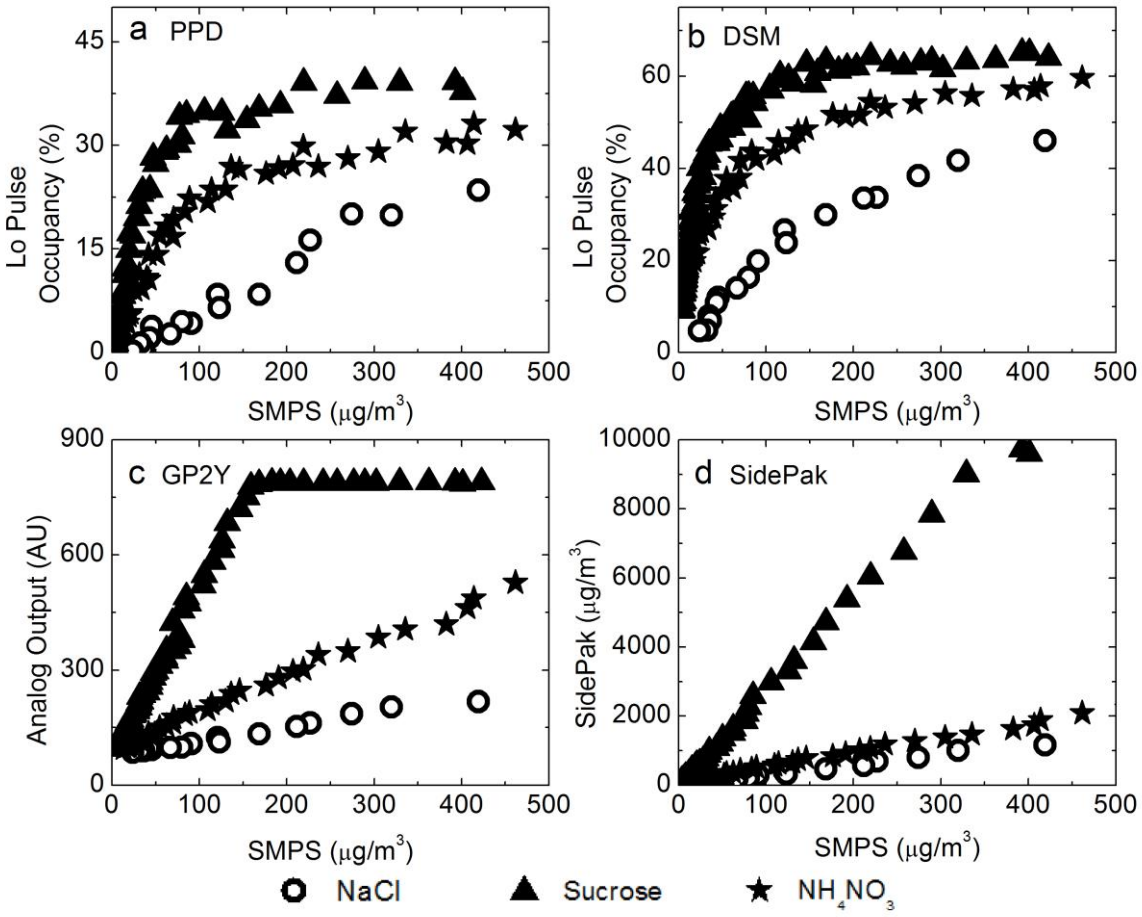

Figure 2.7 Dependence of sensor performance on the composition of particles: (a) PPD, (b) DSM, (c) GP2Y, and (d) SidePak. The reference mass concentrations were calculated from the size distributions measured by the SMPS. The experiments were conducted with atomized NaCl, NH_4NO_3, and sucrose particles, each with a total measurement time of around 2 hr with a sampling interval of 30 s. Note the different scales of y-axes.

The outputs of the particle sensors, together with the readings of the SidePak, were then plotted against the particle concentrations calculated from the size distributions (Figure 2.7).

Due to the difficulty in generating highly concentrated sucrose particles, the performance of the sensors and the SidePak was evaluated in a mass concentration below 500 $\mu g/m^3$. It can be seen that the composition of the particles indeed affected the response of the particle sensors: the outputs increased by up to 10 times when measuring sucrose particles (the GP2Y sensor).

Moreover, different sensors and instruments responded differently when the composition of particles changed, as indicated by the magnitudes of the slopes in Figure 2.7. For example, the GP2Y sensors and the SidePak were more sensitive to the sucrose particles. As discussed by Molenar (2005), the variability of the refractive index of different materials accounts partly for the uncertainties when using light scattering to measure particle mass concentrations. The refractive index is the sum of a real and an imaginary component: $m = n - in'$, where n and n' are correlated with the magnitude of light scattering and light absorption respectively. A higher proportion of light could be absorbed by organic compositions in particles, due to the energy storage in the vibration of carbon bonds, while inorganic materials are reported to absorb negligible radiation, i.e. the imaginary term of the refractive index is close to zero. The phototransistor hence received less light in the test of sucrose particles, and so reported a higher mass concentration. This result implies that particle sensors may overestimate mass concentrations when measuring particles incorporating organic compositions. The outputs of the sensors measuring NaCl and NH_4NO_3 particles were also found to be different from each other, due to the different values of refractive indices. In this study, NH_4NO_3 was used to simulate the measurement of

atmospheric particles in heavily polluted areas, since a large proportion of the inorganic contents of atmospheric particles is attributed to the reaction between NH_3 and HNO_3 (Guo et al., 2014; Jimenez et al., 2009; Seinfeld and Pandis, 2012). The retained sensitivity at higher particle mass concentrations of NH_4NO_3 may promise the application of the three sensors in measuring particle concentrations in polluted ambient environments that contain mostly inorganic particles. However, for human health and exposure studies, particles with different contents may be measured. Due to the uniqueness of each device, a higher accuracy could be guaranteed if calibration factors were determined and applied for the materials being used,.

2.4.5 Dependence on particle size

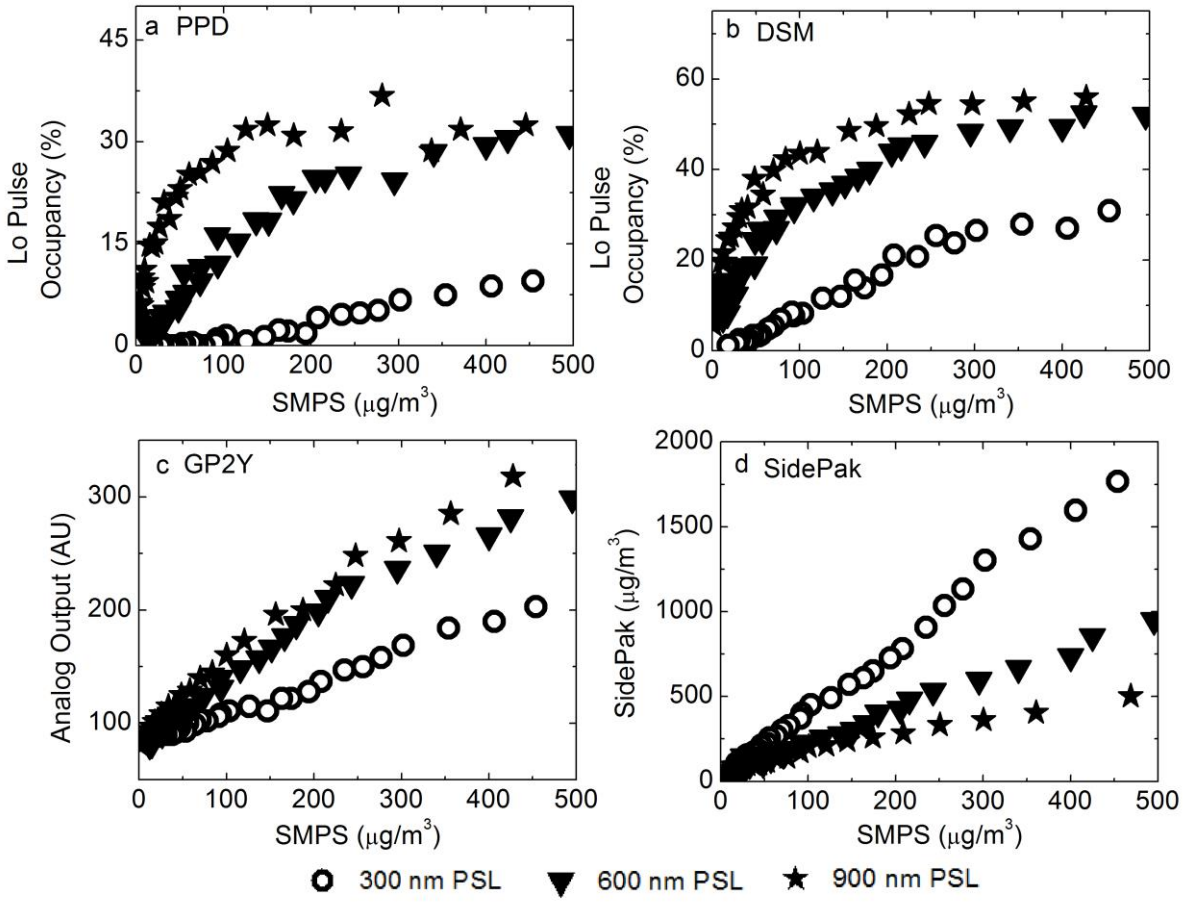

Figure 2.8 Sensor performance for PSL particles with three sizes of 300, 600, and 900 nm, each during a measurement time of around 2 hr with a sampling interval of 30 s: (a) PPD, (b) DSM, (c) GP2Y, and (d) SidePak. The reference mass concentrations were calculated from the size distributions measured by the SMPS. Note the different scales of y-axes.

Figure 2.8 shows the dependence of sensor performance on the size of the tested particles, of which the size distributions are displayed in Figure A1.3 in the supplemental information. The outputs of the particle sensors and the SidePak are plotted against particle mass concentrations calculated from the SMPS measured size distributions in the concentration below 500 μg/m^3. A higher concentration of 900 nm PSL particles could not be obtained,

possibly due to the loss by impaction and interception during the transport of particles. Note that the mass concentrations reported by the SMPS might not accurately represent the actual values, because the narrow size distributions of the PSL particles may not be regarded as a constant value in the transfer function of the DMA (Stolzenburg and McMurry, 2008). Different characteristics were observed among the sensors and the SidePak. Under the same mass concentrations, the outputs of the sensors became higher as particle sizes increased from 300 nm to 900 nm, while the SidePak reported the highest particle concentration for the smallest particles (300 nm). Further observation on the response of the particle sensors indicated that the GP2Y sensor was more sensitive to smaller particles, while the PPD and DSM sensors were more sensitive to larger particles. These properties can be attributed to the type of the irradiated light used in the instruments. For safe handling and reduced cost, infrared radiation between 870 and 940 nm was used in the particle sensors, while the SidePak uses a laser with a wavelength of 670 nm for the light scattering of particles. Although the light scattering of the sensors and the SidePak all fall into the Mie Regime, the relative magnitude of the particle size and the wavelength of the radiation determined that the light scattering in the particle sensors is closer to the Rayleigh regime.

In the experiments, as particle size increased, the response of the particle sensors was enhanced for the same mass concentration (Figures 2.8a, 2.8b, and 2.8c), which could be explained as follows. For the same mass concentration of monodisperse particles, $N_{TOT} d_p^3$ remains a constant, where N_{TOT} is the total number concentration of particles with a size of d_p. The scattered light (I_{scat}) has the form of

$$I_{scat} = I_0 N_{TOT} Q_{scat} \frac{\pi}{4} d_p^2, \quad [5]$$

where I_0 is the incident light, and Q_{scat} is the scattering coefficient. Since the light scattering for the sensors was closer to the Rayleigh regime, for a simple estimation, Q_{scat} was assumed to be proportional to d_p^4 (Friedlander, 2000). Note that this correlation might overestimate the light scattering coefficient in the Mie regime. The scattered light intensity is therefore proportional to $N_{TOT} d_p^6$, and further proportional to d_p^3 under the same mass concentration. Because of the correlation that $I_{scat} = K d_p^3$, where K is a constant, more light was lost due to the extinction of larger particles, less light was received by the phototransistor, and higher concentrations were reported. Based on this result, the particle sensors may underestimate the particle mass concentrations for smaller particles. On the contrary, the SidePak reported a reverse trend for the influence of particle sizes, possibly due to the fluctuations in the light scattering coefficient in the Mie regime, which affected the amount of light lost in the sensor and received by the transistor.

2.4.6 RH and temperature influence

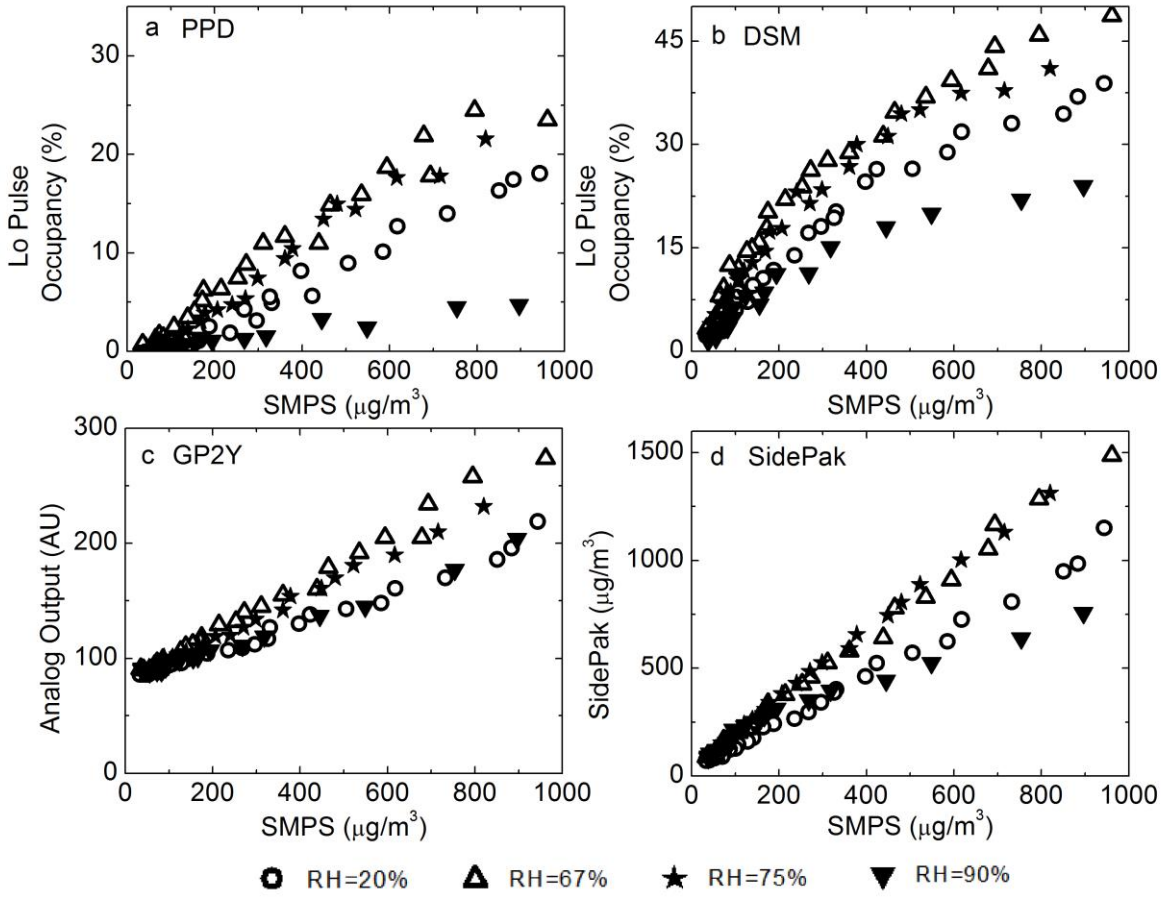

Figure 2.9 Performance of particle sensors under various relative humidity values (20% to 90%), each with a measurement time of around 2.5 hr with a sampling interval of 30 s: (a) PPD, (b) DSM, (c) GP2Y, and (d) SidePak. The reference mass concentrations were calculated from the size distributions measured by the SMPS. Note the different scales of y-axes.

Relative humidity affected the performance of the particle sensors in several ways. First, similar to organic compositions, water absorbs infrared radiation and can cause an overestimate of particle mass concentrations due to the reduced light intensity received by the phototransistor. Second, highly concentrated water vapor may lead to a failure of the circuits

of the particle sensors and result in biased measurement results. Third, the usage of SMPS data as references may not be applicable under high RHs, since the sheath flow inside the DMA may dry the particles and cause an underestimate of particle concentrations measured by the SMPS. As shown in Figure 2.9, similar trends in the performance of the particle sensors and the SidePak were observed as RH altered. For the same particle mass concentration, the outputs of the sensors and the SidePak first increased, and then dropped as RH increased. This result may be a comprehensive effect of the factors mentioned above, clearly showing the dependence of sensor performance on RH values.

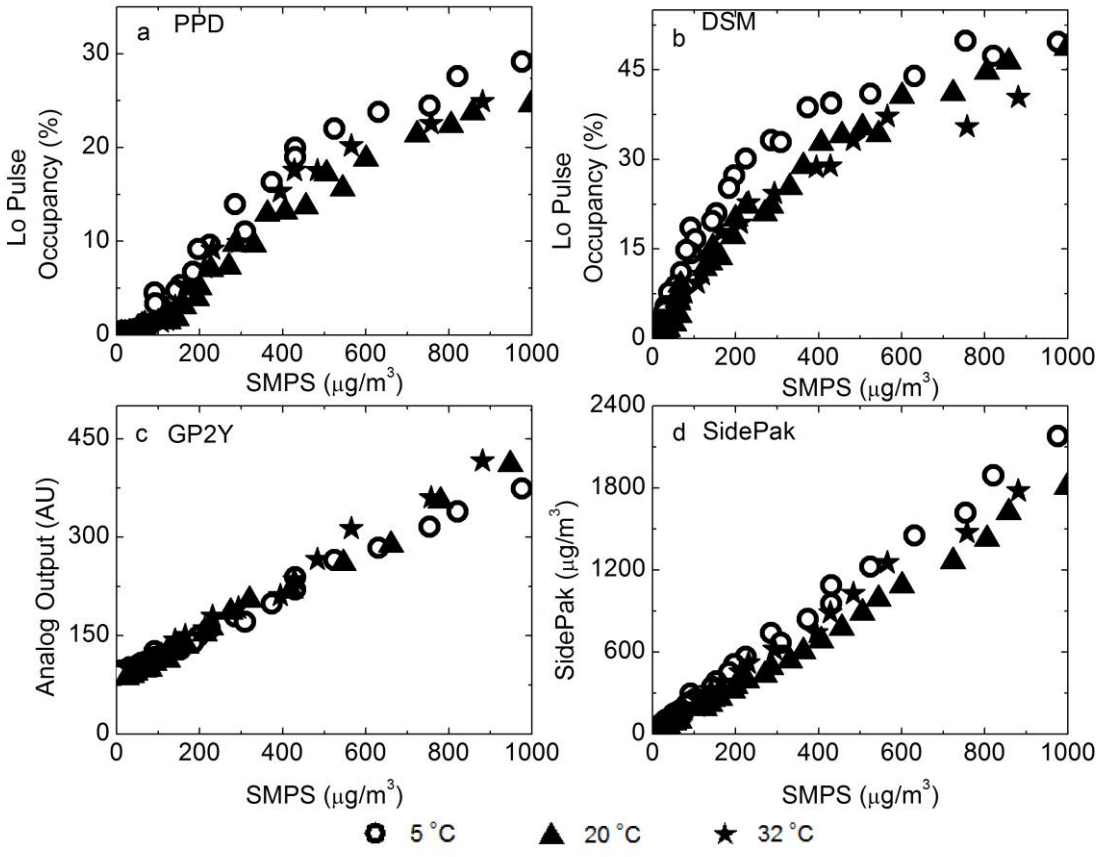

Figure 2.10 Performance of particle sensors at different temperatures of 5 ^{o}C, 20 ^{o}C, and 32 ^{o}C, each with a measurement time of around 2.5 hr with a sampling interval of 30 s: (a) PPD, (b) DSM, (c) GP2Y, and (d) SidePak. The reference mass concentrations were calculated from the size distributions measured by the SMPS. Note the different scales of y-axes.

Compared to relative humidity, temperature had negligible effects on the three particle sensors and the SidePak in the temperature range from 5 ^{o}C to 32 ^{o}C, as shown in Figure 2.10, because theoretically, light scattering and absorption are independent of temperature. However, extreme temperatures of the environment may affect the reported particle concentrations, since the flow rate of the updraft of particles in the PPD and the DSM sensors is determined by the temperature difference between the thermal resistor and the environment.

2.5 Conclusions

Table 2.5. Summary of the characteristics of the particle sensors PPD, DSM and GP2Y.

[#]The linearity of response is evaluated based on the R^2 values in the particle concentration range of 0 to 1000 μg/m^3.
[*]Accuracy is based on the correlations calculated from linear regression methods. Nonlinear correlations are suggested in order to enhance the accuracy of the measurement.

Assessment Aspects		PPD	DSM	GP2Y
Linearity of response[#]		Medium	Low	**High**
Precision of measurement	**Accuracy[*]**	Medium	Low	**High**
	Repeatability	Low	**High**	Medium
Limit of Detection		**Low**	**Low**	High
Dependence on composition		High	High	High
Sensitivity to particle size		High	High	High
RH influence		High	High	High
Temperature influence		Minimal	Minimal	Minimal

This work comprehensively evaluated three low-cost light scattering particle sensors. A brief summary of the characteristics of the three sensors was compiled, and the advantages of each sensor were determined (Table 5). Throughout the experiments, the GP2Y1010AU0F (GP2Y) sensor demonstrated the highest linearity in comparison to measurements by the SidePak. The data quality of the GP2Y sensors could be further enhanced by modifying the flow system and the algorithm for calculating particle concentrations, as indicated by the improvement in the response of an AirAssure monitor. The PPD42NS (PPD) and the DSM501A (DSM) sensors had relatively lower limits of detections than the GP2Y sensors. Some common characteristics were observed, such as the saturated outputs under high

particle concentrations of around 4 mg/m^3, high dependence on the composition and size of particles, and minimal dependence on temperature.

While the relative standard deviation increased with decrease in concentration (these sensors may not be as accurate as more complicated and expensive measurement devices in clean environments), these low cost particle sensors demonstrated the ability to report particle concentrations with relatively high linearity and moderate repeatability. In addition, the uncertainty of the measurement can be further reduced by averaging the measurements over longer periods of time. The compact size and low cost of the sensors favor their wide application in tracking air quality in developing countries and heavily polluted areas, where the demand for monitoring particulate matter is especially urgent for the sake of public health. Large data sets obtained by the sensor network will make amenable applications of concepts of “big data” to improve the air quality.

2.6 References

Biswas, P. and Wu, C.-Y. (2005). Nanoparticles and the environment, J. Air Waste Manage. Assoc., 55, 708-746.

Bohonak, A. J. and Linde, K. V. D. (2004). Reduced major axis regression, http://www.kimvdlinde.com/professional/rma.html.

Cao, J., Chow, J. C., Lee, F. S., and Watson, J. G.(2013). Evolution of PM2. 5 measurements and standards in the US and future perspectives for China, Aerosol Air Qual. Res., 13, 1197-1211.

Cheng, Y. S., Bechtold, W. E., Yu, C. C., and Hung, I. F. (1995) Incense smoke: characterization and dynamics in indoor environments, Aerosol Sci. Tech., 23(3), 271-281.

Chong, C.-Y. and Kumar, S. P.(2003) Sensor networks: evolution, opportunities, and challenges, Proc. IEEE, 91, 1247-1256.

Chowdhury, Z., Edwards, R. D., Johnson, M., Shields, K. N., Allen, T., Canuz, E., and Smith, K. R.(2007). An inexpensive light-scattering particle monitor: field validation, J. Environ. Monit., 9, 1099-1106.

Edwards, R., Smith, K. R., Kirby, B., Allen, T., Litton, C. D., and Hering, S. (2006). An inexpensive dual-chamber particle monitor: laboratory characterization, J. Air Waste Manag. Assoc., 56, 789-799.

EPA, U. S. (2013). 40 CFR Parts 50, 51, 52, 53, and 58-National Ambient Air Quality Standards for Particulate Matter: Final Rule, Federal Register, 78, 3086-3286.

Friedlander, S. K. (2000). Smoke, dust, and haze, Oxford University Press, New York.

Gao, M., Cao, J., and Seto, E. (2015). A distributed network of low-cost continuous reading sensors to measure spatiotemporal variations of PM2. 5 in Xi'an, China, Environ. Pollut., 199, 56-65.

Guo, S., Hu, M., Zamora, M. L., Peng, J., Shang, D., Zheng, J., Du, Z., Wu, Z., Shao, M., and Zeng, L. (2014). Elucidating severe urban haze formation in China, Proc. Natl. Acad. Sci., 2014. 201419604.

Hagler, G., Solomon, P., and Hunt, S. (2014) New technology for low-cost, real-time air monitoring. In: EM (Air Waste Manage. Assoc.), 1, Pittsburg, PA.

Hinds, W. C. (1982). Aerosol technology: properties, behavior, and measurement of airborne particles. John Wiley & Sons, New York.

Holstius, D., Pillarisetti, A., Smith, K., and Seto, E. (2014). Field calibrations of a low-cost aerosol sensor at a regulatory monitoring site in California, Atmos. Meas. Tech. Discuss., 7, 605-632.

Huang, R.-J., Zhang, Y., Bozzetti, C., Ho, K.-F., Cao, J.-J., Han, Y., Daellenbach, K. R., Slowik, J. G., Platt, S. M., and Canonaco, F. (2014). High secondary aerosol contribution to particulate pollution during haze events in China, Nature, 514, 218-222.

Jimenez, J., Canagaratna, M., Donahue, N., Prevot, A., Zhang, Q., Kroll, J., DeCarlo, P., Allan, J., Coe, H., and Ng, N. (2009). Evolution of organic aerosols in the atmosphere, Science, 326, 1525-1529.

Kaiser, H., and Specker, H. (1956) Fresenius' Journal of Analytical Chemistry, 149, 46-66.
Karlsson, H. L., Gustafsson, J., Cronholm, P., and Möller, L. (2009). Size-dependent toxicity of metal oxide particles—a comparison between nano-and micrometer size, Toxicol. Lett., 188, 112-118.
Knutson, E. and Whitby, K. (1975). Aerosol classification by electric mobility: apparatus, theory, and applications, J. Aerosol Sci., 6, 443-451.
Leavey, A., Fu, Y., Sha, M., Kutta, A., Lu, C., Wang, W., Drake, B., Chen, Y., and Biswas, P. (2015). Air quality metrics and wireless technology to maximize the energy efficiency of HVAC in a working auditorium, Build. Environ., 85, 287-297.
Litton, C. D., Smith, K. R., Edwards, R., and Allen, T. (2014). Combined optical and ionization measurement techniques for inexpensive characterization of micrometer and submicrometer aerosols, Aerosol Sci. Tech., 38, 1054-1062.
Long, R., Beaver, M., Williams, R., Kronmiller, K., and Garvey, S. (2014). Procedures and concepts of EPA's ongoing sensor evaluation efforts. In: EM (Air Waste Manage. Assoc.), 8, Pittsburg, PA.
McDonald, J. H. (2009). Handbook of biological statistics, Sparky House Publishing, Baltimore, Maryland, USA.
MEP (2013). Environmental Laws, Published by the Chinese Ministry of Environmental Protection (MEP) of the People's Republic of China, Beijing, China.
Molenar, J. V. (2003). Theoretical analysis of PM2. 5 mass measurements by nephelometry, IMPROVE Project, 1-21.
Mulholland, G. W. and Liu, B. Y. (1980). Response of smoke detectors to monodisperse aerosols, Journal of Research of the National Bureau of Standards, 85, 223-238.
Nafis, C. (2014). Air Quality Monitoring, http://www.howmuchsnow.com/arduino/airquality/.
Olivares, G., Longley, I., and Coulson, G. (2012). Development of a low-cost device for observing indoor particle levels associated with source activities in the home, Proceedings of the International Society of Exposure Science Conference.
Petrozzi, S. (2012). Practical instrumental analysis: methods, quality assurance and laboratory management, John Wiley & Sons, Singapore.
Phalen, R., Cuddihy, R., Fisher, G., Moss, O., Schlesinger, R., Swift, D., and Yeh, H.-C. (1991). Main features of the proposed NCRP respiratory tract model, Radiat. Prot. Dosim., 38, 179-184.
Rajasegarar, S., Zhang, P., Zhou, Y., Karunasekera, S., Leckie, C., and Palaniswami, M. (2014). High resolution spatio-temporal monitoring of air pollutants using wireless sensor networks. Intelligent Sensors, Sensor Networks and Information Processing (ISSNIP), 2014 IEEE Ninth International Conference, IEEE, 1-6.
Sahu, M., Peipert, J., Singhal, V., Yadama, G. N., and Biswas, P. (2011). Evaluation of mass and surface area concentration of particle emissions and development of emissions indices for cookstoves in rural India, Environ. Sci. Technol., 45, 2428-2434.
Schubert, E. F., Gessmann, T., and Kim J. K. (2005) Light emitting diodes, John Wiley & Sons.

Seinfeld, J. H. and Pandis, S. N. (2012). Atmospheric chemistry and physics: from air pollution to climate change, John Wiley & Sons.

Sokal, R. and Rohlf, F. (1981). Correlation and multiple and curvilinear regression, Biometry. Sokal RR and Rohlf FJ. editors. New York. WH Freeman & Co, 1981. 561-690.

Spinelle, L., Gerboles, M., and Aleixandre, M. (2013). Protocol of evaluation and calibration of low-cost gas sensors for the monitoring of air pollution, Publication Office of the European Union, Luxembourg, EUR 26112.

Stocker, T., Qin, D., Plattner, G., Tignor, M., Allen, S., Boschung, J., Nauels, A., Xia, Y., Bex, B., and Midgley, B. (2013). IPCC, 2013: climate change 2013: the physical science basis. Contribution of working group I to the fifth assessment report of the intergovernmental panel on climate change, 2013.

Stolzenburg, M. R. and McMurry, P. H. (2008). Equations governing single and tandem DMA configurations and a new lognormal approximation to the transfer function, Aerosol Sci. Tech., 42, 421-432.

Tiwari, S., Srivastava, A., Bisht, D., Parmita, P., Srivastava, M. K., and Attri, S. (2013). Diurnal and seasonal variations of black carbon and PM 2.5 over New Delhi, India: influence of meteorology, Atmos. Res., 125, 50-62.

US Embassy (2015). Air Quality Data, http://beijing.usembassy-china.org.cn/070109air.html, http://newdelhi.usembassy.gov/airqualitydataemb.html.

Wang, S. C. and Flagan, R. C. (1990). Scanning electrical mobility spectrometer, Aerosol Sci. Tech., 13, 230-240.

Weekly, K., Rim, D., Zhang, L., Bayen, A. M., Nazaroff, W. W., and Spanos, C. J. (2013). Low-cost coarse airborne particulate matter sensing for indoor occupancy detection, IEEE CASE 2013, 32-37.

Zhao, X., Zhao, P., Xu, J., Meng, W., Pu, W., Dong, F., He, D., and Shi, Q. (2013). Analysis of a winter regional haze event and its formation mechanism in the North China Plain, Atmos. Chem. Phys., 13, 5685-5696.

Chapter 3: Evaluation of Nine Low-cost-sensor-based Particulate Matter Monitors

The results of this chapter is under review in Li, J., Mattewal, S., Sameer P. & Biswas, P. Evaluation of Nine Low-cost-sensor-based Particulate Matter Monitors

Abstract

Low-cost sensors have been studied extensively in recent years due to their price advantage, compact size, and moderate accuracy. Different manufacturers use different calibration methodologies and report a factor for the user. This study compared nine types of low-cost PM monitors (AirVisual, Alphasense, APT, Awair, Dylos, Foobot, PurpleAir, Wynd and Xiaomi) in a chamber with a well-defined aerosol. Additionally, two reference instruments (GRIMM and SidePak) were also used. These nine types of monitors were divided into two groups for comparison, according to their working principle and data reporting format. A linear correlation factor based on $PM_{2.5}$ mass concentration was reported for all monitors. Apart from linear correlation, the differences of the $PM_{2.5}$ mass concentrations reported by the various monitors and reference instruments were plotted against their average to demonstrate the degree of improvement that was possible after calibration. A bin-wise calibration was also conducted for monitors reporting size distributions to illustrate any coincidence error that could bias the results. For monitors designed for residential use, an important parameter often reported is the air quality index and is illustrated with a simplified index and color. The color display scheme of various monitors was compared with the US EPA regulation to demonstrate whether they could convey overall air quality levels accurately and promptly. The residential monitors indicate the air quality moderately well, but their different color display schemes make the comparison difficult and possibly misleading. Various monitors with diverse features showed discrepancies in terms of

reporting PM concentration, thus requiring user-defined calibration to improve their accuracy.

3.1 Introduction

As a major atmospheric pollutant, particulate matter (PM) has adverse health effects, therefore, it is routinely monitored to reduce the harm it causes. In 2013, PM was classified as a Group 1 carcinogen by the International Agency for Research on Cancer (IARC), and has been associated with lung cancer, premature mortality, cardiopulmonary diseases, and cardiovascular diseases (Valavanidis et al., 2008; Brook et al., 2010; Stewart and Wild, 2017). PM pollution accounts for nearly 1.2 million premature deaths and approximately 6.4 million annual deaths globally (Smith and Mehta, 2003; Cohen et al., 2005; Burnett et al., 2014). It has been reported that when the mass concentration of fine particulate matter ($PM_{2.5}$, particulate matter with a diameter smaller than 2.5 μm) increases by about 10 $\mu g/m^3$, the risk of lung cancer mortality increases approximately by 8% (Pope III et al., 2002). Due to these adverse health effects, stringent regulations on PM mass concentration have been enacted and enforced by governments and local agencies. The standards for annual $PM_{2.5}$ concentration were set as 12 $\mu g/m^3$ and 10 $\mu g/m^3$ by the United States Environmental Protection Agency (US EPA) and the World Health Organization (WHO) respectively (Organization, 2005). Apart from the PM concentration standard, the US EPA also specified the gravimetric method as the federal reference method (FRM) for PM mass concentration measurement. The gravimetric method calculates the PM mass concentration by weighing the particles accumulated on a filter over a period of time. This conventional method has been considered to be one of the most reliable methods for PM mass concentration measurement,

nevertheless, maintaining the system and weighing filters are laborious. Furthermore, the gravimetric method is not a real-time measurement, and can report only the accumulative PM mass concentration. The cost and labor required by the gravimetric method have hindered application of this method for personal use. Alternative measurement methods, for example, TEOM, GRIMM, FIMS, and SMPS, can measure real-time PM concentration accurately, but still face the challenges of high cost and long-term stability (Allen et al., 1997; Sioutas, 1999; Klepeis et al., 2007; Wang et al., 2018).

As a potential alternative method for PM concentration measurement, low-cost PM sensors have been studied extensively in recent years due to their price advantage, compact size, and moderate accuracy (White et al., 2012; Kumar et al., 2015; Rai et al., 2017; Morawska et al., 2018). Compared to bulky laboratory instruments costing up to thousands of dollars, palm sized low-cost sensors usually cost less than fifty dollars. One thing worth noting is that the term "low-cost PM sensor" refers only to the electrical sensing module, including popular models from Sharp, Shinyei, Samyoung, Oneair, and Plantower (Wang et al., 2015; Sousan et al., 2016b; Kelly et al., 2017; Liu et al., 2017). To make low-cost PM sensors functional, circuit board design, programming, and calibration are necessary to establish the relationship between electrical signals (current, voltage, or pulse width) and the PM concentrations. After fabrication and laboratory calibration, low-cost PM sensors exhibit a good linearity against reference instruments, showing promising potential for personal PM monitors and sensor networks (Wang et al., 2015).

Currently, research on low-cost PM sensors mainly focuses on two aspects: interpreting their signal comprehensively through calibration or characterization, and modifying them for personal or sensor network use. Several groups have tried to explain the deficiencies and limitations of low-cost sensors due to their working principles (Li and Biswas, 2017; Zhang et al., 2018). Some studies also calibrated a variety of low-cost PM sensors for different aerosol sources (e.g., NaCl, Arizona road dust, sucrose, silica, welding fumes, and diesel fumes) in different test environments (laboratory, residential, and ambient) to identify the optimal performance and favorable working conditions of each type of sensor (Hapidin et al.; Wang et al., 2015; Manikonda et al., 2016; Sousan et al., 2016a; Sousan et al., 2016b; Kelly et al., 2017; Liu et al., 2017; Rai et al., 2017; Zikova et al., 2017; Aliyu and Botai, 2018; Johnson et al., 2018). These studies demonstrated the advantages and limitations of these sensors, and laid a solid foundation for further deployment and application. Wireless sensors or sensor networks, as one major application, have been deployed in households, meeting rooms, factories, cities, etc. to monitor the dynamic process of pollution events with high spatiotemporal resolution (Kim et al., 2010; Kim et al., 2014; Rajasegarar et al., 2014; Leavey et al., 2015; Patel et al., 2017; Jeon et al., 2018; Li et al., 2018a). Some of these studies have explored in depth the algorithms for organizing sensor data and extracting the maximum effective information (Li et al., 2018a; Li et al., 2018b). Apart from use in sensor networks, low-cost PM sensors find another important application as low-cost PM monitors, as we elaborate in the following section.

Low-cost PM monitors, whose major components are low-cost PM sensors, are usually assembled and pre-calibrated before distribution to users. Compared to conventional PM measurement instruments, they still have an appealing price advantage, however, accuracy is a still major concern. Compared to just the PM sensors, the assembled monitors' price is higher, but these monitors are advertised with enhanced data quality and stability due to improved algorithms and advanced factory calibration. Occasionally, these monitors have even been chosen as reference instruments to calibrate low-cost sensors. The Air Quality Sensor Performance Evaluation Center (AQ-SPEC), a unit of the South Coast Air Quality Management District (SCAQMD), has evaluated the majority of commercial monitors for multiple sources (Polidori et al., 2017). They have also built a calibration chamber that can maintain a stable and reproducible test environment (Papapostolou et al., 2017). Several popular monitors have been highlighted recently. The Dylos DC1700 Air Quality Monitor (Dylos Cooperation, Riverside, CA, USA) has been evaluated for different scenarios and has been deployed in indoor and outdoor environments (Semple et al., 2013; Holstius et al., 2014; Dacunto et al., 2015; Manikonda et al., 2016; Rai et al., 2017). The Alphasense OPC N3 Particle Monitor (Alphasense Ltd, Great Notley, UK) has been evaluated focusing on its ability to accurately report the mass concentration of PM_1, $PM_{2.5}$, and PM_{10} (Sousan, Koehler, Hallett, et al., 2016; Crilley et al., 2018). The PurpleAir PA-II-SD Air Quality Sensor (PurpleAir, UT, USA) has demonstrated good linearity against reference instruments for both laboratory calibration and ambient field measurement (Kelly et al., 2017). Several other low-cost monitors have also been evaluated and compared in different studies, including

AirVisual Node (AirVisual, Inc., USA), APT low-cost monitor (Applied Particle Technology, MO, USA), Awair air quality monitor (Bitfinder, Inc., CA, USA), Foobot (Airboxlab, San Francisco, CA, USA), Wynd wearable air quality tracker (Air Quality Tracker Wynd Technologies, Inc., CA, USA), and Xiaomi PM2.5 Detector (Beijing Ji Mi Electronics Technology Co., Ltd, China) (Sousan et al., 2017; Moreno-Rangel et al., 2018; Singer and Delp, 2018).

Although low-cost PM monitors have been well characterized, the studies reflect inherent limitations. First, there is no specified boundary between low-cost PM monitors and low-cost PM sensors. Occasionally, low-cost PM monitors are used as reference instruments to calibrate low-cost PM sensors. At other times, they are treated the same as low-cost PM sensors. It is necessary to distinguish low-cost PM monitors from low-cost PM sensors according to the differences mentioned above, however, it is still uncertain whether they are qualified enough as a reference instrument. Second, calibration methods for low-cost PM monitors very likely differ, but differences are not highlighted in the literature. For low-cost PM sensors, a user calibration procedure will establish the relationship between the PM concentration and an electrical signal (e.g., current, voltage, or pulse width). Hence, the major concern is whether low-cost PM sensors can correlate well with reference instruments. However, for low-cost PM monitors, the correlation is between PM concentrations reported by monitors and the reference instrument, and a larger concern is whether the agreement between monitors and the reference instrument is good enough to replace the user calibration. Hence, linear or polynomial regression may not be sufficient to demonstrate the performance

of low-cost monitors. Third, an important function of some residential monitors is indicating air quality through color change, which is a straightforward display. However, few studies have examined whether a color indicator can convey air quality information accurately and promptly. To bridge the scientific gap, in this study, the performance of nine types of popular low-cost PM monitors was compared, including devices from AirVisual Pro, Alphasense, APT, Awair, Dylos, PurpleAir, Foobot, Wynd, and Xiaomi. These monitors were divided into two groups according to their numbers of channels and types of metrics. As for reference instruments, GRIMM (11C, GRIMM Technologies, Inc., GA, USA) and TSI SidePak (AM530, TSI, Inc., MN, USA) were chosen to evaluate these monitors. A chamber was built to provide an adjustable test environment with well-mixed, and evenly distributed PM concentrations, together with humidity and temperature control.

3.2 Methods

In this study, nine popular low-cost personal PM monitors were compared against two reference instruments. The specifications and metrics of the different monitors were compared, as were their features for convenient application. The procedure to compare monitors with different specifications and metrics will be elaborated in this section. A chamber with temperature and humidity control was designed to provide a well-mixed and evenly distributed flow for calibration experiments. The mixing performance of the chamber was examined at random locations to demonstrate its workability. With the temperature around 25 °C and humidity around 50%, three types of aerosols – ARD particles, sea salt particles, and incense particles –were generated from burning incense, atomizer, and dust dispenser to evaluate the performance of different monitors.

3.2.1 Specifications of low-cost PM monitors and reference instruments

Table 3.1 lists the specifications of all low-cost PM monitors tested in this study. Although some of the monitors (for example, the Alphasense and Dylos) have been utilized as reference instruments to calibrate low-cost PM sensors as reported in the literature (Rajasegarar et al., 2014; Prabakar et al., 2015; Gao et al., 2016; Hojaiji et al., 2017), we treated all of them as test units since there are no significant price differences between them and other tested monitors. Monitors were classified into two groups on the basis of their working principle and metrics. The Alphasense, APT (Applied Particle Technology Minima),

Dylos, and PurpleAir, all use a single particle counter which measures the size distribution for sorting into multiple bins. When particles pass through the measurement area one at a time, the scattered light generates a pulse that is detected by a photodiode, and then the particle size is classified according to the pulse height. The particle sensing modules of the AirVisual, Awair, Foobot, Wynd, and Xiaomi monitors report an analog measurement of the total mass concentration. Particles that pass through the measurement area at the same time scatter light onto the photodiode, and the detected light intensity can be correlated with the PM concentration.

Table 3.1 Specifications of low-cost PM monitors

	Monitor	Cost ($)	Size (cm)	Metrics	Data logging	Selected references
Group I	**Alphasense**	506	8×6×6	• 24 bins (0.35 – 40 μm) [#/mL] • PM_1, $PM_{2.5}$, and PM_{10} [μg/m^3] • RH & T [% & ^oC]	• cable + computer software • micro SD card	Sousan et al., 2016a Hojaiji et al., 2017 Rai et al., 2017 Crilley et al., 2018 Zhang et al., 2018
	APT	NA	10×9×3	• 6 bins (0.3 – 10 μm) [#/0.1L] • PM_1, $PM_{2.5}$, and PM_{10} [μg/m^3] • RH & T [% & ^oC]	• Wi-Fi + webpage • micro SD card	NA
	Dylos	425	19×13×9	• 2 bins (>0.5 μm, >2.5 μm) [#/ft^3]	• cable + computer software	Dacunto et al., 2015 Semple et al., 2013 Manikonda et al., 2016 Sousan et al., 2016b Hojaiji et al., 2017 Rai et al., 2017
	PurpleAir	259	5×4×2	• 6 bins (0.3μm – 10μm) [#/0.1L] • PM_1, $PM_{2.5}$, and PM_{10} [μg/m^3] • RH & T [% & ^oF]	• Wi-Fi + webpage • micro SD card	Morawska et al., 2018 Singer and Delp, 2018 Kelly et al., 2017
Group II	**AirVisual**	269	21×12×8	• $PM_{2.5}$ [μg/m^3] • CO_2 [ppb] • RH & T [% & ^oF] • AQI + color [NA]	• Wi-Fi + App • Retrieval through node ID	Morawska et al., 2018 Singer and Delp, 2018
	Awair	200	16×9×5	• $PM_{2.5}$ [μg/m^3] • CO_2 [ppm] • VOC [ppb] • RH & T [% & ^oF] • AQS + color [NA]	• Wi-Fi + App	Singer and Delp, 2018
	Foobot	200	17×8×7	• $PM_{2.5}$ [μg/m^3] • CO_2 [ppm] • VOC [ppb] • RH & T [% & ^oC] • AQI + color [NA]	• Wi-Fi + App • Retrieval through web login	Sousan et al., 2017 Moreno-Rangel et al., 2018 Singer and Delp, 2018
	Wynd	79	7×4×2	• $PM_{2.5}$ [μg/m^3] • AQI + color [NA]	• Bluetooth + App	NA
	Xiaomi	75	6×6×3	• $PM_{2.5}$ [μg/m^3] • Color [NA]	• Wi-Fi + App	NA

Among the first group, the APT and PurpleAir are equipped with a Plantower (Plantower Co., Ltd., Beijing, China) single particle sensing module. The Alphasense and Dylos have their own custom-designed sensing modules. Due to the difference among sensing modules, the data reporting formats of each monitor are different. The APT and PurpleAir monitors, using the low-cost Plantower sensor, report the size distribution of particles ranging from 0.3 – 10 μm in six bins. The Alphasense has a better resolution, and reports the sizes ranging from 0.3 – 38 μm in 24 bins. The Dylos has only two bins for particles larger than 0.5 μm and 2.5 μm respectively. To make the Dylos results comparable with other monitors in the first group, the number concentration of the second bin (>2.5 μm) was subtracted from that of the first bin (>0.5 μm) to represent the number concentration of particles smaller than 2.5 μm. The Alphasense, APT, and PurpleAir not only report the size distribution in the unit of number concentration, but also report mass concentrations of PM_1, $PM_{2.5}$, and PM_{10}.

For data logging, Alphasense and Dylos do not have a wireless module, hence they need to be connected to a computer to display real-time data. The PurpleAir and APT monitors can upload data to a manufacture-provided webpage through a Wi-Fi module. The Alphasense, APT, and PurpleAir also have internal off-line data logging system that can record the data on a micro SD card in case of connection malfunction. The sampling interval of the APT is adjustable, and in our study was set at one minute to be consistent with the Dylos and GRIMM. The Alphasense reported data every one second, and the data was averaged over one minute too. The PurpleAir has a fixed

sampling interval of 80 seconds, hence the data was interpolated to get a one-minute sampling interval.

The monitors in the second group are targeted for residential use, hence they are cheaper and smaller, with an attractive appearance and a straightforward display. Apart from PM mass concentration, the AirVisual, Awair and Foobot also monitor the CO_2 or VOC concentrations for a more comprehensive air quality measurement. Since they are designed for residential use, important features, for example, the sampling interval or working principle, are not explained thoroughly in the manufacturer's descriptions. For data logging, all five monitors have a wireless module, a Bluetooth chip for the Wynd and a Wi-Fi chip for the rest of the monitors, to synchronize the data to tablet or phone applications. For the AirVisual and Foobot, after data is synchronized with the application, it can be accessed online with a ten-minute and a five-minute interval respectively. However, for other monitors, historical data is not accessible since it is not saved. Our study circumvented this problem by video recording the screen with the app running to record the data and time. The data was manually extracted and averaged over one-minute intervals. Apart from measuring PM concentrations, these monitors also report an air quality related index and use different colors to display the air quality more straightforwardly.

Comparing different data logging methods of all tested low-cost PM monitors, a Wi-Fi module or a Bluetooth module can synchronize the data remotely and conveniently

as opposed to connections with cables. Generally, monitors with a Bluetooth module can be configured more easily than monitors with a Wi-Fi module, since the Wi-Fi module usually requires a specific type of wireless internet. The Bluetooth module can be connected to user applications straightforwardly, however, the data transfer relies on the user-end application and is restricted in a confined space. On the other hand, monitors with the Wi-Fi module, can continue collecting the data even without running user-end applications, which allows long-term and remote data collection. The transferred data can then be accessed through user-end applications (AirVisual, Awair, Foobot, Wynd and Xiaomi), through web portals (AirVisual, APT, Foobot and PurpleAir), or through computer software (Alphasense and Dylos).

To compare monitors with different working principles, GRIMM and SidePak were chosen as reference instruments. SidePak reported the $PM_{2.5}$ mass concentration, which can be correlated directly with different monitors. GRIMM, as a federal reference method (FRM), is a single particle counter that measures the sizes of PM ranging from 0.25 – 32 μm and reports the distribution in 31 bins. A bin-wise comparison, as shown in Figure 3.1 was conducted for the monitors of the first group to demonstrate the accuracy of their size distribution measurements. Compared to APT, Dylos, and PurpleAir, the Alphasense has more bins and a different distribution, therefore, common ranges for the Alphasense and GRIMM were selected for bin-wise calibration. The APT, Dylos and PurpleAir use fewer bins than the GRIMM, hence several GRIMM bins were summed to enable comparison.

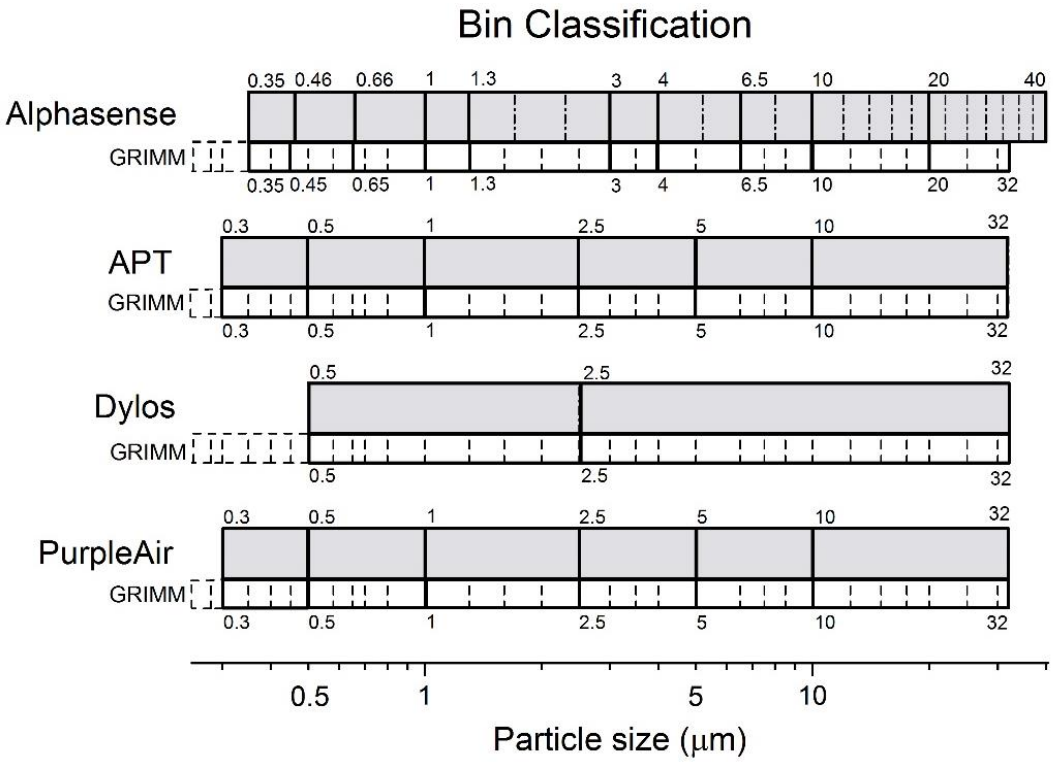

Figure 3.1 Bin classification for monitors in the first group (Alphasense, APT, Dylos, and PurpleAir) in bin-wise comparison against the GRIMM. The dash-dot line and dashed line represent the bin distribution of each monitor and the GRIMM respectively. The 31st bin of GRIMM (>32 μm) is not depicted in this figure. The thick box represents the common range of combined bins for comparison.

3.2.2 Air quality related index and color display

The second group of monitors, the AirVisual, Awair, Foobot, Wynd, and Xiaomi used both numeric indexes and color display to report the air quality. Foobot gives a simplified numeric index on a scale of 0 to 100 indicating air quality ranging from healthy to poor. The Awair presents an air quality score (AQS), and AirVisual and Wynd present the air quality index (AQI). The AQS is scaled from 0 to a 100 to indicate the air quality from poor to healthy. However, neither the product manual nor the literature describes how the AQS is calculated. Compared to the AQS, the AQI is

a more common parameter for presenting the potential airborne hazards. The component species and calculation details of the AQI vary with local regulations, but normally, several common air pollutant are included: PM, ozone, VOC, carbon monoxide, and sulfur dioxide (Gao et al., 2015; Hu et al., 2015; EPA, 2016). A high AQI indicates an unhealthy environment, and the AQI range from low to high is divided into six segments with numeric index ranging from 0 to 500 that describes the overall air quality, from excellent to heavily polluted. Since PM is the major object of this study, the AQI mentioned in the following section is calculated based on the PM mass concentration, following the US EPA regulations published in 2016 (EPA, 2016).

Compared to numeric indexes, color is a more straightforward way of showing air quality. The US EPA divides the AQI into six sections, and each section with a signal color (green indicates “good”, yellow is “moderate”, orange means “unhealthy for sensitive groups”, red represents “unhealthy”, purple indicates “very unhealthy”, and maroon stands for “hazardous”). Ideally, all monitors would use the color scheme of the AQI, which would make the results directly comparable. In reality, only the AirVisual follows the AQI color distribution. The Awair, Foobot, Wynd, and Xiaomi monitors assign colors according to their own schemes, as shown in Figure 3.2. For example, the Foobot uses just two colors, blue and orange, and Xiaomi monitor has only three colors, green, yellow, and red. To examine whether the color display properly conveys the air quality message, the US EPA regulated AQI was first

calculated based on the PM concentration reported by the GRIMM, and the AQI-designated color was used to represent the air quality. The colors reported by the various monitors were recorded at the same time for comparison. Ideally, the colors would all be both identical and accurate representations of the GRIMM-reported PM concentration.

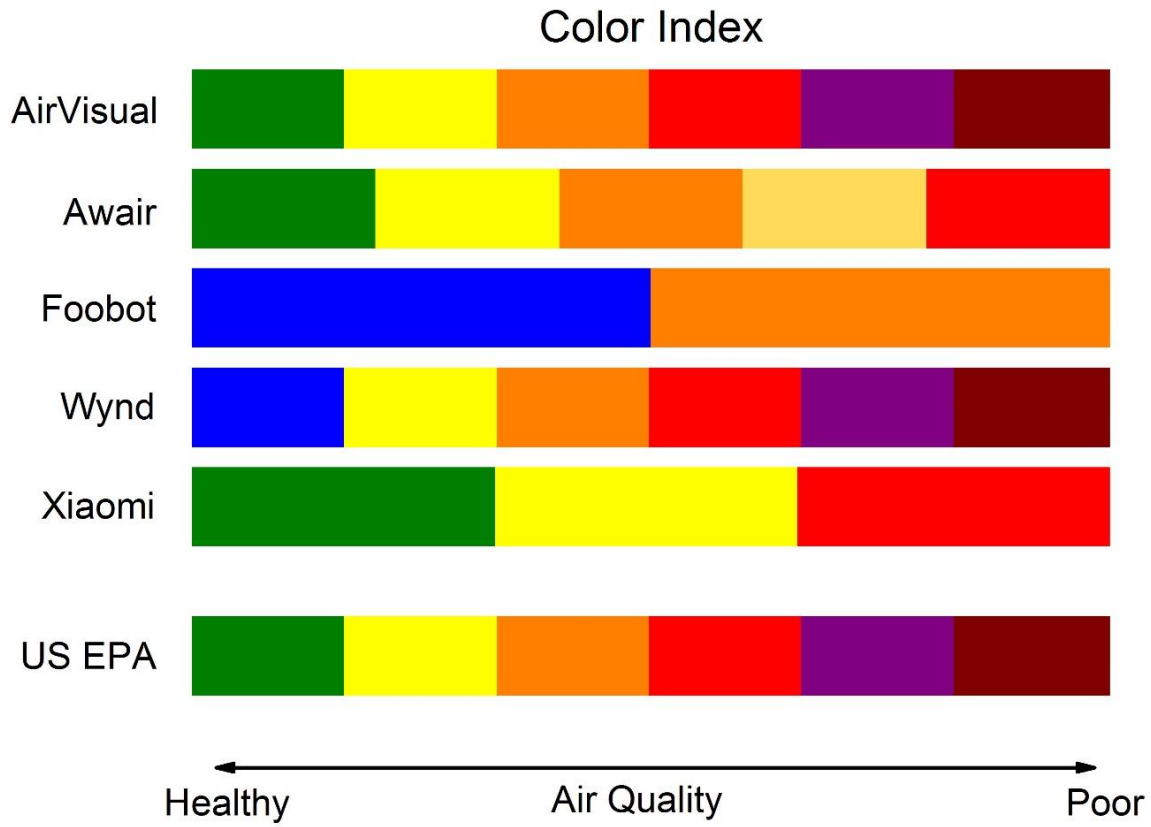

Figure 3.2 Color display pattern of each monitor and US EPA stipulated display.

3.2.3 Test chamber and aerosol sources

A chamber was designed according to Figure 3.3 to provide a well-mixed and evenly-distributed PM flow as the test environment. The aerosol was introduced to the

chamber through the inlet on the top, and then ventilated through the outlet on the bottom. The exhaust air was filtered by a HEPA filter, and a flow controlled vacuum pump was used to adjust the flowrate (2 – 15 L/min) and to control the PM concentration level inside. The interior included a mixing area and a test area, separated by two baffles with a matrix of one-inch holes. In the mixing area, two fans were used to improve the air circulation. A humidifier and a cartridge heater in the mixing area were connected to a humidity sensor and a temperature sensor in the test area to maintain the temperature and humidity in the test area at 23 °C and 50% RH. Particles, heat, and humidity were mixed with distorted streamlines. After sufficient mixing, the streamlines passed through two baffles with densely spaced holes to form an evenly distributed laminar flow passing through the test area. During the experiments, the monitors and the SidePak were placed on the lower-level baffle, and the GRIMM was placed outside the chamber but connected to the test area.

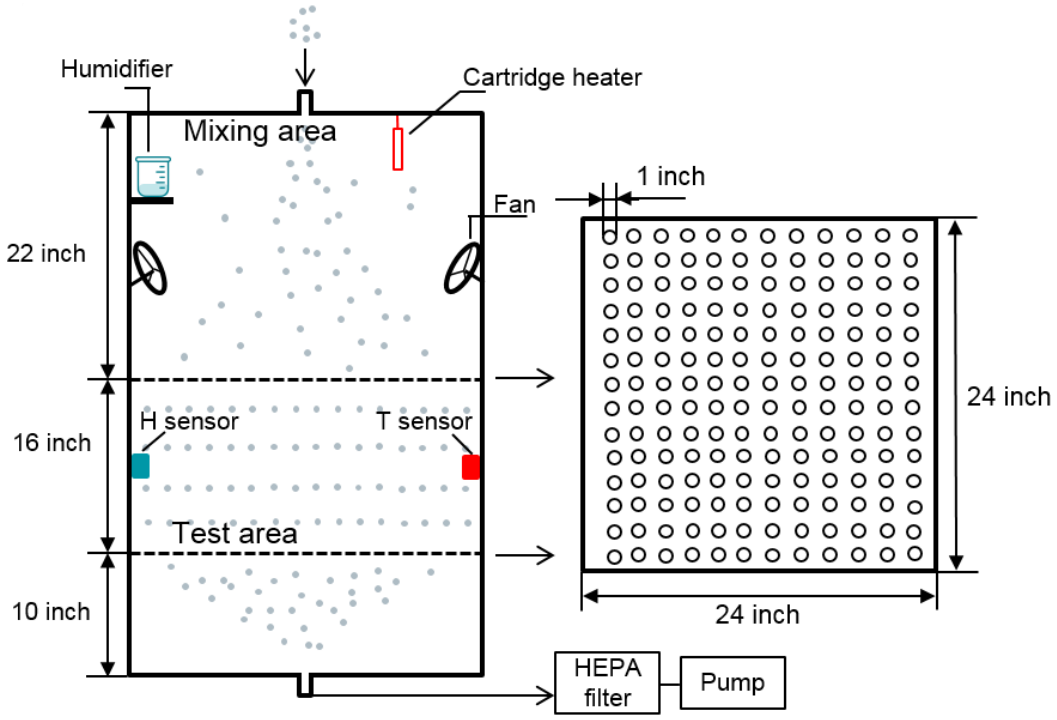

Figure 3.3 The structure of a chamber to provide a well-mixed and evenly-distributed PM flow as a test environment.

Using incense particles, the uniformity of the PM distribution in the test area was examined by the SidePak and the APT monitor, placed at random locations on the lower-level baffle. The response from the APT monitor was correlated with that from the SidePak via a linear regression. The whole procedure was repeated three times by placing the APT monitor at different sampling locations. In all three tests, the response from the APT monitor correlated well with SidePak, with all R^2 values higher than 0.99. The slopes from different tests were approximately similar, 0.847, 0.867, and 0.897, which indicated that the PM was well mixed and evenly distributed in the test area.

After proving the suitability of the chamber, monitors were tested with ARD (Arizona road dust) particles, sodium chloride (sea salt) particles, and incense particles. The normalized mass distribution of each source was reported by GRIMM, as shown in Figure 3.4. Incense particles and sea salt particles peaked around 0.5 and 0.3 μm respectively. ARD were larger and peaked around 2 – 4 μm.

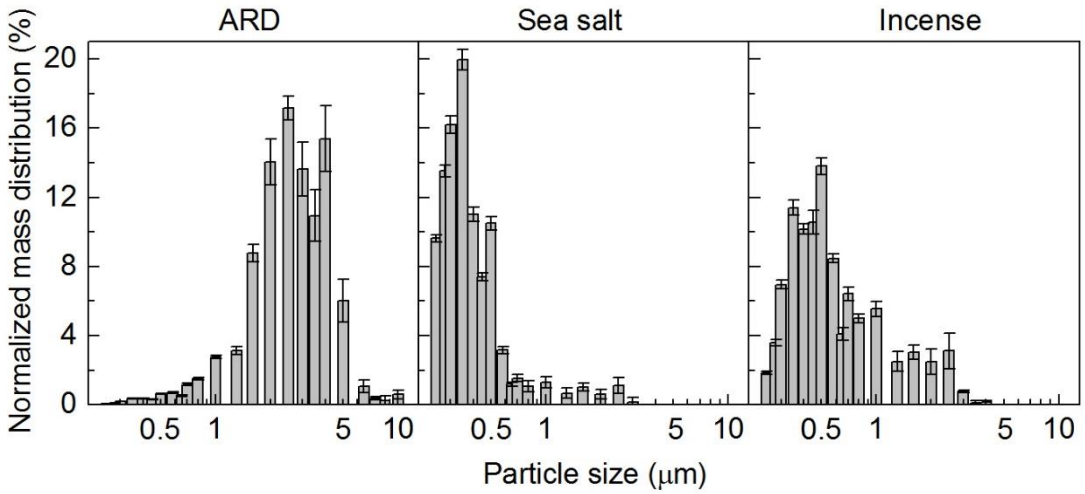

Figure 3.4 Normalized mass concentration distributions of ARD particles, sea salt particles, and incense particles generated during the experiments, measured by GRIMM.

3.3 Results and discussion

3.3.1 Alphasense, Dylos, APT, and PurpleAir monitors

3.3.1.1 Time response and correlation based on $PM_{2.5}$ mass concentration

The $PM_{2.5}$ mass concentrations reported by monitors and reference instruments for different PM sources are plotted with time in Figure 3.5, with a one-minute sampling interval. The red and blue dashed lines represent the GRIMM and SidePak respectively, and the solid lines with different colors represent different low-cost PM monitors. For ARD particles, the GRIMM and SidePak overlapped well with each other, since they were both calibrated with ARD particles in their factory calibrations. While the GRIMM and SidePak responded simultaneously for incense and sea salt particles, their indicated PM levels were different. Such a difference might be due to the different working principles: the GRIMM is a single particle counter, but the SidePak performs ensemble measurement. Other monitors also responded simultaneously to PM concentration fluctuations for incense and sea salt particles, although there was a difference among peak values. However, for ARD particles, a noticeable delay was found for the Dylos monitor in repeated tests. Two reasons may lead to such a delay. First, the other monitors directly reported the mass concentration of $PM_{2.5}$, but for the Dylos monitor, the large bin (>2.5 μm) was subtracted from the small bin (>0.5 μm) to calculate the number concentration of particles from 0.5 – 2.5 μm. Then, the number concentration was converted to the mass concentration by

assuming all these particles were 2.5 μm, with a density of 1200 kg/m^3. These assumptions might introduce errors into the results. Another possible reason is the misclassification of particles ranging from 0.5 – 2.5 μm. Particles in this range were supposed to be classified into the small bin, however, they may have been accidentally classified into the large bin. Misclassification can influence data accuracy, which results in a noticeable delay. According to the number-based size distribution, approximately 30%, of the ARD particles fall in the range of 0.5 – 2.5 μm, but only 6% of incense particles and 1% of sea salt particles fall in this range. Thus, the delay is noticeable for ARD particles, but almost negligible for incense and sea salt particles.

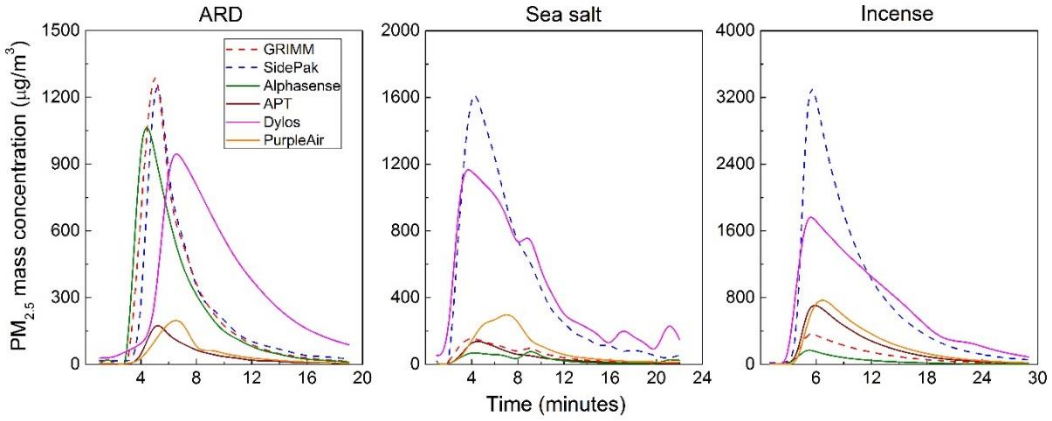

Figure 3.5 The $PM_{2.5}$ mass concentration variation against time for different aerosol sources, reported by reference instruments (GRIMM and SidePak) and monitors (Alphasense, APT, Dylos, and PurpleAir monitors).

The $PM_{2.5}$ mass concentration reported by each monitor was also plotted against the reference instruments for pairwise correlation, as shown in Figure 3.6. These monitors

had been pre-calibrated, hence better accuracy was expected. Apart from a high R^2 value, a slope value approximate to one was expected to demonstrate the agreement between monitors and reference instruments. A slope larger or smaller than one represents a monitors' overestimation or underestimation of the $PM_{2.5}$ mass concentration compared to the reference instruments. The APT and PurpleAir demonstrated good linearity for various sources, with all R^2 values larger than 0.94 and 0.91 respectively. For the Dylos, linear regression may not be the optimal fitting method. For the Alphasense, the data slopes were stable when compared against the GRIMM for different sources. One thing worth noting is that the linear correlation may not be sufficient to demonstrate agreement between monitors and reference instruments. It cannot demonstrate how data quality has been improved after calibration. Thus, we plotted the data in a different manner, which will be illustrated in a later section

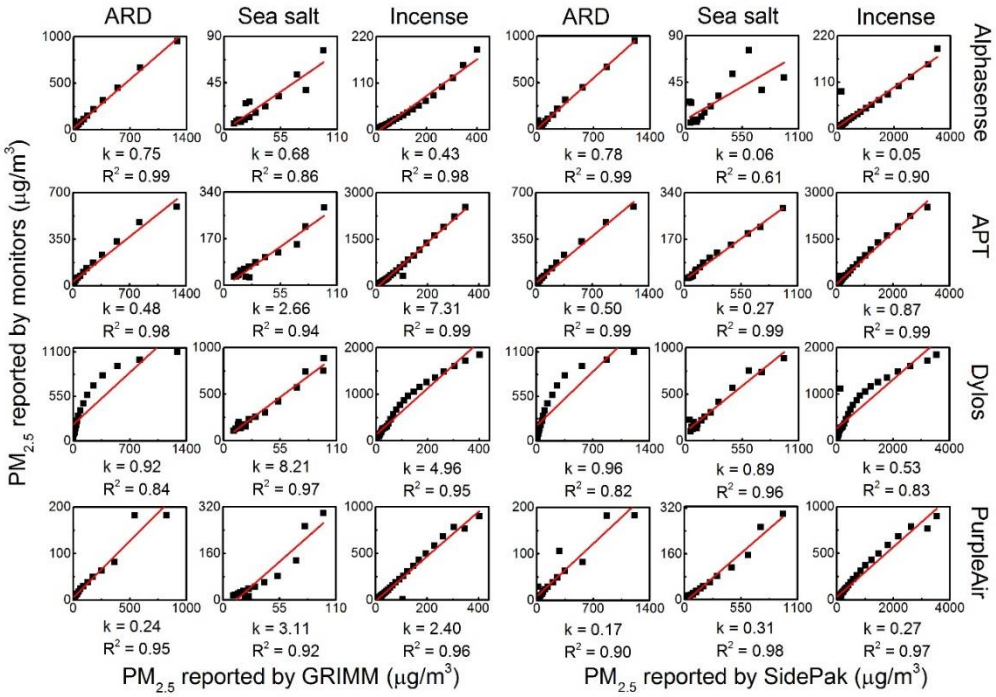

Figure 3.6 Pairwise correlation among the monitors (Alphasense, APT, Dylos, and PurpleAir) and the reference instruments (GRIMM and SidePak) for ARD, sea salt, and incense particles. Slope and R^2 values were calculated by least squares regression.

3.3.1.2 Bin-wise evaluation for size distribution measurement

Based on the bin classification in Figure 3.1, we plotted the number concentration reported by the GRIMM and the tested monitors for different bins in Figure 3.7. The dashed line in the figure represents the 1:1 ratio, where the monitors and the GRIMM reported the same results. For comparison, figures of the same source were plotted under the same scales, except for the correlation between the Dylos and the GRIMM for incense measurement. The legends of different monitors were displayed on the rightmost position of each row.

In Figure 3.7, Alphasense demonstrated an overestimation for tested sources. One more thing worth noting is that after saturation, the response from Alphasense decreased with increasing PM concentration, especially for ARD and incense particles. Such an inverted U-shape may be caused by the coincidence error that several small particles passed the measuring point at the same time and were characterized as a larger particle by mistake. Coincidence error may lead to an inaccurate size distribution due to the underestimation and overestimation for small and large particles respectively. However, the PM mass correlation in Figure 3.6 was not largely influenced by such coincidence error since the misclassified large particle made up the mass loss of small particles. APT monitor showed a very close estimation for ARD particles, however, for sea salt and incense particles, there was an underestimation and overestimation for 0.3 – 0.5 μm and 0.5 – 1 μm particles respectively. Dylos predicted a very close estimation for sea salt particles, however, underestimated ARD and incense particles for smaller bins, and overestimate ARD particles for larger bins. PurpleAir monitor demonstrated an underestimation for tested sources.

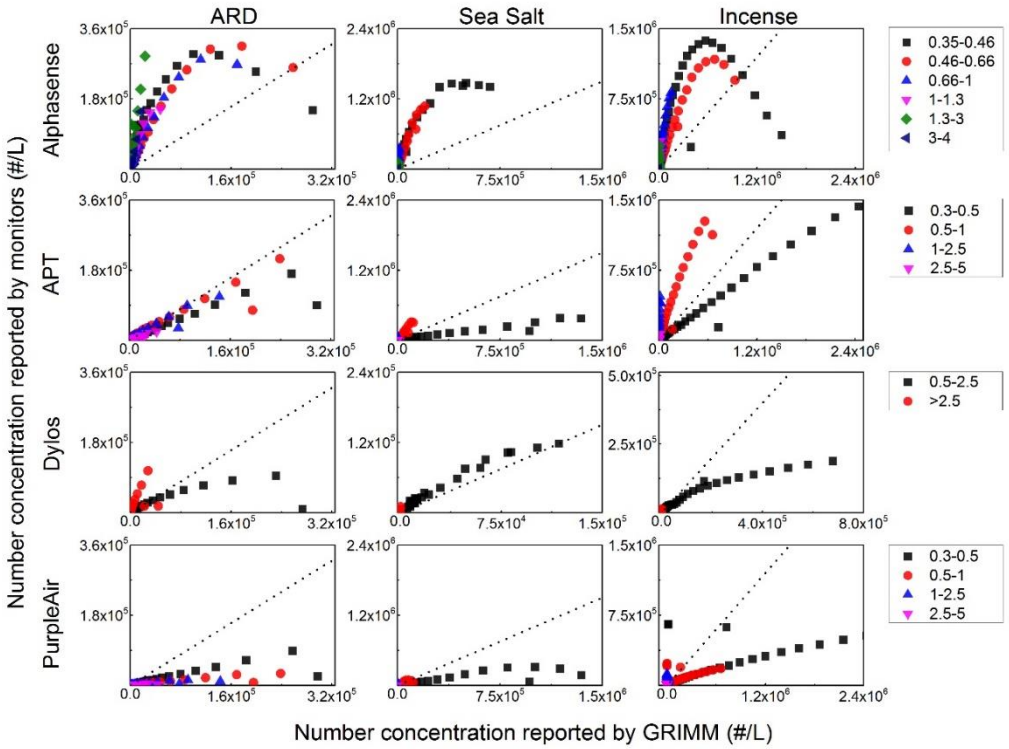

Figure 3.7 Bin-wise number concentration comparison of monitors (Alphasense, APT, Dylos, and PurpleAir) and the reference instrument (GRIMM) for different sources in different concentration ranges.

Figure 3.7 also gave a clue on the question whether the calibration procedures should be the same for the optical particle counters and the monitors performing ensemble measurement. For sensors performing ensemble measurement, calibration procedures established the one-to-one relationship between the sensor output and the PM concentration level. However, for optical particle counters, all different channels together contribute to the final mass concentration estimation, and the one-to-one correlation may oversimplify the situation. In Figure 3.7, most of the data points could not fall in a narrow range, indicating that no unique calibration factors could be

applied for all different channels. On the contrary, different calibration factors from bin-wise size distribution calibration may produce better accuracy. However, a bin-wise calibration may lower the resolution since common ranges between the monitors and the reference instruments need to be selected. In addition, the bin-wise calibration may be influenced by the PM composition too, since the composition will influence the size characterization, which makes the situation more complicated.

To demonstrate a more straightforward comparison, the size distribution reported by different monitors and the GRIMM is displayed in Figure 3.8. Three samples under an approximately stable and high PM concentration were selected for different sources, and the number concentration reported by the GRIMM and the tested monitors were plotted in shaded and yellow columns, respectively, on the left y axis. The bin ratio, which is the ratio of the number concentration reported by the monitors to that reported by the GRIMM, is plotted in a line to be read from the right y axis. The dashed line in the figure represents the bin ratio of 1, where the monitors and the GRIMM reported the same results. Figure 3.8 also indicated that no unique calibration factor can be deployed for all channels, although all sensors predicted a roughly correct size distribution. Alphasense and PurpleAir displayed an underestimation and overestimation for small and large particles respectively, which might be due to the coincidence error. The Dylos has only two bins, therefore it is difficult to compare the size distribution. One thing worth noting is that the noticeable overestimation for larger particles might not be sufficient to assess the monitors' true performance. The

number concentration is very low for larger particles, which may skew the evaluation. The GRIMM detected almost no particles larger than 4 μm, but the PurpleAir, APT, and Alphasense monitors reported the existence of 10 μm particles.

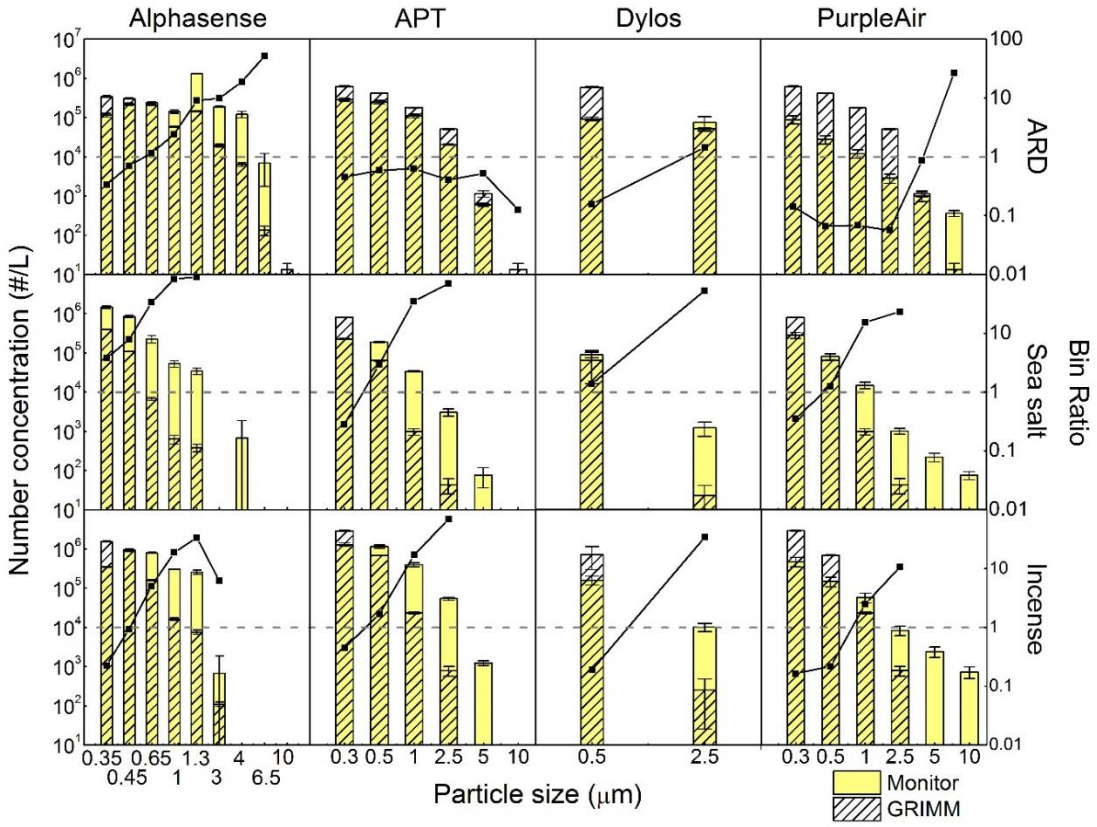

Figure 3.8 Size distributions reported by monitors (Alphasense, APT, Dylos, and PurpleAir) and the reference instrument (GRIMM). The number concentrations reported by the monitors and GRIMM are plotted on the left y axis in yellow and shaded columns respectively. The bin ratio can be read on the right y axis.

3.3.1.3 Agreement before and after calibration

As mentioned in the introduction, a large selling point of these low-cost PM monitors is that they arrive assembled and calibrated for deployment. However, according to the results of the pairwise correlation based on the $PM_{2.5}$ mass concentration and the

bin-wise comparison based on the number concentration, discrepancies existed between measurements. Two reasons can explain such discrepancy: different inherent working principles of these monitors, and errors that can be eliminated by calibrations. In other words, the calibration discrepancy is a systematic error, representing a constant drift that can be corrected. However, the inherent discrepancy cannot be eliminated through further calibrations, similar to random errors that cannot be ruled out.

To distinguish whether the discrepancies were inherent or the result of inadequate calibration, the ARD $PM_{2.5}$ data in Figure 3.6 was replotted as shown in Figure 3.9. For each data point, the differences between the $PM_{2.5}$ mass concentrations reported by the monitors and GRIMM were plotted against their average. This method can demonstrate the agreement between two measurements, and thus examines whether an instrument is a qualified substitute of the reference instruments (Bland and Altman, 1986; Bland and Altman, 2003; Astrua et al., 2007). On each figure, the dashed line in the middle is the mean of differences (σ), and the dotted lines ($\sigma \pm 2SD$) indicate the upper and lower boundaries of the differences, where *SD* is the standard deviation of the differences. A smaller absolute value of σ and a narrower boundary ($4SD$) indicate a better data quality. For the column of before calibration, the data reported by the monitors were used directly to calculate the differences by comparing with the GRIMM data. Since the inherent deficiencies need to be examined after getting rid of the effects of inappropriate calibration, all monitors were calibrated according to

either linear regression (SidePak, APT, and PurpleAir) or secondary polynomial regression (Alphasense and Dylos) to obtain an R^2 value larger than 0.96. The data reported by monitors from direct measurements were recalculated with calibration equations to repeat the previous procedures for the "after calibration" column.

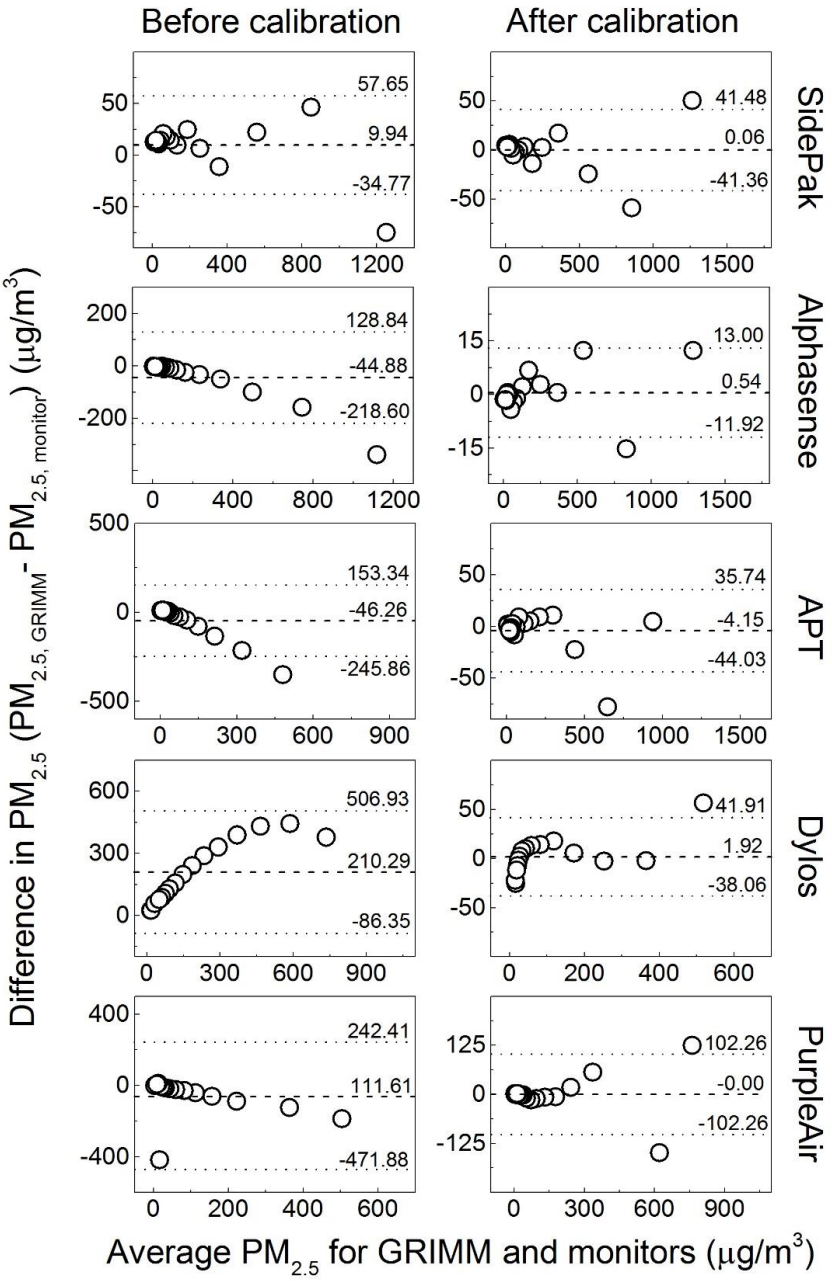

Figure 3.9 Differences and averages of $PM_{2.5}$ mass concentrations reported by the monitors and GRIMM for examining the agreement before and after calibration.

Before calibration, the low-cost PM monitors exhibited a strong relationship between the difference and the average. For the Alphasense, APT, and PurpleAir, the difference increased negatively with the average, which illustrated that the calibration factor provided by the manufacturer was too large. Therefore, these monitors overestimated the $PM_{2.5}$ mass concentration compared to the GRIMM. The overestimation was proportional to the measurement scale; hence the difference and the average demonstrated a strong correlation. The Dylos showed a positive correlation between the difference and average, which may be caused by too small a calibration factor. For all four monitors, the gaps between boundaries (4*SD*) had shrunk observably and the σ had been reset closer to zero after applying calibration equations, which demonstrate that calibration deviations for these four monitors were corrected after user calibration.

One thing worth noting is that no matter whether before or after calibration, the SidePak did not show a strong correlation between the difference and the average. It showed the narrowest gap between boundaries (4*SD*) before calibration, when compared to other monitors. After calibration, the width of the gap (4*SD*) remained the same, and the mean of the difference (σ) was reset closer to the zero. This behavior illustrated that the user calibration did not significantly improve the data

quality of the SidePak. Therefore, user calibration is not necessary for SidePak in measuring ARD $PM_{2.5}$ mass concentration.

In summary, the factory calibration is sufficient for the SidePak for measuring ARD $PM_{2.5}$, however, the user calibration improves the data quality of the other four monitors. After the user calibration, the distribution of differences demonstrated a narrower difference boundary (4*SD*) and a smaller absolute value of σ, which supports the elimination of calibration deviation. After user calibration, the Alphasense demonstrated the best performance, with an even narrower gap of boundaries (4*SD*) than the SidePak. The reason might be that both the GRIMM and the Alphasense use a single particle counter, but the SidePak uses ensemble measurement. Hence, after the user calibration, the Alphasense demonstrated a greater consistency with the GRIMM data.

3.3.2 AirVisual, Awair, Foobot, Wynd, and Xiaomi monitors

3.3.2.1 Time response and correlation based on the $PM_{2.5}$ mass concentration

Similar to the first group, the $PM_{2.5}$ mass concentration reported by different monitors and reference instruments were plotted against time. As shown in Figure 3.10, the monitors responded almost simultaneously to increasing PM concentrations. However, it is noticeable that the AirVisual demonstrated a different shape due to its five-minute sampling interval. The Awair and Wynd saturated very quickly in the

tests, especially for ARD and incense particles. This saturation can be observed more clearly in Figure 11, which plots the $PM_{2.5}$ mass concentration reported by the monitors against the reference instruments.

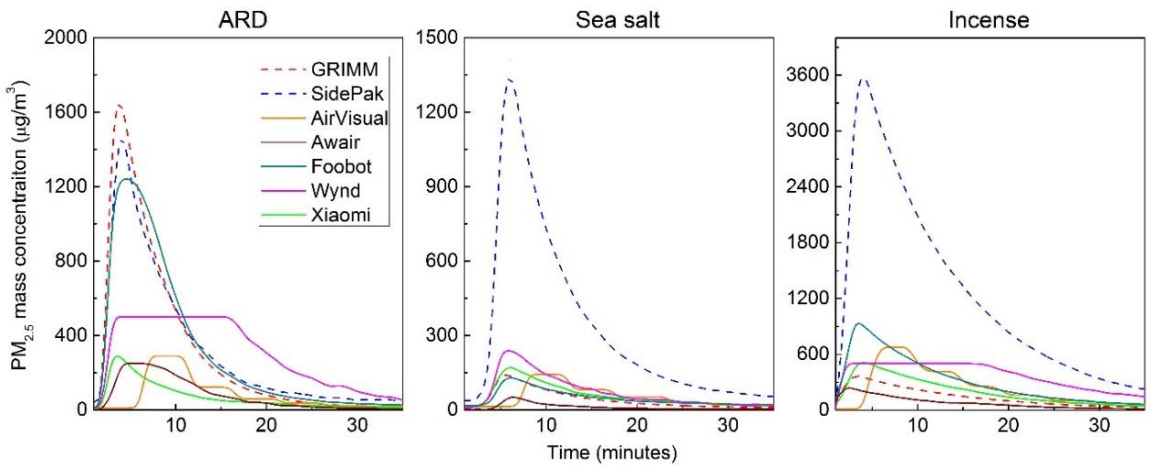

Figure 3.10 $PM_{2.5}$ mass concentration variation against time for different aerosol sources, reported by the reference instruments (GRIMM and SidePak) and monitors (AirVisual, Awair, Foobot, Wynd, and Xiaomi).

Figure 3.11 shows that all five monitors demonstrated good linear correlation with the GRIMM or SidePak. The AirVisual had a longer sampling interval, leading to segmented scattered data. The Awair and Wynd showed lower saturation concentrations, and the linear fitting curve in the figure is based on the unsaturated part. The Foobot and Xiaomi correlated well with the GRIMM and SidePak over the full range for different PM sources. However, for AirVisual, Awair, and Wynd, saturation occurred at a lower concentration level. The Foobot presented a high R^2 value with a slope close to one for ARD particles, hence the Foobot has been calibrated well for ARD particle measurement in the manufactory setting.

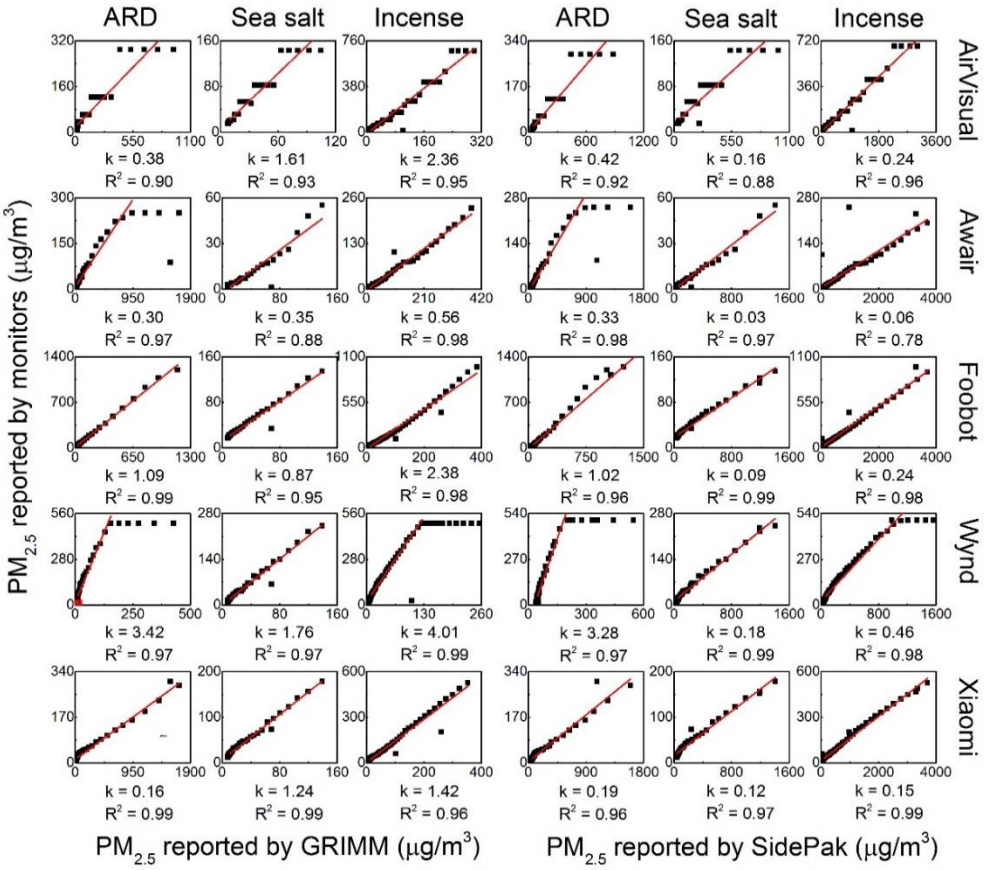

Figure 3.11 Pairwise correlation among the monitors (AirVisual, Awair, Foobot, Wynd, and Xiaomi) and the reference instruments (Grimm and SidePak) for ARD, sea salt, and incense particles. Slope and R^2 values were calculated by the least squares regression for the unsaturated range.

3.3.2.2 Color indication

Unlike the first group of low-cost monitors, the second group of monitors is mainly for residential use. Hence conveying the air quality precisely to users is the first concern, rather than accurately measuring the PM mass concentration. They all convey the air quality though a straightforward color display. Therefore, instead of focusing on the statistics for data quality, we recorded the color change pattern to examine whether each monitor could trigger an air quality alarm promptly. The $PM_{2.5}$

mass concentration reported by the GRIMM was selected as the reference. The US AQI was calculated based on the reference mass concentration, then a color was chosen accordingly per to the US EPA regulations. The color change of the monitors was recorded from their user applications and then correlated with the $PM_{2.5}$ mass concentration reported by the GRIMM, as shown in Figure 3.12.

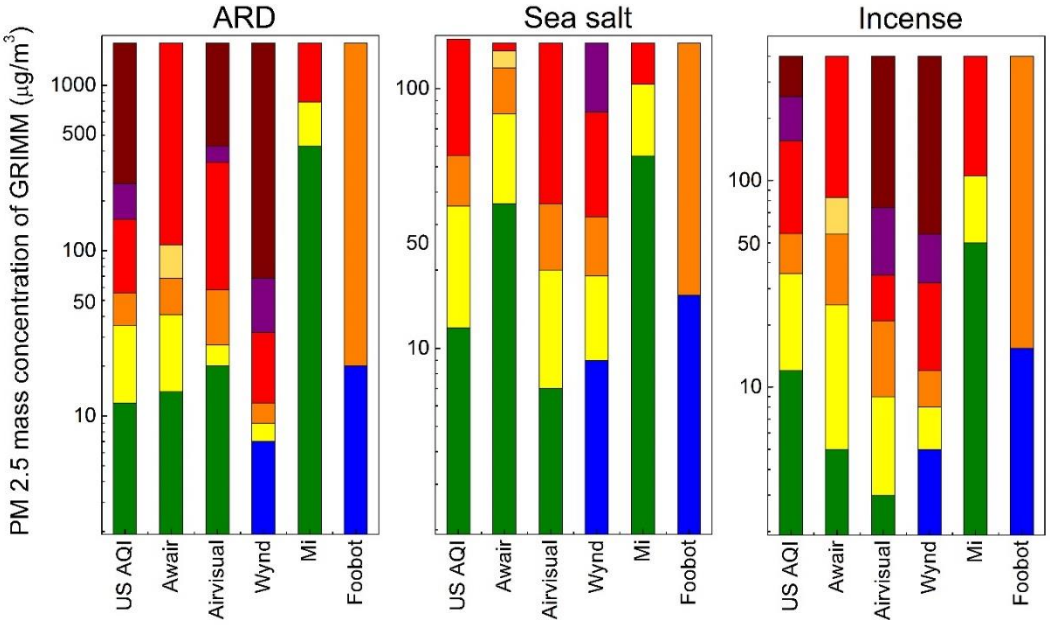

Figure 3.12 Color display patterns of the monitors (AirVisual, Awair, Foobot, Wynd, and Xiaomi) for different aerosol sources. The color change for the US AQI column is based on the $PM_{2.5}$ mass concentration reported by the GRIMM. The color changes of other monitors were recorded from user applications.

Among these monitors, the AirVisual has the same color pattern as to US AQI; the Awair and Wynd each had a similar color pattern. The Awair does not use the maroon color, which represents the poorest air quality in the US AQI. The Wynd uses a blue instead of green for good air quality. The Xiaomi and Foobot have just three and two

colors respectively, a very simplified color scheme that is inconvenient for comparison. For example, for ARD particles, when other monitors turned red or maroon indicating unhealthy air quality, the Xiaomi monitor still displayed green, indicating a healthy environment, which is misleading to users. Among the monitors in the second group, the Foobot most closely predicted the PM mass concentration, but its color pattern is very different from that of the US AQI or other monitors. Nevertheless, for Foobot, the color change between blue and orange always happened when the US AQI was displaying a yellow color, indicating moderate air quality, which can be considered as consistent and accurate. Considering the difficulty of comparing different color patterns, we left the Foobot and Xiaomi out of the comparison, and focused only on the color indicating function of the AirVisual, Awair, and Wynd.

Among the AirVisual, Awair, and Wynd, the Wynd triggered the alarm ahead of the US AQI for all three different sources, hence, the Wynd is qualified as a residential monitor for generating prompt alarms. The Awair had an early response to incense particles, an almost simultaneous response to ARD particles, and a delayed response to sea salt particles. Therefore, the Awair is more sensitive to combustion particles, and may not be very sensitive to sea salt particles. The AirVisual demonstrated an early alarm for incense and sea salt particles, and a late alarm for ARD particles. However, as mentioned before, the AirVisual measured the PM level and synchronized the data every five minutes, which may affect the color display. In

general, apart from the Xiaomi monitor, although each monitor has different responses to various sources, all four other monitors, AirVisual, Awair, Foobot, and Wynd, indicated the air quality moderately well.

3.4 Conclusions

This study compared nine popular low-cost PM monitors, divided into two groups based on their features and working principles. For the first group, including the Alphasense, APT, Dylos, and PurpleAir monitors, we evaluated whether they were qualified substitutes of the reference instruments. Although they all demonstrated a good linearity against the reference instruments, the agreement was not good between them and the reference instruments. In the bin-wise comparisons, no unique calibration factor could be applied to all channels. Thus, bin-wise calibration might improve the data quality more effectively, and user calibration is necessary to guarantee the data quality. Coincidence error, leading to a biased size distribution, has been observed under high concentration level, however, was found to have little impact on the reported mass concentration. In the second group, including the AirVisual, Awair, Foobot, Wynd, and Xiaomi monitors, we examined whether they could report the air quality changes promptly and accurately through their color displays. They all demonstrated a good linearity compared to the reference instruments. Apart from Xiaomi, the other four monitors could demonstrate the air quality through color display with a moderate accuracy.

3.5 References

Aliyu, Y.A. and Botai, J.O. (2018). Reviewing the local and global implications of air pollution trends in zaria, northern nigeria. *Urban Clim.* 26: 51-59.

Allen, G., Sioutas, C., Koutrakis, P., Reiss, R., Lurmann, F.W. and Roberts, P.T. (1997). Evaluation of the teom® method for measurement of ambient particulate mass in urban areas. *J. Air Waste Manage. Assoc.* 47: 682-689.

Astrua, M., Ichim, D., Pennecchi, F. and Pisani, M. (2007). Statistical techniques for assessing the agreement between two instruments. *Metrologia* 44: 385.

Bland, J.M. and Altman, D. (1986). Statistical methods for assessing agreement between two methods of clinical measurement. *The lancet* 327: 307-310.

Bland, J.M. and Altman, D.G. (2003). Applying the right statistics: Analyses of measurement studies. *Ultrasound Obstet. Gynecol.* 22: 85-93.

Brook, R.D., Rajagopalan, S., Pope, C.A., Brook, J.R., Bhatnagar, A., Diez-Roux, A.V., Holguin, F., Hong, Y., Luepker, R.V. and Mittleman, M.A. (2010). Particulate matter air pollution and cardiovascular disease: An update to the scientific statement from the american heart association. *Circulation* 121: 2331-2378.

Burnett, R.T., Pope III, C.A., Ezzati, M., Olives, C., Lim, S.S., Mehta, S., Shin, H.H., Singh, G., Hubbell, B., Brauer, M. and Anderson, H.R. (2014). An integrated risk function for estimating the global burden of disease attributable to ambient fine particulate matter exposure. *Environ. Health Perspect.*, 122(4): 397–403.

Cohen, A.J., Ross Anderson, H., Ostro, B., Pandey, K.D., Krzyzanowski, M., Künzli, N., Gutschmidt, K., Pope, A., Romieu, I. and Samet, J.M. (2005). The global burden of disease due to outdoor air pollution. *J. Toxicol. Environ. Health, Part A* 68: 1301-1307.

Crilley, L.R., Shaw, M., Pound, R., Kramer, L.J., Price, R., Young, S., Lewis, A.C. and Pope, F.D. (2018). Evaluation of a low-cost optical particle counter (alphasense opc-n2) for ambient air monitoring. *Atmos. Meas. Tech.*: 709-720.

Dacunto, P.J., Klepeis, N.E., Cheng, K.-C., Acevedo-Bolton, V., Jiang, R.-T., Repace, J.L., Ott, W.R. and Hildemann, L.M. (2015). Determining pm 2.5 calibration curves for a low-cost particle monitor: Common indoor residential aerosols. *Environ. Sci. Process. Impacts* 17: 1959-1966.

EPA, U.S. (2016). Technical assistance document for the reporting of daily air quality - the air quality index (aqi).

Gao, Q., Liu, J., Li, W. and Gao, W. (2015). Comparative analysis and inspiration of air quality index between china and america. *Huan jing ke xue= Huanjing kexue* 36: 1141-1147.

Gao, Y., Dong, W., Guo, K., Liu, X., Chen, Y., Liu, X., Bu, J. and Chen, C. In (Ed.)^(Eds.) INFOCOM, 2016, pp. 1-9.

Hapidin, D.A., Saputra, C., Maulana, D.S., Munir, M.M. and Khairurrijal, K. Aerosol chamber characterization for commercial particulate matter (pm) sensor evaluation.

Hojaiji, H., Kalantarian, H., Bui, A.A., King, C.E. and Sarrafzadeh, M. In (Ed.)^(Eds.) Sensors Applications Symposium (SAS), 2017 IEEE, 2017, IEEE, pp. 1-6.

Holstius, D.M., Pillarisetti, A., Smith, K. and Seto, E. (2014). Field calibrations of a low-cost aerosol sensor at a regulatory monitoring site in california. *Atmos. Meas. Tech.* 7: 1121-1131.

Hu, J., Ying, Q., Wang, Y. and Zhang, H. (2015). Characterizing multi-pollutant air pollution in china: Comparison of three air quality indices. *Environ. Int.l* 84: 17-25.

Jeon, Y., Cho, C., Seo, J., Kwon, K., Park, H., Oh, S. and Chung, I.-J. (2018). Iot-based occupancy detection system in indoor residential environments. *Build. Environ*.

Johnson, K.K., Bergin, M.H., Russell, A.G. and Hagler, G.S. (2018). Field test of several low-cost particulate matter sensors in high and low concentration urban environments. *Aerosol Air Qual. Res.* 18: 565-578.

Kelly, K., Whitaker, J., Petty, A., Widmer, C., Dybwad, A., Sleeth, D., Martin, R. and Butterfield, A. (2017). Ambient and laboratory evaluation of a low-cost particulate matter sensor. *Environ. Pollut.* 221: 491-500.

Kim, J.-J., Jung, S.K. and Kim, J.T. (2010). Wireless monitoring of indoor air quality by a sensor network. *Indoor Built Environ.* 19: 145-150.

Kim, J.-Y., Chu, C.-H. and Shin, S.-M. (2014). Issaq: An integrated sensing systems for real-time indoor air quality monitoring. *IEEE Sens. J.* 14: 4230-4244.

Klepeis, N.E., Ott, W.R. and Switzer, P. (2007). Real–time measurement of outdoor tobacco smoke particles. *J. Air Waste Manage. Assoc.* 57: 522-534.

Kumar, P., Morawska, L., Martani, C., Biskos, G., Neophytou, M., Di Sabatino, S., Bell, M., Norford, L. and Britter, R. (2015). The rise of low-cost sensing for managing air pollution in cities. *Environ. Int.* 75: 199-205.

Leavey, A., Fu, Y., Sha, M., Kutta, A., Lu, C., Wang, W., Drake, B., Chen, Y. and Biswas, P. (2015). Air quality metrics and wireless technology to maximize the energy efficiency of hvac in a working auditorium. *Build. Environ.* 85: 287-297.

Li, J. and Biswas, P. (2017). Optical characterization studies of a low-cost particle sensor. *Aerosol Air Qual. Res.* 17: 1691-1704.

Li, J., Li, H., Ma, Y., Wang, Y., Abokifa, A.A., Lu, C. and Biswas, P. (2018a). Spatiotemporal distribution of indoor particulate matter concentration with a low-cost sensor network. *Build. Environ.* 127: 138-147.

Li, M., Wang, W.-l., Wang, Z.-y. and Xue, Y. (2018b). Prediction of pm2. 5 concentration based on the similarity in air quality monitoring network. *Build. Environ.* 137: 11-17.

Liu, D., Zhang, Q., Jiang, J. and Chen, D.-R. (2017). Performance calibration of low-cost and portable particular matter (pm) sensors. *J. Aerosol Sci.* 112: 1-10.

Manikonda, A., Zíková, N., Hopke, P.K. and Ferro, A.R. (2016). Laboratory assessment of low-cost pm monitors. *J. Aerosol Sci.* 102: 29-40.

Morawska, L., Thai, P.K., Liu, X., Asumadu-Sakyi, A., Ayoko, G., Bartonova, A., Bedini, A., Chai, F., Christensen, B. and Dunbabin, M. (2018). Applications of low-cost

sensing technologies for air quality monitoring and exposure assessment: How far have they gone? *Environ. Int.* 116: 286-299.

Moreno-Rangel, A., Sharpe, T., Musau, F. and McGill, G. (2018). Field evaluation of a low-cost indoor air quality monitor to quantify exposure to pollutants in residential environments. *J. Sens. Sens. Syst.* 7: 373-388.

Organization, W.H. (2005). Who air quality guidelines for particulate matter, ozone, nitrogen dioxide and sulphur dioxide. Global update 2005. Summary of risk assessment. *Google Scholar*.

Papapostolou, V., Zhang, H., Feenstra, B.J. and Polidori, A. (2017). Development of an environmental chamber for evaluating the performance of low-cost air quality sensors under controlled conditions. *Atmos. Environ.* 171: 82-90.

Patel, S., Li, J., Pandey, A., Pervez, S., Chakrabarty, R.K. and Biswas, P. (2017). Spatio-temporal measurement of indoor particulate matter concentrations using a wireless network of low-cost sensors in households using solid fuels. *Environ. Res.* 152: 59-65.

Polidori, A., Papapostolou, V., Feenstra, B. and Zhang, H. (2017). Field evaluation of low-cost air quality sensors.

Pope III, C.A., Burnett, R.T., Thun, M.J., Calle, E.E., Krewski, D., Ito, K. and Thurston, G.D. (2002). Lung cancer, cardiopulmonary mortality, and long-term exposure to fine particulate air pollution. *Jama* 287: 1132-1141.

Prabakar, J., Mohan, V. and Ravisankar, K. (2015). Evaluation of low cost particulate matter sensor for indoor air quality measurement. *Evaluation* 4.

Rai, A.C., Kumar, P., Pilla, F., Skouloudis, A.N., Di Sabatino, S., Ratti, C., Yasar, A. and Rickerby, D. (2017). End-user perspective of low-cost sensors for outdoor air pollution monitoring. *SciTotal Environ.* 607: 691-705.

Rajasegarar, S., Zhang, P., Zhou, Y., Karunasekera, S., Leckie, C. and Palaniswami, M. In (Ed.)^(Eds.) Intelligent Sensors, Sensor Networks and Information Processing (ISSNIP), 2014 IEEE Ninth International Conference on, 2014, IEEE, pp. 1-6.

Semple, S., Ibrahim, A.E., Apsley, A., Steiner, M. and Turner, S. (2013). Using a new, low-cost air quality sensor to quantify second-hand smoke (shs) levels in homes. *Tob. control*: tobaccocontrol-2013-051188.

Singer, B.C. and Delp, W.W. (2018). Response of consumer and research grade indoor air quality monitors to residential sources of fine particles. *Indoor air*.

Sioutas, C. (1999). Evaluation of the measurement performance of the scanning mobility particle sizer and aerodynamic particle sizer. *Aerosol Sci.Technol.* 30: 84-92.

Smith, K.R. and Mehta, S. (2003). The burden of disease from indoor air pollution in developing countries: Comparison of estimates. *Int. J. Hyg. Environ. Health* 206: 279-289.

Sousan, S., Koehler, K., Hallett, L. and Peters, T.M. (2016a). Evaluation of the alphasense optical particle counter (opc-n2) and the grimm portable aerosol spectrometer (pas-1.108). *Aerosol Sci. Technol.* 50: 1352-1365.

Sousan, S., Koehler, K., Hallett, L. and Peters, T.M. (2017). Evaluation of consumer monitors to measure particulate matter. *J. Aerosol Sci.* 107: 123-133.

Sousan, S., Koehler, K., Thomas, G., Park, J.H., Hillman, M., Halterman, A. and Peters, T.M. (2016b). Inter-comparison of low-cost sensors for measuring the mass concentration of occupational aerosols. *Aerosol Sci. Technol.* 50: 462-473.

Stewart, B. and Wild, C.P. (2017). World cancer report 2014. *Health*.

Valavanidis, A., Fiotakis, K. and Vlachogianni, T. (2008). Airborne particulate matter and human health: Toxicological assessment and importance of size and composition of particles for oxidative damage and carcinogenic mechanisms. *J. Environ. Sci. Health, Part C* 26: 339-362.

Wang, Y., Li, J., Jing, H., Zhang, Q., Jiang, J. and Biswas, P. (2015). Laboratory evaluation and calibration of three low-cost particle sensors for particulate matter measurement. *Aerosol Sci. Technol.* 49: 1063-1077.

Wang, Y., Pinterich, T. and Wang, J. (2018). Rapid measurement of sub-micrometer aerosol size distribution using a fast integrated mobility spectrometer. *J.Aerosol Sci.* 121: 12-20.

White, R.M., Paprotny, I., Doering, F., Cascio, W.E., Solomon, P.A. and Gundel, L.A. (2012). Sensors and'apps' for community-based. *EM: Air and Waste Management Association's Magazine for Environmental Managers*: 36-40.

Zhang, J., Marto, J.P. and Schwab, J.J. (2018). Exploring the applicability and limitations of selected optical scattering instruments for pm mass measurement. *Atmos. Meas. Tech.* 11: 2995.

Zikova, N., Hopke, P.K. and Ferro, A.R. (2017). Evaluation of new low-cost particle monitors for pm2. 5 concentrations measurements. *J. Aerosol Sci.* 105: 24-34.

Chapter 4: Optical characterization studies of a low-cost particle sensor

The results of this chapter have been published in Li, J., & Biswas, P. (2017). Optical characterization studies of a low-cost particle sensor. Aerosol and Air Quality Research, 17(7), 1691-1704.

Abstract

Compact low-cost sensors for measuring particulate matter (PM) concentrations are receiving significant attention as they can be used in larger numbers and in a distributed manner. Most low-cost particle sensors work on optical scattering measurements from the aerosol. To ensure accurate and reliable determination of PM mass concentrations, a relationship of the scattering signal to mass concentration should be established. The scattering signal depends on the aerosol size distributions and particle refractive index. A systematic calibration of a low-cost particle sensor (Sharp GP2Y1010AU0F) was carried out by both experimental and computational studies. Sodium chloride, silica, and sucrose aerosols were used as test cases with size distributions measured using a scanning mobility particle sizer (SMPS). The mass concentration was estimated using the measured size distribution and density of the particles. Calculations of the scattered light intensity were done using these measured size distributions and known refractive index of the particles. The calculated scattered light intensity showed better linearity with the sensor signal compared to the mass concentration. To obtain a more accurate mass concentration estimation, a model was developed to determine a calibration factor (K). K is not universal for all aerosols, but depends on the size distribution and refractive index. This approach not only provides a more accurate estimation of PM concentration, but also provides an estimate of the aerosol number concentration.

4.1 Introduction

Particulate matter (PM) is ubiquitous in the environment and is receiving significant attention due to potential impacts on health (Pope 3rd et al., 1995; Brunekreef and Holgate, 2002; Biswas and Wu, 2005; Oberdörster et al., 2005). Outdoor PM pollution can be attributed to gasoline exhaust, diesel emissions, biomass burning, traffic-related pollutions, and industrial emissions (Chow, 2001; Zheng et al., 2002; Donaldson et al., 2005; Edney et al., 2005). Indoor PM are generally emitted from tobacco smoking, cooking, wood burning, medical treatment, and outdoor PM penetration (Monn et al., 1995; Tuckett et al., 1998; Long et al., 2000; Tucker, 2000; He et al., 2004; Liu et al., 2016; Wang et al., 2017). Developing countries, such as India and China, had to cope with a challenging situation due to the adverse effect of high PM level (Brook et al., 2010; Cheng et al., 2013; Smith and Sagar, 2014; Tripathi et al., 2015; Liu et al., 2016; Sagar et al., 2016). For example, recent studies have indicated that ambient air pollution accounts for 1.6 million deaths every year in China (Cheng et al., 2013; Rohde and Muller, 2015) and 4-6% of the Indian national burden of disease (Smith, 2000).

Indoor PM pollution increases the potential risk for chronic obstructive pulmonary disease and acute respiratory infections (Bruce et al., 2000; Smith et al., 2000; Brunekreef and Holgate, 2002). Most buildings have HVAC (heating, ventilation and air conditioner) systems that filter the air in the indoor environment. However, most systems do not take into account the concentration of pollutants indoors, which may

fluctuate over time (Leavey et al., 2015). By developing a real-time air quality monitoring system, the HVAC system can operate more efficiently. Therefore, distributed and real-time particle concentration measurements are necessary to identify hotspots indoors and provide information for the HVAC system (Kim et al., 2010; Bhattacharya et al., 2012).

Since it is important to monitor PM concentrations, many instruments have been developed, ranging from accurate and expensive laboratory scale instruments (Wang and Flagan, 1990; Chen et al., 1998) to portable instruments for field measurements (Yanosky et al., 2002; Rees and Connolly, 2006). Field and laboratory instruments that are compact typically rely on the measurement of the optical scattering intensity of particles. The governing principles of these instruments can be divided into either single particle light scattering measurements or total particle light scattering measurements; and they report either the number or the mass concentration, respectively. Portable instruments sacrifice some accuracy, but they are more convenient and practical for field measurements. The TSI SidePak™ AM510, weighing 0.46 kg, uses a 670 nm laser to sample aerosol mass concentration from 0.001 to 20 mg/m^3 (Rees and Connolly, 2006; Jiang et al., 2011). The P-Trak®, whose longest dimension is 27 cm, uses isopropanol as the working fluid to monitor 0.02 to 1 μm particle number concentrations, ranging from 0 to 5×10^5 particles/cm^3 (Chao et al., 2003; Zhu et al., 2006). These portable aerosol instruments with light weight

provide reasonable accurate estimations of either the number or the mass concentration.

While several portable instruments are available, cost is still the major concern for deploying such real-time monitoring network systems for indoor and outdoor air quality measurements. Recently, a series of low-cost particle sensors that operate by measuring the total particle light scattering intensity are being touted for use. Their low price (device cost in the range of USD 10 each) alleviates the economic concerns in making widespread measurements in large-scale environments, and their compact size makes them readily portable. These units could be assembled for a total cost of USD 50 and used in a distributed manner. In controlled laboratory tests, low-cost particle sensors have shown high linearity and stability in comparison with commercial instruments with a known particle size and composition (Wang et al., 2015; Manikonda et al., 2016; Sousan et al., 2016; Sousan et al., 2017; Zikova et al., 2017). Several studies in the literature have reported the combination of low-cost particle sensors with "smart" home devices (e.g. temperature, humidity, carbon monoxide sensors, cameras) to provide more comfortable and energy-efficient homes and workplaces (Ivanov et al., 2002; Chung and Oh, 2006; Kim et al., 2010; Bhattacharya et al., 2012; Kim et al., 2014). Moreover, a few studies also applied multiple sensors for outdoor or indoor air quality measurements (Rajasegarar et al., 2014; Patel et al., 2017). One of the disadvantage is that the response of the low-cost particle sensors varies with particle composition and size distributions, which requires

repeated calibration to ensure reliable estimations of mass concentration. This disadvantage has been reported by several groups (Wang et al., 2015; Sousan et al., 2016). However, there is no sufficient study of the reasons and quantification for such variations; nor approaches proposed to enhance the accuracy.

To overcome these limitations, an evaluation of the relationship between particle composition, size, and signal outputs of a low-cost particle sensor is reported in this paper. Sharp GP2Y1010AU0F (Model GP2Y) was selected as the representative low-cost particle sensor due to its high linearity and long-time operational stability in comparison with reference instruments as established in a former study (Wang et al., 2015). To accomplish this, first, experimental studies for calibration were conducted in a chamber with known aerosols. Second, Mie and Rayleigh scattering expressions (Laven, 2006) were used along with the particle size distributions to predict the measured signals of the low-cost particle sensors. The sensor signal output was correlated to the integrated information from more sophisticated size distribution measurement instruments to evaluate accuracy. Finally, based on the light scattering theory, an expression for a calibration factor (K) dependent on refractive index and size distribution parameters (geometric mean diameter, d_{pg}, and geometric standard deviation, σ_g) was derived to predict the mass concentration and number concentration from the sensor signal output.

4.2 Methods

4.2.1 Major components of the wireless sensor

Figure 4.1(a) shows the schematic diagram of the wireless sensor setup. Sharp GP2Y with a fan (Figure 4.1(b)) was evaluated in this study. Sharp GP2Y contains an infrared emitting diode (IRED) and a phototransistor. The IRED illuminates particles in the air flow with a 10 ms pulse-driven waveform whose duty ratio is 0.032. Scattered light intensity is converted to a 0-3.5 V analog signal by the phototransistor. The analog signal becomes fully developed within 0.28 ms, so the voltage on the phototransistor is recorded at exactly 0.28 ms. A 5 V, 2×2 cm^2 brushless mini fan (Mini Cooling Radiator, 2510S) was attached to the back of the sensor to allow air flow through the aperture. Since the sensor was attached on the wall, the natural air convection of the sensor design is limited. Therefore, the fan was equipped with the sensor to direct the air flow through the unit that introduces the particles to the sensing region.

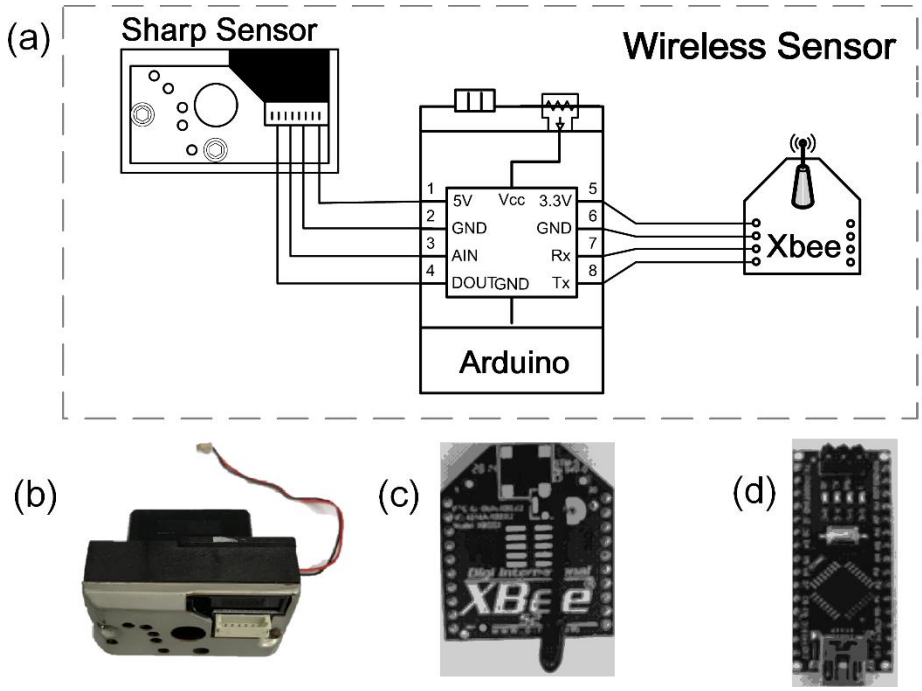

Figure 4.1 Major components of the wireless sensor, (a) Assembled wireless sensor system, (b) Sharp GP2Y1010AU0F (Sharp GP2Y) sensor with a fan in the back, (c) XBee Series 2 wireless module, (d) Arduino Nano ATmega328P Microcontroller.

The communication module used in this experiment is an XBee Series 2 (Figure 4.1(c)). Its operating frequency is 2.4 GHz, and the transmission power output is 2 mW. The range of indoor transmission is 30 meters, and the outdoor free air range is 100 meters. In this study, the XBee was placed on the circuit board as shown in Figure 4.1(a). The microcontroller used in this work was an Arduino Nano ATmega328P (Figure 4.1(d)), which accurately coordinated the data timing between the sensor and the XBee module. In the loop, the Arduino powered the IRED in the sensor with an accurate 10 ms square waveform and then sampled the voltage signal at 0.28 ms after the leading edge of the waveform was detected. After this, the microcontroller converted the analog voltage signal into a digital signal that can be

sent by the XBee module. In these experiments, the sampling interval of the microcontroller (Arduino) was set to 2.5 seconds, and every four samples were averaged before sent to the computer through XBee. Therefore, the log file stored on the computer recorded signal every ten seconds.

4.2.2 Experimental set up

As stated previously, it is important to ensure that the signal output can be accurately used to determine the mass concentration by a calibration factor. The signal from the Sharp GP2Y is dependent on the particle composition and size distribution. Our earlier work has demonstrated that for the same mass concentration of different particle types (e.g. NaCl, sucrose, and NH_4NO_3) and size distributions (e.g. 300 nm, 600 nm, and 900 nm polystyrene latex particles), the sensor signal outputs were different (Wang et al., 2015). However, the patterns of the change, together with the necessity of calibration, has not been clearly presented. Therefore, it is crucial to explain the reason for such difference qualitatively or quantitatively with a systematically study, which is addressed in this study. In this work, a systematical calibration of a Sharp GP2Y was carried out experimentally. Then, with a proposed model, the response of the sensor as a function of particle composition and size distribution parameters was studied.

Initial experiments were done with laboratory generated NaCl, sucrose, and SiO_2 particles. Different sets of tests with various solution concentrations were done to determine the effect of varying size distributions on the measured signal outputs. The experimental system is shown in Figure 4.2. Different concentrations of NaCl solutions, sucrose solutions, and SiO_2 solutions were added in a constant output atomizer (TSI Model 3076) to generate test aerosols with different size distributions. NaCl solutions (0.507 mg/mL, 1.087 mg/mL, and 1.892 mg/mL) and sucrose solutions (1.150 mg/mL, 3.325 mg/mL, 4.315 mg/mL) were prepared by dissolving NaCl (reagent grade ≥ 98%, +80 mesh, Sigma-Aldrich) and sucrose (≥ 99.5%, Sigma Ultra, Sigma-Aldrich) in deionized water. SiO_2 solutions (1% dispersion and 2% dispersion) were prepared by diluting SiO_2 solutions (40 wt. % suspension in H_2O, LUDOX® TM-40 colloidal silica, Sigma-Aldrich) with deionized water. The atomized particles were passing through a diffusion drier to remove the water contents in the particles. Then, the dried particles were sent to a cubic chamber (58 cm × 58 cm × 58 cm) through the inlet tube at the top of the chamber. On the right side of the chamber, a Sharp GP2Y sensor and a sampling tube that connected the chamber with a scanning mobility particle sizer (SMPS, size range 14.6 nm to 661.2 nm, TSI Model 3080) were placed close to each other at the middle of the right panel. The distance between the Sharp GP2Y center and the sampling tube was around 5 cm, small in comparison to the width of the chamber (58 cm). Thus, the PM sampled by the SMPS was assumed to be the same as that detected by the Sharp GP2Y. The SMPS was operated

with a three-minute sampling interval to measure the size distributions ($n_d(d_p)$) of the generated particles in the chamber. And as mentioned before, the data log file of the Sharp GP2Y had a 10-second sampling interval. Therefore, every eighteen samples from the Sharp GP2Y will be averaged to match the sampling interval of the SMPS.

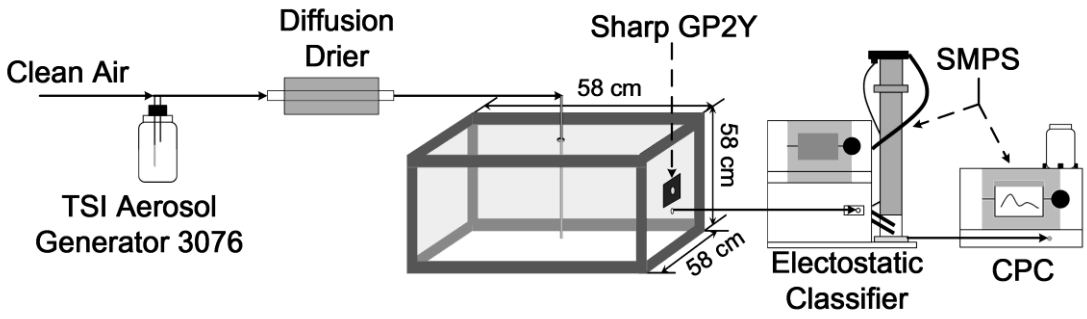

Figure 4.2 Schematic diagram of systems used to compare the performance of the wireless sensor with that of standard aerosol instruments. Constant output atomizer 3076 producing small particles (d_p < 600 nm) with an SMPS reference instrument.

Characteristic size distributions from different solutions are shown in Figure 4.3. Two critical parameters, the geometric mean diameter (d_{pg}) and the geometric standard deviation (σ_g) of each size distribution are reported in Table 4.1. The difference was not large among the size distributions of particles generated from atomizing sucrose and SiO_2 solution. This is mainly caused by the larger standard deviations of the size distributions as shown in Table 4.1, so that the size distributions were broadened, covering each other.

Table 4.1 Densities and size distribution parameters of the particles generated from different solutions.

	Solution conc.	Test number	Particle density	Size distributions from SMPS	
	mg/cc		g/cc	d_{pg}	σ_g
I. NaCl	0.507	1	2.16	92.02	1.77
	1.087*	2		119.55	1.69
	1.892	3		156.95	1.48
II. Sucrose	1.150	4	1.59	115.78	1.91
	3.325	5		126.99	1.99
	4.315	6		155. 57	1.87
III. SiO_2	1%	7	2.32	150.93	2.07
	2%	8		176.06	1.91

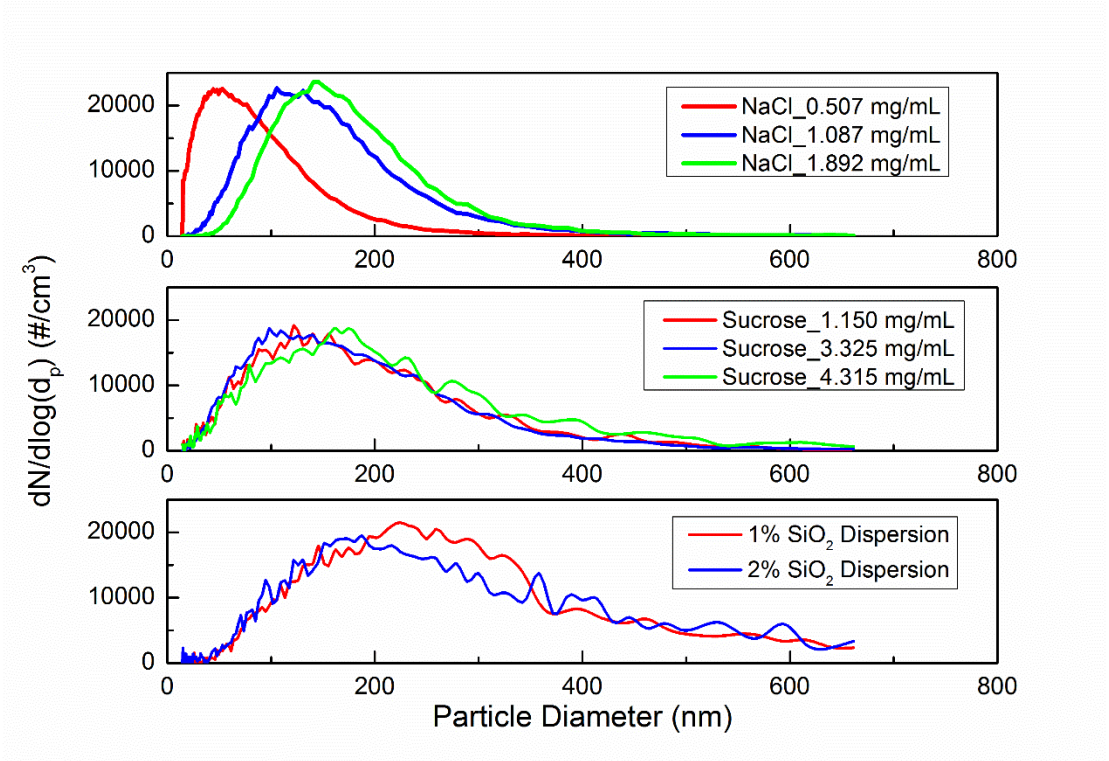

Figure 4.3 Characteristic size distributions of particles generated by the constant output atomizer with different solutions.

With the experimental setup, we can obtain the signal output from sensor and the size distribution from SMPS, which is necessary to calculate the mass concentration and the total scattered light intensity. The detailed expressions of the mass concentration and the total scattered light intensity are presented in the next section.

4.2.3 Mass concentration (m_{total}) and calculated total scattered light intensity (I)

The mass concentrations (m_{total}) were calculated based on the size distribution function, $n_d(d_p)$, assuming that all particles are spherical (Friedlander, 2000):

$$m_{total} = \int \rho_p \frac{\pi d_p^3}{6} n_d(d_p) \cdot d(d_p), \tag{4.1}$$

where ρ_p is the particle density, d_p is the particle diameter. In this work, $n_d(d_p)$ was measured by the SMPS as described in the experimental set up section.

The total scattered light intensity (I), was calculated based on the working principle of the Sharp GP2Y sensor, as shown in Figure 4.4. Total scattered light intensity is a summation of the product of the scattered light intensity of a single particle, i_{dp}, and the size distribution function, $n_d(d_p)$, as Eq. (4.2) (Friedlander, 2000).

$$I = \int i_{dp} n_d(d_p) \cdot d(d_p), \tag{4.2}$$

As shown in the right side of Figure 4.4, i_{dp} is the scattered light intensity detected by the phototransistor when a single particle passing through the measuring point. i_{dp} can be determined by the structure of the Sharp GP2Y and particle properties. Structure

parameters include: the scattering angle (θ), the distance between the illuminated particles and the phototransistor (R), the wavelength of light source (λ), and the incident light intensity (I_0). Particle properties include the particle size (d_p) and the refractive index (m). The refractive index can be expressed as a combination of real and imaginary terms ($m = m_{real} - m_{img}\,i$). However, practically, particles would pass the measuring point as a combination of different particle diameters with different number concentrations, rather than pass through the measuring point one by one, which is the situation shown in the left side of Figure 4.4. Therefore, i_{dp} needs to be coupled with $n_d\,(d_p)\cdot d(d_p)$, the number concentration of particles whose size is d_p. Then, it needs to be integrated from the minimum size to the maximum size.

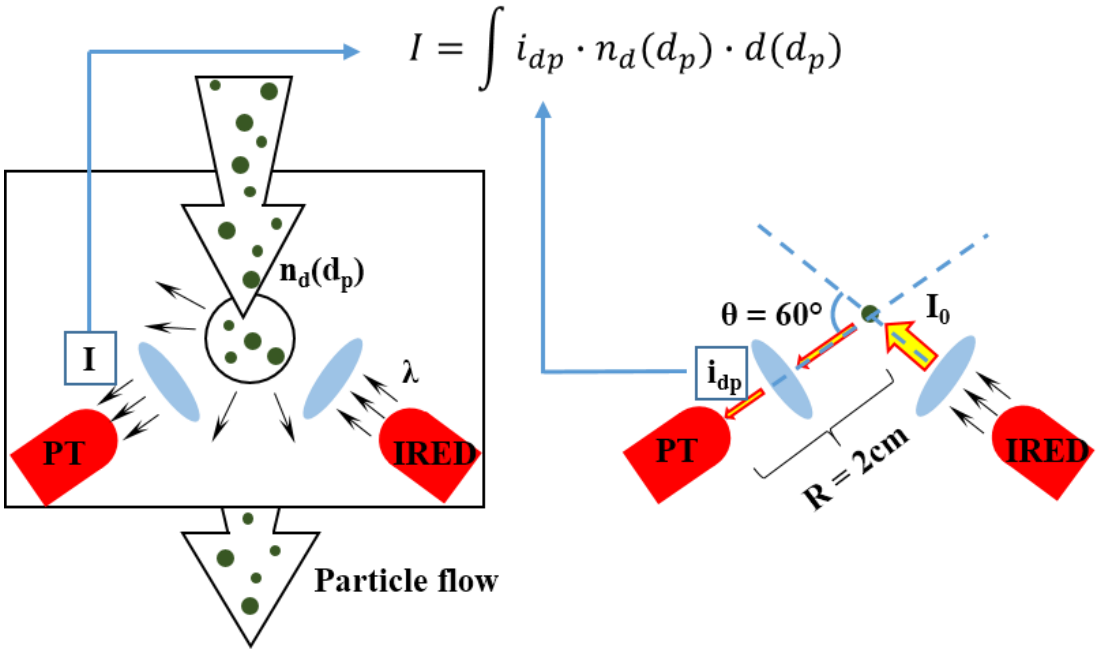

Figure 4.4 Working principle and critical parameters of the Sharp GP2Y low-cost particle sensor. "PT" and "IRED" represent the phototransistor and the infrared emitting diode respectively.

In this study, the sensor parameters are, θ = 60°, R = 2 cm, λ=860 nm, and *m*=1.536 (NaCl particles), 1.5376 (sucrose particles), and 1.486 (SiO_2 particles) (Hand and Kreidenweis, 2002). MiePlot V4.5 (Laven, 2006) was used to calculate the scattered light intensity of a single particle (i_{dp}) as a function of particle diameter (d_p) with the mentioned constraints.

4.2.4 Expression for calibration factor (K) to relate sensor signal output (S) to mass concentration (m_{total}) from experiments

A calibration factor (K) linking the mass concentration (m_{total}) with the sensor signal output (S) is defined as follows:

$$m_{total} = K(S - S_0) \tag{4.3}$$

S_0 is a signal output obtained at a particle concentration of zero due to a certain drift in the electronics of the system. In the following section, there will be: K_{exp}, $K_{eq,6}$, and $K_{eq,12}$, representing the calibration factor fitted from the experimental results (K_{exp}) or calculated from the proposed model ($K_{eq,6}$ and $K_{eq,12}$).

In the experiments, mass concentration (m_{total}) can be calculated from Eq. (4.1) with the $n_d(d_p)$ measured by the SMPS and the ρ_p reported in Table 4.1. The sensor signal output (S) was recorded in the log file on the computer. So, K_{exp} can be obtained by fitting experimental results into Eq. (4.3).

4.2.5 Estimation the calibration factor (K) with lognormal size distribution

To further analyze how other parameters will influence the calibration factor, (S-S_0) was expressed as a function of the total scattered light intensity, I

$$S - S_0 = \eta\, I\,, \tag{4.4}$$

where η is the response coefficient of the sensor, which is determined by the optical characteristics of the phototransistor. The value of η is determined experimentally by calibration. With Eq. (4.4), Eq. (4.3) can be written as

$$m_{total} = \eta\, K\, I \tag{4.5}$$

According to Eq. (4.1) and Eq. (4.2), m_{total} and I are functions of $n_d\,(d_p)$ and i_{dp}. By substituting Eqs. (4.1-4.2) into Eq. (4.5), the calibration factor ($K_{eq,6}$) can be expressed as Eq. (4.6), which is dependent on the properties (density, size distribution, and refractive index) of the measured PM.

$$K_{eq,6} = \frac{1}{\eta}\frac{m_{total}}{I} = \frac{1}{\eta}\frac{\int \rho_p \frac{\pi d_p^3}{6} n_d(d_p)\cdot d(d_p)}{\int i_{dp} n_d(d_p)\cdot d(d_p)} \tag{4.6}$$

Eq. (4.6) indicated that the PM size distribution and the PM properties have a complex influence on the calibration factor. The integration in the numerator and the denominator are too complicated for either qualitative analysis or practical

implementation. To simplify the integration, lognormal size distribution assumption and method of moments were applied in the following derivation.

The definition of lognormal size distribution is shown as follows, where N_∞, σ_g, and d_{pg} represent the total number concentration, the geometric standard deviation, and the geometric mean diameter, respectively (Friedlander, 2000).

$$n_d(d_p) = \frac{N_\infty}{(2\pi)^{1/2} d_p \ln \sigma_g} \exp[-\frac{(\ln d_p - \ln d_{pg})^2}{2\ln^2 \sigma_g}] \tag{4.7}$$

The method of moments is defined as Eq. (4.8) (Friedlander, 2000).

$$M_r = \int d_p^r n_d(d_p) \cdot d(d_p) \tag{4.8}$$

where M_γ is the general moment of the particle size distribution, where γ represents the order of the moment. The geometric standard deviation (σ_g) and the geometric mean diameter (d_{pg}) can be used to express M_γ as shown in Eq. (4.9). M_0 is the zeroth moment, which represents total number concentration (Friedlander, 2000) and M_0 can be cancelled out later.

$$\ln(M_\gamma / M_0) = \gamma \ln d_{pg} + \frac{\gamma^2}{2} \ln^2 \sigma_g \tag{4.9}$$

In order to apply the method of moments to Eq. (4.6), apart from lognormal size distribution assumption, i_{dp} needs to be expressed as a polynomial function of particle size (d_p). Therefore, we expect to fit the relationship between i_{dp} and d_p for the simplification. Eq. (4.10) was applied to describe the relationship between i_{dp} and d_p.

i_{dp} was enlarged with a factor of 10^{15} to increase the accuracy of fitting since i_{dp} was too small for calculation. The relationship between i_{dp} and d_p can be divided into two ranges, proportional to d_p^6 and d_p^2 for small particles in the Rayleigh regime and large particles in the geometric scattering regime respectively. Although the transition regime, Mie regime is not included here in Eq. (4.10), it can still quantitatively cover the light scattering properties in the whole size range. The fitting results of Eq. (4.10) will be discussed in detail in the Results and Discussion section.

$$\frac{1}{i_{dp}} = \frac{a}{d_p^2} + \frac{b}{d_p^6} \tag{4.10}$$

Eq. (4.10) could be further simplified as Eq. (4.11) under the following two situations. When most of the measured particles are small, Rayleigh regime will be the dominate regime, and Eq. (4.10) can be simplified as Eq. (4.11a). On the contrary, when the measured particles are larger, geometric scattering regime will be the dominant regime. Therefore, Eq. (4.10) can be simplified as Eq. (4.11b)

$$i_{dp} \approx \frac{d_p^6}{b} \quad \text{when } d_p < 500 \text{ nm and } \sigma_g < 1.3 \tag{4.11a}$$

$$i_{dp} \approx \frac{d_p^2}{a} \quad \text{rest of the situations} \tag{4.11b}$$

The calibration factor ($K_{eq,12}$) can be expressed as Eq. (4.12) after plugging in Eqs. (4.6, 4.8-4.11).

$$K_{eq,12} = \frac{1}{\eta} \cdot \frac{m_{total}}{I} = \frac{1}{\eta} \cdot \frac{\frac{\rho_p \pi}{6} M_3}{\frac{M_6}{b}} = \frac{1}{\eta} \cdot \frac{\rho_p b \pi M_3}{6 M_6}$$
$$= \frac{1}{\eta} \cdot \frac{\rho_p b \pi}{6} \cdot \frac{M_0 \cdot e^{3 \ln d_{pg} + \frac{9}{2} \ln^2 \sigma_g}}{M_0 \cdot e^{6 \ln d_{pg} + 18 \ln^2 \sigma_g}} = \frac{1}{\eta} \cdot \frac{\rho_p b \pi}{6} \cdot e^{-3 \ln d_{pg} - \frac{27}{2} \ln^2 \sigma_g} \quad (4.12a)$$

$$K_{eq,12} = \frac{1}{\eta} \cdot \frac{m_{total}}{I} = \frac{1}{\eta} \cdot \frac{\frac{\rho_p \pi}{6} M_3}{\frac{M_2}{a}} = \frac{1}{\eta} \cdot \frac{\rho_p a \pi M_3}{6 M_2}$$
$$= \frac{1}{\eta} \cdot \frac{\rho_p a \pi}{6} \cdot \frac{M_0 \cdot e^{3 \ln d_{pg} + \frac{9}{2} \ln^2 \sigma_g}}{M_0 \cdot e^{2 \ln d_{pg} + 4 \ln^2 \sigma_g}} = \frac{1}{\eta} \cdot \frac{\rho_p a \pi}{6} \cdot e^{\ln d_{pg} + \frac{5}{2} \ln^2 \sigma_g} \quad (4.12b)$$

The errors of the calibration factor predicted by the proposed model ($K_{eq,6}$ and $K_{eq,12}$) can be calculated by Eq. (4.13), regarding to the experimental results (K_{exp})

$$error = \frac{K_{\exp} - K_{eq,6} \text{ or } K_{eq,12}}{K_{\exp}} \quad (4.13)$$

4.2.6 Estimation of the number concentration

A method of estimating number concentration with given parameters is presented as follows. Mass concentration and number concentration are relevant to the third and the zeroth moment of size distributions respectively. In addition, the mass concentration can be derived from Eq. (4.3). Therefore, the number concentration (M_0) is a function of calibration factor (K), sensor signal output (S), and size distribution parameters (σ_g and d_{pg}) as shown in Eqs. (4.14-4.15).

$$m_{total} = \frac{\rho_p \pi}{6} M_3 = \frac{\rho_p \pi}{6} M_0 \cdot e^{3 \ln d_{pg} + \frac{9}{2} \ln^2 \sigma_g} \quad (4.14)$$

$$N = M_0 = \frac{6m_{total}}{\rho_p \pi \cdot e^{3\ln d_{pg} + \frac{9}{2}\ln^2 \sigma_g}} = \frac{K(S - S_0)}{\rho_p \pi \cdot e^{3\ln d_{pg} + \frac{9}{2}\ln^2 \sigma_g}} \quad (4.15)$$

The number concentration estimated from Eq. (4.15) were compared with the number concentration measured by the SMPS. The errors between the two values were calculated with Eq. (4.16). N_{SMPS} and $N_{eq,15}$ represent the number concentrations measured by the SMPS and evaluated from Eq. (4.15) respectively.

$$error = \frac{N_{SMPS} - N_{eq,15}}{N_{SMPS}} \quad (4.16)$$

4.3 Results and discussion

4.3.1 Relationship between the scattered light intensity of a single particle (i_{dp}) and the particle size (d_p)

The scattered light intensity of a single particle (i_{dp}) is plotted in Figure 4.5 as a function of particle size (d_p). Figure 4.5 (a, c, and e) show the calculated scattered light intensity of a single particle (i_{dp}) as a function of particle diameter (d_p). According to the plots, the slopes of the curve change from 6 to 2 with increasing particle diameter on logarithm scale, which demonstrated that i_{dp} is proportional to d_p^6 and d_p^2 for small and large particles respectively. This linearity is consistent with the different light scattering characteristics in the Rayleigh, Mie, and geometric scattering regimes. In the Rayleigh regime, the scattered light intensity is proportional to dp^6, while in the geometric scattering regime, the scattered light intensity is proportional to dp^2. The transition regime between the above two regimes is the Mie regime.

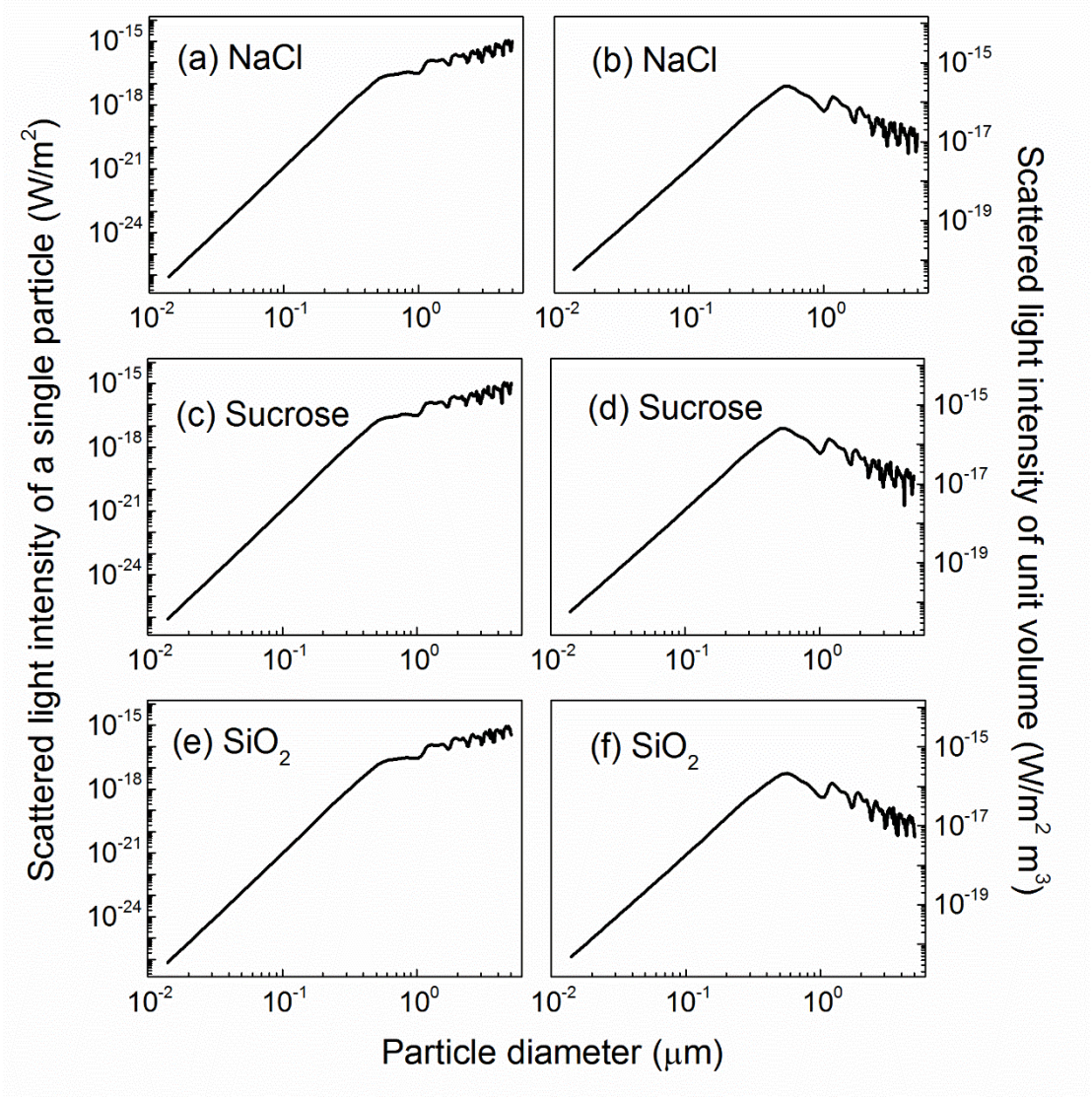

Figure 4.5 Scattered light intensity of a single particle as a function of particle diameter for (a) NaCl particles, (c) sucrose particles, and (e) SiO_2 particles. Scattered light intensity of unit volume as a function of particle diameter for (b) NaCl particles, (d) sucrose particles, and (f) SiO_2 particles.

Since the final aim is to estimate the mass concentration with the sensor signal output, we also plot the scattered light intensity of unit volume against particle diameter in Figure 4.5 (b, d, and f). The scattered light intensity of unit volume is calculated by dividing the calculated scattered light intensity of a single particle (i_{dp}) by the volume

of the particle ($\frac{\pi d_p^3}{6}$). After assuming the density of the particle (shown in Table 4.1) is a constant, the curves can be interpreted as the scattered light intensity of unit mass. For NaCl, sucrose, and SiO_2 particles, the peaks of responsive curve occur around 600 nm to 1000nm, which illustrates that Sharp GP2Y is more sensitive to above range for mass concentration prediction.

4.3.2 Relationship among the mass concentration (m_{total}), the calculated total scattered light intensity (I), and the sensor signal output (S)

With i_{dp} from Figure 4.5 and n_d (d_p) from SMPS, calculated total scattered light intensity (I) and total mass concentration (m_{total}) can be determined by Eqs. (4.1-4.2). Figure 4.6 shows the plots of the calculated total scattered light intensity (I) and the total mass concentration (m_{total}) versus the signal output (S) over the range of measurements. The parameters: slope, intercept, and R^2 for the various cases are shown in the column 3-6 of Table 4.2. Column 3 and column 4 report the fitting equations and the R^2 values of the calculated total scattered light intensity (I) versus the sensor signal output (S), while column 5 and column 6 report the fitting equations and the R^2 values of the total mass concentration (m_{total}) versus the sensor signal output (S). The R^2 values are larger than 0.951 in all separate tests, which demonstrates that the sensor signal outputs are proportional to both the mass

concentration and the calculated scattered light intensity. However, while plotting experiments of a same component with different concentrations on one graph, the calculated total scattered light intensities are easier to line up on a single straight line against sensor output, as shown in Figure 4.6. In Figure 4.6(a-f), the fitting equations and the R^2 values are obtained by combining all tests of the same composition, while Figure 4.6(g, h) showed the fitting results of all tests from all compositions. In detail, the R^2 values of calculated scattered light intensity (Figure 4.6 (a, c)) are larger than the R^2 values of mass concentration (Figure 4.6 (b, d)) for NaCl and sucrose tests. The R^2 values are comparable for the SiO_2 tests (Figure 4.6 (e, f)). In Figure 4.6 (g, h), the R^2 value for scattered light intensity (Figure 4.6(g)) is significantly larger than the R^2 value for mass concentration (Figure 4.6(h)) after plotting all measurement data together. This indicates that the correlation between the signal output and the total calculated scattered light intensity is better. On the contrary, when estimating the total mass concentration from the signal output, although high linearity was preserved in the separate tests (selected size distributions), the intercept and the calibration factor (K_{exp}) changed with the particle size distributions and the particle composition.

Table 4.2 Detail properties of the generated particles and the fitting results for mass concentration and calculated total scattered light intensity against sensor signal output.

	Test number	Calculated scattered light intensity fitted equation Scattered light int. (*y*, UA) versus sensor output (*x*, UA)		Mass fitted equation (experimental data) Mass conc. (*y*, μg m^{-3}) versus sensor output (*x*, UA)		Calibration factor (*K*)		
		Equation	R^2	Equation	R^2	K_{exp} from fitting	$K_{eq,6}$ from Eq. (4.6)	Error from Eq. (4.13)
I. NaCl	1	$y = 3.20\times10^{-16}x - 5.35\times10^{-14}$	0.978	$y = 11.26(x – 146.98)$	0.951	11.26	8.42	25.22%
	2	$y = 2.58\times10^{-16}x - 3.73\times10^{-14}$	0.995	$y = 7.03(x – 146.98)$	0.996	7.03	7.13	NA
	3	$y = 3.26\times10^{-16}x - 4.24\times10^{-14}$	0.977	$y = 12.74(x – 146.98)$	0.961	12.74	8.89	30.21%
II. Sucrose	4	$y = 2.16\times10^{-16}x - 3.08\times10^{-14}$	0.990	$y = 3.75(x – 146.98)$	0.989	3.75	3.66	2.40%
	5	$y = 1.81\times10^{-16}x - 2.42\times10^{-14}$	0.996	$y = 2.44(x – 146.98)$	0.993	2.44	3.43	-40.57%
	6	$y = 2.39\times10^{-16}x - 3.43\times10^{-14}$	0.966	$y = 3.04(x – 146.98)$	0.977	3.04	3.28	-7.90%
III. SiO_2	7	$y = 2.74\times10^{-16}x - 3.80\times10^{-14}$	0.984	$y = 4.84(x – 146.98)$	0.996	4.84	5.56	-4.91%
	8	$y = 2.56\times10^{-16}x - 3.66\times10^{-14}$	0.995	$y = 5.30(x – 146.98)$	0.994	5.30	6.04	-28.00%

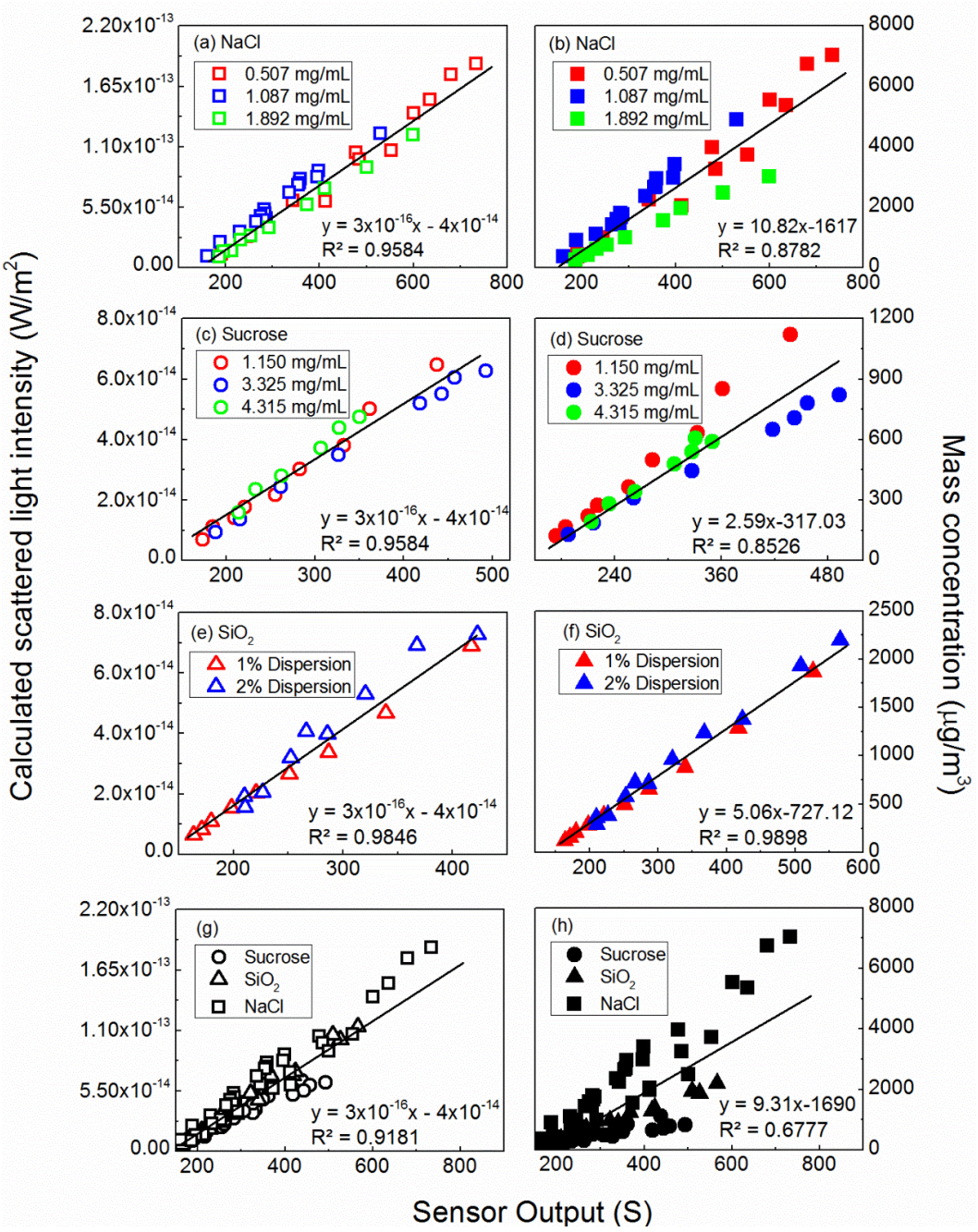

Figure 4.6 Relationship of the calculated total scattered light intensity and the mass concentration as a function of the sensor outputs. Hollow symbols represent calculated scattered light intensity for (a) NaCl particles, (c) sucrose particles, and (e) SiO_2 particles. Solid symbols represent mass concentration for (b) NaCl particles, (d) sucrose particles, and (f) SiO_2 particles. (g) and (h) are combinations of (a, c, and e) and (b, d, and f) respectively.

Apart from reporting the fitting results, Table 4.2 also includes the estimated calibration factor calculated from Eq. (4.6) in column 8. Test 2 (NaCl 1.087 g/cc) was

chosen as calibration to calculate the response coefficient (η) due to its highest R^2 value for both mass fitting and intensity fitting. After substituting the density (ρ_p = 2.16 g/cc), the size distribution parameters (d_{pg} = 119.55 nm, σ_g = 1.69), and the scattered light intensity (i_{dp}) into Eq. (4.6), η is equal to 3.85×10^{15}. By combining the value of η and Eq. (4.6), the calibration factor of each test can be estimated. To evaluate the accuracy of Eq. (4.6), the errors between the calibration factor from experiments (K_{exp}) and the calibration factor from Eq. (4.6) ($K_{eq,6}$) were calculated with Eq. (4.13) and reported in column 9 of Table 4.2. The error range of $K_{eq,6}$ can be controlled within ±30% except for Test 5. The calibration factor from the mass fitting result of Test 5 (K_{exp}=2.44) was the smallest within seven tests, so the denominator in Eq. (4.13) was small, which might lead to a larger error. The error range demonstrated that Eq. (4.6) can provide moderate accuracy for calibration factor estimation.

The *K* values of low-cost particle sensors varying with regards of aerosol composition and size distributions have been reported by several groups (Wang et al., 2015; Sousan et al., 2016). Wang et al. (2015) compared the response of three sensors and an instrument (the Shinyei PPD42NS, the Samyoung DSM501A, the Sharp GP2Y, and the SidePak^{TM}) to three types of particles (NaCl particles, Sucrose particles, and NH_4NO_3 particles) and recommended repeated calibration for different types of particles to obtain higher accuracy. Sousan et al. (2016) also demonstrated the same conclusion that the sensors require repeated calibration, since the size distribution, the refractive index, and the shape of the particles would influence sensors' performance. However, there is no systematic study on how *K* changes and how to improve the sensors' performance without repeated calibration.

4.3.3 Estimation of K for lognormally distributed particles

As presented in Table 4.2 and Figure 4.6, calibration factor is not universal for all aerosols, but depends on the size distribution parameters and particle composition (refractive index). To further analyze how these parameters would influence the calibration factor, we assumed lognormal distribution as shown in Eq. (4.7). The size distribution generated by Eq. (4.7) was plugged into Eq. (4.6) to evaluate the influence of each parameter.

By assuming lognormal parameters, $ln\sigma_g$ ranging from 0.1 to 0.7 and d_{pg} ranging from 0.2 to 2 μm respectively, we simulated the calibration factor of various size distributions for NaCl particles, sucrose particles, and SiO_2 particles as shown in Figure 4.7. The values of calibration factors significantly differ from various combinations of $ln\sigma_g$ and d_{pg}. Figure 4.7 could be an important tool for estimating how much error will be created by a one-time calibration. For example, if the sensor is calibrated with SiO_2 particles ($ln\sigma_g$ = 0.7, d_p = 1.0 μm), then, the error can be controlled within ± 60% while using this calibration factor to measure particles ranges from 0.1-2.0 μm whose $ln\ \sigma_g$ is 0.7. However, if the sensor is calibrated with NaCl particles ($ln\sigma_g$ = 0.1, d_p = 0.6 μm), then, the error would be enlarged to ± 700% while using this calibration factor to measure particles ranges from 0.1-2.0 μm whose $ln\sigma_g$ is 0.1. Furthermore, two rules can be summarized to describe the variation. First, with a small $ln\sigma_g$ value, the calibration factor is nonmonotonically related to d_{pg} value. Generally, the calibration factor initially decreases with the increasing d_{pg} value. However, after the turning point, the calibration factor increases with the increasing d_{pg} value in the successive stage. Second, for a larger $ln\sigma_g$ value, the calibration factor is a monotonic function of d_{pg}, and it increases with increasing d_{pg} value. Above two rules are common for NaCl, sucrose, and SiO_2 particles.

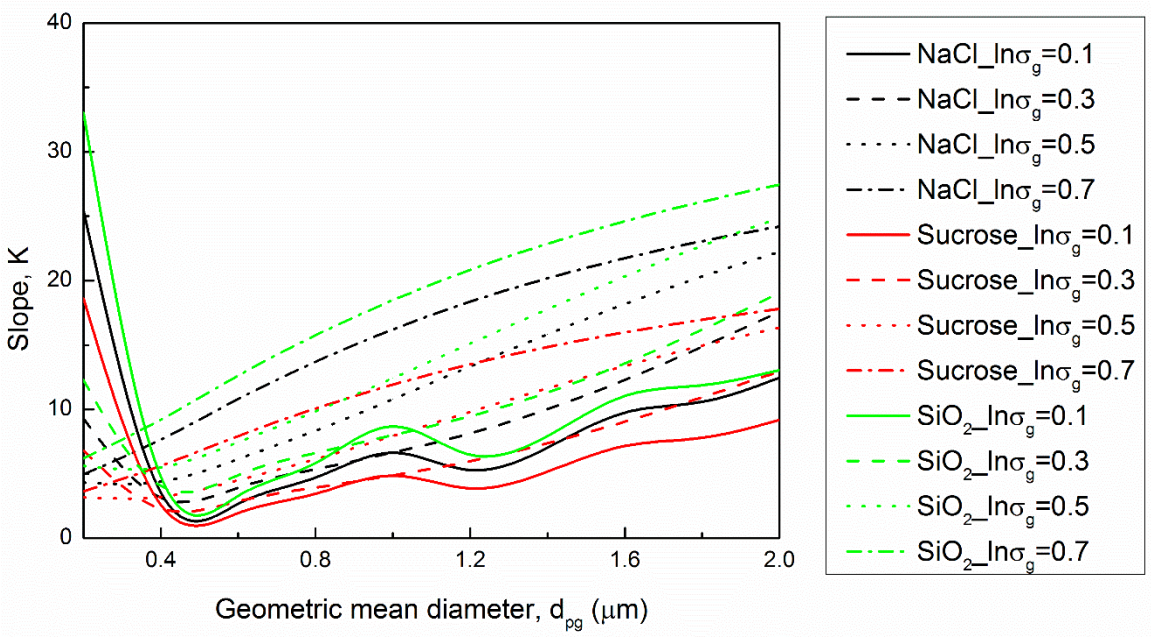

Figure 4.7 Slope estimated from Eq. (4.6) for lognormally distributed particles. Black, red, and green lines represent NaCl, sucrose, and SiO_2 particles respectively. Solid, dash, dot, and dash dot lines represent $ln\sigma_g$ equal to 0.1, 0.3, 0.5, and 0.7 respectively.

To further investigate the above phenomena, i_{dp} was simplified as a function of particle diameter (d_p). The details of fitting i_{dp} with d_p for values of a and b with six types of substances – NaCl, sucrose, SiO_2, elemental carbon, Al_2O_3, and Fe_2O_3 are shown in Figure 4.8. We included elemental carbon, Al_2O_3, and Fe_2O_3 to demonstrate that Eq. (4.10) should be universal for different species. i_{dp} for element carbon whose refractive index has an imaginary part is slightly different from others. The parameters, a, b, and R^2 varying with the refractive indices of the different materials for each set are listed in Table 4.3. The R^2 values vary from 0.7313 to 0.983. Element carbon demonstrated the highest R^2 value, since the imaginary part reduced the wrinkle of the i_{dp} curve, which improved the accuracy of fitting. For other species, lower R^2 values were resulted from the fluctuation of the i_{dp} curve.

Table 4.3 Details of fitting i_{dp} as a function of d_p in Eq. (4.10) for NaCl, sucrose, SiO_2, Fe_2O_3, Al_2O_3, and elemental carbon particles.

	Refractive index	a ($\times 10^{-15}$)	b ($\times 10^{-15}$)	R^2
NaCl	1.536	29.44	1.394	0.7508
Sucrose	1.5376	29.58	1.012	0.7344
SiO_2	1.486	33.64	0.932	0.7313
Element carbon	1.96-0.66i	172.8	0.258	0.983
Fe_2O_3	3.011	32.19	0.1582	0.7849
Al_2O_3	1.765	25.27	0.447	0.8567

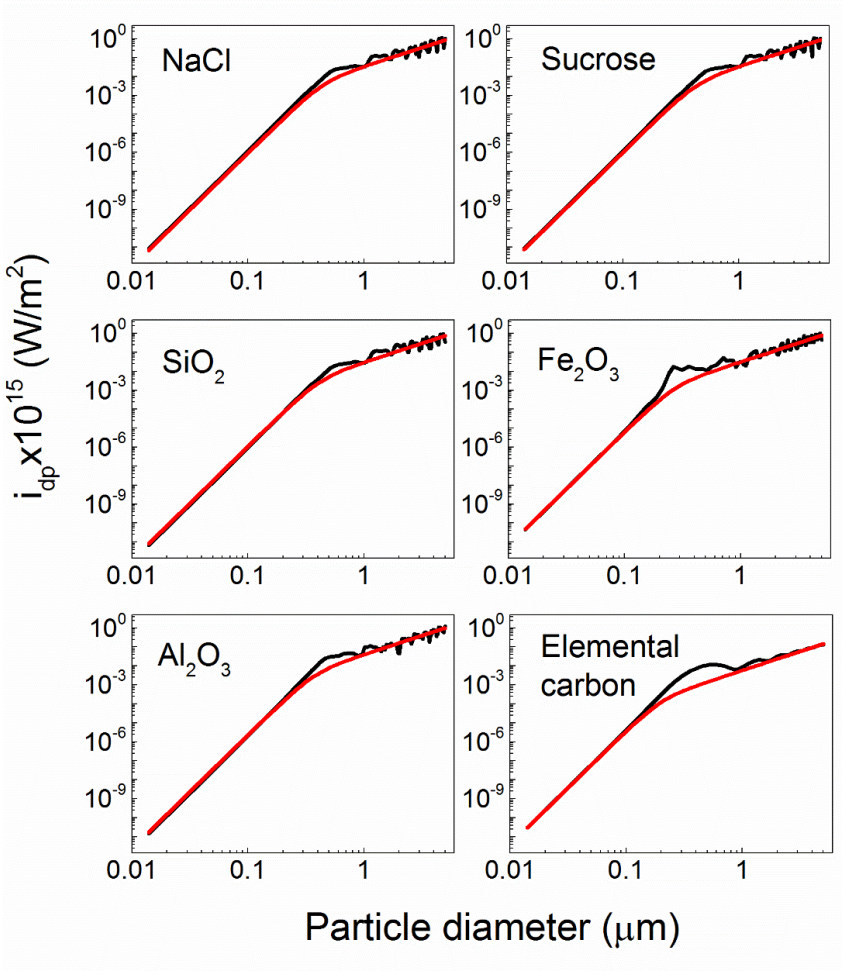

Figure 4.8 The scattered light intensity of a single particle simulated by MiePlot (black solid line) and fitted by Eq. (4.9) (red solid line) for NaCl, sucrose, SiO_2, Fe_2O_3, Al_2O_3, and elemental carbon particles.

Regarding the fitting results as shown in Figure 4.8 and Table 4.3, Eq. (4.10) is capable of depicting the correlation between i_{dp} and d_p. i_{dp} is proportional to the d_p^6 and d_p^2 for small particles and large particles respectively, which leads to the phenomena we summarized from Figure 4.7. For small $ln\sigma_g$, the feature of the aerosol whose geometric mean diameter is d_{pg} is similar to the feature of monodisperse particles with only size d_{pg}, so Eq. (4.6) can be simplified as Eq. (4.17).

$$K = \frac{1}{\eta} \cdot \frac{\int \rho_p \frac{\pi d_p^3}{6} n_d(d_p) \cdot d(d_p)}{\int i_{dp} n_d(d_p) \cdot d(d_p)} \approx \frac{1}{\eta} \cdot \frac{N \rho_p \frac{\pi d_{pg}^3}{6}}{i_{dp} N} = \frac{1}{\eta} \cdot \frac{\rho_p \frac{\pi d_{pg}^3}{6}}{i_{dpg}} \qquad (17)$$

where i_{dpg} is the scattered light intensity of particles whose size equals to d_{pg}. When d_{pg} is small, K is proportional to d_{pg}^{-3}, where K decreases with increasing d_{pg}. After some turning point, d_{pg} is large enough to fall in the range where i_{dp} is proportional to the d_p^2, so K is proportional to d_{pg} and increases with increasing d_{pg}. However, when $ln\sigma_g$ is larger, the characteristics mentioned above will disappear since the particles tend to be distributed evenly through the size range rather than monodisperse. Under this situation, the larger particles under the size distribution are more influential, so i_{dp} is approximately proportional to the d_p^2, so K is proportional to d_{pg} and increases with increasing d_{pg}.

Apart from qualitatively explaining the trends in Figure 4.7, the method of moments and further simplification of i_{dp} were applied to overcome the disadvantage of repeated calibration.

4.3.4 Estimate *K* with simplified equation for practical use

As shown in Eq. (4.11), Eq. (4.10) can be simplified for small and large particles separately. With Eq. (4.11), Eq. (4.6) is further simplified as Eq. (4.12). An expression for *K* as a function of geometric mean diameter, geometric standard deviation, and refractive is established by assuming lognormal distribution, as shown in Eq. (4.12). While some information (σ_g, d_{pg} and m) will need to be known for determining the value of *K*; estimates can be inferred for a specific type of aerosol in a region. Eq. (4.12a) can be applied when most of particles are smaller than 0.5-0.8 μm. On the contrary, Eq. (4.12b) can be applied when most of particles are larger than 0.5 – 0.8 μm. Generally, whether to choose Eq. (4.12a) or Eq. (4.12b) needs to be considered regarding particle size distribution parameters.

To validate the equations, Eq. (4.12) was applied to the experimental results with parameters we calculated before. η is still equal to 3.85×10^{15}. The values of a and b for each composition are from Table 4.3. The density and size distribution parameters for each experiment is from Table 4.1. Since NaCl solutions produced particles with smaller σ_g and d_{pg}, Eq. (4.14a) was applied to Test 1-3. Compared to NaCl particles, sucrose and SiO_2 solutions generated particles with larger σ_g and d_{pg}, so Eq. (4.14b) was applied to Test 4-8. The calibration factor estimated from Eqs. (4.12) ($K_{eq,12}$) are listed in Table 4.4. The errors between K_{exp} and $K_{eq,12}$ were calculated with Eq. (4.13) and listed in the last column of Table 4.4. The errors can be controlled within ±40%, thus proving that the accuracy of Eq. (4.12) is reasonable.

Table 4.4 Parameters and results of estimating calibration factor from Eq. (4.12).

	Refractive index	Test No.	Equation	K_{exp} from experiments	$K_{eq,12}$ from Eq. (4.12)	Error from Eq. (4.13)
NaCl	1.536	1	12a	11.26	8.04	28.6%
		2		7.03	7.27	-3.4%
		3		12.74	16.60	-30.3%
Sucrose	1.5376	4	12b	3.75	2.57	31.5%
		5		2.44	3.25	-33.2%
		6		3.04	3.24	-6.6%
SiO_2	1.486	7	12b	4.84	7.51	-41.7%
		8		5.30	6.64	-40.7%

One thing worth noting is that one-time calibration probably would introduce serious errors for mass concentration estimation. For example, if we just calibrate the sensor once and use the calibration factor of Test 5 (K_{exp}= 2.44) for other measurements, the errors will be enlarged to -422.13% for the aerosol from Test 3 (K_{exp}= 12.74). And compared to this, the errors of the proposed model are reasonable and acceptable.

In general, the calibration factor can be adjusted according to former calibration results and three parameters (m, σ_g, and d_{pg}) for mass concentration estimation. It will be more accurate than singly using a fixed calibration factor for all types of aerosols. More field comparison studies are to be conducted to further verify and validate this approach.

4.3.5 Estimate number concentration with known parameters

As mentioned above, with an estimation of size distribution parameters, the calibration factor can be predicted with moderate accuracy. Furthermore, with known parameters, number concentrations can be derived from Eq. (4.15)

With Eq. (4.15) and the calibration factor from Eq. (4.12), the number concentrations for each experiment were calculated. Table 4.5 summarizes the number concentrations both estimated from proposed model and reported by the SMPS. The errors between SMPS reported number concentration and model predicted number concentration can be controlled within ±50% for most of tests, except for Test 1.

The calibration method presented here for estimating mass concentration and number concentration requires particle properties and size distributions. However, the adjusted calibration factor increases the data accuracy for mass concentration. Furthermore, the number concentration is critical for practical use too. Both the improved data quality and additional number concentration will benefit the field measurements. Based on the structure of low-cost particle sensors, these are limited improvements that could be achieved.

Table 4.5 Examples of estimating number concentrations from the proposed model. Each test has several data points, and the statistics reports the maximum and minimum errors of all data points.

	Solution conc.	Test number	Distribution characterization		Statistics			Examples		
								Number concentration		
	mg/cc		d_{pg}	σ_g	No. of points	max	min	Signal	SMPS	From Eq. (4.16)	Error
I. NaCl	0.507	1	92.02	1.77	12	75.52%	-57.50%	554.0	7.70×10^5	8.57×10^5	-11.29%
								245.2	1.67×10^5	2.07×10^5	-23.90%
	1.087	2	119.55	1.69	9	17.91%	-26.68%	373.8	2.53×10^5	2.47×10^5	2.11%
								195.5	5.25×10^4	5.29×10^4	-0.72%
	1.892	3	156.95	1.48	16	37.10%	-41.84%	396.4	4.65×10^5	4.74×10^5	-1.99%
								231.0	1.38×10^5	1.60×10^5	-15.36%
II. Sucrose	1.150	4	115.78	1.91	9	61.23%	45.52%	332.9	1.09×10^5	5.62×10^5	48.52%
								220.8	4.30×10^4	2.23×10^5	48.11%
	3.325	5	126.99	1.99	8	38.63%	8.59%	418.2	6.71×10^4	6.13×10^4	8.59%
								215.9	2.18×10^4	1.56×10^4	28.42%
	4.315	6	155. 57	1.87	8	31.60%	24.28%	350.3	4.76×10^4	3.60×10^4	24.28%
								213.9	1.64×10^4	1.19×10^4	27.82%
III. SiO_2	1%	7	150.93	2.07	10	55.92%	14.76%	526.4	7.42×10^4	6.30×10^4	15.05%
								220.7	1.60×10^4	1.22×10^4	23.46%
	2%	8	176.06	1.91	12	35.97%	14.72%	508.8	7.05×10^4	5.51×10^4	21.93%
								210.4	1.18×10^4	9.65×10^3	18.48%

4.4 Conclusions

The calculated total scattered light intensity based on scattering theories were well correlated to the experimentally measured signals from the low-cost particle sensor. The experimental results also indicated the important dependency on the size distribution and the composition of the particles. The sensor signal outputs were not well correlated to the mass concentration. A model was proposed to determine the calibration factor (K) which would provide a more accurate estimate of the mass concentrations from the signal outputs. Based on the proposed model, an equation for K as a function of the refractive index and the size distribution parameters (geometric standard deviation and geometric mean diameter) was derived. The use of this value of K resulted in a better accuracy in the estimation of the mass concentration; and additionally, could provide an estimate of the number concentration. From experimental and simulation results, the low-cost sensor's ability of evaluating mass concentration has been confirmed with particles of a single composition. However, the ability to extend the application to more complex aerosol systems encountered in the ambient environment would need to be carefully examined.

4.5 References

Bhattacharya, S., Sridevi, S. and Pitchiah, R. Indoor air quality monitoring using wireless sensor network. Sensing Technology (ICST), 2012 Sixth International Conference on, 2012, IEEE, pp. 422-427.

Biswas, P. and Wu, C.-Y. (2005). Nanoparticles and the environment. *J. Air Waste Manage. Assoc.* 55: 708-746.

Brook, R.D., Rajagopalan, S., Pope, C.A., Brook, J.R., Bhatnagar, A., Diez-Roux, A.V., Holguin, F., Hong, Y., Luepker, R.V. and Mittleman, M.A. (2010). Particulate matter air pollution and cardiovascular disease. *Circulation* 121: 2331-2378.

Bruce, N., Perez-Padilla, R. and Albalak, R. (2000). Indoor air pollution in developing countries: A major environmental and public health challenge. *Bulletin of the World Health Organization* 78: 1078-1092.

Brunekreef, B. and Holgate, S.T. (2002). Air pollution and health. *The lancet* 360: 1233-1242.

Chao, C.Y., Wan, M. and Cheng, E.C. (2003). Penetration coefficient and deposition rate as a function of particle size in non-smoking naturally ventilated residences. *Atmos. Environ.* 37: 4233-4241.

Chen, D.-R., Pui, D.Y., Hummes, D., Fissan, H., Quant, F. and Sem, G. (1998). Design and evaluation of a nanometer aerosol differential mobility analyzer (nano-dma). *J. Aerosol Sci.* 29: 497-509.

Cheng, Z., Jiang, J., Fajardo, O., Wang, S. and Hao, J. (2013). Characteristics and health impacts of particulate matter pollution in china (2001–2011). *Atmos. Environ.* 65: 186-194.

Chow, J.C. (2001). Diesel engines: Environmental impact and control. *J. Air Waste Manage.* 51: 1258-1270.

Chung, W.-Y. and Oh, S.-J. (2006). Remote monitoring system with wireless sensors module for room environment. *Sens. Actuators, B*113: 64-70.

Donaldson, K., Tran, L., Jimenez, L.A., Duffin, R., Newby, D.E., Mills, N., MacNee, W. and Stone, V. (2005). Combustion-derived nanoparticles: A review of their toxicology following inhalation exposure. *Part. Fibre Toxicol.* 2: 1.

Edney, E., Kleindienst, T., Jaoui, M., Lewandowski, M., Offenberg, J., Wang, W. and Claeys, M. (2005). Formation of 2-methyl tetrols and 2-methylglyceric acid in secondary organic aerosol from laboratory irradiated isoprene/nox/so 2/air mixtures and their detection in ambient pm 2.5 samples collected in the eastern united states. *Atmos. Environ.* 39: 5281-5289.

Friedlander, S.K. (2000). *Smoke, dust, and haze*. Oxford university press New York.

Hand, J.L. and Kreidenweis, S.M. (2002). A new method for retrieving particle refractive index and effective density from aerosol size distribution data. *Aerosol Sci. Technol.* 36: 1012-1026.

He, C., Morawska, L., Hitchins, J. and Gilbert, D. (2004). Contribution from indoor sources to particle number and mass concentrations in residential houses. *Environ. Sci. Technol.* 38: 3405-3415.

Ivanov, B., Zhelondz, O., Borodulkin, L. and Ruser, H. Distributed smart sensor system for indoor climate monitoring. KONNEX Scientific Conf., Mnchen, 2002, pp. 10-11.

Jiang, R.-T., Acevedo-Bolton, V., Cheng, K.-C., Klepeis, N.E., Ott, W.R. and Hildemann, L.M. (2011). Determination of response of real-time sidepak am510 monitor to secondhand smoke, other common indoor aerosols, and outdoor aerosol. *J. Environ. Monit.*13: 1695-1702.

Kim, J.-J., Jung, S.K. and Kim, J.T. (2010). Wireless monitoring of indoor air quality by a sensor network. *Indoor Built Environ.*19: 145-150.

Kim, J.-Y., Chu, C.-H. and Shin, S.-M. (2014). Issaq: An integrated sensing systems for real-time indoor air quality monitoring. *Sensors Journal, IEEE* 14: 4230-4244.

Laven, P. (2006). Mieplot: A computer program for scattering of light from a sphere using mie theory & the debye series. *PhilipLaven. com* 10.

Leavey, A., Fu, Y., Sha, M., Kutta, A., Lu, C., Wang, W., Drake, B., Chen, Y. and Biswas, P. (2015). Air quality metrics and wireless technology to maximize the energy efficiency of hvac in a working auditorium. *Build. Environ.*85: 287-297.

Liu, J., Mauzerall, D.L., Chen, Q., Zhang, Q., Song, Y., Peng, W., Klimont, Z., Qiu, X., Zhang, S., Hu, M., Lin, W., Smith, K.R. and Tong, Z. (2016). Air pollutant emissions from chinese households: A major and underappreciated ambient pollution source. *Proc. Natl. Acad. Sci. U.S.A.* 113: 7756-7761.

Long, C.M., Suh, H.H. and Koutrakis, P. (2000). Characterization of indoor particle sources using continuous mass and size monitors. *J. Air Waste Manage. Assoc.* 50: 1236-1250.

Manikonda, A., Zíková, N., Hopke, P.K. and Ferro, A.R. (2016). Laboratory assessment of low-cost pm monitors. *J. Aerosol Sci.*102: 29-40.

Monn, C., Fuchs, A., Kogelschatz, D. and Wanner, H.-U. (1995). Comparison of indoor and outdoor concentrations of pm-10 and pm-2.5. *J. Aerosol Sci.* 26: S515-S516.

Oberdörster, G., Oberdörster, E. and Oberdörster, J. (2005). Nanotoxicology: An emerging discipline evolving from studies of ultrafine particles. *Environ. Health Perspect.*: 823-839.

Patel, S., Li, J., Pandey, A., Pervez, S., Chakrabarty, R.K. and Biswas, P. (2017). Spatio-temporal measurement of indoor particulate matter concentrations using a wireless network of low-cost sensors in households using solid fuels. *Environ. Res.*152: 59-65.

Pope 3rd, C., Bates, D.V. and Raizenne, M.E. (1995). Health effects of particulate air pollution: Time for reassessment? *Environ. Health Perspect.*103: 472.

Rajasegarar, S., Zhang, P., Zhou, Y., Karunasekera, S., Leckie, C. and Palaniswami, M. High resolution spatio-temporal monitoring of air pollutants using wireless sensor networks. Intelligent Sensors, Sensor Networks and Information Processing (ISSNIP), 2014 IEEE Ninth International Conference on, 2014, IEEE, pp. 1-6.

Rees, V.W. and Connolly, G.N. (2006). Measuring air quality to protect children from secondhand smoke in cars. *Medicine: Am. J. Prev. Med.* 31: 363-368.

Rohde, R.A. and Muller, R.A. (2015). Air pollution in china: Mapping of concentrations and sources. *PloS one* 10: e0135749.

Sagar, A., Balakrishnan, K., Guttikunda, S., Roychowdhury, A. and Smith, K.R. (2016). India leads the way: A health-centered strategy for air pollution. *Environ. Health Perspect.* 124: A116.

Smith, K.R. (2000). National burden of disease in india from indoor air pollution. *Proc. Natl. Acad. Sci. U.S.A.* 97: 13286-13293.

Smith, K.R. and Sagar, A. (2014). Making the clean available: Escaping india's chulha trap. *Energy Policy* 75: 410-414.

Smith, K.R., Samet, J.M., Romieu, I. and Bruce, N. (2000). Indoor air pollution in developing countries and acute lower respiratory infections in children. *Thorax.* 55: 518-532.

Sousan, S., Koehler, K., Thomas, G., Park, J.H., Hillman, M., Halterman, A. and Peters, T.M. (2016). Inter-comparison of low-cost sensors for measuring the mass concentration of occupational aerosols. *Aerosol Sci. Technol.* 50: 462-473.

Sousan, S., Koehler, K., Hallett, L. and Peters, T.M. (2017). Evaluation of consumer monitors to measure particulate matter. *J. Aerosol Sci.* 107: 123-133.

Tripathi, A., Sagar, A.D. and Smith, K.R. (2015). Promoting clean and affordable cooking. *Economic Political Weekly* 50: 81.

Tucker, W.G. (2000). An overview of pm 2.5 sources and control strategies. *Fuel Process. Technol.* 65: 379-392.

Tuckett, C., Holmes, P. and Harrison, P. (1998). Airborne particles in the home. *J. Aerosol Sci.* 29: S293-S294.

Wang, S.C. and Flagan, R.C. (1990). Scanning electrical mobility spectrometer. *Aerosol Sci. Technol.* 13: 230-240.

Wang, Y., Li, J., Jing, H., Zhang, Q., Jiang, J. and Biswas, P. (2015). Laboratory evaluation and calibration of three low-cost particle sensors for particulate matter measurement. *Aerosol Sci. Technol.* 49: 1063-1077.

Wang, Y., Li, J., Leavey, A., O'Neil, C., Babcock, H.M. and Biswas, P. (2016). Comparative study on the size distributions, respiratory deposition, and transport of particles generated from commonly used medical nebulizers. *J. Aerosol Med. Pulm. Drug Deliv.*

Yanosky, J.D., Williams, P.L. and MacIntosh, D.L. (2002). A comparison of two direct-reading aerosol monitors with the federal reference method for pm 2.5 in indoor air. *Atmos. Environ.* 36: 107-113.

Zheng, M., Cass, G.R., Schauer, J.J. and Edgerton, E.S. (2002). Source apportionment of pm2. 5 in the southeastern united states using solvent-extractable organic compounds as tracers. *Environ. Sci. Technol.* 36: 2361-2371.

Zhu, Y., Yu, N., Kuhn, T. and Hinds, W.C. (2006). Field comparison of p-trak and condensation particle counters. *Aerosol Sci. Technol.* 40: 422-430.

Zikova, N., Hopke, P.K. and Ferro, A.R. (2017). Evaluation of new low-cost particle monitors for pm 2.5 concentrations measurements. *J. Aerosol Sci.* 105: 24-34.

Chapter 5: Algorithm for multi-wavelength optical signal inversion to obatain accurate PM characterization

1. Lorenz-Mie theory

Lorenz-Mie theory describes the absorption and scattering of plane electromagnetic waves by uniform isotropic particles, in another word, the interactions between light and small particles. In the development of Lorenz-Mie theory, a lot of scientists have contributed to improving the theory, especially the following three scientists. Ludvig Lorenz (1829 – 1891) was the first physicist try to solve the problem. Later, Gustav Mie (1868 – 1957) developed the Mie theory to understand the varied colors of gold particles suspended in water. Then, Peter Debye (1884 – 1966) developed the theory in his doctoral dissertation for an application of Lorenz-Mie theory in astrophysical problem. The study of light propagation in different media (e.g., Snell's law) can date back to early 1600s. As shown in Figure 1(a), the direction of the light will be altered when passing from one medium to another. The pattern of light scattering for a slab and a spherical particle are shown in Figure 5.1(a) and 5.1(b) respectively. Lorenz-Mie theory is critical for detecting or characterizing liquid or solid particles, and a lot of instruments are based on light scattering principles. We first introduced how to calculate the scattered light intensity at a specific angle based on Lorenz-Mie theory, referring to *Craig F. Bohren and Donald R. Huffman's* book *Absorption and Scattering of Light by Small Particles.*[1] Then, using GRIMM personal dust monitor as an example, we analyze factors may challenge the accuracy of instruments.

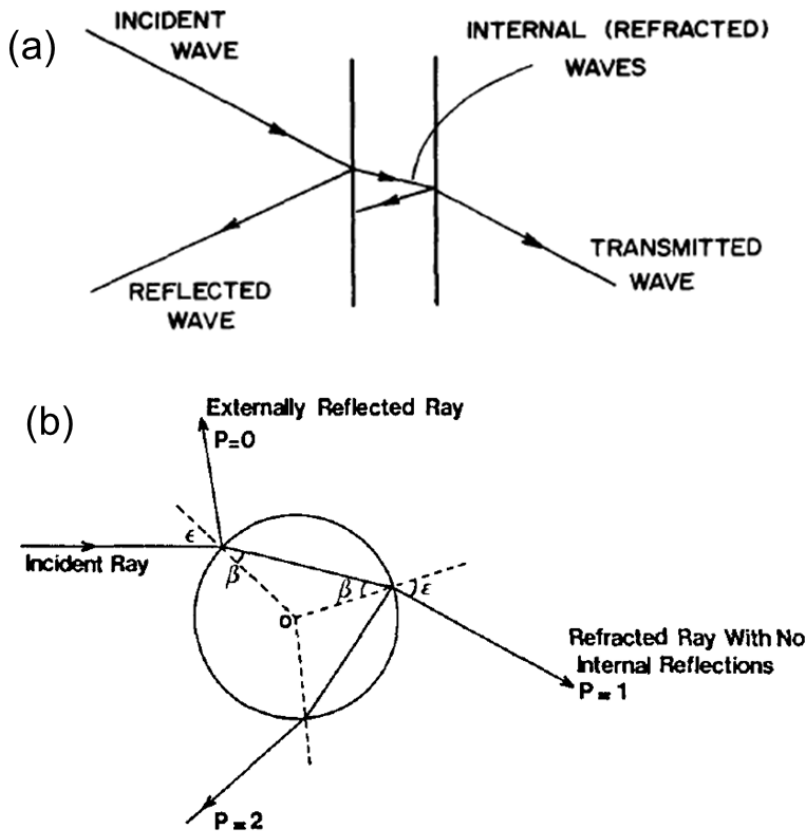

Figure 5.1 Analogy between scattering by a particle (b) and reflection-transmission by a slab (a).[1]

When incident light cast on a particle, the electric charges inside of the particle start to oscillate due to the electric field of incident light. These excited electric charges may scatter electromagnetic energy in all directions, which is known as scattering. At the same time, the excited charges can convert energy into different forms, such as heat, which is known as absorption. Lorenz-Mie theory is confined to the scattering of light of an arbitrary wavelength with a single particle. Some assumptions are made to simplify the derivation procedure of Lorenz-Mie theory. First, the light source is a plane wave, which is a wave of constant frequency and amplitude whose wave fronts are an infinitely long straight line. Plane waves travel in the direction perpendicular to the wave fronts. Second, the focus of the theory is elastic scattering:

the frequency of the scattered light is the same as that of the incident light. Scattering due to fluctuation was excluded. Third, the particle is idealized to homogeneous and spherical. When referring to a collection of many particles, the assumption is that the number of particles is sufficiently small and the separation between particles are sufficiently large. Therefore, the total scattered intensity is the summation of the scattered intensity of each small particle.

Lorenz-Mie solution is the solution of Maxwell's equations for a homogeneous spherical particle in a spherical polar coordinate system, as shown in Figure 2. Maxwell's equations describe how waves physically propagated through space. Maxwell's equations are from several well-established laws. Equation 1a is Gauss's law that the electric flux through any closed surface is proportional to the enclosed electric charge. Followed by Equation 1b, the Gauss's law for magnetism, no magnetic monopoles exist. Then, Equation 1c is the Faraday's law of induction, indicating time varying magnetic field produces an electric filed. The last equation is the Ampere's circuital law, showing that currents and a time-varying electric fields will induce magnetic fields. Maxwell's equations describe the relationships between electricity and magnetism in a neat and symmetrical manner.

$$\nabla \cdot \vec{E} = 0 \tag{1a}$$

$$\nabla \cdot \vec{B} = 0 \tag{1b}$$

$$\nabla \times \vec{E} = -\frac{\partial \vec{B}}{\partial t} \tag{1c}$$

$$\nabla \times \vec{B} = \mu_0 \varepsilon \frac{\partial \vec{E}}{\partial t} \tag{1d}$$

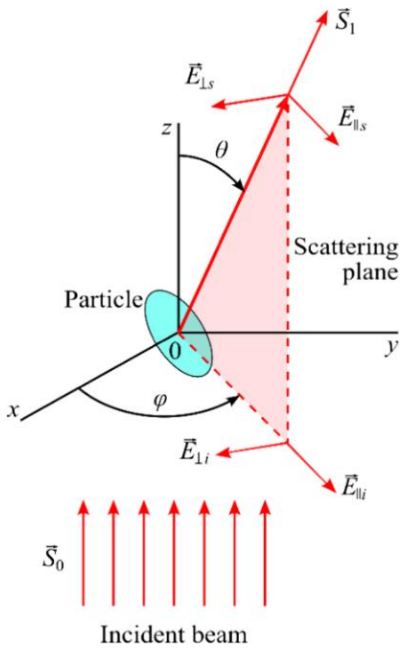

Figure 5.2 Spherical polar coordinate system centered on a spherical particle.

The derivation of Lorenz-Mie theory is difficult and complicated; therefore, we leave out the procedures of solving equations and directly show useful equations and conclusions derived from the Lorenz-Mie theory. The equations here can be used to calculate the scattered light intensity at an angle θ of a particle with diameter d_p and refractive index m. The vibration of the polarized incident light ($i_{unpolorized}$, wavelength = λ) can be decomposed on two directions, $i_{\perp}$ and $i_{//}$ for perpendicular and parallel to the scattering plain. No matter for incident light or scattered light, the relationship between $i_{\perp}$, $i_{//}$, and $i_{unpolorized}$ are universal as defined by Equation 2.

$$i_{unpolarized} = \frac{1}{2}(i_{\perp} + i_{\parallel}) \tag{2}$$

The scattered light intensity $i_{\perp}$ and $i_{//}$ at a certain angle θ can be calculated from the following equations, where S_1 and S_2 are defined amplitude functions. Using S_1 and S_2 can simplify the phase function that describes the angular distribution of scattered intensity.

$$i_{\perp} = |S_1|^2 \tag{3a}$$

$$i_{\parallel} = |S_2|^2 \tag{3b}$$

$$S_1 = \sum_n \frac{2n+1}{n(n+1)} (a_n \pi_n + b_n \tau_n) \tag{4a}$$

$$S_2 = \sum_n \frac{2n+1}{n(n+1)} (a_n \tau_n + b_n \pi_n) \tag{4b}$$

S_1 and S_2 are functions of a_n, b_n, π_n, and τ_n, which are coefficients derived when solving the Maxwell's equations using the boundary conditions at the particle-medium interface. a_n and b_n can be calculated from Equations 5a and 5b, where m is the refractive index of particles and x is the dimensionless parameter defined as Equation 6.

$$a_n = \frac{m\psi_n(mx)\psi_n'(x) - \psi_n(x)\psi_n'(mx)}{m\psi_n(mx)\xi_n'(x) - \xi_n(x)\psi_n'(mx)} \tag{5a}$$

$$b_n = \frac{\psi_n(mx)\psi_n'(x) - m\psi_n(x)\psi_n'(mx)}{\psi_n(mx)\xi_n'(x) - m\xi_n(x)\psi_n'(mx)} \tag{5b}$$

$$x = \pi d_p / \lambda \tag{6}$$

The φ_n and ξ_n in Equations 5a and 5b are functions of the spherical Bessel function of the first kind (j_n) and the second kind (y_n), as shown in Equations 7a and 7b. The φ_n' *and* ξ_n' are derivatives of φ_n and ξ_n and can be calculated as Equations 7c and 7d. Since x is defined as the dimensionless size parameter, we use ρ instead of x as variables.

$$\psi_n(\rho) = \rho j_n(\rho) \tag{7a}$$

$$\xi_n(\rho) = \rho[j_n(\rho) + iy_n(\rho)] \tag{7b}$$

$$\psi_n'(\rho) = \psi_{n-1}(\rho) - \frac{n\psi_n(\rho)}{\rho} \tag{7c}$$

$$\xi_n'(\rho) = \xi_{n-1}(\rho) - \frac{n\xi_n(\rho)}{\rho} \tag{7d}$$

Bessel functions are first defined by Daniel Bernoulli and generalized by Friedrich Bessel. The plots of Bessel functions of the first and second kind are shown in Figure 5.3.

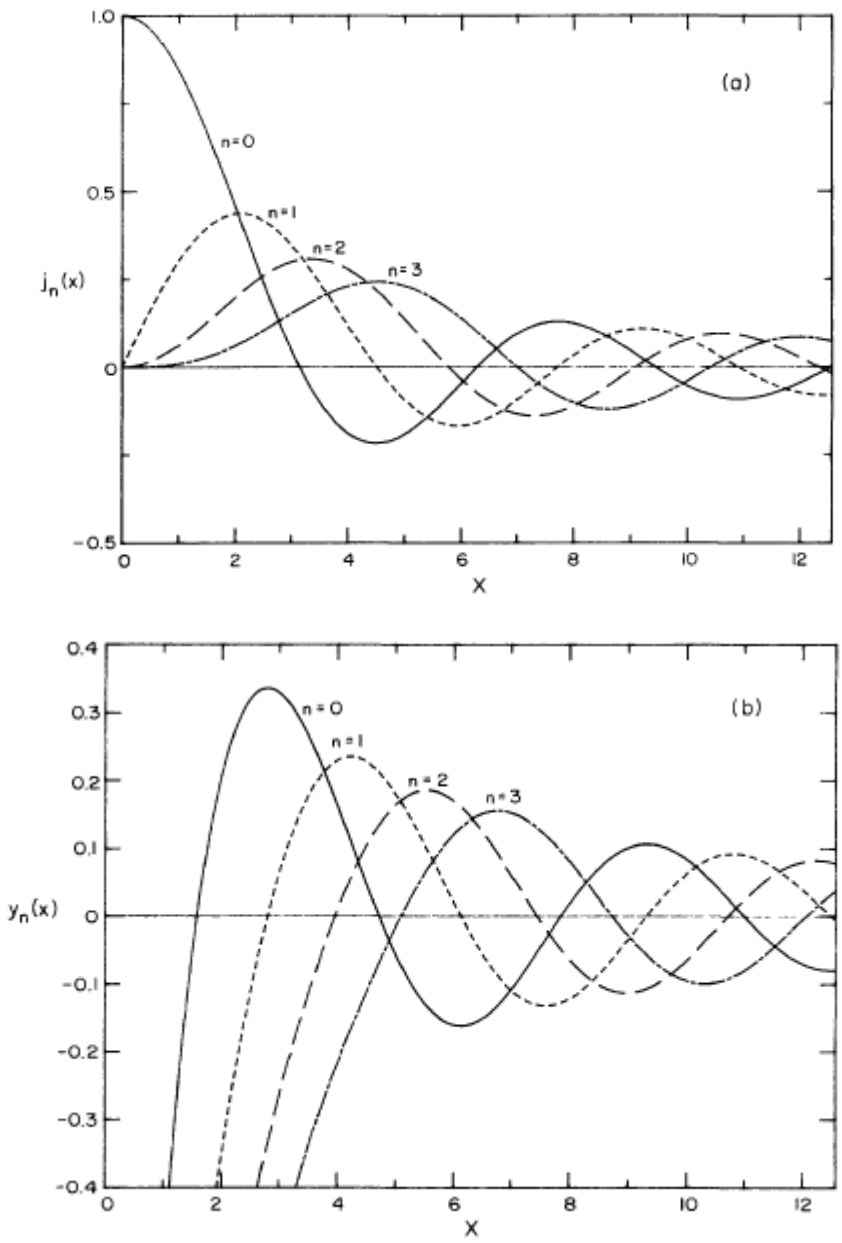

Figure 5.3 Plots of Bessel functions of the (a) first kind and (b) the second kind.[1]

With Equations 5 to 7, a_n and b_n can be calculated for a certain wavelength (λ), a particle with known diameter (d_p), and the refractive index m. To calculate S_1 and S_2, we still need to calculate π_n and τ_n. π_n and τ_n are related to the scattering angle and are in recurrence relationship as shown by Equations 8(a) and 8(b).

$$\pi_n = \frac{2n-1}{n-1}\mu\pi_{n-1} - \frac{n}{n-1}\pi_{n-2} \quad (8a)$$

$$\tau_n = n\mu\pi_n - (n+1)\pi_{n-1} \quad (8b)$$

The initial values π_0 and τ_0 are defined as Equations 9(a) to 9(c).

$$\pi_0 = 0 \quad (9a)$$

$$\pi_1 = 1 \quad (9b)$$

$$\mu = cos\theta \quad (9c)$$

The polar plots of π_0 and τ_0 are shown in Figure 5.4, indicating the scattering intensity's dependence on the scattering angle θ. As demonstrated in Figure 5.4, with an increasing n, the lobes of the plots increase. At the same time, the forward scattering lobes becomes narrowed and the backward scattering lobes are usually negative or disappeared. This agrees with the phenomenon that normally forward scattering is stronger than backward scattering.

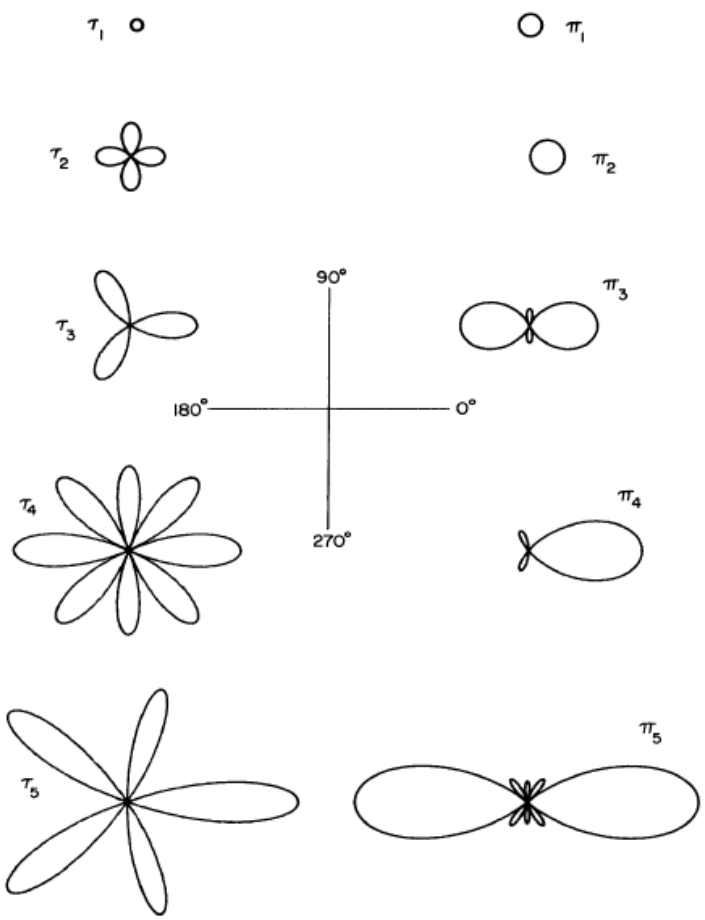

Figure 5.4 Polar plots of the first five angle-dependent functions π_n and τ_n. Both functions are plotted to the same scale.[1]

Above equations are widely used to solve the light scattering problems. There are some software packages available that have already incorporated these equations, which can provide scattering phase functions after entering the properties of the particle and the incident light. Two software packages have been used in this study. MiePlot, based on graphical user interface, is easy to use.[3] It can calculate the scattered light intensity as a function of wavelength, size distribution, and scattering angle, together with several additional optical properties (e.g., scattering or absorbing coefficient). Another software is PyMieScatt, which is integrated with Python. Compared to MiePlot, PyMieScatt is more powerful, and users can

program according to their own requirement with pre-defined functions in PyMieScatt software package.[4]

5.2 Limitation of optical instruments

The accuracy of optical instruments is a major concern in their application and deployment. Currently, the most reliable and accurate method of measuring the PM concentration is the gravimetric method. This method uses the high-volume air sampler to maintain particles on a filter. By weighing the filter, the PM mass concentration can be determined. A limitation of this method is its temporal resolution. The high-volume air sampler usually operates over a long period of time, and the PM concentration variation during this period is neglected. On the other hand, PM mass concentration is only one metric to evaluate the PM concentration. Other parameters, including the number concentration and size distribution, are also important to characterize the PM. Optical instruments are dominant for measuring these parameters. For example, the aerodynamic particle sizer (APS) uses time of flight measurement to determine the aerodynamic diameter of particles. The condensation particle counter (CPC) measures the count of magnified particles to determine the total number concentration. CPC combined with differential mobility analyzer (DMA) can form a scanning mobility particle sizer (SMPS) for measuring size distribution functions. The optical particle counter (OPC) can also measure the PM size distribution by measuring the scattered light intensity of each single particle. All these methods mentioned above involve optical measurement more or less. Here we analyze some parameters that may bias the accuracy of optical measurement with the GRIMM personal dust monitor as an example.

GRIMM, a federal reference method (FRM), measures the PM number concentration, mass concentration and size distribution functions, and it has been widely used to evaluate or calibrate low-cost PM sensors. The working principle of GRIMM is shown as in Figure 5.5. The 683 nm laser diode illuminate each particle when it passes through the sensing volume. The scattered light from 30° to 150° is captured by the parabolic mirror then focused on a photodetector. On the opposite side, the scattered light from 81° to 99° directly cast on the photodetector. Using optics to collect the scattered light at a wider angle decreases the signal to noise ratio, which lowers the cut-off size. At the same time, the design can smooth the fluctuation of Lorenz-Mie scattering curve, therefore, enhance the accuracy for size measurement. When a particle passes through the sensing volume, a pulse will be generated reflecting the intensity of scattered light. The pulse height is related to particle size. The number of the pulses is related to the number concentration.

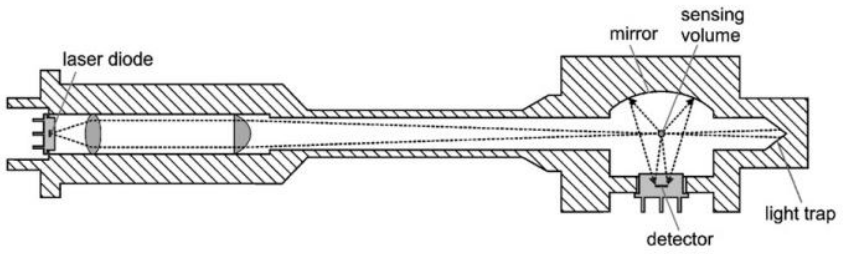

Figure 5.5 Schematic of the cross-section of the Grimm 1.109 OPC. The aerosol flow through the sensing volume is perpendicular to the image plane[2].

Based on the working principle of the GRIMM, the pulse height detected by the optical detector in the GRIMM, proportional to the scattered light intensity collected by the photodetector, can be simulated. Assuming the refractive index is 1.45, the response curve we simulated by PyMieScatt (Figure 5.6a) agrees well with that in previous literature (Figure 5.6b). The response curve demonstrates that the pulse height increases with an increasing particle

diameter. The fluctuations of light scattering intensity in Mie regime will interfere the accuracy of particle size classification.

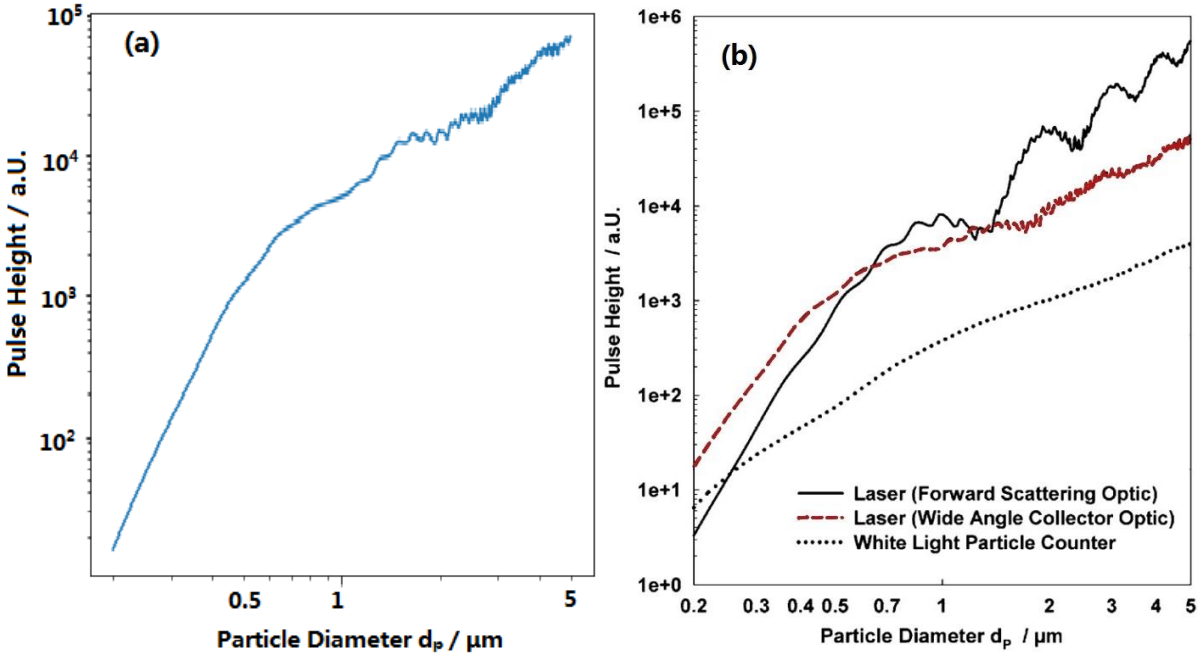

Figure 5.6 (a) The pulse height varying with particle diameter simulated by PyMieScatt. (b) The response curve from previous literature.

Particle's optical properties can also influence instruments' accuracy. Figure 5.6 is simulated based on refractive index equals to 1.45. Figure 5.7 simulated how GRIMM's response curves vary with different refractive index. The real part of the refractive index has minor influence on the response curve. However, the imaginary part of the refractive index significantly lowers the response value, which is a major reason of size misclassification. For example, a 2 µm particle whose refractive index equals to 1.59+0.03j might be classified as a 1 µm particle.

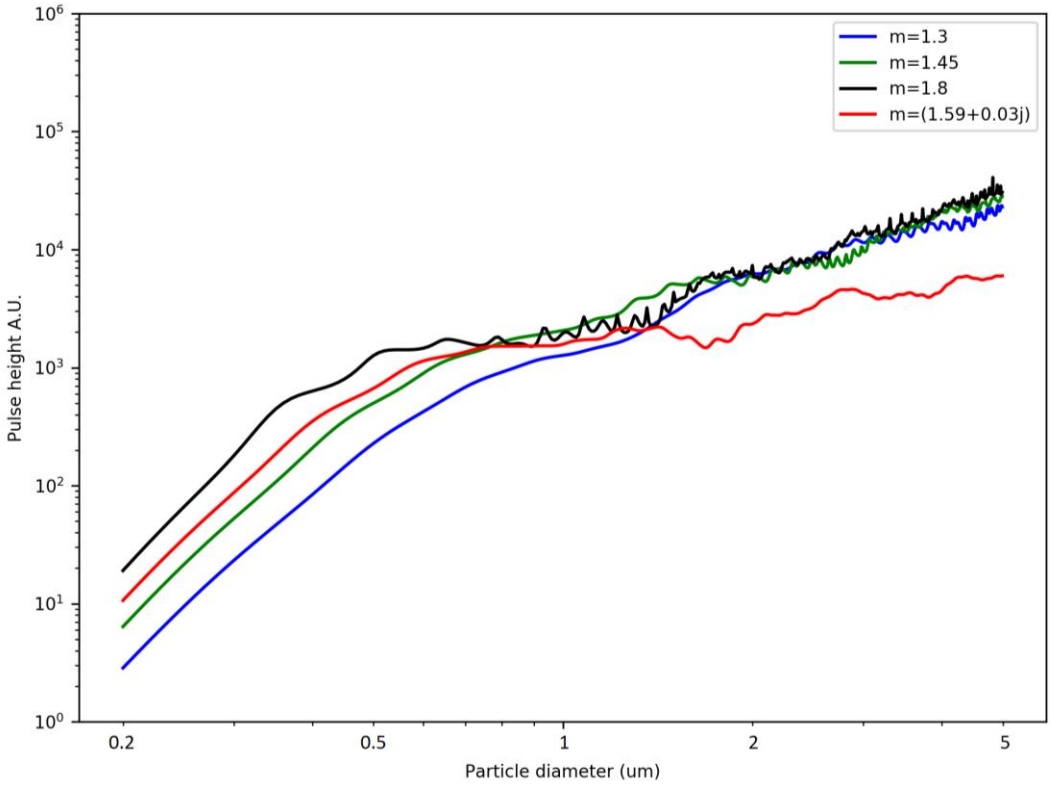

Figure 5.7 The response curve of GRIMM varies with the refractive index of aerosols.

5.2 Data inversion algorithm

Sensor's dependence on PM composition and size distribution has been investigated extensively in calibration and characterization. The composition will influence the optical properties, together with the refractive index, which interfere size classification and mass concentration estimation. Such dependency also influences the performance of research-grade instruments. Therefore, we proposed an algorithm to improve the performance of low-cost PM sensors.

The refractive index is a complex number, containing a real component (m_{real}) and an imaginary component (m_{img}), as shown in Equation 10. The real and imaginary component are related to

the light scattering and absorbing ability respectively. The speciation influence the optical properties, together with the refractive index, therefore reduce the accuracy of sensors' performance. Underestimation and overestimation are mainly due to the size misclassification caused by refractive index variation. Distinguishing between light absorbing and light scattering material will be very helpful for revising the accuracy of low-cost PM sensors.

$$m = m_{real} + m_{img}i \tag{10}$$

Here we propose an algorithm that can approximately distinguish between light scattering and light absorbing materials. The method relies on the calibration slope *k*, also known as the calibration coefficient. The slope *k* can be obtained from the correlation between the mass concentrations and the signal outputs. We assume that the measurements of both the mass concentration and the signal outputs are accurate, and the density of the aerosols are the same. The structure of the sensing component is similar to the Sharp GP2Y sensor, with a scattering angle from 60° to 90°. We randomly generated 2000 data sets and each dataset contains four parameters: the geometric mean diameter (d_{pg}), geometric standard deviation (σ_g), total number concentration (N), and refractive index (m). The range of d_{pg} and σ_g are 50 nm – 10 μm, and 1.1 – 1.9 respectively. The refractive indices of half of the data only have the real part within a range of 1.49 – 1.51. The refractive indices of the other half of the data have an additional imaginary part within a range of 0.05 – 0.9. The slope *k* (the ratio of the scattered light intensity and the mass concentration) of the generated parameters was simulated with PyMieScatt and plotted in Figure 5.8. The simulated slopes for the light scattering materials are much higher than that of the light absorbing materials. Compared to light scattering materials, to achieve the same level of response, higher concentration is needed for light absorbing aerosols.

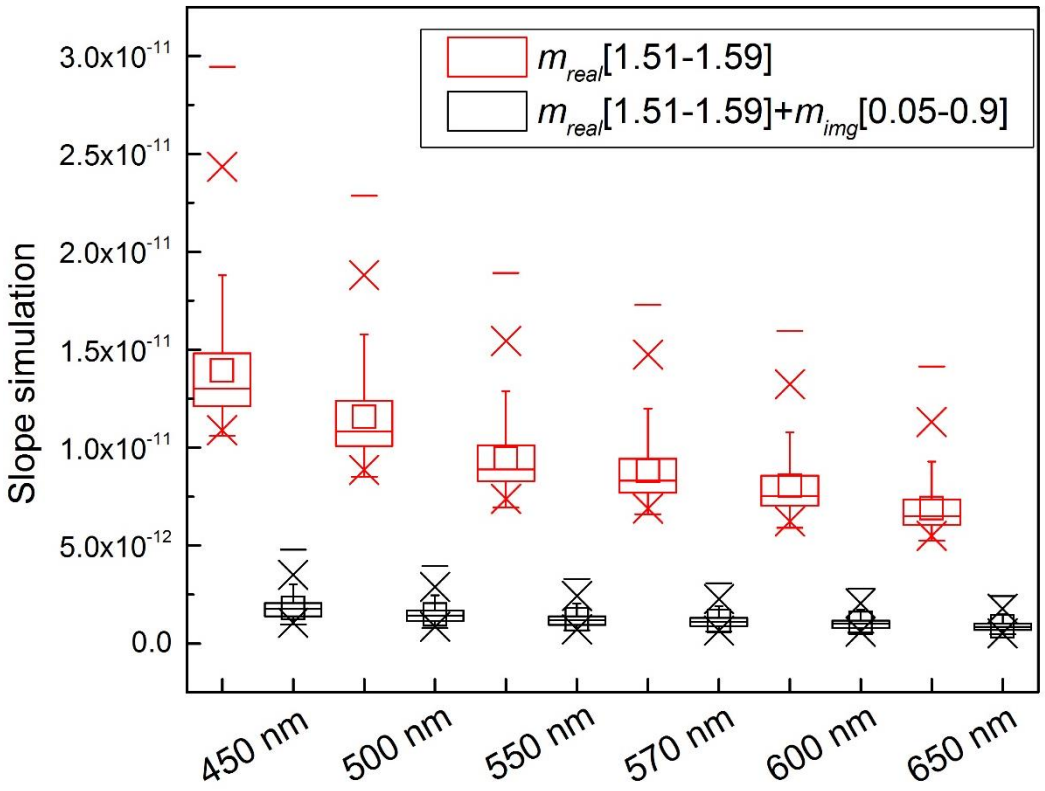

Figure 5.8 The simulated slope *k* of randomly generated refractive index and size distribution parameters varying with the wavelength of the incident light.

The method proposed here can realize rough speciation by distinguish the light scattering material from the light absorbing material. However, there are some limitations. First, this method did consider the accuracy of the mass concentration measurement. Second this system has only been tested with the single-component aerosols. However, aerosols with multiple compositions are the dominant situation in practical deployment. Third, the method is based on the slope by correlating the mass concentration with the light scattering measurement. A wider range of concentration is needed to establish the correlation. Therefore, this method may not be applicable for measurements with steady concentration.

To overcome the limitations mentioned above, we propose two more advance algorithms targeting enhancing the accuracy of the optical PM measurement. The first algorithm is based on

single particle measurement that uses lasers with multiple wavelengths to measure particle size and determine its refractive index. The second algorithm is based on multi-wavelength measurement and use the total scattered light intensity

To retrieve the refractive index, the necessary input of the first algorithm is the scattered light intensity at a certain angle for three different wavelengths, together with the particle size (d_p). Assuming red, green, and blue lasers were used, and the scattered light intensity was the integrated angular measurement from 60° to 90°, and were denoted as I_{red}, I_{green}, and I_{blue}. With particle size (d_p), the scattered light intensity can be plotted on a 2D space, where the x axis is real component of the refractive index (m_{real}) and the y axis is the imaginary component of the refractive index (m_{img}). Each point on the 2D space is a combination of m_{real} ranging from 1 to 3 and m_{img} ranging from 0 to 1. With known d_p, for each point on the 2D space, the scattered light intensity can be calculated and plotted as the z axis, which forms the green, red, and blue surfaces. On a surface plot, we can find the contour with the iso-response values equals to the scattered light intensity of the measurement. For example, on the green surface plot, we can use a plane parallel to the 2D x-y space ($z = I_{green}$) to find refractive indices (combinations of m_{real} and m_{img}) meet the requirements. These refractive indices will make the scattered light intensity integrated from 60° to 90° exactly equals to I_{green} for particles of size d_p. Intersection between the contours from the green and red surface plots are shown in Figure 5.9, the same as the contours from the red and blue surface plots. The common solution is the refractive indices that meet all requirements.

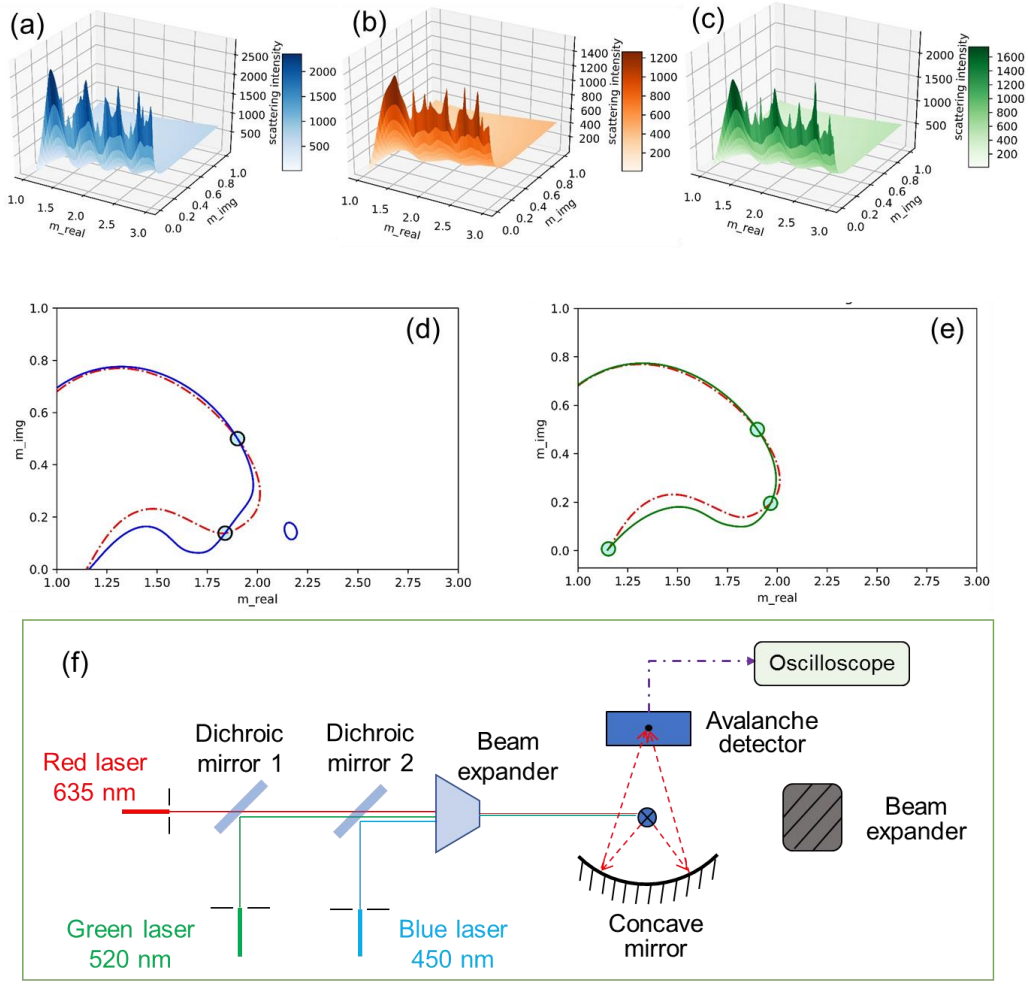

Figure 5.9. An example of data inversion routine with input of d_p = 1 μm, I_{red}, I_{green}, and I_{blue}. (a) (b) and (c) are 3D surface plots for d_p = 1 μm, where x and y axes are the real and imaginary part of refractive index (m_{real} and m_{img}) and the z axis is the scattered light intensity of particle. (d) and (e) are the contour plots whose intersections are the retrieved refractive index. (f) schematic diagram designed for the algorithm.

However, this method is very sensitive to the accuracy of input parameters. Even an error of ±1% in particle size or scattered light intensity will lead to invalid solutions. This is due to the noisy peaks of the scattered light intensity in the Mie regime, which is straightforward in the red, green, or blue surface plots shown in Figure 5.9 and Figure 5.10. Therefore, a small error will lead to different contour plots, and possibly no intersections among contour plots. In addition, accurately measuring the particle size and the scattered light of a single particle is difficult to realize.

To accommodate these limitations, we developed another algorithm that is based on the size distribution and the total scattered light intensity. The input parameters include the size distribution (n_d) and the scattered light intensity measured from 60° to 90° for the specified size distribution at different wavelengths ($I_{nd,\lambda}$). The procedure is similar to the algorithm mentioned above. The scattered light intensity of the specified PM size distribution will be calculated for different combinations of m_{real} and m_{img}, and contours will be found for given $I_{nd,\,red}$, $I_{nd,\,green}$, and $I_{nd,\,blue}$. The intersections of the contours are the retrieved refractive index.

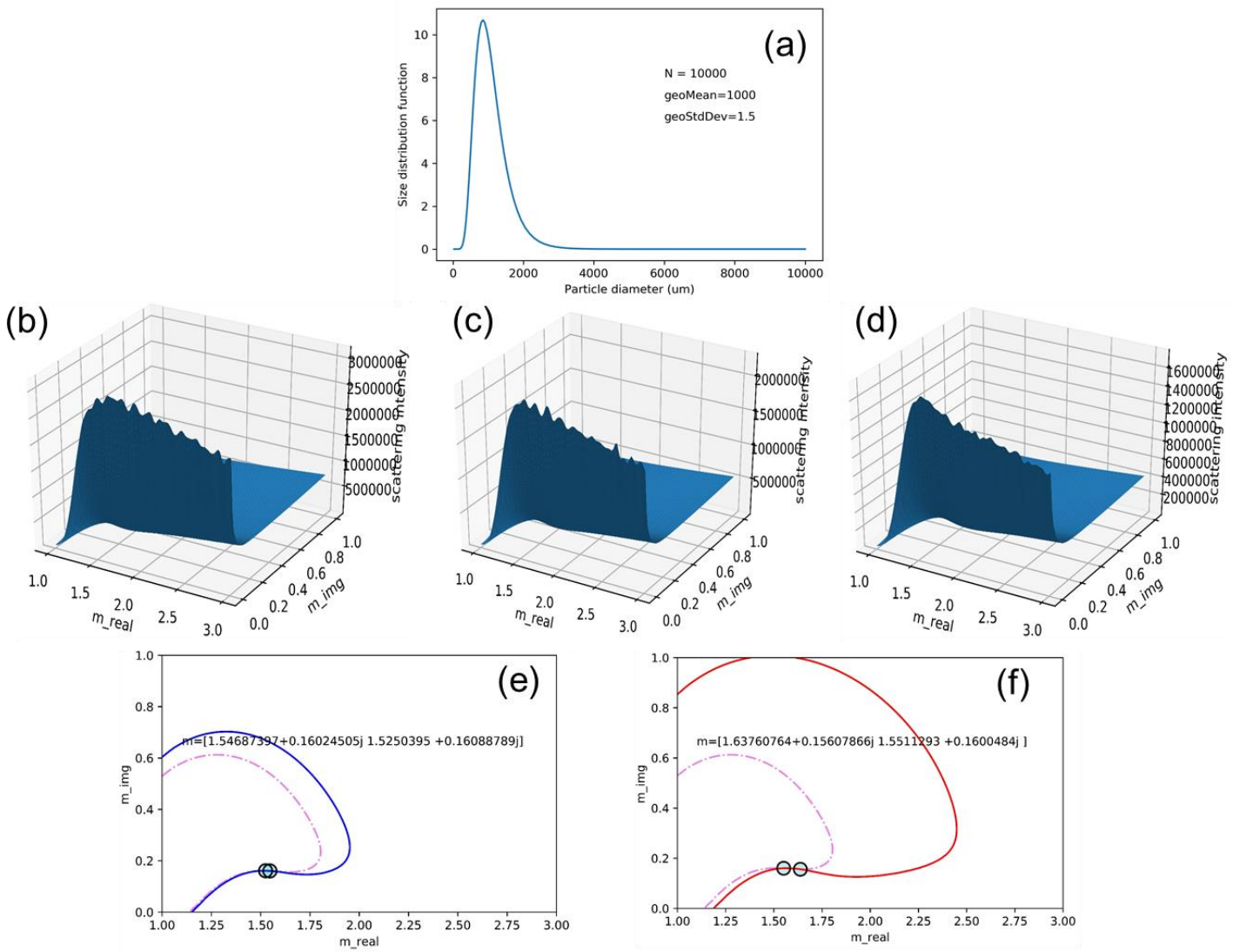

Figure 5.10 An example of data inversion routine with input of size distribution shown in (a), I_{red}, I_{green}, and I_{blue}. (b) (c) and (d) are 3D surface plots the size distribution in (a), where *x* and *y* axes are the real and imaginary part of refractive index (m_{real} and m_{img}) and the *z* axis is the scattered light intensity of particle. (e) and (f) are the contour plots whose intersections are the retrieved refractive index.

5.3 Summary

In this chapter, we introduced the Lorenz-Mie theory, which is the theoretical foundation of optical sensors. With the Lorenz-Mie theory, we simulated the performance of GRIMM dust monitor, demonstrating that the performance of optical sensors or optical instruments inevitably depends on PM optical properties. The variation on optical properties can influence the scattered light intensity of a single particle, leading to size misclassification, which will underestimate or overestimate mass concentration. To overcome such a dependency, we proposed two designs, together with two data inversion algorithms for retrieving the refractive index, which can eliminate the dependency on PM optical properties. The algorithms used a graphical solution to find the combinations of the real and imaginary parts of the refractive index that can meet requirements. However, the proposed data inversion algorithms did not take the measurement accuracy into consideration. Further discussion is needed to test the robustness of the algorithm after introducing measurement errors.

5.4 References

1. Bohren, C. F.; Huffman, D. R., *Absorption and scattering of light by small particles*. John Wiley & Sons: 2008.
2. Heim, M.; Mullins, B. J.; Umhauer, H.; Kasper, G., Performance evaluation of three optical particle counters with an efficient "multimodal" calibration method. *Journal of aerosol science* **2008,** *39*, (12), 1019-1031.

3. Laven, P. (2006). MiePlot.

4. Sumlin, B. J., Heinson, W. R., & Chakrabarty, R. K. (2018*). Retrieving the aerosol complex refractive index using PyMieScatt: A Mie computational package with visualization capabilities*. Journal of Quantitative Spectroscopy and Radiative Transfer, 205, 127-134.

Chapter 6: Particulate Matter Sensors Mounted on a Robot for Environmental Aerosol Measurements

The results of this chapter have been published in Cashikar A., Li, J., & Biswas, P. (2019). Particulate Matter Sensors Mounted on a Robot for Environmental Aerosol Measurements. Journal of Environmental Engineering.

Abstract

In recent years, miniaturized particulate matter (PM) sensors have been studied intensively as an alternative device for air quality measurement due to their price advantage, moderate accuracy, and portable size. The accuracy of these sensors has been studied by calibration against conventional laboratory instruments. Such sensors have been connected in a network for spatiotemporal air quality measurements or used as a personal monitor for exposure estimation. Another important application is combining low-cost PM sensors with drones or other unmanned vehicles for sampling environments where the setup of a static sensor network may not be viable. In this study, a mobile robot cart with a low-cost PM sensor (AAQRL-ROBOPM ©) was developed to map spatial PM distributions over time. The robot can be moved either manually via Bluetooth inputs from an Android device, autonomously by following preprogrammed instructions, or with basic artificial intelligence (AI) and an algorithm. PM concentration readings are sent to the Android device for monitoring and storage. The mobile sensor module was tested for both indoor and outdoor environments, and effectively found the locations of the highest PM concentrations. Using such a device has advantages over a sensor network, such as lower overall cost and lesser complexity of setup. This mobile sensor module provides a more cost- and time-efficient method of finding PM hotspots. Once hotspots are located in the sampled environment, static sensors can be placed for the greatest effectiveness in measuring PM concentration over time. Furthermore, the mobile sensor module was manufactured with low-cost components, making it broadly affordable.

6.1 Introduction

Aerosols or particulate matter (PM) is a general term for solid or liquid particles with different sizes suspended in air. Inhalation of PM can cause health concerns, and its ubiquity in both indoor and outdoor environments makes exposure inevitable. Exposure to environments with high PM concentrations has been linked to weakened lung function (Strak et al. 2012). In addition, an estimated two million deaths occur annually as a result of damage to the respiratory system caused by PM (Shah et al. 2013). PM inhalation has been associated with exacerbation of respiratory diseases including asthma and chronic obstructive pulmonary disease (COPD) (Guarnieri and Balmes 2014; Ling and van Eeden 2009). Short-time exposure can cause cardiovascular disease, but long-time exposure significantly increases the mortality rate and decreases life expectancy (Brook et al. 2010). Seniors and infants are most susceptible to PM pollution; however, healthy middle-aged adults may also suffer from coughing or other short-term adverse effects. PM pollution contributes to 3% and 5% of mortality from cardiopulmonary disease and respiratory system cancers, respectively (Cohen et al. 2005). This issue is more concerning in developing countries, where high PM concentrations occur in their rapidly growing economies (Burnett et al. 2014; Smith 1993). Due to its adverse health effects, PM concentration is routinely monitored and regulated by most governments. Indoor PM can be generated from smoking, cooking, incense burning, heating, or other human activities (Ferro et al. 2004; Löfroth et al. 1991). Sources of outdoor PM include vehicle emission, industrial emission, secondary aerosol formation and sea spray (Viana et al. 2008). PM has been classified as a Group I carcinogen by the International Agency for Research on Cancer (IARC) (Hamra et al. 2014).

There are various methods for performing PM concentration measurements, with different costs and accuracies. Normally, regulated PM concentration is determined by either mass concentration (the mass of PM in a unit volume of air) or number concentration (the number of PM in a unit volume of air). The gravimetric method, a federal reference method (FRM) regulated by the US Environmental Protection Agency (EPA), weighs the mass of PM retained on a filter after high-flowrate sampling and calculates the mass concentration accordingly. An alternative method involves the use of a tapered element oscillating microbalance (TEOM) to provide online PM mass concentrations by correlating the changes in oscillation frequency of the device with the mass increment due to PM landing on the filter (Patashnick and Rupprecht 1991). The PM concentrations reported by monitoring sites are crucial for PM exposure estimations. The prediction of PM concentrations at a certain location is based on the data provided by nearby monitoring sites. Inadequate distributions of monitoring sites hinder the accurate prediction of spatiotemporal PM concentrations. Moreover, the conventional methods listed above are laborious and costly, which limits the number of monitoring sites for PM measurements that can be simultaneously used. Therefore, improving spatial and temporal resolution and reducing the expense and maintenance labor of such networks are all major concerns in air quality monitoring.

Low-cost PM sensors have become popular in recent studies due to their price advantage and acceptable accuracy. The accuracy of low-cost PM sensors has been examined by comparing them with commercial instruments in laboratory measurements (Kelly et al. 2017; Manikonda et al. 2016; Sousan et al. 2017; Sousan et al. 2016; Wang et al. 2015). Wang et al. (2015) compared three low-cost PM sensors in laboratory experiments and demonstrated their high linearity with a SidePak (AM520, TSI Inc., Shoreview, MN, USA) after being properly calibrated according to

EPA recommendations. Although factors such as the PM composition, size distribution, and ambient temperature and humidity may bias the predicted mass concentration, low-cost PM sensors are capable of roughly estimating PM concentrations after calibration and evaluation (Li and Biswas 2017; Sousan et al. 2016; Wang et al. 2015). Sousan et al. (2016) calibrated multiple low-cost PM sensors in a controlled laboratory environment along with a reference sensor at PM concentrations of up to 6500 $\mu g/m^3$. Although the low-cost sensors misclassified fine and coarse particles, the coefficient of determination between the low-cost and reference sensors was 0.99, indicating a high degree of correlation. In addition, Li and Biswas (2017) determined a method for ensuring accurate and consistent measurement of PM using these sensors. They developed a mathematical model to determine a calibration factor, unique to each type of aerosol. Low-cost PM sensors have also been calibrated and evaluated outside the laboratory in field measurements (Holstius et al. 2014; Kelly et al. 2017; Shi et al. 2017; Zikova et al. 2017). Zikova et al. (2017) assessed the ability of 66 low-cost Speck PM sensors to measure PM concentrations in both indoor and outdoor real use environments. The data from the low-cost PM sensors had a high correlation, indicating a high degree of consistency between the sensors. Kelly et al. (2017) compared the performance of a low-cost PM sensor to two federal equivalent and gravimetric federal reference methods outdoors during the winter. They demonstrated a high association of the low-cost PM sensor with gravimetric methods in these ambient conditions. These studies have demonstrated the overall effectiveness of low-cost PM sensors for further application in field measurements.

After calibration, these sensors have been used to monitor indoor and outdoor air quality (Ivanov et al. 2002; Kelleher et al. 2018; Kim et al. 2014). Kim et al. (2014) explored the challenges of using a low-cost sensor system to measure indoor air quality. Ivanov et al. (2002) presented three

solutions for smart home automation of climate control by monitoring PM, CO_2, and other substance concentrations: a wall mount, a wearable, and a microchip sensor system. Kelleher et al. (2018) developed a weatherproof air sampler using a low-cost PM sensor for wildland fire monitoring. Low-cost PM sensor networks have been deployed to map high-resolution PM distributions (Leavey et al. 2015; Li et al. 2018; Patel et al. 2017; Rajasegarar et al. 2014; Sousan et al. 2018). Leavey et al. (2015) utilized a condensation particle counter alongside temperature and CO_2 sensors to produce energy savings of up to 79% from increasing the efficiency of an HVAC system in an auditorium. Patel et al. (2017) examined the PM concentrations in a rural Indian household. A high-resolution PM sensor network installed in the kitchen area and around the house showed that PM decay rates throughout the household varied greatly from day to day, owing to the varying natural air exchange rates. Rajasegarar et al. (2014) increased the accuracy of PM measurements by replacing a few expensive PM sensors in their setup with a higher quantity of low-cost sensors. This allowed for higher spatial resolution because of the relative closeness of the low-cost sensors. To achieve accurate and representative large area mapping results with a limited number of sensors, the choice of sampling locations is critical (Li et al. 2018). Li et al. (2018) demonstrated the accurate placement of low-cost PM sensors to measure the PM distribution in a woodworking shop. Sensors were placed in areas such that they would simulate the PM intake of different workers and bystanders in the shop. Using Kriging interpolation, gradient maps were created to display the ventilation of PM through the shop as it was emitted.

Sensor networks have extended the application of low-cost PM sensors; however, the location of each sensor in a network is crucial for generating an accurate PM distribution map. Mobile low-cost PM sensors could help optimize sampling locations. One possible method to mobilize PM

sensors is using robots. Robots have been used in environmental monitoring (Dunbabin and Marques 2012). Gas sensors have been installed on mobile robots to map distributions of hydrogen, carbon monoxide, carbon dioxide, methane, VOCs, ammonia, and hydrogen sulfide, among other gases (Chen et al. 2012; Reggente and Lilienthal 2009; Trincavelli et al. 2008). However, few studies have examined PM monitoring with robots. Ferri et al. (2010) presented the DustCart, a mobile robot equipped with a DustTrak® (8520, TSI Inc.) sensor to monitor PM concentrations. Data collected by the DustCart was used to reconstruct the spatial distribution of pollutants. Compared to a DustTrak, low-cost PM sensors are more compact, lightweight, and readily integrated with a miniaturized mobile cart. Furthermore, the robot cart in the above study costs roughly $20,000.

In this paper, a programmable and agile mobile robot cart combined with a low-cost sensor referred to as the AAQRL-ROBOPM © was developed. The overall cost of the AAQRL-ROBOPM is reasonable and lower than other reported systems. The AAQRL-ROBOPM was demonstrated to collect real-time data in pre-designed paths for repeated sampling to find PM hotspots in both indoor and outdoor environments.

6.2 Methods

The AAQRL-ROBOPM consists of a Sharp GP2Y1010AU0F (GP2Y, Sharp Corp., Osaka, Japan), a representative low-cost PM sensor, with an in-house designed and constructed robot cart, shown in Figure 6.1. The robot has three operation modes. Under the manual control mode, the robot receives real-time commands from an Android device (ZenPad C 7.0, AsusTek Computer Inc., Taipei, Taiwan) dictating instructions for movement and the sampling of PM concentrations. In the straight autonomous mode, the robot follows a pre-programmed linear path and conducts sampling along that path. In the quadrant algorithm mode, the robot uses basic AI programming to find a PM hotspot without requiring manual PM concentration data collection or analysis. To realize these three operation modes, the robot consists of three parts: a PM sensor module, a control module, and a Bluetooth module. The sampling inlet is attached with a 3D printed intake accessory to reduce directional selectivity caused by cart movement. The system was tested in an indoor area with multiple incense cones as a PM source, and near an outdoor construction site.

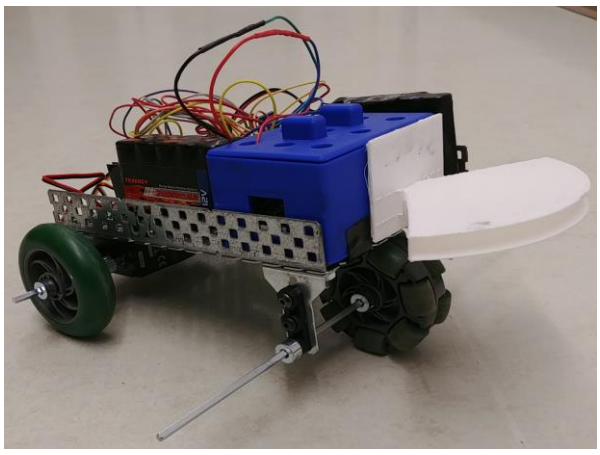

Figure 6.1 The handbuilt AAQRL-ROBOPM with a low-cost PM sensor for mobile field measurement. The sensor module is contained within the blue case.

6.2.1 Major Components of the AAQRL-ROBOPM

Table 1 shows the major components of the AAQRL-ROBOPM and their prices. The sensor module is responsible for sampling PM concentration. It contains a Sharp GP2Y1010AU0F, Keyes temperature (KY-013, Keyes) and humidity sensor (KY-015, Keyes), and an Arduino Nano (ATmega328, Arduino Inc., S.R.L, Italy). Pictures of these components are shown in Figure 6.2.

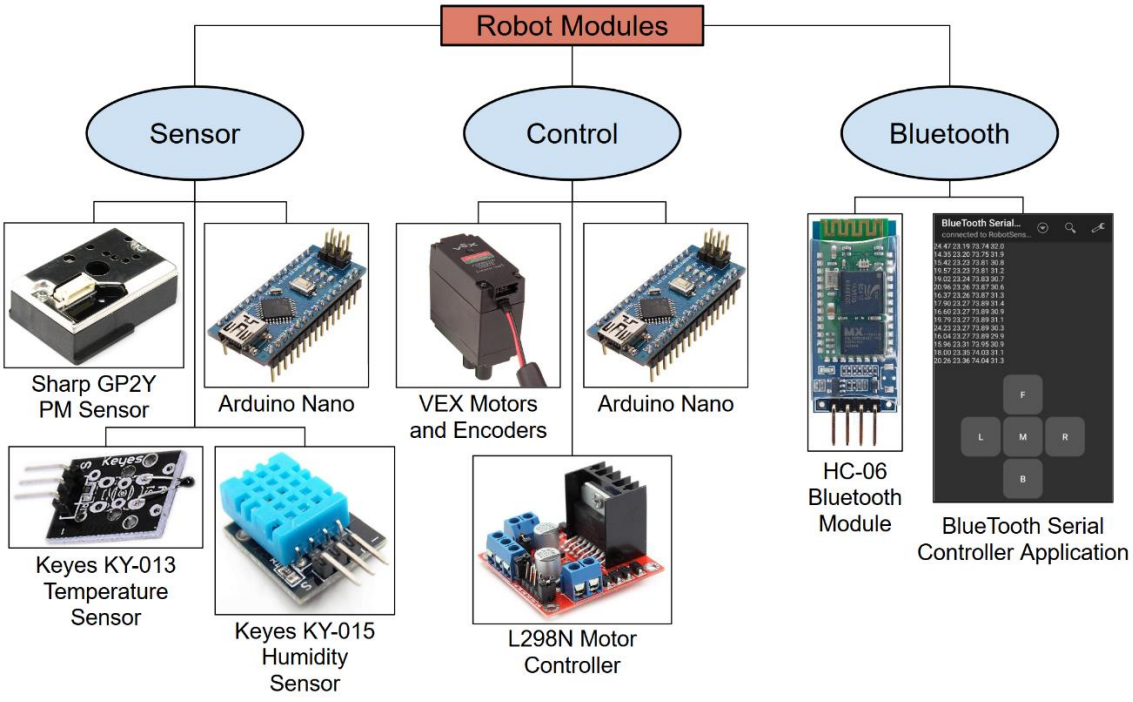

Figure 6.2 Major components of the robot, separated by module.

In the sensor module, the Sharp GP2Y illuminates the particles with an infrared emitting diode (IRED) and detects the scattered light intensity with a phototransistor. The IRED is powered by a square-wave voltage with a 0.32-millisecond pulse width. The phototransistor converts the light intensity into voltage as an output. A larger voltage output from the Sharp GP2Y represents a

higher PM concentration that scatters more light towards the phototransistor. The Sharp GP2Y is a passive sampling sensor, so a small fan was positioned behind the sensor to bring a greater volume of air through the sensor inlet. The Arduino is the central microcontroller that executes measurements and communication. Once triggered, the Arduino can measure the PM concentration and send the readings to the Android device via the Bluetooth module. Although the sensor module operates continuously, measurements are only recorded when instruction to conduct sampling is received. Upon receiving such a command from the control module, 100 measurements are taken from the PM sensor over the span of one second, with a pulse cycle of ten milliseconds. The measurements are then averaged and reported. The temperature sensor and humidity sensor were used to monitor environmental conditions and confirm that the testing area was stable.

The control module allows the robot either to be actively guided by commands received via Bluetooth communication from the Android device, or to move autonomously, following preprogrammed instructions. The module consists of another Arduino Nano separate from the one contained in the sensor module, two VEX motors (393, VEX Robotics, Inc., Greenville, Texas, USA) with integrated encoder modules (VEX Robotics, Inc.), and an L298N motor controller (L298N, Qunqi C). The Arduino in the control module interprets signals from the Android device via the Bluetooth module. It also moves the robot by commanding the motors to turn via the L298N motor controller. The encoders measure the distance that each motor moves; therefore, the distance and direction that the robot travels relative to its starting position can be accurately programmed. To achieve better traction with the surfaces being tested on, the robot was moved at a speed slower than its maximum in all trials.

In the Bluetooth module, a Bluetooth chip (HC-06, HiLetgo E-Commerce Co. LTD, Shenzhen, China) communicates between the Arduinos on the robot and the external Android device. The module is a Class 2 Bluetooth device that can communicate wirelessly with a connected device up to ten meters away. Although Class 1 Bluetooth devices have a range of up to 100 meters, most Bluetooth-enabled devices contain only a Class 2 device; therefore, a Class 2 module was chosen for economy. An application, Bluetooth Serial Controller (NEXT PROTOTYPES, 2015), was used on the external Android device to communicate with the robot. The user interface was configured with four movement-related buttons (forward, backward, left, and right) and a button to take a PM concentration measurement. In addition to Bluetooth communication, the two Arduinos are also linked via Serial communication.

To power the electrical components, a 6-volt and a 12-volt rechargeable nickel metal hydride (NiMH) battery (Tenergy, Fremont, California, USA) were utilized. Two separate batteries were required because, when the system was tested with a single battery, the high current draw of the motors hindered the stable operation of the other electrical components. The 12-volt battery was used to power the motors, while the remaining components were powered by the 6-volt battery. When the robot was tested with both batteries fully charged, the 12-volt battery began running out of charge first, after about three hours of continuous robot movement.

6.2.2 Robot Operation Modes

In manual control mode, the buttons on the Android device screen move the robot and conduct PM concentration measurements. When a button is pressed, a character corresponding to the dedicated task is sent to the control module via the Bluetooth module. If the task is a movement,

the Arduino in the control module commands the motors accordingly. If the task is PM measurement, the command is passed from the Arduino in the control module to the Arduino in the sensor module via Serial communication. After the reading is taken, it is printed directly to the terminal window on the Android device via the Bluetooth module.

The straight autonomous mode allows the robot to complete a cycle of conducting PM concentration measurements after a single start command is sent. Once the robot receives the start command, it conducts a series of programmed movements and PM concentration measurements. The robot can also be programmed to stand by for another start signal after completing a cycle.

The quadrant algorithm mode uses basic AI to move the robot towards a PM source or hotspot in the environment being tested in. As shown in Figure 6.3, the robot moves in a square path, taking a measurement at each corner of said path. The process is then repeated in the quadrant of the original path with the highest PM concentration measurement. The robot continues entering smaller quadrants until the side length of a new quadrant would fall below 0.3 meters. The robot then moves to and stops at the location in the current quadrant with the highest PM concentration, which represents the closest measurement point to the source of PM.

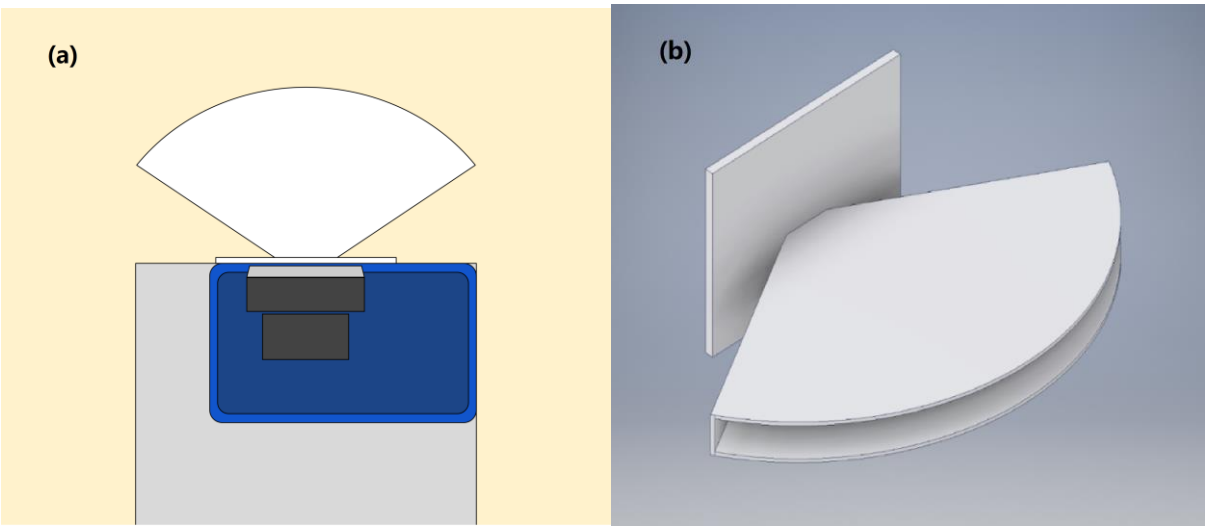

Figure 6.3 (a) A top-down diagram of the PM sensor inlet is shown. Note that the intake accessory covers the entire front of the robot, and that the fan is placed just behind the PM sensor. (b) The 3D model of the intake accessory to the PM sensor.

6.2.3 Sensor Module Case and Inlet Design

To diminish any possible interference caused by PM entering the sensor from behind, a case was designed and 3D printed to encase the sensor module. The case, as seen in Figure 6.1, is roughly shaped like a rectangular prism, with a vented lid covering the top. This allows for the fan to pull particles through the PM sensor inlet and subsequently remove them from around the sensor.

During pre-experimentation, a source of PM was placed in various positions surrounding the front of the AAQRL-ROBOPM. It was observed that the sensor could only sense the PM source when it was directly in front of its inlet; therefore, an intake accessory (shown in Figure 6.4) was designed and 3D printed to increase the PM collection radius to surround the whole front of the robot. With the accessory, sampling occurs more nearly along a line parallel to the front of the robot rather than at a single point directly in front of the sensor inlet. The edges of the wide-angle wedge-shaped accessory extend slightly beyond the sides of the robot frame, with the

farthest points on the wedge 137 millimeters apart. The accessory is 11 millimeters thick, with the mouth cavity occupying 9 millimeters of that thickness. It sits in front of the sensor on the case.

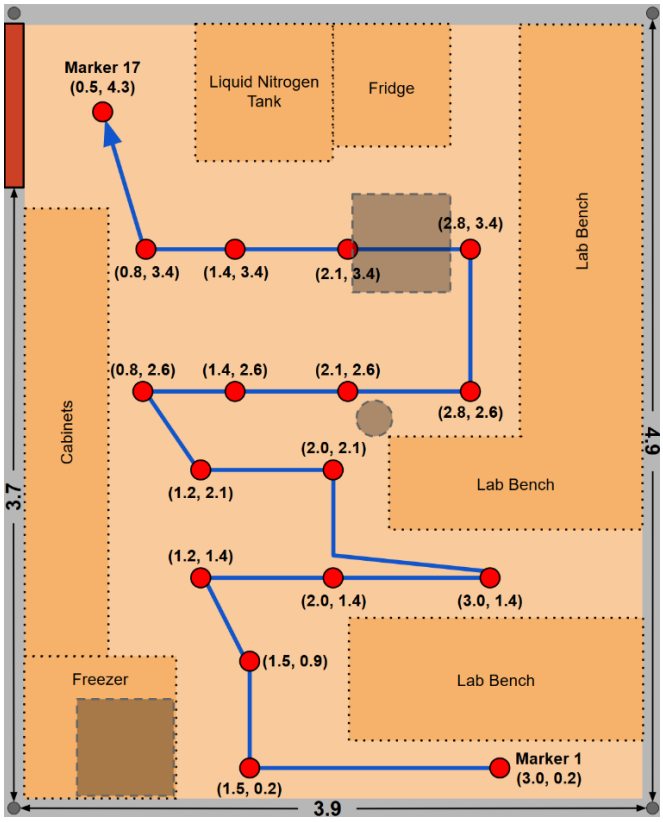

Figure 6.4 Floor print of room with 17 markers where the robot stopped and recorded PM concentrations. The transparent squares and circle with dashed borders represent the HVAC ports and ventilation port in the room, respectively.

6.2.4 Manual Control Mode Test

The manual control mode was tested in an indoor, controlled laboratory environment with a large initial base PM concentration of roughly 12 mg/m^3 being slowly reduced by normal operating ventilation. Multiple incense cones were lit in a room 4.9 meters long by 3.9 meters wide. After the incense cones had produced PM for 10 minutes, they were fully extinguished and removed

from the room, causing a decay over time of the base PM concentration. The particles gradually ventilated out of the room through a ceiling ventilation port and the HVAC system, and this decay was monitored for the following 20 minutes. To monitor the PM concentration distribution during the ventilation process, seventeen points on the open floor were selected as sampling locations, as shown in Figure 6.5.

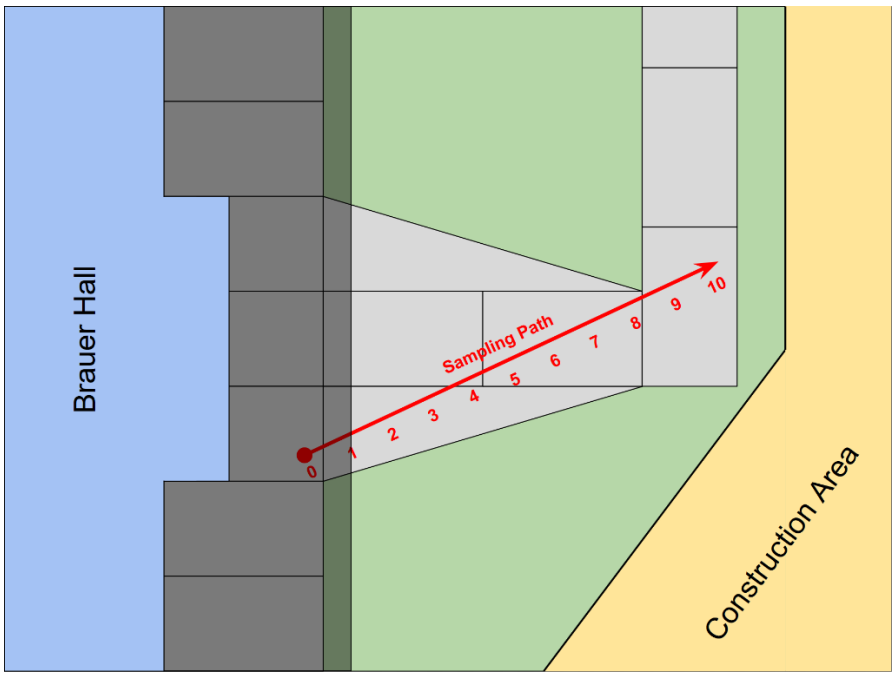

Figure 6.5 A top-down map of the area the straight autonomous mode was tested. The shaded area represents an area where the ground was covered by the building. The numbers on the sampling path represent the locations where the PM concentration was sampled, as well as the distance in meters away from the robot's starting position.

The robot was directed through the 17 points sequentially, as shown by the blue path. At each sampling location, the robot stopped, read the PM concentration from the sensor, and sent the measurement to the Android device. After the robot completed a measurement set, its position was manually reset to the first marker to begin the next measurement set. The time for the robot to sample all 17 locations was two minutes. We assumed that the PM concentration around the

sampling environment was relatively stable during the sampling process. To perform a real-time verification of the accuracy of the Sharp sensor PM measurements, a SidePak aerosol monitor was placed next to Marker 4 and set to take a PM measurement every second for real-time dynamic calibration. We consider the SidePak as a reference instrument in this experimentation due to its higher accuracy and reliability compared to low-cost sensors.

6.2.5 Straight Autonomous Mode Test

The straight autonomous mode was tested in an outdoor environment. Construction on the Danforth Campus of Washington University in Saint Louis created environmental PM for measurement by the robot. The robot was tested along a 10-meter stretch of pavement near the construction over a 20-minute period, sampling once every meter along the sampling path. The path led from the entrance to Brauer Hall to just outside the construction area, as shown in Figure 6.5.

6.2.6 Quadrant Algorithm Mode Test

The quadrant algorithm was tested in an unfinished laboratory, with a single incense cone used as a PM source. The incense was suspended above the ground such that the robot would not run into it during testing. Figure 6.6 shows an example of the quadrant algorithm being used. During each run, the robot conducted sampling at each corner of the square path, then repeated the process within the quadrant containing the highest PM concentration reading. The process repeated and the path size grew smaller until the path side length threshold was reached, at which point the robot would stop at the location it determined was the location of PM source.

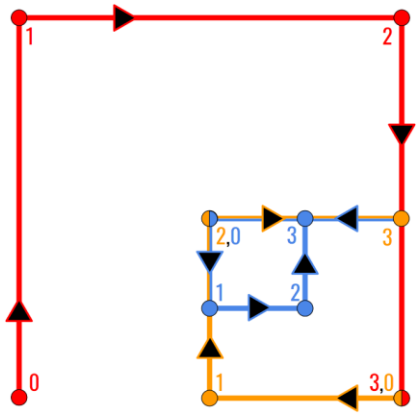

Figure 6.6 A drawing of a potential run of the quadrant algorithm. The number(s) at each point represent the order they were sampled at in. In this example, the robot finds that the highest PM concentrations are at the points labeled with the red 3, orange 2, and blue 3 in each colored quadrant. The PM source would be located near the blue 3, and the robot would stop there.

6.3 Results and discussion

6.3.1 AAQRL-ROBOPM Performance and Cost

The robot had satisfactory movement and handling when operated manually or autonomously. The robot stopped at all measurement locations and performed PM measurements as intended. All data packages sent between the Arduinos and between the robot and Android device were received. The robot could turn on a central axis in a 23.18 cm diameter circle, and could move forward at a maximum speed of 28.0 cm/s. In experiments, the speed of the robot was reduced to 11.0 cm/s for increased control and traction.

As Table 1 demonstrates, the overall cost of the robot was lower than solutions explored in other studies. The major components on the entire AAQRL-ROBOPM cost approximately $170, below the cost of a laboratory-grade PM sensor which could cost thousands of dollars with no mobile capabilities and only marginal increases in measurement accuracy.

Table 6.1 Cost of major components for the robot cart

Component	Quantity	Unit Cost	Cost
Arduino Nano ATmega328 Microprocessor	2	$3.20	$6.40
HiLetgo HC-06 Bluetooth Module	1	$6.99	$6.99
Qunqi L298N Motor Drive Controller	1	$6.99	$6.99
Sharp Optical Dust Sensor - GP2Y1010AU0F	1	$11.95	$11.95
Tenergy 12V 2000mAh NiMH Rechargeable Battery	1	$23.92	$23.92
Tenergy 6V 2000mAh NiMH Rechargeable Battery	1	$10.99	$10.99
F310R-05LLC 5VDC Wired Fan	1	$7.85	$7.85
VEX Motor 393	2	$14.99	$29.98
VEX Integrated Encoder Module	2	$15.00	$30.00
VEX 5x15 Aluminum Plate	2	$2.50	$5.00
VEX 2x2x15 Aluminum Angle	2	$5.00	$10.00
VEX 2.75” Wheel	2	$2.50	$5.00
VEX 2.75” Omni-Directional Wheel	1	$10.00	$10.00
Miscellaneous (tape, nuts and bolts, etc.)	-	$2.00	$2.00
Total Cost			**$167.07**

6.3.2 Manual Control Test Results

The data from both the SidePak and Sharp sensor at Marker 4 (Figure 6.4) were plotted in Figure 6.7, SidePak vs. Robot PM Measurements, to show a real-time correlation. Because the AAQRL-ROBOPM conducts PM measurement at Marker 4 only once per measurement set, the time duration between measurements is two minutes. Figure 6.7 demonstrates that the raw voltage data from the Sharp sensor has a strong correlation with the SidePak data throughout the experimentation period. Therefore, not only can the Sharp sensor data be verified, but its output voltages can also be fitted to the equation produced by the correlation, providing an accurate conversion method to PM concentrations. The SidePak conducts optical measurements, and this optical-to-optical comparison is better for verifying the Sharp sensor than comparison with other types of federal equivalent method measurements.

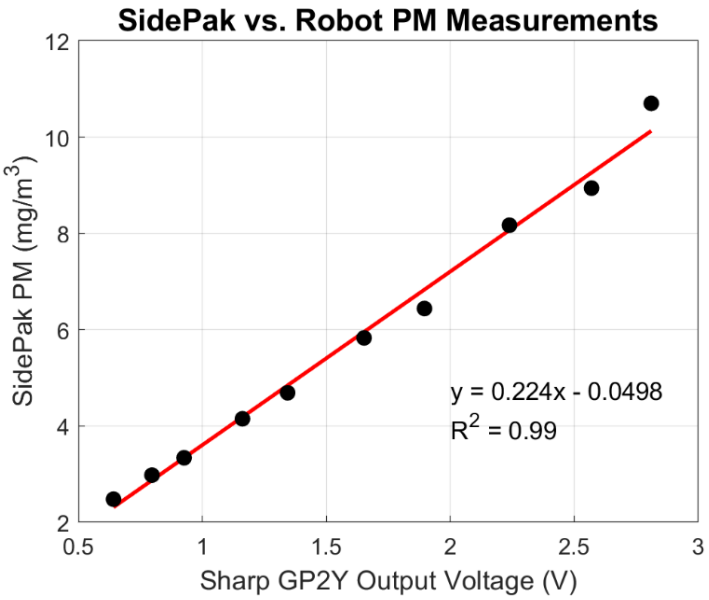

Figure 6.7 The correlation between the Sharp sensor and the SidePak was strong ($R^2 = 0.99$).

The data collected by the robot was interpolated to produce PM spatiotemporal distribution maps, shown and discussed in Figure 6.8. Boundaries were defined where walls or other obstacles stood in the way of the robot's movement across the floor. PM concentrations were set to zero at these boundaries to improve the accuracy of the PM maps. Interpolation of measurement locations and boundary layers was used to generate PM concentrations at locations that were not measured at, as in Li et al. (2018). The incense cones generated many particles, increasing the PM concentrations throughout the whole room. Once the incense cones were removed from the room, the particles ventilated out of the room, causing a decrease in base PM concentration over the next 20 minutes. The PM concentration gradient surrounding the ventilation ports suggests there are local PM hotspots underneath the ventilation ports.

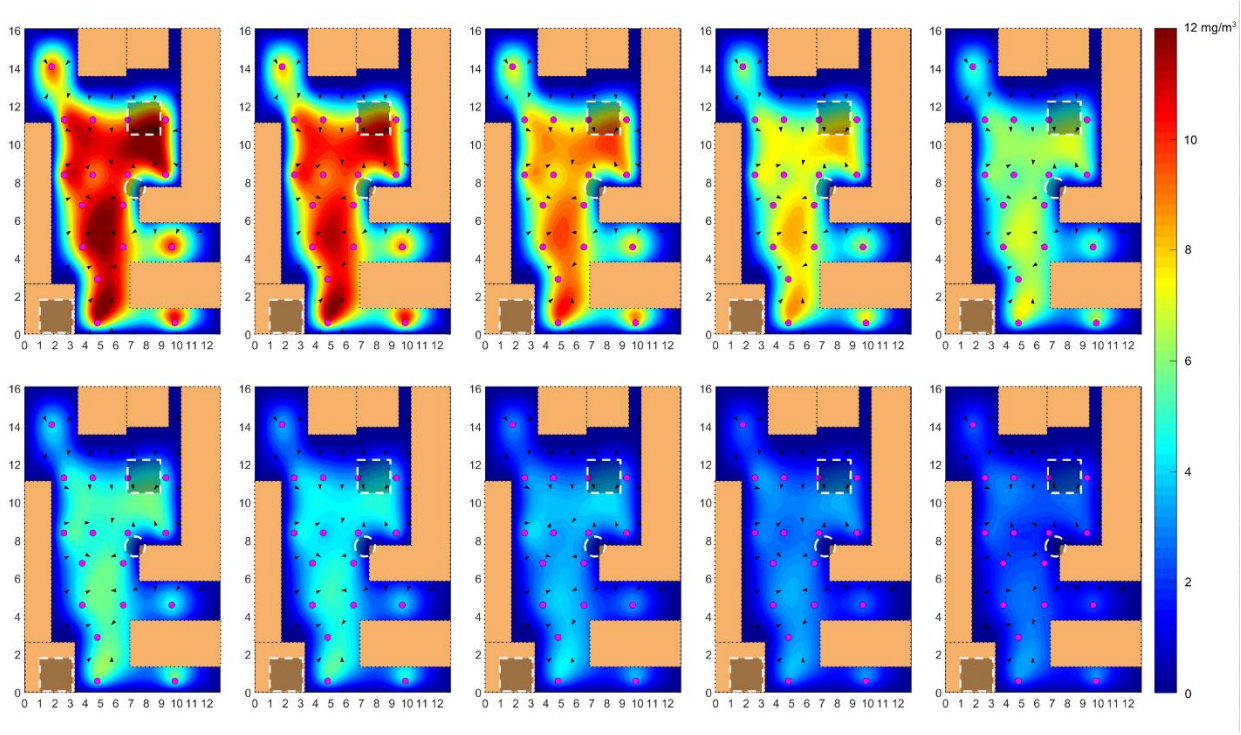

Figure 6.8 Spatial distribution maps of PM concentrations from the manual control mode experiment. The 17 markers in the room are each represented by a magenta point. After the 17th marker in each measurement set was sampled, the robot was moved back to the first marker and the next set of measurements were started. Since each measurement set took two minutes, the PM concentration values shown at the same marker in two different measurement sets are also two minutes apart. By the tenth measurement set (bottom-right), PM concentrations had returned to pre-experimentation values.

According to the interpolation results in Figure 6.8, the PM spatiotemporal concentration variance within the room is large, so measurement at a single position is not sufficient to represent the PM concentration distribution in the room. Because the robot cart took some time to move between markers, the results from each run cannot be compared by a gradient map using the absolute concentrations at each point. Rather, a contour plot overlaid with a quiver plot was created to demonstrate the relative concentration at many locations based on an inverse distance relationship. The further away a marker is from a point being considered, the less weight that marker carries on the estimated PM concentration magnitude and direction of the quiver plot

vector at that point. The results show that PM gathered underneath the three ventilation ports, and that some stagnation of air flow was present near Markers 1, 6, and 17. The 17 markers in the room are each represented by a magenta point. After the 17th marker in each measurement set was sampled, the robot was moved back to the first marker and the next set of measurements were started. Since each measurement set took approximately two minutes, the PM concentration values shown at the same marker in two different measurement sets are also approximately two minutes apart. By the tenth measurement set (bottom-right), the generated PM had been mostly ventilated.

6.3.3 Straight Autonomous Test Results

Results from the straight autonomous mode testing show a development of PM hotspots over time as construction near the testing site began to produce PM. Figure 6.9 demonstrates a gradual increase in base PM levels as well as a development of PM hotspots as the experiment proceeds. PM production from the nearby construction site began at 2:52PM, just before the fourth test was started. As shown by the gradient for each test, PM hotspots became evident at three and eight meters away from the starting position of the AAQRL-ROBOPM.

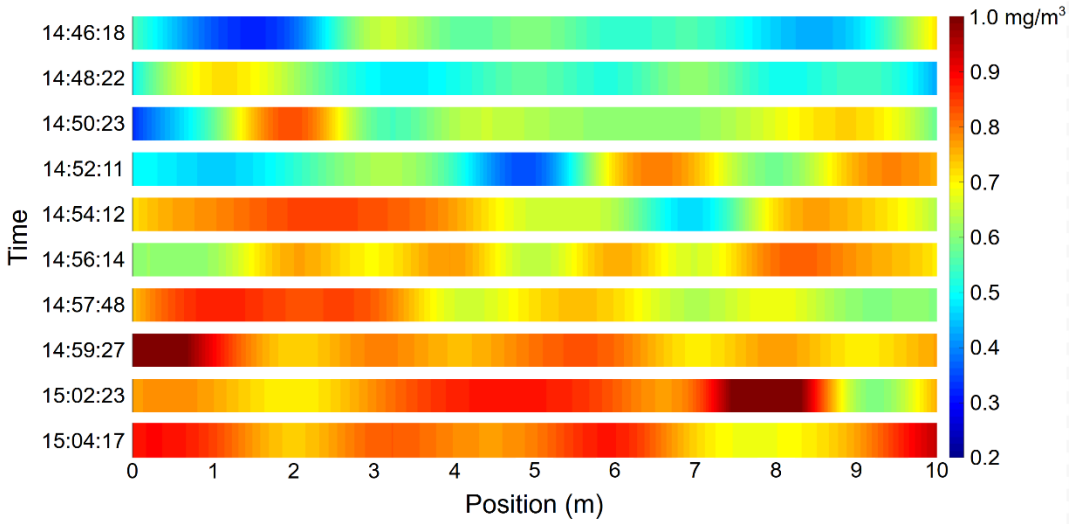

Figure 6.9 Data from all ten tests, mapped and shown top to bottom chronologically. The time the test started is shown to the left of each map. Once PM production from construction started around the fourth test, hotspots developed at approximately three and eight meters away from the starting position.

6.3.4 Quadrant Algorithm Test Results

The robot was always able to properly execute the quadrant algorithm, regardless of initial position, orientation, or loop size. Square loops with side lengths of 0.6 m, 1.2 m, and 1.8 m were each tested four times, with the robot at a different point on the initial square path in each test. However, the robot could not make precise 90 degree turns in every instance, leading to a gradual drift from the initial square path in some tests. This is due to the manufacturing tolerances of the VEX motors, which allows about a $1/16^{th}$ rotation of the wheel where the shaft freely spins within the motor. With a more tightly fitting shaft, this free rotation could be eliminated, resulting in more precise movement, particularly turning. Another concern is the requirement of a stable source of PM for accurate location of the PM source. The robot's maximum speed would become a more significant factor as loop size was increased, as the robot would take a much longer time to locate the PM source.

6.4 Conclusions

This study extends work published about low cost-PM sensors in mapping concentration, as well as the development of mobile sensor modules on buggies, drones, and other robotic implementations. An affordable, programmable, and agile mobile sensor module, AAQRL-ROBOPM, presented here was demonstrated to conduct PM concentration sampling by either manual or autonomous control, and can also autonomously find a PM hotspot using basic artificial intelligence routines. During manual scanning of PM concentrations, the path of the robot can be changed instantaneously via commands from the Android device, and the PM concentrations at various locations in the sampling area are reported in real-time. With the recorded spatial distribution, hotspots can be identified, which can be useful for determining potential static sensor locations. For instance, placing static sensors where they will be most effective can greatly reduce the cost and complexity of sensor networks for long-term PM monitoring. Using the straight autonomous mode, the robot can conduct routine sampling in a region over long periods of time without any human supervision. However, the capacity of the power supply, surrounding terrain, atmospheric conditions, and weather must be considered for such long-term autonomous measurement. Although the quadrant algorithm was able to correctly identify the location of the PM source in every test, improvements like obstacle detection and collision prevention could be made to the robot to improve the algorithm's effectiveness and reduce necessary human interaction with the robot and testing environment.

Due to its flexibility, the AAQRL-ROBOPM can determine the optimal locations for static PM sensors even in environments with unknown PM sources and unknown PM distributions. The ability to conduct a pre-scan and develop instructions for static sensor deployment using a mobile sensor makes them a valuable asset when attempting to gather accurate information using

the lowest number of sensors possible. However, the system also has some limitations. The AAQRL-ROBOPM measures PM concentrations at only a few inches above the ground, not at breathing height. In addition, the AAQRL-ROBOPM cannot traverse rugged terrain, and has only basic intelligence and data analysis capability. A future version of the AAQRL-ROBOPM is expected to include a function to adjust the height of the PM sensor to estimate exposure for humans of different heights, as well as usability in various landscapes. It is also expected to have more advanced and precise algorithms that will diminish and eliminate the need of human monitoring. Expected improvements to the AAQRL-ROBOPM include real-time PM concentration mapping, sampling across multiple heights, and greater sampling and movement speed.

Further development of such a low-cost mobile PM sensor module has exciting possibilities. For example, the sensor module could be retrofitted onto flying drones or cars to conduct PM sampling and hotspot detection in much larger indoor and outdoor environments. However, the effects on sensor readings due to turbulence from movement of such mobile platforms would need to be addressed. Public transportation such as buses and trains could be specifically targeted to identify stops along their routes where PM concentrations are stable at a high level. Bus stops and train stations where hotspots were identified could be retrofitted with static sensors to create PM concentration gradient maps of entire cities.

6.5 References

Brook, R. D., Rajagopalan, S., Pope, C. A., Brook, J. R., Bhatnagar, A., Diez-Roux, A. V., Holguin, F., Hong, Y., Luepker, R. V., and Mittleman, M. A. (2010). "Particulate matter air pollution and cardiovascular disease." *Circulation*, 121(21), 2331-2378.

Burnett, R. T., Pope, C. A., 3rd, Ezzati, M., Olives, C., Lim, S. S., Mehta, S., Shin, H. H., Singh, G., Hubbell, B., Brauer, M., Anderson, H. R., Smith, K. R., Balmes, J. R., Bruce, N. G., Kan, H., Laden, F., Pruss-Ustun, A., Turner, M. C., Gapstur, S. M., Diver, W. R., and Cohen, A. (2014). "An integrated risk function for estimating the global burden of disease attributable to ambient fine particulate matter exposure." *Environ Health Perspect*, 122(4), 397-403.

Chen, Y., Anderson, G., Mahdi, S., Khidir, J., and Wilson, E. "A proposed robotic air quality monitoring system." *Proc., World Automation Congress (WAC), 2012*, IEEE, 1-5.

Cohen, A. J., Ross Anderson, H., Ostro, B., Pandey, K. D., Krzyzanowski, M., Künzli, N., Gutschmidt, K., Pope, A., Romieu, I., and Samet, J. M. (2005). "The global burden of disease due to outdoor air pollution." *Journal of Toxicology and Environmental Health, Part A*, 68(13-14), 1301-1307.

Dunbabin, M., and Marques, L. (2012). "Robots for environmental monitoring: Significant advancements and applications." *IEEE Robotics & Automation Magazine*, 19(1), 24-39.

Ferri, G., Mondini, A., Manzi, A., Mazzolai, B., Laschi, C., Mattoli, V., Reggente, M., Stoyanov, T., Lilienthal, A., and Lettere, M. "DustCart, a mobile robot for urban environments: Experiments of pollution monitoring and mapping during autonomous navigation in urban scenarios." *Proc., Proceedings of the IEEE International Conference on Robotics and Automation (ICRA 2010) Workshop on Networked and Mobile Robot Olfaction in Natural, Dynamic Environments*.

Ferro, A. R., Kopperud, R. J., and Hildemann, L. M. (2004). "Source strengths for indoor human activities that resuspend particulate matter." *Environmental science & technology*, 38(6), 1759-1764.

Guarnieri, M., and Balmes, J. R. (2014). "Outdoor air pollution and asthma." *Lancet*, 383(9928), 1581-1592.

Hamra, G. B., Guha, N., Cohen, A., Laden, F., Raaschou-Nielsen, O., Samet, J. M., Vineis, P., Forastiere, F., Saldiva, P., and Yorifuji, T. (2014). "Outdoor particulate matter exposure and lung cancer: a systematic review and meta-analysis." *Environmental health perspectives*, 122(9), 906.

Holstius, D. M., Pillarisetti, A., Smith, K., and Seto, E. (2014). "Field calibrations of a low-cost aerosol sensor at a regulatory monitoring site in California." *Atmospheric Measurement Techniques*, 7(4), 1121-1131.

Ivanov, B., Zhelondz, O., Borodulkin, L., and Ruser, H. "Distributed smart sensor system for indoor climate monitoring." *Proc., KONNEX Scientific Conf., Mnchen*, 10-11.

Kelleher, S., Quinn, C., Miller-Lionberg, D., and Volckens, J. (2018). "A low-cost particulate matter (PM2.5) monitor for wildland fire smoke." *Atmospheric Measurement Techniques*, 11(2), 1087-1097.

Kelly, K., Whitaker, J., Petty, A., Widmer, C., Dybwad, A., Sleeth, D., Martin, R., and Butterfield, A. (2017). "Ambient and laboratory evaluation of a low-cost particulate matter sensor." *Environmental Pollution*, 221, 491-500.

Kim, J.-Y., Chu, C.-H., and Shin, S.-M. (2014). "ISSAQ: An integrated sensing systems for real-time indoor air quality monitoring." *IEEE Sensors Journal*, 14(12), 4230-4244.
Leavey, A., Fu, Y., Sha, M., Kutta, A., Lu, C., Wang, W., Drake, B., Chen, Y., and Biswas, P. (2015). "Air quality metrics and wireless technology to maximize the energy efficiency of HVAC in a working auditorium." *Building and Environment*, 85, 287-297.
Li, J., and Biswas, P. (2017). "Optical Characterization Studies of a Low-Cost Particle Sensor." *Aerosol and Air Quality Research*, 17(7), 1691-1704.
Li, J., Li, H., Ma, Y., Wang, Y., Abokifa, A. A., Lu, C., and Biswas, P. (2018). "Spatiotemporal distribution of indoor particulate matter concentration with a low-cost sensor network." *Building and Environment*, 127, 138-147.
Ling, S. H., and van Eeden, S. F. (2009). "Particulate matter air pollution exposure: role in the development and exacerbation of chronic obstructive pulmonary disease." *Int J Chron Obstruct Pulmon Dis*, 4, 233-243.
Löfroth, G., Stensman, C., and Brandhorst-Satzkorn, M. (1991). "Indoor sources of mutagenic aerosol particulate matter: smoking, cooking and incense burning." *Mutation Research/Genetic Toxicology*, 261(1), 21-28.
Manikonda, A., Zíková, N., Hopke, P. K., and Ferro, A. R. (2016). "Laboratory assessment of low-cost PM monitors." *Journal of Aerosol Science*, 102, 29-40.
Patashnick, H., and Rupprecht, E. G. (1991). "Continuous PM-10 measurements using the tapered element oscillating microbalance." *Journal of the Air & Waste Management Association*, 41(8), 1079-1083.
Patel, S., Li, J., Pandey, A., Pervez, S., Chakrabarty, R. K., and Biswas, P. (2017). "Spatio-temporal measurement of indoor particulate matter concentrations using a wireless network of low-cost sensors in households using solid fuels." *Environmental research*, 152, 59-65.
Rajasegarar, S., Zhang, P., Zhou, Y., Karunasekera, S., Leckie, C., and Palaniswami, M. "High resolution spatio-temporal monitoring of air pollutants using wireless sensor networks." *Proc., Intelligent Sensors, Sensor Networks and Information Processing (ISSNIP), 2014 IEEE Ninth International Conference on*, IEEE, 1-6.
Reggente, M., and Lilienthal, A. J. "Using local wind information for gas distribution mapping in outdoor environments with a mobile robot." *Proc., Sensors, 2009 IEEE*, IEEE, 1715-1720.
Shah, A. S. V., Langrish, J. P., Nair, H., McAllister, D. A., Hunter, A. L., Donaldson, K., Newby, D. E., and Mills, N. L. (2013). "Global association of air pollution and heart failure: a systematic review and meta-analysis." *Lancet*, 382(9897), 1039-1048.
Shi, J., Cai, Y., Fan, S., Cai, J., Chen, R., Kan, H., Lu, Y., and Zhao, Z. (2017). "Validation of a light-scattering PM2. 5 sensor monitor based on the long-term gravimetric measurements in field tests." *PloS one*, 12(11), e0185700.
Smith, K. R. (1993). "Fuel combustion, air pollution exposure, and health: the situation in developing countries." *Annual Review of Energy and the Environment*, 18(1), 529-566.
Sousan, S., Gray, A., Zuidema, C., Stebounova, L., Thomas, G., Koehler, K., and Peters, T. (2018). "Sensor Selection to Improve Estimates of Particulate Matter Concentration from a Low-Cost Network." *Sensors-Basel*, 18(9).
Sousan, S., Koehler, K., Hallett, L., and Peters, T. M. (2017). "Evaluation of consumer monitors to measure particulate matter." *Journal of Aerosol Science*, 107, 123-133.
Sousan, S., Koehler, K., Thomas, G., Park, J. H., Hillman, M., Halterman, A., and Peters, T. M. (2016). "Inter-comparison of low-cost sensors for measuring the mass concentration of occupational aerosols." *Aerosol Science and Technology*, 50(5), 462-473.

Strak, M., Janssen, N. A. H., Godri, K. J., Gosens, I., Mudway, I. S., Cassee, F. R., Lebret, E., Kelly, F. J., Harrison, R. M., Brunekreef, B., Steenhof, M., and Hoek, G. (2012). "Respiratory Health Effects of Airborne Particulate Matter: The Role of Particle Size, Composition, and Oxidative Potential-The RAPTES Project." *Environmental Health Perspectives*, 120(8), 1183-1189.

Trincavelli, M., Reggente, M., Coradeschi, S., Loutfi, A., Ishida, H., and Lilienthal, A. J. "Towards environmental monitoring with mobile robots." *Proc., Intelligent Robots and Systems, 2008. IROS 2008. IEEE/RSJ International Conference on*, IEEE, 2210-2215.

Viana, M., Kuhlbusch, T., Querol, X., Alastuey, A., Harrison, R., Hopke, P., Winiwarter, W., Vallius, M., Szidat, S., and Prévôt, A. (2008). "Source apportionment of particulate matter in Europe: a review of methods and results." *Journal of aerosol science*, 39(10), 827-849.

Wang, Y., Li, J., Jing, H., Zhang, Q., Jiang, J., and Biswas, P. (2015). "Laboratory evaluation and calibration of three low-cost particle sensors for particulate matter measurement." *Aerosol Science and Technology*, 49(11), 1063-1077.

Zikova, N., Hopke, P. K., and Ferro, A. R. (2017). "Evaluation of new low-cost particle monitors for PM 2.5 concentrations measurements." *Journal of Aerosol Science*, 105, 24-34.

Chapter 7: Spatiotemporal Distribution of Indoor Particulate Matter Concentration with a Low-cost Sensor Network

The results of this chapter have been published in Li, J., Li, H., Ma, Y., Wang, Y., Abokifa, A. A., Lu, C., & Biswas, P. (2018). Spatiotemporal distribution of indoor particulate matter concentration with a low-cost sensor network. Building and Environment, 127, 138-147.

Abstract

Real-time measurement of particulate matter (PM) is important for the maintenance of acceptable air quality. The high cost of conventional instruments typically limits the number of monitoring sites, which in turn undermines the accuracy of real-time mapping of sources and hotspots of air pollutants with sufficient spatial resolution. In this study, a wireless network of low-cost particle sensors that can be deployed indoors was developed. To overcome the well-known limitations of low sensitivity and poor signal quality associated with low-cost sensors, a sliding window and a low pass filter were developed to enhance the signal quality. Utility of the networked system with improved sensitivity was demonstrated by deploying it in a woodworking shop. Data collected by the networked system was utilized to construct spatiotemporal PM concentration distributions using an ordinary Kriging method and an Artificial Neural Network model to elucidate particle generation and ventilation processes.

7.1 Introduction

Particulate matter (PM) is a routinely monitored air pollutant in outdoor and indoor environments [1-3]. High $PM_{2.5}$ exposure levels tend to trigger cardiovascular disease and mortality via various mechanisms including pulmonary and systemic inflammation, accelerated atherosclerosis, and altered cardiac autonomic function [4, 5]. Worldwide, outdoor $PM_{2.5}$ pollution accounts for 6.4 million deaths annually [6]. Indoor PM, carrying allergens and endotoxins, may exacerbate asthmatic symptoms [7]. Due to these adverse health effects, many countries have enacted regulations in an effort to lower PM concentrations, and regulatory agencies commonly require long-term measurements to monitor air quality [8, 9]. The designated US Environmental Protection Agency (US EPA) federal reference method (FRM), gravimetric sampling, measures PM mass concentration by collecting the particles on a filter for a set time in a high-volume air sampler [10-12]. There are around hundreds of monitoring sites across the country that provide the daily concentrations of total suspended particles (TSP), PM_{10}, and $PM_{2.5}$. Using these data to generate a spatiotemporal distribution map showing how the pollutants vary with location and time aids exposure assessment and health effect studies. To generate the spatiotemporal distribution on the basis of limited data from scattered monitoring sites, researchers need to predict the pollutant concentration at unsampled locations.

Geostatistical interpolation and land use regression (LUR) are common methods to predict the spatiotemporal distribution in outdoor atmospheric studies. Geostatistical interpolation (also called spatial interpolation) characterizes the relationship between pollutant concentrations and their locations, and utilizes the relationship to predict the pointwise pollution concentration. There are four general *weighted average* algorithms for geostatistical interpolation: spatial averaging, nearest neighbor, inverse distance weighting, and Kriging [13]. Among the four

algorithms, since Kriging produces the best linear unbiased estimate of the pollution surface [14], it has become the most widely used algorithm for predicting air pollution distribution [15]. Using Kriging, Jerrett et al. [16] interpolated the $PM_{2.5}$ concentrations from 42 monitoring sites and demonstrated that these concentrations are relevant to ischemic heart disease. Kriged ozone concentrations have been used for monthly exposure assessment in the southeastern United States [17], and have been applied to correlate exposure with pediatric asthma presentation rates [18]. LUR, the other predictive method, associates pollution data with multiple variables, including the wind field, traffic count, land use, population, and emissions [19]. LUR has been used to predict the PM concentration distributions across New York City and Los Angeles [20, 21]. Neither of these predictive methods consistently outperformed the other. The distributions they predicted may vary according to their principles [13, 22]. Furthermore, the scattered monitoring sites limit the resolution and the accuracy of the spatiotemporal distribution map, which will further undermine the confidence of the spatiotemporal distribution.

Recently, advances in the low-cost particle sensor techniques have altered the conventional data collecting and data mining processes. Conventional gravimetric sampling is off-line and laborious, whereas low-cost particle sensors offer adequate accuracy, are compact, and require only modest maintenance. The networking capability of particle sensors enhances the possibility of wider application. Laboratory evaluations have demonstrated that low-cost particle sensors operate with high linear correlation to standard commercial instruments for fixed PM sources [23-25]. In combination with other sensors and wireless communication chips, low-cost particle sensors can be networked to collect air quality data efficiently and conveniently. The data mining process of the networked low-cost particle sensor is a trending topic. By distributing 8000 low-cost iSPEX (a smart phone add-on) sensors across Netherlands, Snik et al. [26]

obtained a map of aerosol optical thickness with higher spatial resolution than conventional maps generated by the satellite. In a similar study, Shinyei PPD sensors were deployed in Xi'an, China, to determine the spatiotemporal variations of $PM_{2.5}$ [27]. However, one shortcoming of low-cost particle sensors is their low signal to noise ratio, which allows accurate measurements only under higher concentration scenarios or after long periods of averaging to increase data quality. To eliminate high-frequency noise and to accurately represent the measurement data, digital filters were added to the sensor system. Common digital filters include sliding window filter, low-pass filter (e.g. finite impulse response (FIR) filter and fast Fourier transform (FFT) filter), and model-based filter (e.g. Kalman filter) [28-30]. The advantages of sliding window filter and low-pass filter are model-independent, light computational weight, and specifically tailored for filtering high frequency noises [28, 31].

In addition to the conventional geostatistical models, such as ordinary kriging, machine-learning techniques were also previously used for the spatial interpolation of environmental variables as a cost-effective method where monitoring resources are limited [32, 33]. For example, Chowdhury et al. [34] implemented Artificial Neural Networks (ANNs) for the spatial mapping of complex patterns of groundwater arsenic levels based on sampling data at finite locations. They demonstrated that the use of non-linear pattern learning techniques, such as ANNs, could yield more accurate results than the ordinary Kriging method. Antonic et al. [35] used neural networks to build empirical spatio-temporal models for various climatic variables such as temperature, relative humidity, precipitation, solar irradiation, and evapotranspiration. In addition, ANN models were used to forecast outdoor particulate matter concentrations such as PM_{10} and $PM_{2.5}$ [36, 37].

Apart from atmospheric measurements, low-cost particle sensors can perform multi-point indoor measurements. Indoor air quality, referring to PM concentrations and trace gas concentrations, is critical to human health, since a human being spends on average approximately 88% of their time inside buildings [38-43]. The application of low-cost sensors and their networks enables sampling PM and trace gas under various scenarios [44-47]. Generally, the exposure level estimated from indoor or personal low-cost sensors is more accurate than the Kriging or LUR predicted values from scattered fixed monitoring sites. Compared to outdoor field measurements, indoor measurements are usually limited by confined space and room arrangements. It is common to neglect the indoor spatiotemporal distribution and use a single-point measurement to represent the whole room, which introduces errors to exposure intake estimation [48]. The sensors' low price and the compact size allow deploying multiple sampling points in households, which is very helpful for understanding ventilation process and monitoring occupancy [49-51]. However, very few studies using networked sensor systems reported the dynamic evolution of the particle concentrations as a function of location and time. Rajasegarar et al. [52] conducted one of such studies that reported the PM concentration distribution mapped by networked low-cost particle sensors in a garage. Patel et al. [49] deployed low-cost particle sensors in a household to monitor the transport of particles produced from biomass burning. Leavey et al. [53] implemented several wireless PM sensors, gas sensors, and temperature sensors in an auditorium room and analyzed the energy consumption of different operation modes. However, neither of these studies reported the spatial evolution of the PM concentration.

The focus of indoor air quality mapping should be different from that of outdoor atmospheric studies. The scale of an atmospheric study is obviously large, possibly also ranging from county to country in scale, while indoor measurements are confined to several hundreds or thousands of

square feet. Due to these space limitations, indoor measurements usually involve fewer than ten sampling locations, but the density (sampling locations/unit area) is high. In addition, there are no boundary conditions for atmospheric measurements, but the PM concentrations at the boundaries of a room should be zero, since it is a confined space and particles are scavenged at the wall. Additional variables (e.g., traffic and land use) that can be incorporated in atmospheric measurements are inapplicable for indoor sampling. Furthermore, in Kriging and the LUR method, the PM concentration distributions are considered steady and stable, hence yearly-average concentrations are commonly used as inputs. For indoor measurements, capturing instant emission events is of major interest. In general, spatially depicting the dynamic evolution of the PM concentration with a limited number of sensors in a confined space is the goal of deploying low-cost sensors for indoor measurements.

In this study, a networked wireless particle sensor system coupled with a sliding window filter and a low pass filter to enhance the sample quality by increasing the signal to noise ratio, while preserving the time resolution is presented. After calibrating the networked wireless sensor system, its use is demonstrated by conducting spatiotemporal measurements in a student woodworking shop to identify PM concentration hotspots. Kriging interpolation and artificial neural network (ANN) methods are used, and the pros and cons of each are compared. The total exposure to PM of woodworkers is estimated from calculations based on the predicted spatiotemporal PM concentration distribution.

7.2 Materials and Methods

The networked wireless sensor system consists of multiple end devices to monitor the PM concentration, and a base station that receives the data from the sensors for further processing. For each end device, a Sharp GP2Y1010AU0F (GP2Y, Sharp Corp., Osaka, Japan) PM sensor, an Arduino Nano ATmega328 (Arduino, Arduino Inc., S.R.L, Italy), and an XBee radio (Digi International Inc., Minnetonka, MN) were mounted on a printed circuit board. The base station that collects and translates the data package sent from the end devices integrates a Raspberry Pi 2 embedded computer (Adafruit Industries., New York City, NY) and an XBee radio. The system and the major components are shown in Figure 7.1.

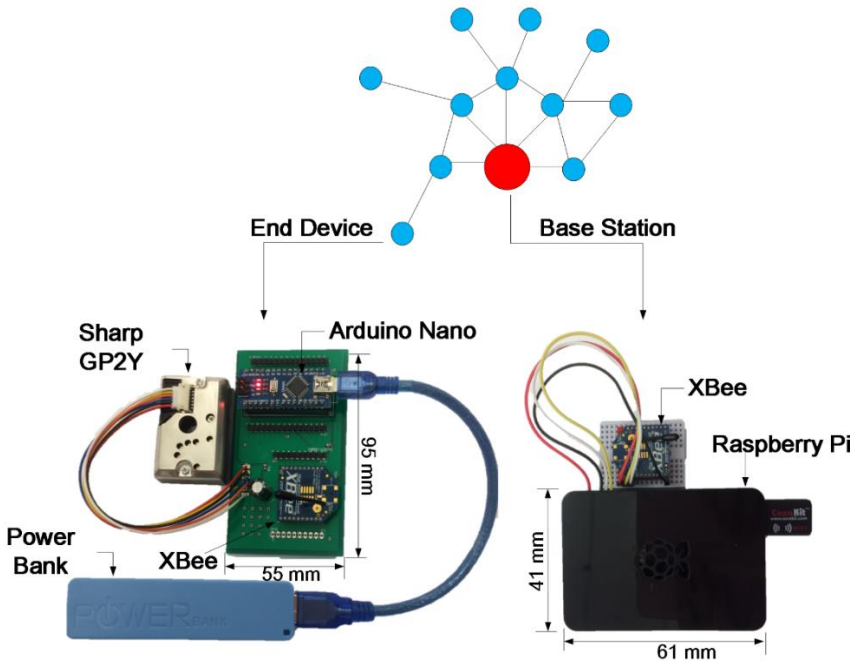

Figure 7.1 Network arrangement of the end devices and base station. The end device contains a Sharp GP2Y, an Arduino, an XBee, and a power bank; the base station contains a Raspberry Pi and an XBee to receive the signal sent from the end devices.

7.2.1 Major components

The Sharp GP2Y measures a scattered light signal that is correlated with aerosol concentration. When the infrared emitting diode inside the Sharp GP2Y is powered with a square wave voltage with a 32 ms pulse width, the particles passing through the testing location are illuminated and the light is reflected towards a phototransistor. The light is reflected or scattered more at higher aerosol concentrations since more particles alter the path of light. The infrared-sensitive phototransistor converts the scattered light intensity into a voltage signal. An earlier study [23] showered that the Sharp GP2Y demonstrates the highest linearity against commercialized instruments among the low-cost particle sensors tested, and is stable under humidity and temperature fluctuation.

The Arduino chip works as a controller to manage the sequential order and information flow inside the end (sensor) devices. It provides the square wave voltage to power the emitting diode in the Sharp GP2Y and samples the resultant fully developed voltage signal from the phototransistor 28 ms after the leading edge of the square wave has passed. After digitally recording the voltage amplitude signal, the Arduino constructs a data package with voltage amplitude information, then forwards it to the XBee wireless transmitter. All of the XBees on the end devices in the network operate in router mode, relaying the package to the base station for further processing.

The base station is a Raspberry Pi 2 embedded computer connected with an XBee radio. Upon receiving a package from an end device, the base station tags the data with a time stamp, an 8-bit node identification, and an 8-bit package serial number before pushing the new data object into a buffer. A data processing routine periodically processes all the data objects in the buffer and clears the buffer for new packages. The processed data objects at the base station can be

uploaded to a server or website for real-time access. The network is easy to set up, and the cost is around $40 for each end device, which is lower in comparison to conventional instruments (e.g. SidePak for around $3000) for real-time PM monitoring.

7.2.2 Digital filter

As mentioned above, the application of low-cost sensors is hindered by their low signal to noise ratio. The noise increases the limit of detection since the small response to a low concentration will be buried under the noise. In order to lower the limit of detection and to preserve high temporal resolution, an online sliding window filter and a low pass digital filter are incorporated in the system. The sliding window filter can eliminate the fluctuations by averaging the results over time; however, this approach sacrifices the time resolution. The equations for both off-line Eq. (7.1) and online Eq. (7.2) sliding window filters are shown below, where k is the time slot, w is the size of the window, and $S_i(j)$ represents the PM concentration value from sensor i at time j.

$$value_{i,j} = \frac{\sum_{j=k-\frac{w}{2}}^{k+\frac{w}{2}} S_i(j)}{w} \tag{7.1}$$

$$value_{i,j} = \frac{\sum_{j=k-w}^{k} S_i(j)}{w} \tag{7.2}$$

For an off-line sliding window filter, time j is put at the center of the window, and the data received during the window-sized interval is averaged to represent the value at time j. However, using an on-line sliding window filter, we do not have data after the current time to calculate the

average of the window, so a window-size data set before the current time is selected as the trailing average for calculation. In this study, the sampling interval is 0.25 second and a one second window-size filter is applied for data smoothing. The digital online sliding window filter is integrated into the Arduino program, and the processed data is used for the online real-time display.

To further process the data from the base station, a low pass filter is applied to attenuate the background noise and to lower the limit of detection. The noise fluctuates at a higher frequency than the signal, so it can be separated accordingly. The data is processed with a 29^{th} order finite-duration impulse response (FIR) low pass digital filter in Matlab *fir1*(n, ω_n) with a 0.04 Hz cut-off frequency, and the one second resolution is preserved [28, 54]. Normally, a low pass filter is closer to an ideal filter when operating at higher order, at the expense of a longer implementation time. The cut-off frequency sets the threshold for distinguishing between noise and signal. Using the processed data, our low-cost sensors were calibrated against a SidePak (AM510, TSI Inc., Minneapolis, MN) in a cubical chamber with controlled air flow air-tight to correlate their output signals with SidePak equivalent PM concentrations in prior research [23].

7.2.3 Sensor calibration

The method for sensor calibration was similar to that in Wang et al. [23], which can be summarized as follows. An incense stick that was the source of PM was set at the center of the chamber, and the SidePak and sensors were close to each other around the center of the chamber to measure the generated aerosol in one-second intervals. Eight sensors were divided into two batches for calibration to keep the positions of sensors and Sidepak symmetrical and close to the

center. Four small circulating fans were installed at the bottom four corners to obtain a well-mixed uniformed concentration distribution inside the chamber. Although linear fitting has been recommended for the Sharp GP2Y in former studies, the differences between the 1st to the 5th degrees of polynomial fitting were examined with the least squares method as given in Eq. (7.3) and Eq. (7.4).

$$y_{n,i,j} = p_{i,1}x_{i,j}^{n} + p_{i,2}x_{i,j}^{n-1} + \Lambda + p_{i,n}x_{i,j} + p_{i,n+1}, \quad n = 1,2,3,4,5 \tag{7.3}$$

$$S_i = \sum_{j=1}^{N} (y_{sidepak,j} - y_{n,i,j})^2 \tag{7.4}$$

where n is the degree of the polynomial fitting, and $x_{i,j}$ and $y_{n,i,j}$ represent the smoothed data and the calibrated PM concentration with the n^{th} order at time j for sensor i. S_i is the summation of the square of the PM concentration difference between the SidePak and the calibrated GP2Y over the sampling period of sensor i. Our goal is to find $P_{i,k}$, (i =1, 2, …, 8; k =1, 2, …, n+1) that minimize S_i, so that the calibrated data and the SidePak results are more comparable. They are identical when S_i equals zero. The results from one specific sensor show no significant differences between linear fitting and higher order fittings, though there is some improvement when more complicated equations are used. Thus, linear fitting, as given by Eq. (7.5), was chosen for convenience in calibrating all the other sensors.

$$y_{1,i,j} = p_{1,i}x_{i,j} + p_{i,2} \tag{7.5}$$

7.2.4 Demonstration in a woodworking shop

After calibration, an eight-sensor system was installed in a student woodworking shop in the Sam Fox School of Art and Architecture, Washington University in St. Louis. The woodworking shop is equipped to saw, drill and sand wood for making models. A vacuum dust collection system traps wood dust near the operating machines and collects it in a cyclone separator. However, high concentrations of wood particles are still emitted directly into the room as clearly observed by the naked eye. These coarse particles that deposit in various parts of the room are readily re-entrained and become airborne. Several studies have demonstrated that particles generated during wood machining elevate the risk for respiratory diseases [55, 56]. So, in this study, we focused on the PM exposure dose of both an active worker, the woodworking manager who moves among high concentration PM sources most of the time, and two passive receivers, the student assistants on duty who often sit at a table near the door. The sensors were placed near each machine where concentrated particles might be released, at the ventilation port where particles were extracted for filtration, and the table next to the door.

7.2.5 Kriging and biharmonic spline interpolation

The sampling in the woodworking shop lasted around four thousand seconds, and in each second, eight PM concentrations from eight sensors were recorded. The eight data samples in each second were entered into Statgraphics Centurion XVII (StatPoint, Inc., 2014) for Kriging interpolation. Kriging is a *weighted average* algorithm, so the predicted values at the unsampled points are determined by the values and the weights of the sampled points in the vicinity. The basic formula to predict the PM concentration (z) at an unsampled point (x_0) is shown as

follows, where λ_i and $z(x_i)$ represent the weight and the measured PM concentrations of the eight sensors [13].

$$z(x_0) = \sum_{i=1}^{n} \lambda_i \cdot z(x_i) \; and \; \sum_{i=1}^{n} \lambda_i = 1 \tag{7.6}$$

To determine the weight (λ_i), Kriging uses a variogram to evaluate the differences among measured values. With the PM concentration data from eight points, the empirical variogram, $\gamma(h)$, was estimated at two locations separated by a distance of h, as shown in Eq. (7.7). $N(h)$ represents the number of pairs of samples separated by a distance of h. $Z(x_i)$ and $Z(x_i + h)$ are the measured PM data at positions x_i and x_i+h.

$$\gamma(h) = \frac{1}{2N(h)} \sum_{i=1}^{N(h)} (Z(x_i) - Z(x_i + h))^2 \tag{7.7}$$

By plotting $\gamma(h)$ against h, a graph with scattered points can be obtained, showing the spatial relationship of the sampled points. Generally, if h is small, $\gamma(h)$ increases with h, indicating that the differences between observations increase with distance. On the contrary, when h is large, the differences between observations will stabilize, so that $\gamma(h)$ does not change with h. This tendency of $\gamma(h)$ vary with h implies that nearby observations tend to be similar or related, while more remote observations tend to be different or unrelated.

A variogram with scattered points is not sufficient to calculate the weight (λ_i) for all directions and distances, hence a continuous curve must be fitted to the variogram datasets. The model fitting the datasets with the highest correlation coefficient (R^2) is chosen to calculate the weight (λ_i). For each second, an empirical variogram of the data from eight sensors can be obtained;

then, six mathematical models – exponential, circular, Gaussian, pentaspherical, power function, and spherical function – were tested separately in the Statgraphics Centurion to adjust the empirical variogram for best performance. The spherical model was chosen for data interpolation because it yielded the highest validation (R^2). Based on the spherical model, 2600 Kriged points, evenly distributed in the measured area, together with the validation and variance estimations, were calculated for each second. Then, 94 boundary points were forced to zero according to the physical requirements. The boundary points and the 2600 Kriged values were used as input data for biharmonic spline interpolation in Matlab, which refined the local mesh with negligible influence on the spatial prediction from the Kriged results. The resolutions for Kriging interpolation and biharmonic spline interpolation were 0.546 m and 0.100 m, respectively.

7.2.6 Artificial neural network for interpolation

An artificial neural network (ANN) is a powerful tool for solving complex and highly nonlinear problems. The elements of the ANN toolbox in Matlab are an input, an output, and a hidden layer. The nodes in the hidden layer nonlinearly propagate the linear combination of the input multiplied by different weight coefficients to obtain a value that is close to the output. The output y of each neuron k can be written as:

$$y_k = g(\sum_{r=1}^{I} x_r w_{r,k} + w_{0,k}) \tag{7.8}$$

where x_r is the input of neuron r, $w_{r,k}$ is the weight assigned to the link between the input neuron r and the output neuron k. $w_{0,k}$ is the bias assigned to neuron k, and g is the hyperbolic tangent activation function defined as:

$$g(z) = \frac{e^z - e^{-z}}{e^z + e^{-z}} \tag{7.9}$$

In our case, the input is the time and the coordinates, while the outputs are the measured PM concentrations. The hidden layer connecting the input data and the output data was set to have two layers and thirty neurons in each layer. After running the ANN toolbox with the input data, a function was established predicting the PM values for given coordinates and times. With the function, we recalculated the PM concentrations of eight sampled points for each second and calculated the root mean square error (RMSE) between the predicted PM concentrations and the sampled concentrations.

Compared to Kriging interpolation, the ANN's inclusion of time as a variable is a significant difference. Originally, data points from all 4000 seconds of measurements were fed to the toolbox together, however, the results were unusable. After visualization, a large pollution plume dominated the entire 4000-second period, for reasons that will be discussed in a later section. Accordingly, the sliding window strategy was applied to handle the time variable. The data were divided into several segments with the same window size. The data in each segment were fed separately to the ANN toolbox for training. For example, if the window size was ten, data from the 1st second to the 10th second were used to train the ANN. The resulting function was used to predict the PM concentrations and calculate the RMSE. The process was repeated

with the segment from the 11th second to the 20th second, the 21th second to the 30th second, and so on, until the last second. The effect of the window size will also be discussed later.

A rotating boundary method was applied to include the conditions at walls. The problem with including boundary conditions is similar to that encountered in Kriging. In each second, the 94 zeros (boundary points) lowered the accuracy of the training model. In contrast to the boundary conditions, the priority of the data from the eight sensors is essential. Hence, the trained model must fit the data from the eight sensors first, and consider the boundary conditions afterwards, if possible. Accordingly, a good option is to reduce the points forced to zeros on the boundaries. In addition, time is included as a variable, so there is a temporal relationship among the data for similar time, which is helpful for further reducing the number of forced zeros on the boundaries. Therefore, four points at four corners of the room were forced to zeros at the current second, and four points in the middles of each boundary were forced to zeros in the next second. The corner points and midpoints were rotated second by second to obtain the boundary conditions.

To evaluate the performance of the ANN toolbox, the root-mean-square error ($RMSE_{T_{tot}}$) over the overall four thousand seconds was calculated as follows, where n is the serial number of the sensor and t is time. $C_{sens,n,t}$ and $C_{ANN,n,t}$ are the PM concentrations measured from a sensor and predicted by the ANN toolbox at the same location, respectively. N and T_{tot} are the total number of sensors and the overall sampling duration, which were 8 and 4000 seconds respectively in this study.

$$RMSE_{T_{tot}} = \left[\sum_{t=1}^{t=T_{tot}} \sum_{n=1}^{n=N} \left(C_{sens,n,t} - C_{ANN,n,t} \right)^2 \right] / T_{tot} \tag{10}$$

7.3 Results and discussion

7.3.1 Data smoothing and calibration

One sensor was selected to demonstrate the improvement of the data quality and the accuracy of the calibration after applying the digital filters. Figure 7.2a shows the highly fluctuating raw data due to noise, and the smoothed data in arbitrary units. The signal quality from the Sharp GP2Y is clearly enhanced by applying the sliding window filter and the low pass filter. The calibrated PM concentration ($\mu g/m^3$) data is shown in Figure 7.2b. Calibration factors were obtained by correlating the smoothed data with that from the SidePak data, both at one second resolution, using linear fitting as in Eq. (7.5). The detailed calibration results for four of the eight sensors are reported in Figure 7.3. The results show the Sharp GP2Y data is in good agreement with the commercial SidePak particle mass concentration monitor, SidePak. After calibration, a series of measurements were conducted in the woodworking shop, demonstrating the efficacy of the networked sensor system.

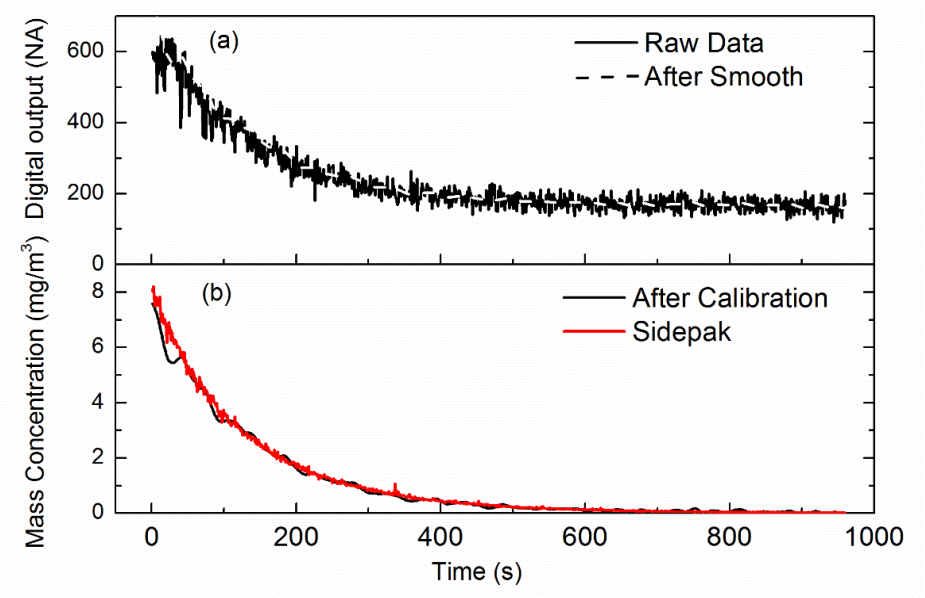

Figure 7.2. (a) The raw data, the data processed by the sliding window filter and low pass filter. (b) The calibrated data compared with the SidePak data.

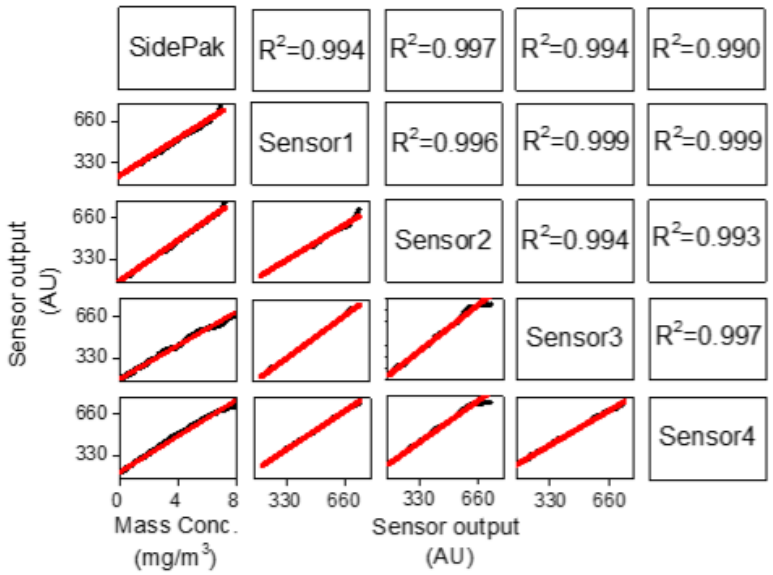

Figure 7.3 Linear fitting results between the responses of sensors and SidePak.

7.3.2 Demonstration in woodworking shop

The sensor system was deployed in the woodworking shop, which was 26 meters long and 19 meters wide. The overall sampling time was around 4000 seconds. As shown in Figure 7.4 and 5, the sensor network system monitored the PM concentrations at various locations for a series of activities (fabricating wood drawers). The activities included cutting a wooden board to proper size, drilling holes for the drawer pulls, assembling the boards with a wood stapler and wood glue, and sanding the drawer. Due to the space limitation on the drilling platform, a sensor was placed on the saw table with coordinates (3, 21) to monitor the PM emission from both the drilling platform and the saw table. Another sensor was placed at (13, 21) to monitor the emission from saw table on the other side. The sensor at (17, 13) monitored the emission from sanding table, and sensors at (15, 2) and (15, 6) were used to monitor the area of stapling and gluing. Against the door, we set a sensor at (5, 6) to monitor the PM concentration exchange between indoor and outdoor air. Apart from the person fabricating the drawers, a student assistant on duty sat at the second table, with coordinates of (15, 9). An air filtration system located at coordinates (3, 12) collected air-dispersed dust. Each sensor was assigned a coordinate as shown in Figure 7.4 and Figure 7.5.

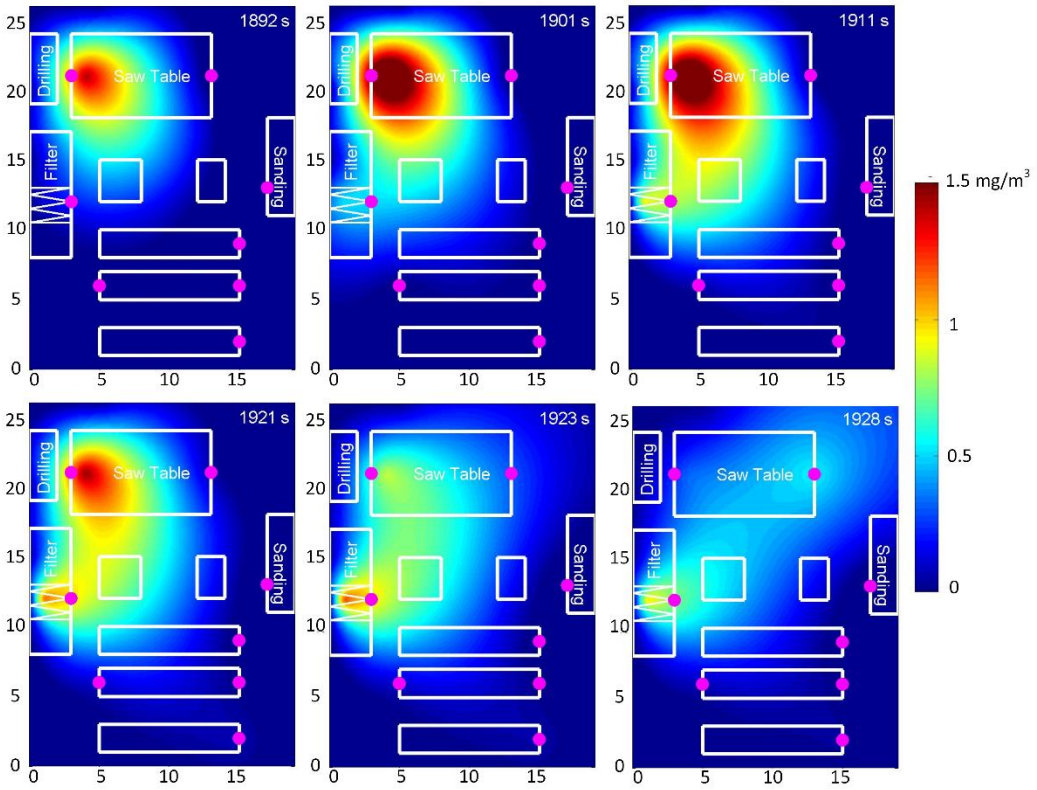

Figure 7.4. Particle mass concentration distribution predicted by Kriging, displaying particle generation and flow according to floor plan for sawing and drilling.

During the sampling period, sawing, drilling, and sanding are identified as characteristic events that emitted high PM concentrations. The maximum concentrations and the average concentrations during sawing, drilling, and sanding were respectively 2.163 and 1.489, 1.194 and 1.141, 1.300 and 0.794 mg/m^3. Although the vacuum dust collection system was on, the PM concentrations were extremely high during these woodworking processes. The highest concentrations the manager and the student were exposed to were 2.114 and 0.127 mg/m^3, respectively, and the average exposures of the manager and the student were 0.228 and 0.017 mg/m^3, respectively. The estimated exposure illustrates the potential risk for both people engaging in woodworking and passive observers.

7.3.3 Kriging interpolation

With Kriging, the spatiotemporal distribution of the PM concentrations was interpolated second by second. During characteristic events, such as sawing, drilling, and sanding, the validation (R^2) of the interpolation ranged from 56.33% to 91.26%, with an average of 74.28%. From Statgraphics, the RMSE of each second between the predicted values and the measured values given was between 0.011 and 0.128. Since sawing and drilling were performed in close sequence, these two events were combined. Figure 7.4 shows the Kriging interpolation results for the evolution of PM concentrations around the saw table and drilling platform. Figure 7.5 shows that the PM concentrations generated during sanding were ventilated gradually. The interpolation results for each second are combined as animations demonstrating the time evolution of PM concentrations during these two processes (published online). The spatiotemporal distributions show that the particulate plume fills the region between the ventilation port and the pollutant source. The room-averaged PM concentration can be estimated based on the interpolated results, eliminating the error that would be introduced by considering the aerosol in the room or chamber as a homogeneous medium.

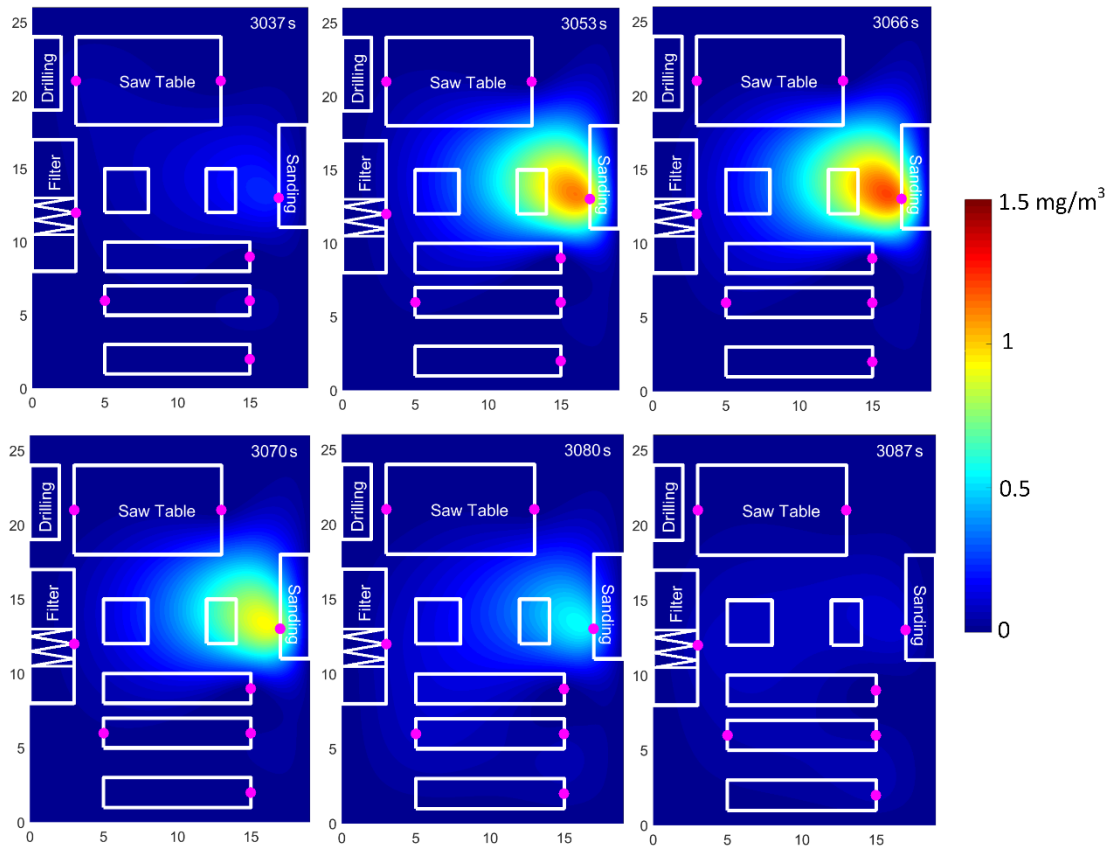

Figure 7.5 Particle mass concentration distribution predicted by Kriging, displaying particle generation and flow according to floor plan for sanding.

One thing worth noting is that the time pattern is pseudo-temporal, although the animations report the spatiotemporal distributions changing with time. In the Kriging method, time is discrete and is not involved in the interpolation process. The time is a sequence number that groups the data second by second and helps order the interpolation results. Thus, if the sampling interval is one second, it is not possible to know the distribution between consecutive seconds. In addition, since time cannot be fed to the Statgraphics system as a variable, data need to be manually processed second by second, which is tedious and inconvenient.

Kriging interpolation strongly depends on the spatial relationship between observations. As mentioned in the Methods section, we interpolated the data from sensors first and smoothed the data with boundary conditions afterwards. The boundary conditions were not included in the Kriging interpolation since they weakened the spatial relationship. Before the boundary conditions were added, the data from eight sensors obeyed the principle that observations far away are less correlated and observations nearby are comparable. However, after the boundary conditions were added, there was no difference, even for the points that were separated by the longest distance, the diagonal of the room. Hence, the spatial relationship, which is essential for the Kriging interpolation, was deteriorated. The software reported errors and could not predict the interpolation due to the poor relationship. Apart from adding all boundary conditions at the same time, we also tried to add fewer zeros on the boundaries, however, the results were disappointing. Even when we added only one zero at (0, 21) to restrict the size of the plume generated at the sawing table, the validation (R^2) of the interpolation decreased. It ranged from 7.06% to 28.12%, with an average of 13.65%. Therefore, for Kriging interpolation, adding boundary conditions adversely influenced the spatial relationship and compromised the accuracy of interpolation.

7.3.4 Artificial neural network interpolation

As mentioned earlier, the ANN toolbox in Matlab was used for interpolation. After each training, the ANN toolbox generated an equation that predicted the PM concentrations as a function of time and coordinates. Figure 7.6 shows the evolution of PM concentrations around the saw table and drilling platform. Figure 7.7 shows the PM concentrations generated during sanding decreased gradually. The interpolation results for each second are combined as

animations demonstrating the time evolution of PM concentrations during these two processes (published as supporting information).

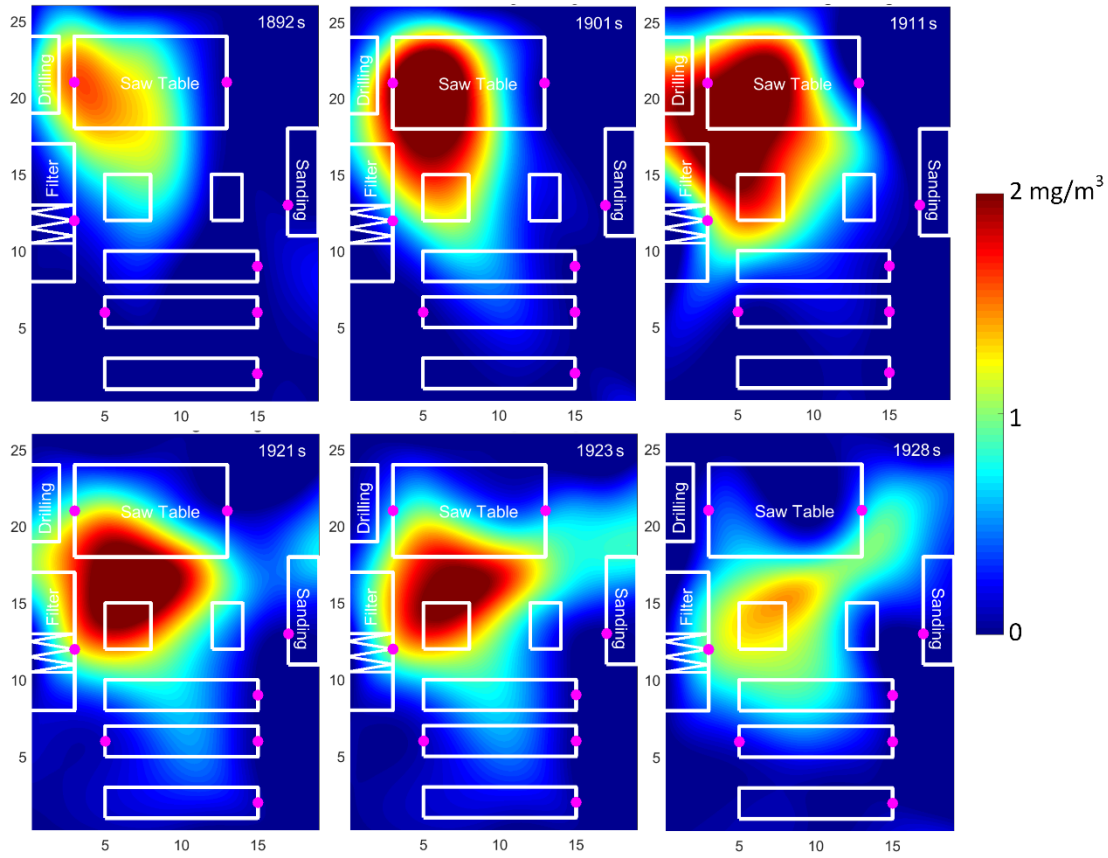

Figure 7.6 Particle mass concentration distribution predicted by ANN, displaying particle generation and flow according to floor plan for sawing and drilling.

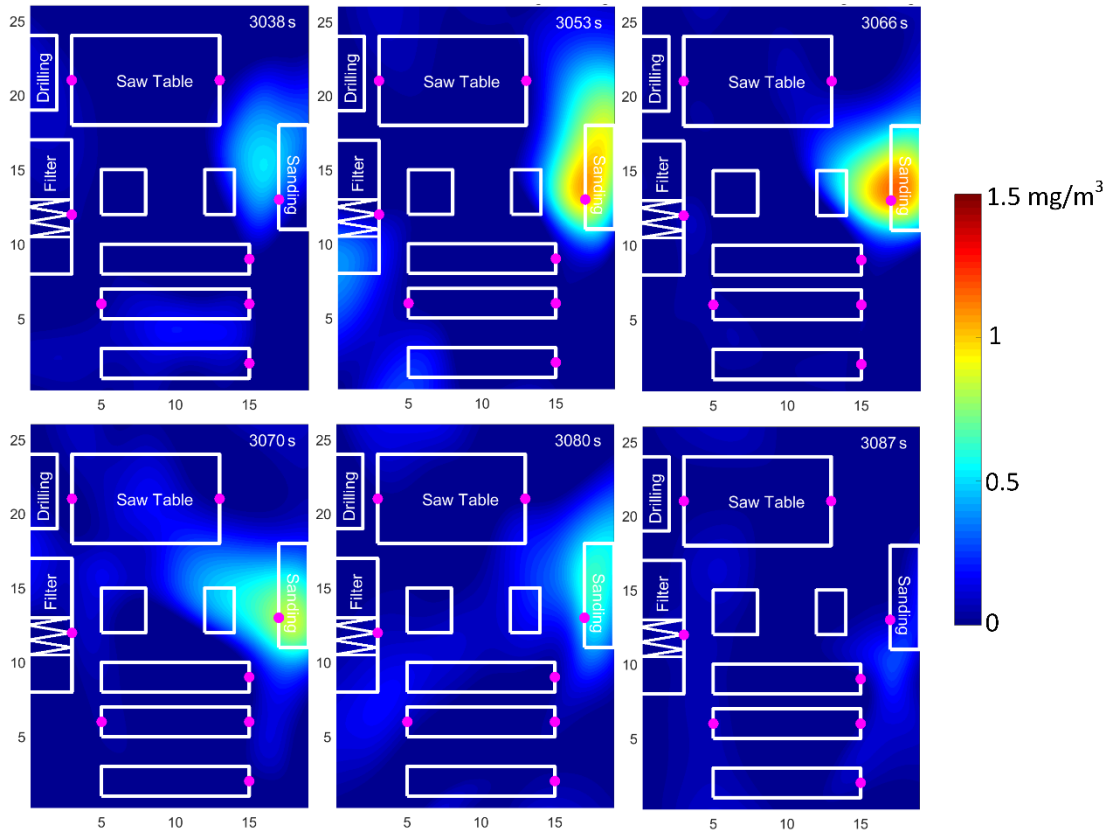

Figure 7.7 Particle mass concentration distribution predicted by Kriging, displaying particle generation and flow according to floor plan for sanding.

A distinctive feature of the ANN model is including time as a continuous variable, which means that even though the sampling interval is one second, the distribution at any time can be predicted. With time included as a variable, the input data collected from history will be used to predict the output at the current time. Therefore, the ANN toolbox can not only predict the distribution regardless of the sampling interval, but also improve the continuity of the spatial distribution.

To select a proper window size, the $RMSE_{T_{tot}}$ of the overall 4000 seconds was plotted against the window size in Figure 7.8. The $RMSE_{T_{tot}}$ initially decreases with increasing window size, and

after a turning point, the $RMSE_{T_{tot}}$ increases with window size. In the first range, increasing the length of the window enlarged the training data sets and consequently improved the prediction accuracy. However, as the window size and hence the training data set becomes overly large. the prediction accuracy drops due to overfitting. The window size was therefore selected as 30 for the spatiotemporal prediction.

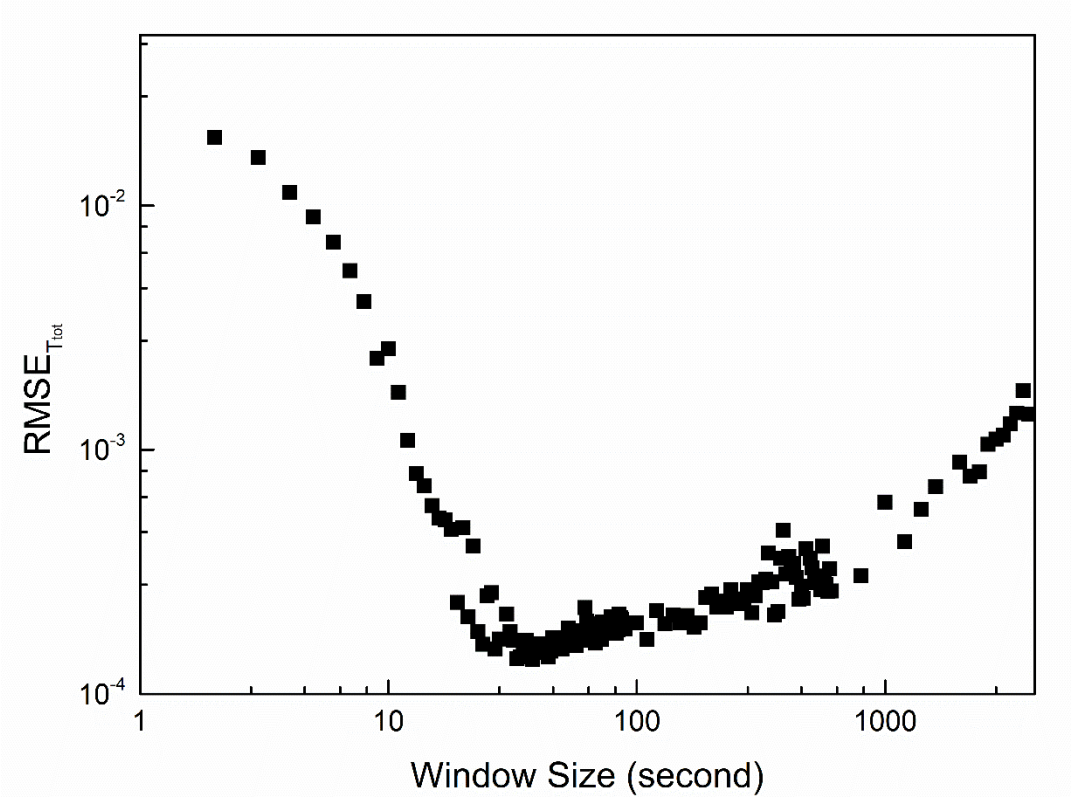

Figure 7.8 $RMSE_{Ttot}$ varying with window different size, displaying that insufficient data sets and over fitting bias the predicted PM spatial temporal distribution.

The ANN method exhibited higher variance in its performance. On the contrary, the Kriging predicted similar results if the input and the subtype model were fixed. Four intervals (500-530 sec, 1000-1030 sec, 1900-1930 sec, and 3040-3070 sec) were selected to examine the

repeatability of ANN and to compare the difference between ANN and Kriging. The first two intervals were randomly selected, and no PM emission events were observed during the intervals. The next two intervals belonged to Sawing event and Sanding event respectively. ANN was repeated for 30 times for each time interval, and the room-averaged concentrations during the 30 seconds were computed with the interpolation results from Kriging and ANN. The variation and the comparison of the two methods are reported in Figure 7.9, where the red dot is the PM concentration from Kriging, and the box plot is that from ANN. ANN reported slightly higher concentrations than Kriging, however, these methods quantitatively match with each other.

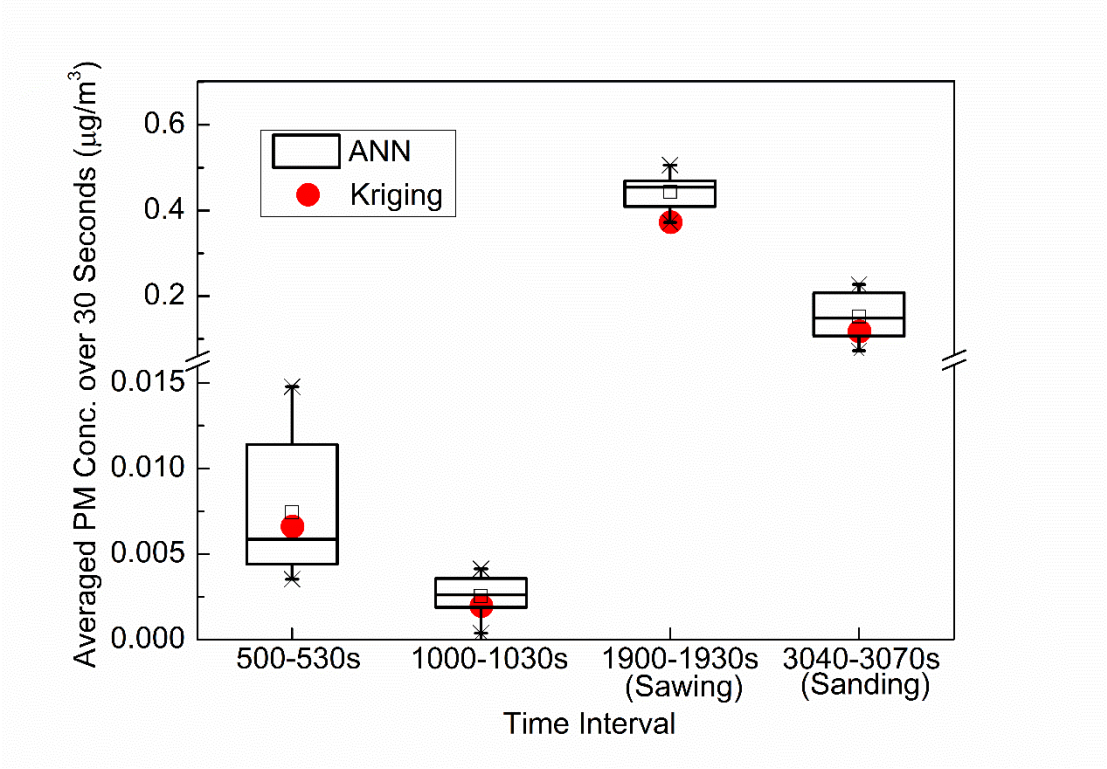

Figure 7.9 The room averaged PM concentrations of four sampling intervals predicted by Kriging and thirty repeated training in ANN.

In summary, neither Kriging interpolation nor the ANN method dominated each other. Kriging is a standard solution to spatiotemporal problems, but it strongly depends on the spatial relationship of the observations, which increase the difficulty of including boundary conditions. In addition, the process of entering data second by second and selecting models one by one is tedious. For indoor measurements, PM evolution indicating hotspots and ventilation efficacies has the top priority, and requires a larger dataset. Nonetheless, the results predicted by Kriging can be interpreted easily, while predictions produced by the ANN method are less intuitive. On the other hand, ANN method is independent of spatial relationship, can predict temporal dynamics, and is easy to program for processing large data sets. However, further study is required to understand how to constrain the ANN training and how to interpret the functions from the training.

Due to the scale of this study, uncertainties remain in how the quantity and locations of sensor nodes would influence the interpolation results. Limited to the scattered sampling locations, removing any sensors around the hotspots would significantly influence the interpolation results, making the cross-validation unreasonable. It is challenging to quantify the influence of sensor quantity and location on the accuracy of the prediction results with current settings, and more efforts are needed in future studies with wider sampling space and more sensor nodes. In this way, the number and locations of the sensors could be optimized, and further detailed cross-validation could reveal critical information on the stability and credibility of the sensor network.

7.4 Conclusions

The monitoring of indoor aerosols in this study demonstrates the capability of the sensor network platform for measuring real-time spatial aerosol concentrations in a wide range of scenarios. The online sliding window filter and the low pass filter subtract the signal from large background noise successfully. The combination of Kriging interpolation and biharmonic interpolation predicts the spatial distribution. The ANN predicts similar distribution as the Kriging interpolation and further includes time as a variable for predicting spatiotemporal distribution. The pros and cons of these methods were illustrated in this paper. Finally, based on our study it is strongly recommended that the workers wear protective personal equipment (PPE) to prevent inhaling these particles during woodworking.

7.5 References

[1] P. Biswas, C.-Y. Wu, Nanoparticles and the environment, J. Air Waste Manage. Assoc. 55(6) (2005) 708-746.

[2] J. Jiang, G. Oberdörster, P. Biswas, Characterization of size, surface charge, and agglomeration state of nanoparticle dispersions for toxicological studies, J. Nanopart. Res. 11(1) (2009) 77-89.

[3] J.C. Chow, J.G. Watson, H. Kuhns, V. Etyemezian, D.H. Lowenthal, D. Crow, S.D. Kohl, J.P. Engelbrecht, M.C. Green, Source profiles for industrial, mobile, and area sources in the Big Bend Regional Aerosol Visibility and Observational study, Chemosphere. 54(2) (2004) 185-208.

[4] R.D. Brook, S. Rajagopalan, C.A. Pope, J.R. Brook, A. Bhatnagar, A.V. Diez-Roux, F. Holguin, Y. Hong, R.V. Luepker, M.A. Mittleman, Particulate matter air pollution and cardiovascular disease, Circulation. 121(21) (2010) 2331-2378.

[5] C.A. Pope, R.T. Burnett, G.D. Thurston, M.J. Thun, E.E. Calle, D. Krewski, J.J. Godleski, Cardiovascular mortality and long-term exposure to particulate air pollution, Circulation 109(1) (2004) 71-77.

[6] A.J. Cohen, H. Ross Anderson, B. Ostro, K.D. Pandey, M. Krzyzanowski, N. Künzli, K. Gutschmidt, A. Pope, I. Romieu, J.M. Samet, The global burden of disease due to outdoor air pollution, J. Toxicol. Environ. Health Part A. 68(13-14) (2005) 1301-1307.

[7] J.A. Bernstein, N. Alexis, H. Bacchus, I.L. Bernstein, P. Fritz, E. Horner, N. Li, S. Mason, A. Nel, J. Oullette, The health effects of nonindustrial indoor air pollution, Journal of Allergy and Clinical Immunology 121(3) (2008) 585-591.

[8] R.M. Harrison, A.M. Jones, Multisite study of particle number concentrations in urban air, Environ. Sci. Technol. 39(16) (2005) 6063-6070.

[9] J.C. Chow, Measurement methods to determine compliance with ambient air quality standards for suspended particles, J. Air Waste Manage. Assoc. 45(5) (1995) 320-382.

[10] J.Y. Kim, S.R. Magari, R.F. Herrick, T.J. Smith, D.C. Christiani, Comparison of fine particle measurements from a direct-reading instrument and a gravimetric sampling method, J. Occup. Environ. Hyg. 1(11) (2004) 707-715.

[11] P.M. Fine, G.R. Cass, B.R. Simoneit, Chemical characterization of fine particle emissions from fireplace combustion of woods grown in the northeastern United States, Environ. Sci. Technol. 35(13) (2001) 2665-2675.

[12] H. Adams, M. Nieuwenhuijsen, R. Colvile, M. McMullen, P. Khandelwal, Fine particle (PM 2.5) personal exposure levels in transport microenvironments, London, UK, Sci. Total Environ. 279(1) (2001) 29-44.

[13] D.W. Wong, L. Yuan, S.A. Perlin, Comparison of spatial interpolation methods for the estimation of air quality data, J. Exposure Sci. Environ. Epidemiol. 14(5) (2004) 404-415.

[14] P. Burrough, R. McDonnell, 1998: Principles of geographical information systems. Oxford: Oxford University Press, (1998).

[15] M. Jerrett, A. Arain, P. Kanaroglou, B. Beckerman, D. Potoglou, T. Sahsuvaroglu, J. Morrison, C. Giovis, A review and evaluation of intraurban air pollution exposure models, J. Exposure Sci. Environ. Epidemiol. 15(2) (2005) 185-204.

[16] M. Jerrett, R.T. Burnett, R. Ma, C.A. Pope III, D. Krewski, K.B. Newbold, G. Thurston, Y. Shi, N. Finkelstein, E.E. Calle, Spatial analysis of air pollution and mortality in Los Angeles, Epidemiology 16(6) (2005) 727-736.

[17] A.S. Lefohn, H.P. Knudsen, L.R. McEvoy, The use of kriging to estimate monthly ozone exposure parameters for the Southeastern United States, Environ. Pollut. 53(1-4) (1988) 27-42.
[18] P.E. Tolbert, J.A. Mulholland, D.L. Macintosh, F. Xu, D. Daniels, O.J. Devine, B.P. Carlin, M. Klein, A.J. Butler, D.F. Nordenberg, Air quality and pediatric emergency room visits for asthma and Atlanta, Georgia, Am. J. Epidemiol. 151(8) (2000) 798-810.
[19] G. Hoek, R. Beelen, K. De Hoogh, D. Vienneau, J. Gulliver, P. Fischer, D. Briggs, A review of land-use regression models to assess spatial variation of outdoor air pollution, Atmos. Environ.42(33) (2008) 7561-7578.
[20] Z. Ross, M. Jerrett, K. Ito, B. Tempalski, G.D. Thurston, A land use regression for predicting fine particulate matter concentrations in the New York City region, Atmos. Environ. 41(11) (2007) 2255-2269.
[21] D. Moore, M. Jerrett, W. Mack, N. Künzli, A land use regression model for predicting ambient fine particulate matter across Los Angeles, CA, J. Environ. Monit. 9(3) (2007) 246-252.
[22] D.J. Briggs, S. Collins, P. Elliott, P. Fischer, S. Kingham, E. Lebret, K. Pryl, H. Van Reeuwijk, K. Smallbone, A. Van Der Veen, Mapping urban air pollution using GIS: a regression-based approach, Int. J. Geogr. Inf. Sci. 11(7) (1997) 699-718.
[23] Y. Wang, J. Li, H. Jing, Q. Zhang, J. Jiang, P. Biswas, Laboratory Evaluation and Calibration of Three Low-Cost Particle Sensors for Particulate Matter Measurement, Aerosol Sci. Technol 49(11) (2015) 1063-1077.
[24] S. Sousan, K. Koehler, G. Thomas, J.H. Park, M. Hillman, A. Halterman, T.M. Peters, Inter-comparison of low-cost sensors for measuring the mass concentration of occupational aerosols, Aerosol Sci. Technol 50(5) (2016) 462-473.
[25] J. Li, P. Biswas, Optical Characterization Studies of a Low-Cost Particle Sensor, Aerosol Air Qual. Res. 17 (2017) 1591-1604.
[26] F. Snik, J.H. Rietjens, A. Apituley, H. Volten, B. Mijling, A. Di Noia, S. Heikamp, R.C. Heinsbroek, O.P. Hasekamp, J.M. Smit, Mapping atmospheric aerosols with a citizen science network of smartphone spectropolarimeters, Geophys. Res. Lett. 41(20) (2014) 7351-7358.
[27] M. Gao, J. Cao, E. Seto, A distributed network of low-cost continuous reading sensors to measure spatiotemporal variations of PM2. 5 in Xi'an, China, Environ. Pollut. 199 (2015) 56-65.
[28] J. Kaiser, W. Reed, Data smoothing using low-pass digital filters, Rev. Sci. Instrum. 48(11) (1977) 1447-1457.
[29] T. Parks, J. McClellan, Chebyshev approximation for nonrecursive digital filters with linear phase, IEEE Transactions on Circuit Theory. 19(2) (1972) 189-194.
[30] R.E. Kalman, A new approach to linear filtering and prediction problems, J. Basic Eng. 82(1) (1960) 35-45.
[31] Y.-T. Kuo, T.-J. Lin, C.-W. Liu, Complexity-aware quantization and lightweight VLSI implementation of FIR filters, EURASIP J. Adv. Signal Process. 2011(1) (2011) 357906.
[32] J. Li, A.D. Heap, A. Potter, J.J. Daniell, Application of machine learning methods to spatial interpolation of environmental variables, Environ. Modell. Software 26(12) (2011) 1647-1659.
[33] A.A. Abokifa, K. Haddad, C.S. Lo, P. Biswas, Detection of Cyber Physical Attacks on Water Distribution Systems via Principal Component Analysis and Artificial Neural Networks, World Environmental and Water Resources Congress 2017, pp. 676-691.
[34] M. Chowdhury, A. Alouani, F. Hossain, Comparison of ordinary kriging and artificial neural network for spatial mapping of arsenic contamination of groundwater, Stochastic Environ. Res. Risk Assess. 24(1) (2010) 1-7.

[35] O. Antonić, J. Križan, A. Marki, D. Bukovec, Spatio-temporal interpolation of climatic variables over large region of complex terrain using neural networks, Ecological Modelling 138(1) (2001) 255-263.
[36] H.J. Fernando, M. Mammarella, G. Grandoni, P. Fedele, R. Di Marco, R. Dimitrova, P. Hyde, Forecasting PM 10 in metropolitan areas: efficacy of neural networks, Environ. Pollut. 163 (2012) 62-67.
[37] X. Feng, Q. Li, Y. Zhu, J. Hou, L. Jin, J. Wang, Artificial neural networks forecasting of PM 2.5 pollution using air mass trajectory based geographic model and wavelet transformation, Atmos. Environ. 107 (2015) 118-128.
[38] A.P. Jones, Indoor air quality and health, Atmos. Environ. 33(28) (1999) 4535-4564.
[39] J. Robinson, W. Nelson, National human activity pattern survey data base, USEPA, Research Triangle Park, NC (1995).
[40] Y. Wang, J. Li, A. Leavey, C. O'Neil, H.M. Babcock, P. Biswas, Comparative study on the size distributions, respiratory deposition, and transport of particles generated from commonly used medical nebulizers, J. Aerosol Med. Pulm. Drug Deliv. 30(2) (2017) 132-140.
[41] C.A. O'neil, J. Li, A. Leavey, Y. Wang, M. Hink, M. Wallace, P. Biswas, C.-A.D. Burnham, H.M. Babcock, C.f.D. Control, P.E. Program, Characterization of Aerosols Generated During Patient Care Activities, Clin. Infect. Dis. 65(8) (2017) 1342-1348.
[42] W. Liang, X. Yang, Indoor formaldehyde in real buildings: Emission source identification, overall emission rate estimation, concentration increase and decay patterns, Build. Environ. 69 (2013) 114-120.
[43] J. Li, A. Leavey, Y. Wang, C. O'Neil, M.A. Wallace, C.-A.D. Burnham, A.C. Boon, H. Babcock, P. Biswas, Comparing the performance of 3 bioaerosol samplers for influenza virus, J. Aerosol Sci. (2017).
[44] A. Caron, N. Redon, F. Thevenet, B. Hanoune, P. Coddeville, Performances and limitations of electronic gas sensors to investigate an indoor air quality event, Build. Environ.107 (2016) 19-28.
[45] Z. Du, P. Xu, X. Jin, Q. Liu, Temperature sensor placement optimization for VAV control using CFD–BES co-simulation strategy, Build. Environ.85 (2015) 104-113.
[46] T. Lovett, J. Lee, E. Gabe-Thomas, S. Natarajan, M. Brown, J. Padget, D. Coley, Designing sensor sets for capturing energy events in buildings, Build. Environ.110 (2016) 11-22.
[47] N. Madrid, R. Boulton, A. Knoesen, Remote monitoring of winery and creamery environments with a wireless sensor system, Build. Environ.119 (2017) 128-139.
[48] D. Licina, Y. Tian, W.W. Nazaroff, Inhalation intake fraction of particulate matter from localized indoor emissions, Build. Environ. 123 (2017) 14-22.
[49] S. Patel, J. Li, A. Pandey, S. Pervez, R.K. Chakrabarty, P. Biswas, Spatio-temporal measurement of indoor particulate matter concentrations using a wireless network of low-cost sensors in households using solid fuels, Environ. Res. 152 (2017) 59-65.
[50] T.H. Pedersen, K.U. Nielsen, S. Petersen, Method for room occupancy detection based on trajectory of indoor climate sensor data, Build. Environ. 115 (2017) 147-156.
[51] A.S. Ali, Z. Zanzinger, D. Debose, B. Stephens, Open Source Building Science Sensors (OSBSS): A low-cost Arduino-based platform for long-term indoor environmental data collection, Build. Environ. 100 (2016) 114-126.
[52] S. Rajasegarar, P. Zhang, Y. Zhou, S. Karunasekera, C. Leckie, M. Palaniswami, High resolution spatio-temporal monitoring of air pollutants using wireless sensor networks, Intelligent Sensors,

Sensor Networks and Information Processing (ISSNIP), 2014 IEEE Ninth International Conference on, IEEE, 2014, pp. 1-6.
[53] A. Leavey, Y. Fu, M. Sha, A. Kutta, C. Lu, W. Wang, B. Drake, Y. Chen, P. Biswas, Air quality metrics and wireless technology to maximize the energy efficiency of HVAC in a working auditorium, Build. Environ. 85 (2015) 287-297.
[54] J. Esper, E.R. Cook, F.H. Schweingruber, Low-frequency signals in long tree-ring chronologies for reconstructing past temperature variability, Science 295(5563) (2002) 2250-2253.
[55] G. Van Wicklen, F. Beard, Respirable Aerosol Generation by Woodworking Equipment, Appl. Eng. Agric. 9(4) (1993) 391-395.
[56] E.D. Bruschweiler, B. Danuser, C.K. Huynh, P. Wild, P. Schupfer, D. Vernez, P. Boiteux, N.B. Hopf, Generation of polycyclic aromatic hydrocarbons (PAHs) during woodworking operations, Front. Oncol. 2 (2012).

Chapter 8: Integrating Low-cost Sensor Networks with Fixed and Satellite Monitoring Systems for Enhanced Accuracy, Reliability, and Applicability

The results of this chapter is under review in Li, J., Zhang, H., Chao, C, Chieh, C, Wu, C, Chen, L., Luo, C., & Biswas, P. Integrating Low-cost Air Quality Sensor Networks with Fixed and Satellite Monitoring Systems for Enhanced Accuracy, Reliability, and Applicability

Abstract

The particulate matter (PM) mass concentration reported by monitoring stations is a reliable data source for air quality communications, pollution mapping, and exposure estimation. Achieving a better understanding of PM transport on a regional and global scale requires a high density of monitoring stations, but deploying and maintaining these stations is expensive. To increase the measurement density, a network of low-cost PM sensors is a promising supplement. Another source to retrieve PM concentrations is the aerosol optical depth (AOD) data from remote sensing, but these datasets are usually compromised by weather conditions and aerosol optical properties. To construct a highly spatially resolved PM distribution map, we synergize the data from 75 monitoring stations, 2,363 AirBox low-cost sensors, and Terra remote sensing data for the main island of Taiwan. A machine learning method identifies useful data from the massive AirBox datasets. Then, the AirBox and remote sensing datasets are calibrated with data from collocated monitoring stations. The maps created from these three data sources with Kriging interpolation demonstrate an approximate 30-fold synergistic improvement in the spatial resolution of PM mapping, with minimal bias. This method will greatly assist the validation of PM transport models and enhance the accuracy of exposure estimations.

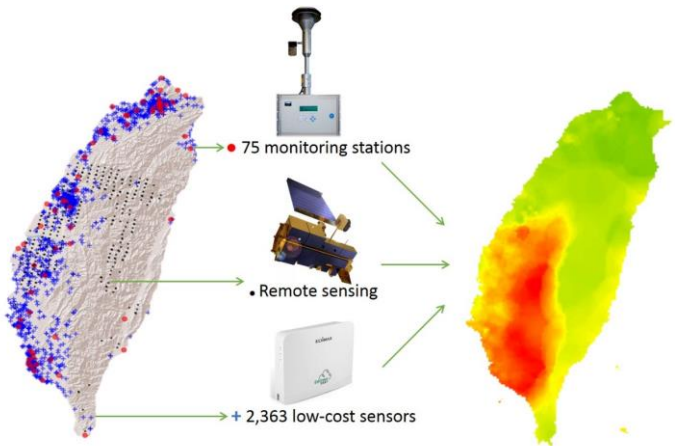

8.1 Introduction

Knowledge of the distribution of particulate matter (PM) is vital for identifying hotspots, estimating exposure, and establishing PM transport models.[1-3] Aerosol physical processes (e.g., deposition, coagulation, and cloud scavenging)[4] and atmospheric conditions (e.g., wind speed and temperature gradients)[5] can cause spatial heterogeneity and temporal variation, which are the major uncertainties in PM transport modeling and exposure estimation. Current monitoring stations, also known as the ground measurement, can accurately measure the PM concentration at fixed locations with relatively expensive research-grade instruments; however, due to their high cost and maintenance requirements, current monitoring stations are highly heterogeneously located, concentrated around heavily polluted or populated areas. Therefore, while pollution mapping based on monitoring sites can demonstrate a general trend, its low spatiotemporal resolution compromises the accuracy of the mapping.

As an alternative ground measurement method, low-cost PM sensors have great potential to achieve higher spatiotemporal resolution[6-11]. The accuracy and reliability of these low-cost PM sensors have been validated in laboratory characterizations[12-14] and field evaluations[15-18]. Pilot studies of sensor networks[6-8, 19-23] and mobile sensing nodes[24] have already explored various applications, revealing a promising future in detecting spatial heterogeneity and temporal variations.

PM concentration can also be derived from remote-sensing aerosol optical depth (AOD) data by the semi-empirical model[25, 26], the simulation-based method[27, 28], and multivariate statistical regression[29-31]. The AOD data are typically derived from the moderate resolution

spectroradiometer (MODIS) on a satellite, and the data can cover the earth in one day, with both 3 km and 10 km spatial resolution.[32] The relationship between AOD data and PM concentrations depends on meteorological conditions (e.g., relative humidity and the atmospheric boundary layer) and PM properties (e.g., composition and size distribution)[29, 31, 33-35], although aerosol data cannot be retrieved under overcast conditions. Despite the uncertainty in correlation, the advantage of AOD data is its coverage of unpopulated and remote areas.

In this study, we include the data from all three methods to realize a high spatial-resolution mapping that covers both the urban and suburban areas of the main island of Taiwan. The $PM_{2.5}$ mass concentration data from monitoring stations were chosen as the standard to calibrate the low-cost sensor (AirBox) data and remote sensing AOD data. Machine learning was used to identify useful low-cost PM sensor data. Ordinary Kriging (OK) interpolation was used to visualize the pollution distribution and demonstrate the distinctive characteristics of each dataset.

8.2 Methods

8.2.1 Data source and spatial distribution

PM and AOD data from monitoring stations and remote sensing are well-documented in public datasets. On the main island of Taiwan, 75 monitoring stations, as shown in Figure 8.1 report the hourly $PM_{2.5}$ mass concentrations measured by β-ray attenuation analyzers and tapered element oscillating microbalances (TEOM). With research grade instruments, rigid sampling intervals and detailed documentation, the monitoring stations provide the most reliable $PM_{2.5}$ mass concentration.

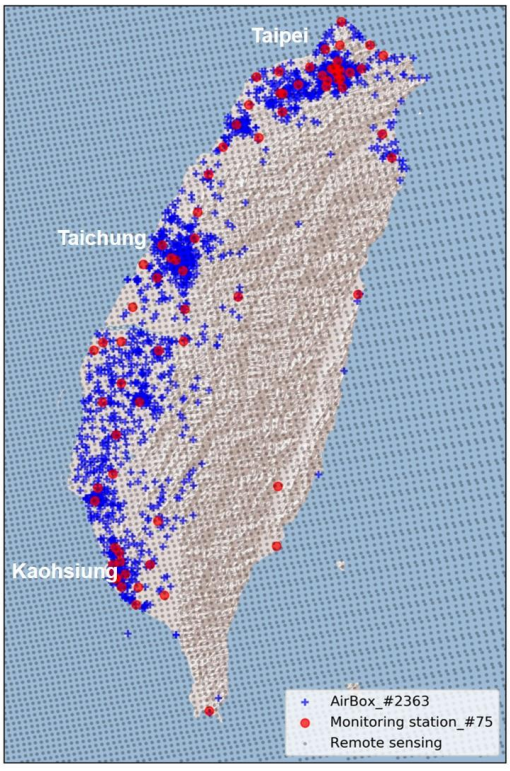

Figure 8.1 The spatial distribution of monitoring stations (red dots), AirBox devices (blue crosses), and ideal (assuming all data valid) remote sensing data points (grey dots).

The Terra 3-km dataset was selected as a representative remote sensing AOD dataset in this study. Theoretically, 4,000 data points can be retrieved for Taiwan daily (Figure 8.1). However, the quality of remote sensing data is largely influenced by weather conditions, which limit the number of effective data points. In October 2018, for Taiwan, there were only seven days with more than 2,000 daily effective data points, and 14 days had fewer than 500 data points. Clearly, meteorological interference creates the largest uncertainty and unpredictability in remote sensing datasets.

As for the low-cost PM sensors, under the management of Academia Sinica, 2,363 AirBox devices are deployed in Taiwan, comprising one of the world's largest open framework low-cost sensor deployments.[36-39] The AirBox dataset of this study includes measurement results from July to October of 2018. Each AirBox measures PM_1, $PM_{2.5}$, PM_{10}, relative humidity, and temperature, together with a global positioning system (GPS) logs real-time longitude and latitude. The major component of the AirBox is a Plantower PMS5003, whose accuracy and reliability have been extensively evaluated in earlier literature.[15, 40-42] Approximately 75% of AirBox devices have sampling intervals of less than 35 minutes. Statistics of each dataset are listed in Table 8.1.

Table 8.1 Statistics of AOD datasets, monitoring station datasets, and AirBox datasets. The data ranges given for the average, 50th percentile, and 90th percentile are obtained by analyzing monthly data.

	AOD datasets	**Monitoring station datasets**	**AirBox datasets**
Time period	03/2018-10/2018	03/2018-10/2018	07/2018-10/2018
Maximum value	0.999	158 μg/m^3	500 μg/m^3
Minimum value	0.001	2 μg/m^3	0 μg/m^3
Averaged value	0.180-0.360	10-24 μg/m^3	13-25 μg/m^3
50th percentile	0.135-0.334	10-22 μg/m^3	16-31 μg/m^3
90th percentile	0.314-0.634	29-44 μg/m^3	35-49 μg/m^3

8.2.2 Selecting effective low-cost sensor data

The AirBox datasets are enormous due to the great number of devices and their short sampling interval. Every month, there are over 3,000,000 entries in the AirBox dataset; in comparison, there are only approximately 5,000 entries in the monitoring station dataset. One convenience of low-cost sensors is their low maintenance, but this in turn introduces uncertainty about the quality of the data because malfunctions can go undetected for long periods. Therefore, an unsupervised learning method, called balanced iterative reducing and clustering using hierarchies (BIRCH), was used in this study to exclude erroneous data from the enormous datasets.[43] Basically, suspicious data have two features. First, they are isolated from regular data by extreme values. Second, their derivatives with respect to time are very large, representing a temporal discontinuity. The BIRCH method uses a clustering feature tree to classify the sensor data into different clusters (or groups) based on these two features. Figure 8.2 (supporting information) shows an example of the BIRCH method identifies outlier datum.

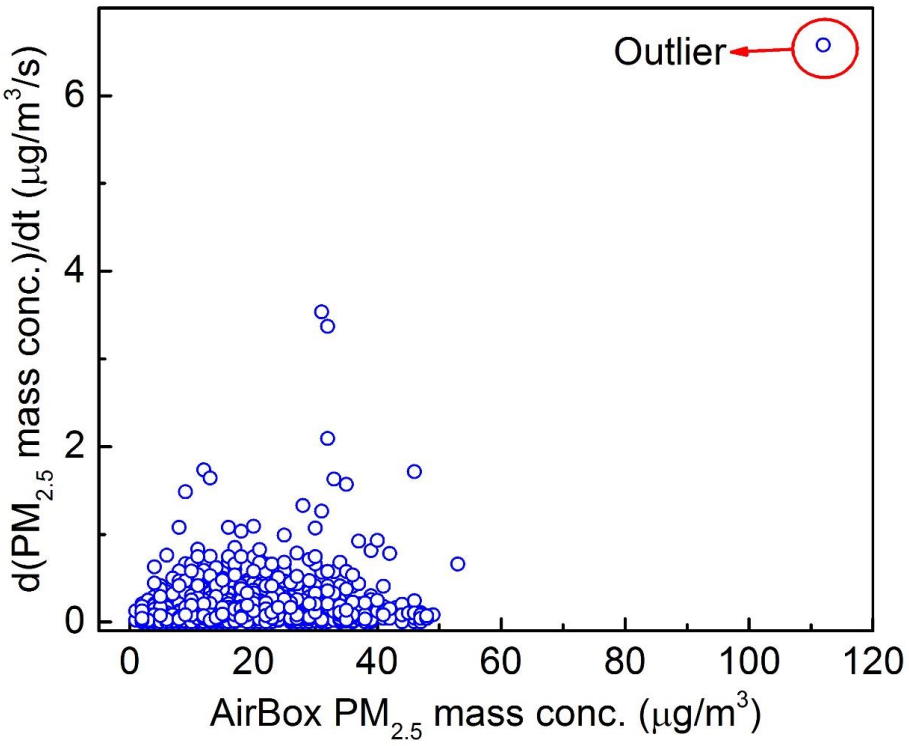

Figure 8.2 An outlier datum, identified by the BIRCH method, whose value is extremely far from the regular range. Its high derivative with respect to time represents temporal discontinuity.

8.2.3 Collocation calibration and visualization

The collocations for comparing the AOD datasets with the monitoring station datasets and the AirBox datasets are regulated by grids formed by AOD data points enclosing approximately 9 km^2, and the AOD value inside the polygon is taken as the average of the actual AOD data from the four corners. Figure 8.3 in the supporting information, showing data for October 4th, 2018, demonstrates the collocation method for comparing AOD datasets with monitoring station datasets and AirBox datasets.

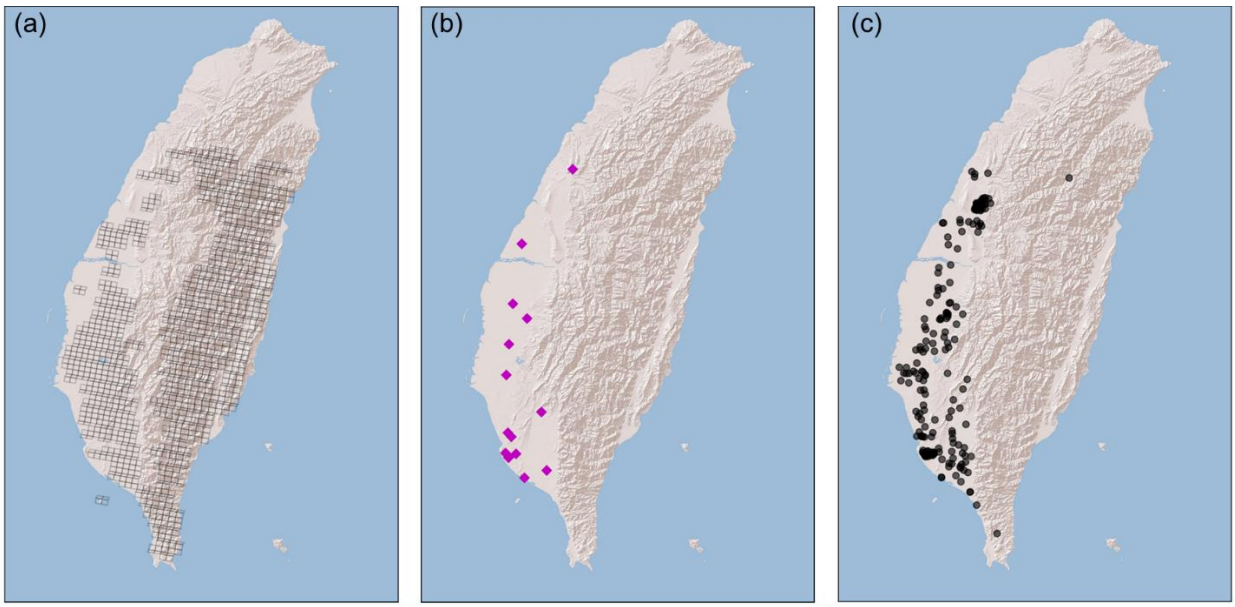

Figure 8.3 An example (October 4th, 2018) of the collocation method for associating remote sensing datasets with monitoring station datasets and AirBox datasets. (a) Grids consist of squares formed by valid remote sensing data. (b) Monitoring stations that can be paired with remote sensing data under the grids shown in (a). (c) AirBox devices that can be paired with remote sensing data under the grids shown in (a)

An effective distance (r) was defined to correlate the AirBox datasets with monitoring station datasets. Circles were drawn with monitoring stations as center points and a certain effective distance as the radius, to match the AirBox data with nearby monitoring stations. It is common for a monitoring station to pair with multiple AirBox devices. The paired data meeting the criterion of the same effective distance were combined to calculate the correlation coefficient (R) and the p-value with linear regression. A series of effective distances, ranging from 50 meters (m) to 2 kilometers (km), was chosen to examine the correlation between the AirBox datasets and the monitoring station datasets. Figure 8.4 illustrates an example (r = 1 km) of the collocation method for comparing AirBox datasets and monitoring station datasets.

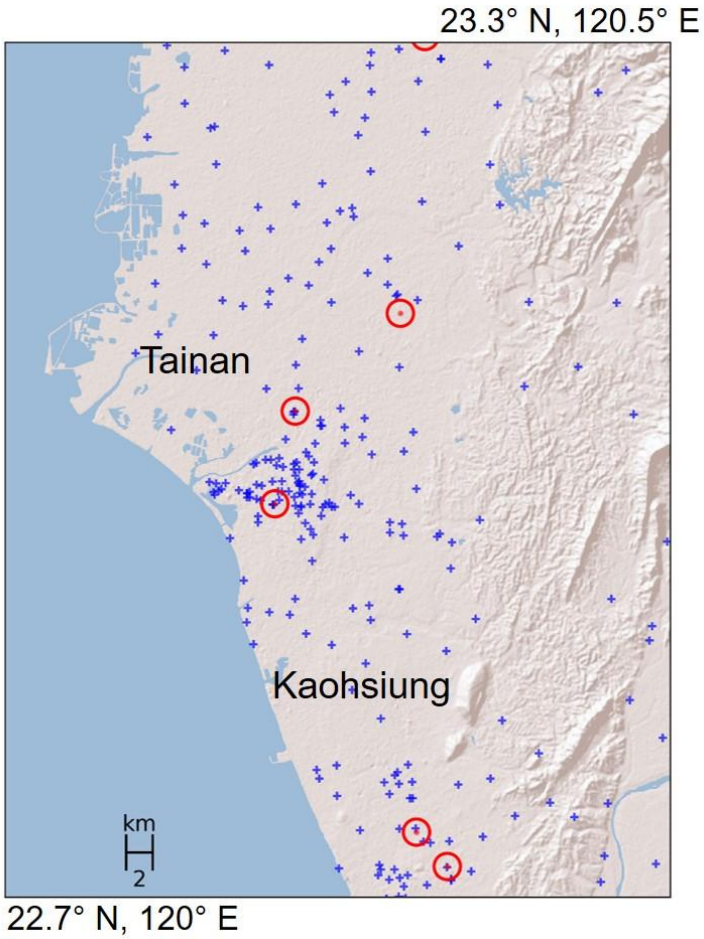

Figure 8.4 An example (r = 1 km) of the collocation method for associating AirBox datasets and monitoring station datasets. Blue crosses are locations of AirBox devices. A red circle with a red dot at the center represents the effective boundary with a monitoring station at the center. Blue crosses within the red circle can be paired with the monitoring station at the center.

To visualize the PM pollution distribution, datasets were interpolated by ordinary Kriging (OK) to predict values at unsampled locations. The OK method predicts the values at unsampled locations through a fitted model, based on the spatial dependence among measurements, and this method has been used to interpolate air pollution data.[6, 44-47] In this study, the ordinary Kriging module in ArcGIS was used to interpolate and visualize the data.

8.3 Results and discussion

8.3.1 Correlation among the AOD, monitoring station, and AirBox datasets

As can be seen in Figure 8.5, the AOD datasets and the monitoring station datasets demonstrate a strong linear correlation ($p < 0.01$), with R equal to 0.513. This value of R is moderate compared to values reported in previous literature, where R values ranged from 0.32 to 0.80.[28-30, 48] Several factors led to a strong linear correlation but a moderate R value. First, as mentioned above, the AOD data depends on weather conditions. Taiwan is rainy, with both tropical and subtropical monsoon climates, and this wet weather reduces the data size and introduces unpredictability.[49] Second, aerosols compositions, size distributions, and optical properties may all influence the correlation between AOD and $PM_{2.5}$ mass concentration. Therefore, in the previous literature, dividing the original datasets into different seasons retrieved a higher R value, since the variation caused by aerosol properties was minimized.[49, 50] Third, relative humidity (RH) also influences the correlation, and the highest correlation between AOD and $PM_{2.5}$ mass concentration can be achieved under low RH (RH < 50 %).[31, 34] In fact, according to the daily average RH reported by monitoring stations, there are only two entries from a low RH condition within the twenty thousand entries from March to October. Fourth, to obtain enough data points, in this study, daily comparisons between AOD data and monitoring station data were conducted, instead of the monthly, seasonal, or annually averaged comparisons in previous works, where averaging over such longer periods of time stabilizes the fluctuation, for a better R value.[28, 34, 49] The AOD datasets were converted to $PM_{2.5}$ mass concentration according to the linear fitting equation shown in Figure 8.5a. The correlation between the AOD datasets and the AirBox datasets also demonstrates a strong linear correlation, but with a slightly lower R value. Apart from the

reasons mentioned above that might influence the *R* value, individual differences between AirBox devices may also weaken the correlation.

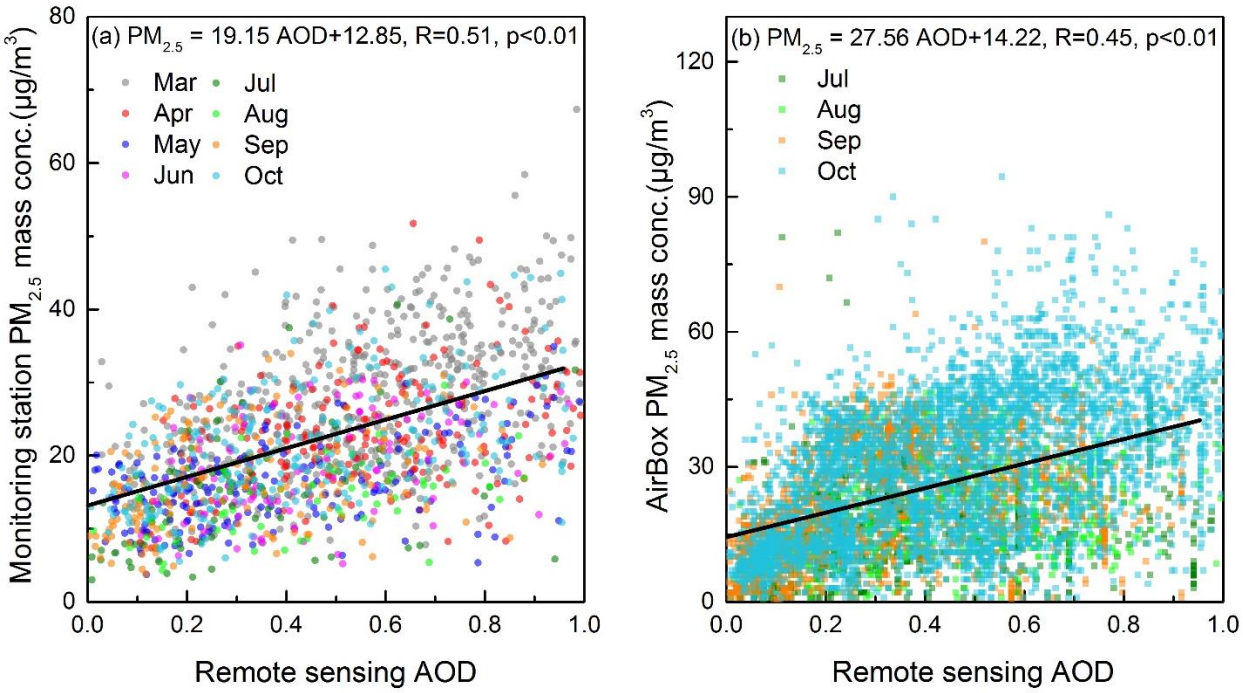

Figure 8.5. The correlation between (a) remote sensing AOD and the $PM_{2.5}$ mass concentration reported by monitoring stations, from March to October of 2018; (b) remote sensing AOD and the $PM_{2.5}$ mass concentration reported by AirBox devices, from July to October of 2018

8.3.2 Correlation between AirBox datasets and monitoring station datasets

Following the method described in the collocation calibration section, the AirBox datasets were paired with monitoring station datasets to calibrate low-cost sensors. The AirBox data was processed by month due to the large dataset. A similar trend was observed from July to October; thus, only the calibration results for October are shown as an example in Figure 8.6a. When *r* equals 0.05 km (Figure 8.6b), only one AirBox device in the vicinity of the XiZhi monitoring station can be paired successfully within the circle, leading to the high linearity ($R = 0.87$). Then, as *r* increases ($0.05 < r < 1$ km, Figure 8.6c), more AirBox devices can be paired with their

nearby monitoring stations, and the *R* value fluctuates in the range of 0.60 – 0.65. In this range, the quantity of paired data increases with increasing *r*, and irrelevant data may also be included. These two factors, the quantity of the paired data and the irrelevance of some of the data, in turn determine the correlation factor *R*. When *r* increases continuously (*r* > 1 km, Figure 8.6d), irrelevant data becomes dominant, and therefore the correlation factor *R* decreases with increasing *r*.

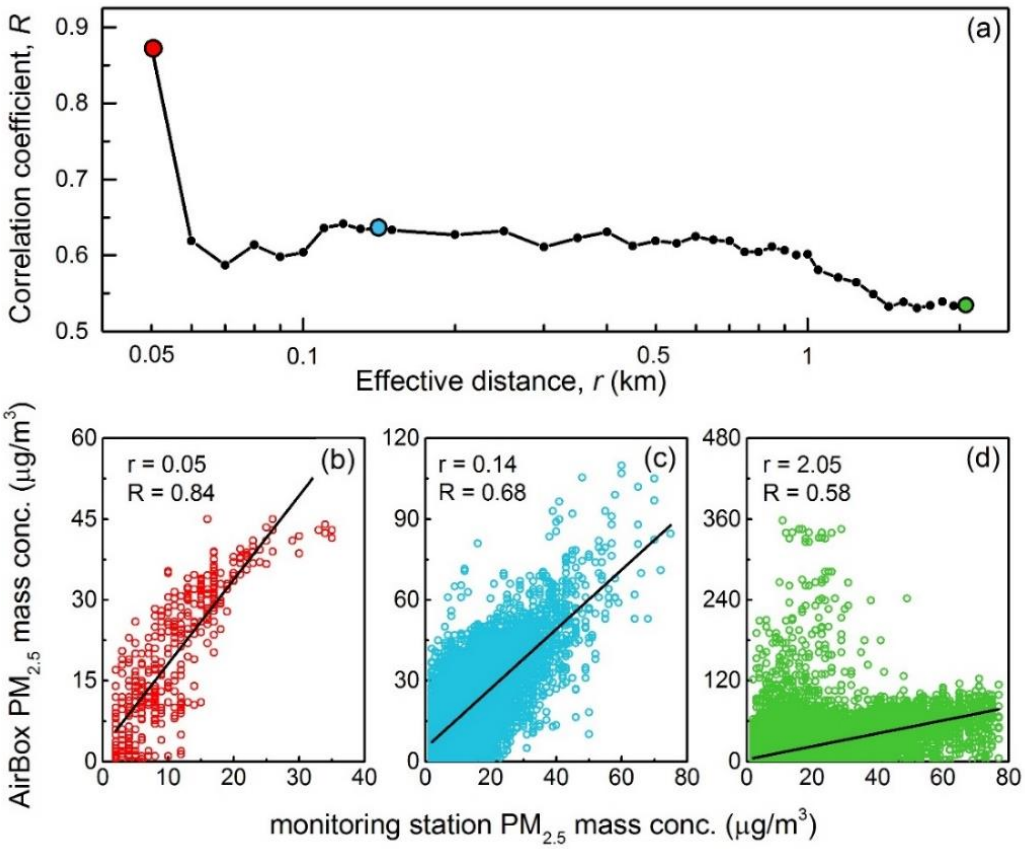

Figure 8.6. The correlation of the $PM_{2.5}$ mass concentration between monitoring station datasets and AirBox datasets. Specific examples of (b) *r* = 0.05 km, (c) *r* = 0.14 km, and (d) *r* = 2.05 km are chosen to demonstrate the variation of *R* versus *r*.

Figures 8.6b and 8.6c demonstrate the strong linearity between AirBox datasets and monitoring station datasets. In Figure 8.6d, many points appear in the upper left corner, representing a high

AirBox response and a low response from a nearby monitoring station. These data points indicate that pollution events happened nearby, but were not captured by the monitoring station, although they were observed by AirBox devices. These pollution events are typical cases demonstrating the spatial heterogeneity of PM distribution and the necessity of high spatial resolution sampling, which is a feature of low-cost PM sensor networks.

8.3.3 Pollution map visualization

AOD data were converted to the $PM_{2.5}$ mass concentration with the equation from Figure 8.5a. AirBox $PM_{2.5}$ mass concentration data were calibrated according to Figure 8.6c, with a 450 m effective distance ($PM_{2.5,\ calibrated} = 0.91\times PM_{2.5,\ AirBox} - 4.55$, $R = 0.68$). The converted $PM_{2.5}$ mass concentrations from three datasets were combined as the all-combined datasets. The monitoring stations' datasets have the highest priority, followed by the AirBox datasets and then the AOD datasets. Therefore, monitoring station data will overwrite the other two types of data if they overlap at the same location in the all-combined datasets. Figure 8.7 shows the pollution maps of October 2rd, 2018, depicted from monitoring station datasets, AirBox datasets, remote sensing datasets, and all-combined datasets, with the OK method.

The dark dots in Figures 7a-7c represent the locations of measured data, which are the inputs to the OK methods. The visualized maps interpolated from monitoring station datasets are highly similar to the one from AirBox datasets, due not only to the accuracy of the low-cost PM sensors but also to the similar spatial deployment of monitoring stations and AirBox devices. The majority of monitoring stations and AirBox devices are clustered in western Taiwan, in populated metropolitan areas (Taipei) and industrial areas (Kaohsiung). As seen in Fig. 3, the uneven spatial distribution of AirBox devices and monitoring stations biases the prediction of the

OK method in areas with low data density. The central and eastern mountain area is almost devoid of sensors and can be covered only by remote sensing data under appropriate weather conditions. The remote sensing map (Figure 8.7c) demonstrates a slightly different pattern. Although the hotspot is still located around Kaohsiung, there is a distinct boundary line between the mountain area and the residential area. This line is vague in the monitoring station and AirBox maps due to the lack of data in western Taiwan needed to define such a sharp change. After combining data from monitoring stations, AirBox devices, and remote sensing, Figure 8.7d shows a PM distribution map with improved accuracy and greater detail.

With the all-combined datasets and the OK method, the pollution distribution was mapped from October 2nd to 5th, 2018, as shown in Figure 8.8. The PM spatial distribution varied due to a wind field change when Typhoon Kong-rey approached. Although the wind field is complicated, and other factors can influence the PM distribution, the pollution map can be still approximately explained by wind field variation. On October 2nd and 3rd, the prevailing wind direction was north-east, and pollution from industrial cities was confined in the southwestern areas. On October 4th, as Kong-rey was approaching, a west wind in southern Taiwan carried the pollution to mountain areas, leading to higher PM concentrations in mountain areas compared to other days. On October 5th, the west wind prevailed in northern Taiwan, which brought external pollution from the nearby continent and created the hotspot in northern Taiwan. This case illustrates that this method can provide highly resolved PM distribution maps for validating PM transport models over a larger scale in future studies.

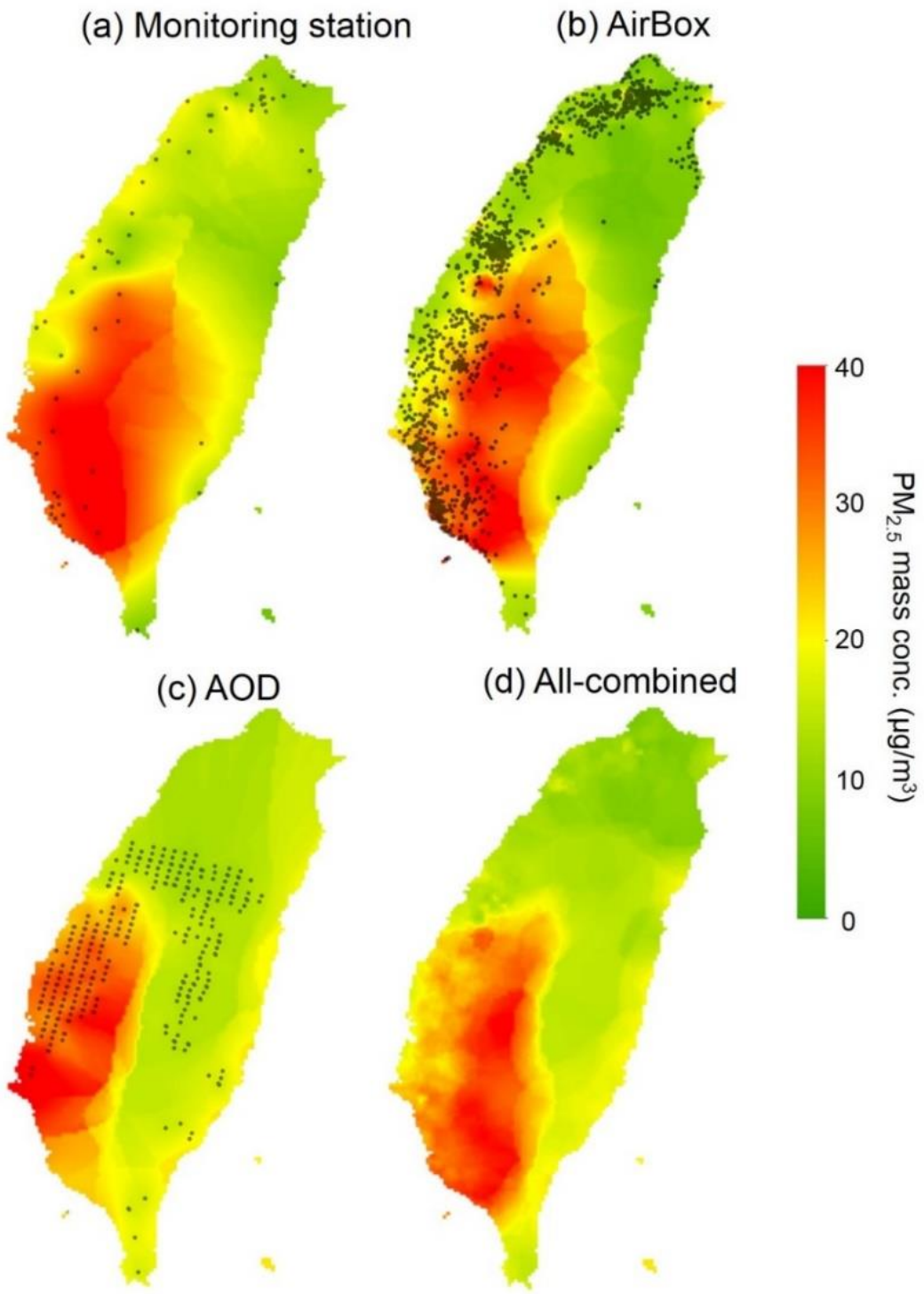

Figure 8.7 Using ordinary Kriging to visualize the pollution distribution of October 2rd, 2018, with (a) monitoring station datasets, (b) AirBox datasets, (c) AOD remote sensing datasets, and (d) all-combined datasets. Black dots represent locations of measurements for each method.

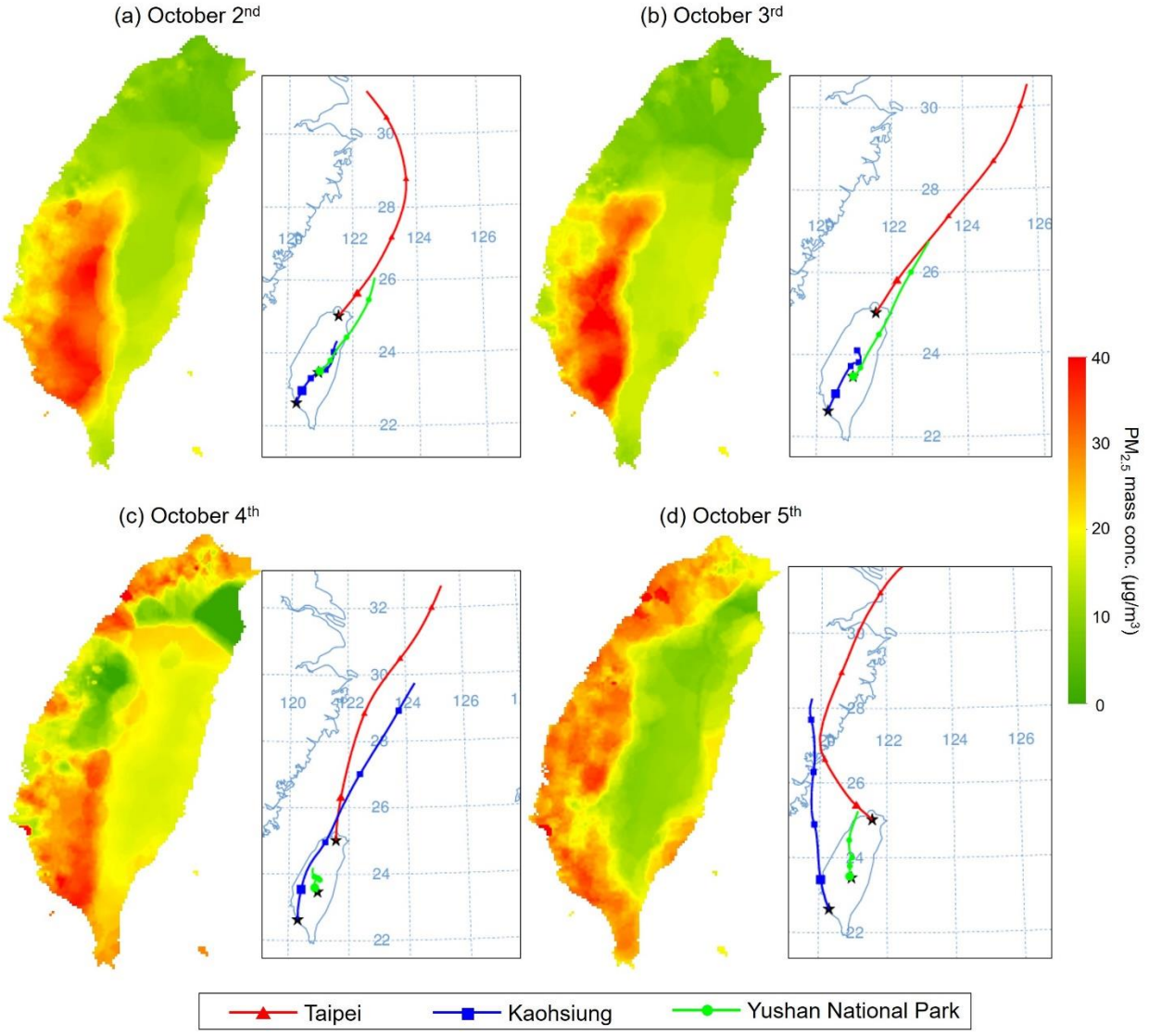

Figure 8.8 From October 2nd to 5th, Typhoon Kong-rey approached Taiwan and caused PM spatial distribution variation. $PM_{2.5}$ distribution maps on the left are Kriging interpolation results of the all-combined datasets from each day. Figures on the right are 24-hour backward trajectories of wind in Taipei (Red triangle), Kaohsiung (Blue square), and Yushan National Park (green circle), predicted by NOAA HYSPLIT trajectory model.

This study enables another possible application of the low-cost sensor network and reveals the uniqueness of each measurement method. Monitoring stations, although they provide the most reliable $PM_{2.5}$ mass concentration, are highly limited in pollution mapping due to their spatial sparseness. AirBox devices, which also directly report the $PM_{2.5}$ mass concentration, sacrifice

some data quality but provide a cost-effective solution to enhance the spatial resolution. The AOD data from the remote sensing may be biased when converted to the $PM_{2.5}$ mass concentrations and are unavailable under cloudy conditions, but they provide unique information in rural and sparsely populated mountain areas. Using the example of October 2rd, 2018, we can see that integrating the datasets of the monitoring stations, low-cost PM sensors, and the remote sensing significantly enhances the number measurements from 75 (for monitoring stations) to 2402 (all-combined datasets). Integration also improves the spatial resolution from 447 km^2/measurement (for monitoring stations) to 15 km^2/measurement (all-combined datasets). The case identified in Figure 8.8 demonstrates that such an improved spatial resolution is essential for understanding the heterogeneity of PM distribution, which will be useful in validating transport models and exposure estimations in future studies.

There are some limitations of this study. First, the accuracy of the predicted map has not been evaluated thoroughly. Apart from the Kriging interpolation, machine learning method can also be used to predict the PM spatial distribution. Machine learning algorithms have been applied to spatial data mining and modeling for environmental studies, including the artificial neural network and classification tree methods.[51,52] These methods are also applicable for this case study. The jackknife resampling method can be used to examine the bias and variance of pollution mapping. Furthermore, more variables can be included to improve the spatial relationship. The land use regression (LUR) and the machine learning methods can cooperate more variables (e.g., the population density, traffic distribution, and wind direction) to further enhance mapping accuracy.

8.4 References

1. Greco, S. L.; Wilson, A. M.; Spengler, J. D.; Levy, J. I., Spatial patterns of mobile source particulate matter emissions-to-exposure relationships across the United States. *Atmospheric Environment* **2007,** *41*, (5), 1011-1025.
2. Harrison, R. M.; Yin, J., Particulate matter in the atmosphere: which particle properties are important for its effects on health? *Science of the total environment* **2000,** *249*, (1-3), 85-101.
3. Burnett, R. T.; Pope III, C. A.; Ezzati, M.; Olives, C.; Lim, S. S.; Mehta, S.; Shin, H. H.; Singh, G.; Hubbell, B.; Brauer, M., An integrated risk function for estimating the global burden of disease attributable to ambient fine particulate matter exposure. *Environmental health perspectives* **2014,** *122*, (4), 397-403.
4. Hinds, W. C., *Aerosol technology: properties, behavior, and measurement of airborne particles*. John Wiley & Sons: 2012.
5. Seinfeld, J. H., Atmospheric Chemistry and Physics of Air Pollution Wiley. *New York* **1986,** *986*.
6. Li, J.; Li, H.; Ma, Y.; Wang, Y.; Abokifa, A. A.; Lu, C.; Biswas, P., Spatiotemporal distribution of indoor particulate matter concentration with a low-cost sensor network. *Building and Environment* **2018,** *127*, 138-147.
7. Patel, S.; Li, J.; Pandey, A.; Pervez, S.; Chakrabarty, R. K.; Biswas, P., Spatio-temporal measurement of indoor particulate matter concentrations using a wireless network of low-cost sensors in households using solid fuels. *Environmental research* **2017,** *152*, 59-65.
8. Rajasegarar, S.; Zhang, P.; Zhou, Y.; Karunasekera, S.; Leckie, C.; Palaniswami, M. In *High resolution spatio-temporal monitoring of air pollutants using wireless sensor networks*, Intelligent Sensors, Sensor Networks and Information Processing (ISSNIP), 2014 IEEE Ninth International Conference on, 2014; IEEE: 2014; pp 1-6.
9. Wang, Y.; Li, J.; Jing, H.; Zhang, Q.; Jiang, J.; Biswas, P., Laboratory evaluation and calibration of three low-cost particle sensors for particulate matter measurement. *Aerosol Science and Technology* **2015,** *49*, (11), 1063-1077.
10. Li, J.; Biswas, P., Optical Characterization Studies of a Low-Cost Particle Sensor. *Aerosol and Air Quality Research* **2017,** *17*, (7), 1691-1704.
11. Liu, D.; Zhang, Q.; Jiang, J.; Chen, D.-R., Performance calibration of low-cost and portable particular matter (PM) sensors. *Journal of Aerosol Science* **2017,** *112*, 1-10.
12. Sousan, S.; Koehler, K.; Hallett, L.; Peters, T. M., Evaluation of consumer monitors to measure particulate matter. *Journal of Aerosol Science* **2017,** *107*, 123-133.
13. Papapostolou, V.; Zhang, H.; Feenstra, B. J.; Polidori, A., Development of an environmental chamber for evaluating the performance of low-cost air quality sensors under controlled conditions. *Atmospheric Environment* **2017,** *171*, 82-90.
14. Austin, E.; Novosselov, I.; Seto, E.; Yost, M. G., Laboratory evaluation of the Shinyei PPD42NS low-cost particulate matter sensor. *PloS one* **2015,** *10*, (9), e0137789.
15. Kelly, K.; Whitaker, J.; Petty, A.; Widmer, C.; Dybwad, A.; Sleeth, D.; Martin, R.; Butterfield, A., Ambient and laboratory evaluation of a low-cost particulate matter sensor. *Environmental Pollution* **2017,** *221*, 491-500.
16. Levy Zamora, M.; Xiong, F.; Gentner, D.; Kerkez, B.; Kohrman-Glaser, J.; Koehler, K., Field and Laboratory Evaluations of the Low-Cost Plantower Particulate Matter Sensor. *Environmental science & technology* **2018,** *53*, (2), 838-849.

17. Zikova, N.; Hopke, P. K.; Ferro, A. R., Evaluation of new low-cost particle monitors for PM2. 5 concentrations measurements. *Journal of Aerosol Science* **2017,** *105*, 24-34.
18. Johnson, K. K.; Bergin, M. H.; Russell, A. G.; Hagler, G. S., Field Test of Several Low-Cost Particulate Matter Sensors in High and Low Concentration Urban Environments. *Aerosol and Air Quality Research* **2018,** *18*, 565-578.
19. Gao, M.; Cao, J.; Seto, E., A distributed network of low-cost continuous reading sensors to measure spatiotemporal variations of PM2. 5 in Xi'an, China. *Environmental pollution* **2015,** *199*, 56-65.
20. Steinle, S.; Reis, S.; Sabel, C. E.; Semple, S.; Twigg, M. M.; Braban, C. F.; Leeson, S. R.; Heal, M. R.; Harrison, D.; Lin, C., Personal exposure monitoring of PM2. 5 in indoor and outdoor microenvironments. *Science of the Total Environment* **2015,** *508*, 383-394.
21. Masiol, M.; Zíková, N.; Chalupa, D. C.; Rich, D. Q.; Ferro, A. R.; Hopke, P. K., Hourly land-use regression models based on low-cost PM monitor data. *Environmental research* **2018,** *167*, 7-14.
22. Thomas, G.; Sousan, S.; Tatum, M.; Liu, X.; Zuidema, C.; Fitzpatrick, M.; Koehler, K.; Peters, T., Low-cost, distributed environmental monitors for factory worker health. *Sensors* **2018,** *18*, (5), 1411.
23. Saha, P. K.; Zimmerman, N.; Malings, C.; Hauryliuk, A.; Li, Z.; Snell, L.; Subramanian, R.; Lipsky, E.; Apte, J. S.; Robinson, A. L., Quantifying high-resolution spatial variations and local source impacts of urban ultrafine particle concentrations. *Science of the Total Environment* **2019,** *655*, 473-481.
24. Cheng, K.-C.; Tseng, C.-H.; Hildemann, L. M., Using Indoor Positioning and Mobile Sensing for Spatial Exposure and Environmental Characterizations: Pilot Demonstration of PM2. 5 Mapping. *Environmental Science & Technology Letters* **2019**.
25. Tian, J.; Chen, D., A semi-empirical model for predicting hourly ground-level fine particulate matter (PM2. 5) concentration in southern Ontario from satellite remote sensing and ground-based meteorological measurements. *Remote Sensing of Environment* **2010,** *114*, (2), 221-229.
26. Song, W.; Jia, H.; Huang, J.; Zhang, Y., A satellite-based geographically weighted regression model for regional PM2. 5 estimation over the Pearl River Delta region in China. *Remote Sensing of Environment* **2014,** *154*, 1-7.
27. Van Donkelaar, A.; Martin, R. V.; Park, R. J., Estimating ground-level PM2. 5 using aerosol optical depth determined from satellite remote sensing. *Journal of Geophysical Research: Atmospheres* **2006,** *111*, (D21).
28. Van Donkelaar, A.; Martin, R. V.; Brauer, M.; Kahn, R.; Levy, R.; Verduzco, C.; Villeneuve, P. J., Global estimates of ambient fine particulate matter concentrations from satellite-based aerosol optical depth: development and application. *Environmental health perspectives* **2010,** *118*, (6), 847-855.
29. Liu, Y.; Sarnat, J. A.; Kilaru, V.; Jacob, D. J.; Koutrakis, P., Estimating ground-level PM2. 5 in the eastern United States using satellite remote sensing. *Environmental science & technology* **2005,** *39*, (9), 3269-3278.
30. Wang, J.; Christopher, S. A., Intercomparison between satellite-derived aerosol optical thickness and PM2. 5 mass: Implications for air quality studies. *Geophysical research letters* **2003,** *30*, (21).

31. Gupta, P.; Christopher, S. A.; Wang, J.; Gehrig, R.; Lee, Y.; Kumar, N., Satellite remote sensing of particulate matter and air quality assessment over global cities. *Atmospheric Environment* **2006,** *40*, (30), 5880-5892.
32. Remer, L.; Mattoo, S.; Levy, R.; Munchak, L., MODIS 3km aerosol product: algorithm and global perspective. **2013**.
33. Guo, J.; Xia, F.; Zhang, Y.; Liu, H.; Li, J.; Lou, M.; He, J.; Yan, Y.; Wang, F.; Min, M., Impact of diurnal variability and meteorological factors on the PM2. 5-AOD relationship: Implications for PM2. 5 remote sensing. *Environmental Pollution* **2017,** *221*, 94-104.
34. Lin, C.; Li, Y.; Yuan, Z.; Lau, A. K.; Li, C.; Fung, J. C., Using satellite remote sensing data to estimate the high-resolution distribution of ground-level PM2. 5. *Remote Sensing of Environment* **2015,** *156*, 117-128.
35. Chan, K., Aerosol optical depths and their contributing sources in Taiwan. *Atmospheric environment* **2017,** *148*, 364-375.
36. Huang, G.; Chen, L. J.; Hwang, W. H.; Tzeng, S.; Huang, H. C., Real-time PM2. 5 mapping and anomaly detection from AirBoxes in Taiwan. *Environmetrics* **2018,** *29*, (8), e2537.
37. Mahajan, S.; Chen, L.-J.; Tsai, T.-C., Short-Term PM2. 5 Forecasting Using Exponential Smoothing Method: A Comparative Analysis. *Sensors* **2018,** *18*, (10), 3223.
38. Chen, L.-J.; Ho, Y.-H.; Hsieh, H.-H.; Huang, S.-T.; Lee, H.-C.; Mahajan, S., ADF: An anomaly detection framework for large-scale PM2. 5 sensing systems. *IEEE Internet of Things Journal* **2018,** *5*, (2), 559-570.
39. Chen, L.-J.; Ho, Y.-H.; Lee, H.-C.; Wu, H.-C.; Liu, H.-M.; Hsieh, H.-H.; Huang, Y.-T.; Lung, S.-C. C., An open framework for participatory PM2. 5 monitoring in smart cities. *IEEE Access* **2017,** *5*, 14441-14454.
40. Jayaratne, R.; Liu, X.; Thai, P.; Dunbabin, M.; Morawska, L., The influence of humidity on the performance of a low-cost air particle mass sensor and the effect of atmospheric fog. *Atmospheric Measurement Techniques* **2018,** *11*, (8), 4883-4890.
41. Zheng, T.; Bergin, M. H.; Johnson, K. K.; Tripathi, S. N.; Shirodkar, S.; Landis, M. S.; Sutaria, R.; Carlson, D. E., Field evaluation of low-cost particulate matter sensors in high-and low-concentration environments. *Atmospheric Measurement Techniques* **2018,** *11*, (8), 4823-4846.
42. Johnson, N. E.; Bonczak, B.; Kontokosta, C. E., Using a gradient boosting model to improve the performance of low-cost aerosol monitors in a dense, heterogeneous urban environment. *Atmospheric Environment* **2018,** *184*, 9-16.
43. Zhang, T.; Ramakrishnan, R.; Livny, M. In *BIRCH: an efficient data clustering method for very large databases*, ACM Sigmod Record, 1996; ACM: 1996; pp 103-114.
44. Rohde, R. A.; Muller, R. A., Air pollution in China: mapping of concentrations and sources. *PloS one* **2015,** *10*, (8), e0135749.
45. Wong, D. W.; Yuan, L.; Perlin, S. A., Comparison of spatial interpolation methods for the estimation of air quality data. *Journal of Exposure Science and Environmental Epidemiology* **2004,** *14*, (5), 404.
46. Kim, S.-Y.; Sheppard, L.; Kim, H., Health effects of long-term air pollution: influence of exposure prediction methods. *Epidemiology* **2009**, 442-450.
47. Anselin, L.; Le Gallo, J., Interpolation of air quality measures in hedonic house price models: spatial aspects. *Spatial Economic Analysis* **2006,** *1*, (1), 31-52.
48. Toth, T.; Zhang, J.; Campbell, J.; Hyer, E.; Reid, J.; Shi, Y.; Westphal, D., Impact of data quality and surface-to-column representativeness on the PM 2.5/satellite AOD relationship for the contiguous United States. *Atmospheric Chemistry and Physics* **2014,** *14*, (12), 6049-6062.

49. Jung, C.-R.; Hwang, B.-F.; Chen, W.-T., Incorporating long-term satellite-based aerosol optical depth, localized land use data, and meteorological variables to estimate ground-level PM2. 5 concentrations in Taiwan from 2005 to 2015. *Environmental Pollution* **2018,** *237*, 1000-1010.
50. Li, C.; Mao, J.; Lau, K.-H. A.; Chen, J.-C.; Yuan, Z.; Liu, X.; Zhu, A.; Liu, G., Characteristics of distribution and seasonal variation of aerosol optical depth in eastern China with MODIS products. *Chinese Science Bulletin* **2003,** *48*, (22), 2488-2495.
51. Rogan, J., Franklin, J., Stow, D., Miller, J., Woodcock, C. and Roberts, D., Mapping land-cover modifications over large areas: A comparison of machine learning algorithms. *Remote Sensing of Environment* 2008, 112(5), pp.2272-2283.
52. Kanevski, M., Parkin, R., Pozdnukhov, A., Timonin, V., Maignan, M., Demyanov, V. and Canu, S.,. Environmental data mining and modeling based on machine learning algorithms and geostatistics. *Environmental Modelling & Software*, **2004**, *19*(9), pp.845-855.

Chapter 9: Summary

As a new trending topic, low-cost PM sensors have brought increasing publications and commercial products. The appealing superiority of these sensors, their low-cost, portable size, and minimal siting requirement make them a good supplement to current monitoring techniques. However, accuracy, stability, and repeatability are major concerns before application. In this thesis, we first made an evaluation of sensing modules and commercial units (Chapter 2&3). These sensors demonstrated a good linearity and a low limit of detection, which proves they are capable of field deployment. We also explored their dependency on PM properties (size and composition) and environmental parameters (relative humidity and temperature). To enhance the performance, detail reasons may bias sensors performance were discussed (Chapter 4&5). Modifying the structure of PM sensors with advancing algorithms may help us obtain more effective information from these sensors. After calibration and characterization, these sensors have been innovatively applied to various scenarios. They have been integrated with a low-cost robot for remote or autonomous sampling (Chapter 6). A sensor network has been deployed in a woodworking shop, which captured how pollutions were generated and ventilated gradually in complicated indoor environments (Chapter 7). For outdoor deployment, by synergizing the low-cost PM sensor networks with the ground measurement and satellite remote sensing, we demonstrated the great potential of low-cost PM sensors for enhancing the accuracy of pollution mapping and exposure estimating (Chapter 8).

In the future study, there are some questions still need to address. We have introduced various methods to evaluate sensors' performance in laboratory calibration. This method mainly focuses

on evaluating the performance of an individual sensor. However, the accuracy of an individual sensor may not be the most important parameter. Combining low-cost sensor networks with epidemiologic studies and evaluating low-cost PM sensors in practical applications may introduce new metrics to evaluate aerosols' adverse health effect, which will be a future direction in the field. The applications of low-cost PM sensors should consider the cut-off size of optical sensors, which cannot efficiently detect particles smaller than 300 nm. In future studies, lowering the cut-off size is as important as lowering the limit of detections. While optical sensors have such a limitation, innovative new techniques can be used to solve this problem.

In studies related to this thesis, low-cost PM sensors have demonstrated superiority in achieving high spatiotemporal sampling, leading to numerous applications in future studies. Integrating low-cost PM sensors with various gas sensors to form an air monitoring platform might be a trending topic of the field in the near future. Deploying these monitoring platforms under a regional or global scale will help us understand and validate the transport model of PM or other pollutants. Correlating the $PM_{2.5}$ with AOD is always a hot topic in geoscience. Low-cost PM sensors may play an important role in this procedure. Till now, majority applications of low-cost PM sensors focus on the ground-level measurement. Using low-cost PM sensors to measure vertical distributions can be vital for establishing the relationship between $PM_{2.5}$ and AOD.

Appendix I: Calibration of sensors

(supporting materials for Chapter 2)

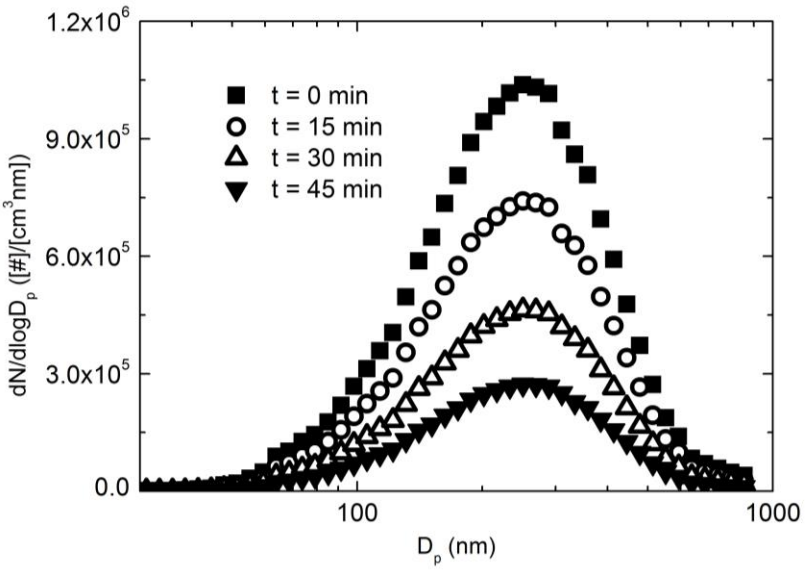

Figure A1.1 Size distribution of particles generated by burning incense as a function of time. The mode size was approximately 260 nm.

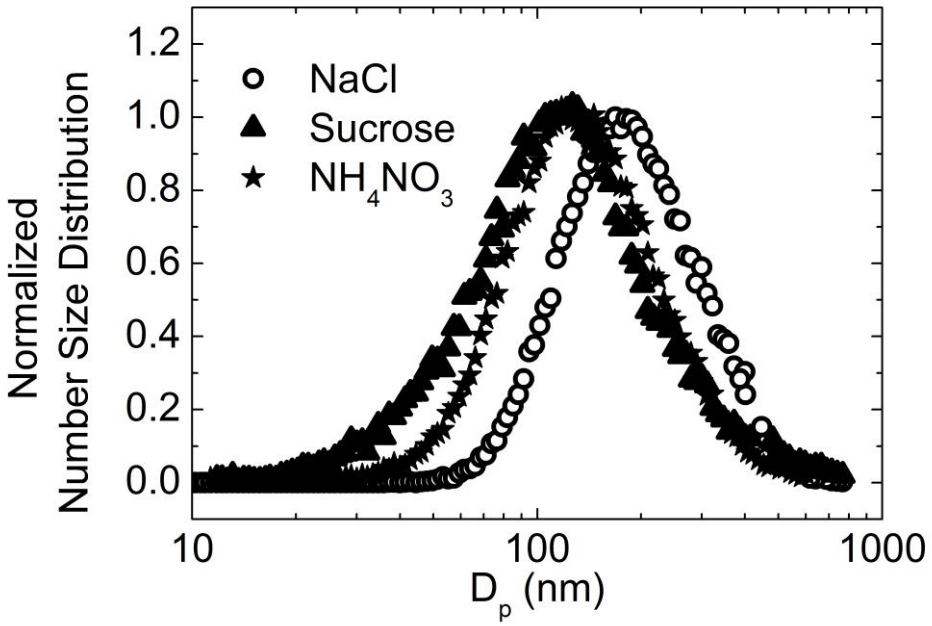

Figure A1.2 Normalized size distributions of atomized particles for studying the material dependence of sensor performance. Size distributions of the particles could be fitted by lognormal distributions.

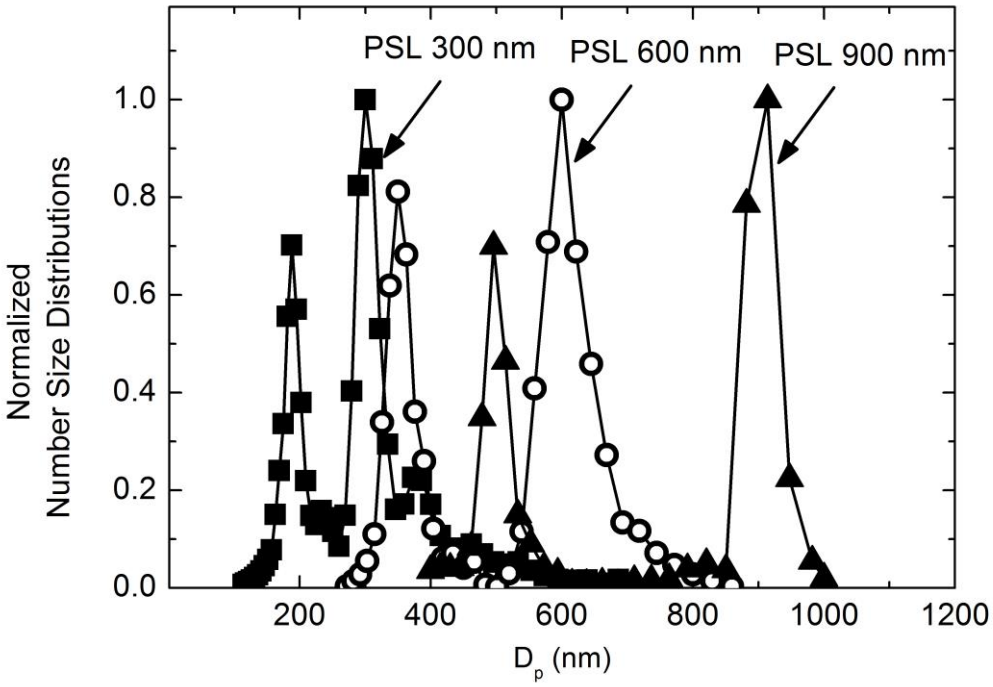

Figure A1.3 Normalized size distributions of atomized PSL particles used to study of the effect of particle size on sensor performance. Doubly charged PSL 300 nm, 600 nm, and 900 nm particles were also detected at 187 nm, 347 nm, and 502nm, respectively.

Appendix II: Comparing the performance of 3 bioaerosol samplers for influenza virus

The results of this chapter have been published in Li, J., Leavey, A., Wang, Y., O'Neil, C., Wallace, M. A., Burnham, C. A. D., ... & Biswas, P. (2018). Comparing the performance of 3 bioaerosol samplers for influenza virus. Journal of Aerosol Science, 115, 133-145.

Abstract

Respiratory viral diseases can be spread when a virus-containing particle (droplet) from one individual is aerosolized and subsequently comes into either direct or indirect contact with another individual. Increasing numbers of studies are examining the occupational risk to healthcare workers due to proximity to patients. Selecting the appropriate air sampling method is a critical factor in assuring the analytical performance characteristics of a clinical study. The objective of this study was to compare the physical collection efficiency and virus collection efficiency of a 5 ml compact SKC BioSampler®, a gelatin filter, and a glass fiber filter, in a laboratory setting. The gelatin filter and the glass fiber filter were housed in a home-made filter holder. Submersion (with vortexing and subsequent centrifugation) was used for the gelatin and glass fiber filters. Swabbing method was also tested to retrieve the viruses from the glass fiber filter. Experiments were conducted using the H1N1 influenza A virus A/Puerto Rico/8/1934 (IAV-PR8), and viral recovery was determined using culture and commercial real-time-PCR. The SKC BioSampler demonstrated a U-shaped physical collection efficiency, lowest for particles around 30 – 50 nm, and highest at 10 nm and 300-350 nm within the size range examined. The physical collection efficiency of the gelatin filter was strongly influenced by air flow and time: a stable collection across all particle sizes was only observed at 2 L/min for the 9 min sampling time, otherwise, degradation of the filter was observed. The glass fiber filter demonstrated the highest physical collection efficiency of all tested samplers, however, its overall virus recovery efficiency fared the worst. The highest viral collection efficiencies for the SKC BioSampler and gelatin filter were 5% and 1.5%, respectively. Overall, the SKC BioSampler outperformed the filters.

1. Introduction

Respiratory viral diseases can be spread when a virus-containing particle is aerosolized, frequently through coughing, sneezing, and talking, and subsequently comes into either direct or indirect contact with another individual via the mouth, eyes or nose, or by being inhaled into the lungs (Gao, Li, & Leung, 2009; Verreault, Moineau, & Duchaine, 2008, Belser, Gustin, Katz, Maines, & Tumpey, 2014). The infectivity of an airborne virus depends on factors such as relative humidity (RH), temperature, aerosolization medium, and residence time in the air (Verreault et al., 2008). Common diseases that can be transmitted through the air include chickenpox, measles, tuberculosis (TB), and influenza virus (Gao et al., 2009). In an age of globalization, increasingly mobile populations exacerbate the potential health risks from airborne infectious diseases by both increasing their spatial influence, and decreasing the time it takes to reach them (Charu et al., 2017; Fidler, 2004). This has led to several well-known pandemics including the emergence of Severe Acute Respiratory Syndrome (SARS) in 2003, which was associated with more than 700 fatalities in only a few months (WHO, 2004), and the influenza A (H1N1) virus, which by May 2009, had over 10,000 laboratory-confirmed cases across 41 countries (WHO, 2009).

The influenza virus has been the subject of much research since its discovery more than 70 years ago, and debate continues over the relative importance of its different potential transmission routes: airborne, droplet, or contact (Brankston, Gitterman, Hirji, Lemieux, & Gardam, 2007; Teunis, Brienen, & Kretzschmar, 2010; Weber & Stilianakis, 2008). Currently, the airborne route followed by inhalation at a close proximity is considered to have high infectivity, and may be a pathway for influenza transmission in an indoor environment (Teunis et al., 2010; Weber & Stilianakis, 2008). Many studies attempted to assess the importance of this route within a clinical

setting. Bischoff et al., (2013) used three Anderson air samplers to detect the aerosolized influenza virus (RNA) in 26 of the 61 symptomatic patients admitted to the emergency department of a medical center, with the highest concentrations occurring within 1 foot from the patient's head; however, the virus was also detected in particles (<4.7 μm) up to 6 feet away. Lindsley et al., (2010) detected viable influenza virus with a NIOSH two-stage bioaerosol cyclone sampler and an SKC BioSampler® from the coughs of 38 of the 58 patients presenting with symptoms at a student health clinic; the majority (42%) of viruses were detected in particles <1 μm, while 35% were detected in particles >4 μm. Lednicky and Loeb (2013) sampled influenza H3N2 with a Sioutas Personal Cascade Impactor and an SKC BioSampler and suggested that viable virus may be produced by influenza patients. Marchand et al., (2016) sampled the surrounding air during bronchoscopy procedures with a wet wall cyclonic sampler and an impactor to examine whether the aerosolized particles contained pathogens that were dangerous to healthcare workers. Although the influenza virus was not detected, several bacteria were, leading authors to conclude that aerosolized pathogens could possibly pose an occupational health risk. Another study by Leung et al., (2016) sampled with cyclone samplers in the rooms of hospital patients with confirmed influenza virus. Although no aerosolizing procedures were conducted during the measurement period, they detected the virus in 50% of collected air samples by PCR, and highlighted the need for additional studies that collected air samples during routine patient procedures, in order to gain further understanding regarding the risks posed to healthcare workers.

Although influenza is generally considered to be spread by larger droplets, these findings support the possibility that influenza transmission can also occur via an airborne route, especially within the immediate vicinity of an influenza patient. This poses significant challenges for healthcare

workers, who currently adopt face masks to prevent transmission, with special ventilation controls only for certain circumstances (Bischoff et al., 2013; Brankston et al., 2007). Nevertheless, there have been numerous cases of healthcare workers being infected during routine healthcare procedures (Lau, 2004), and calls for further research on the viability of airborne influenza viruses and the risk of transmission have been made (Lindsley et al., 2010).

Airborne influenza virus is highly infectious. As such, it is imperative that efficient samplers are used to collect and quantify these pathogens in order to determine their spread. This will not only benefit aerobiological research, but also enable us to evaluate whether standard precautions currently undertaken in a clinical setting are adequate to protect patients and health-workers from infection. Samplers currently used to collect pathogens include: solid impactors (the Anderson sampler, slit sampler, and cyclone sampler); liquid impactors (All-glass Impinger (AGI) and SKC BioSampler); and filters (gelatin filter and polytetrafluoroethylene (PTFE) filter). The Anderson sampler is most efficient at capturing larger particles (0.65-7.5 μm), and also at providing size distributions (Verreault et al., 2008). Slit samplers are capable of determining the aerosol concentration of bacteria as a function of time (Verreault et al., 2008). The AGI and SKC BioSamplers operate on similar principles and demonstrate comparable performances (Hogan et al., 2005). Filters are widely used because of their high physical collection efficiencies, for example, the gelatin filter was reported to have a high physical collection efficiency (>93%) for MS2 virus (Burton, Grinshpun, & Reponen, 2007). Burton et al. (2007) recommend 0.3-μm PTFE filters for long-term virus sampling. The glass fiber filter was evaluated for capturing endotoxin and influenza virus during air sampling (Thorne et al., 1997; Blachere et al., 2007). In this study, we evaluated the performance of the 5 mL SKC BioSampler

(also referred to as an impinger), gelatin filter, and glass fiber filter in a laboratory setting with aerosolized solutions of influenza virus.

The SKC BioSampler is being increasingly used in clinical settings to capture viruses and bacteria due to its relatively higher collection efficiency for viable virus capture compared to the gelatin filter. It has also been used to capture the bacteriophage MS2, which was generated from a vomiting simulation machine to study the transmission of the human noroviruses (Tung-Thompson, Libera, Koch, Francis III, & Jaykus, 2015). The SKC BioSampler was chosen by Cao et al. as the reference with which to evaluate the NIOSH two-stage cyclone bioaerosol sampler and the SKC AirCheck TOUCH personal air sampler (Cao, Noti, Blachere, Lindsley, & Beezhold, 2011; Nguyen et al., 2017). Fabian et al. (2009) reported that the gelatin filter, cascade impactor, and Teflon filter recovered around 7-22% of the amount of infectious virus recovered from the SKC BioSampler. This may be attributed to the liquid media in the collection vessel, which provides a favorable condition for viral preservation (Lindsley et al., 2010). However, while it has been reported to efficiently collect submicrometer particles, it was unable to adequately collect bioaerosols in the 30–100 nm size range (Hogan et al., 2005).

The gelatin filter has a high physical collection efficiency in the 100-900 nm size range (Burton et al., 2007), and it even outperformed the SKC BioSampler for the influenza A virus when sampling over a short period of time (under two minutes) (Wu, Shen, & Yao, 2010).

The glass fiber filter has been used for a variety of applications, for example, ambient air sampling of trace elements in particulate matter (Jena & Singh, 2017; Tian, Pan, Wang, & Wang, 2016), and aromatic amines in cigarette smoke (Zhang, Bai, Zhou, Liu, & Zhou, 2017). Although high collection efficiencies have been reported for fine particles (VanOsdell, Liu,

Rubow, & Pui, 1990), there are only limited studies that have applied glass fiber filter technology to aerobiology research. For viral aerosols, the available data on glass fiber filter performance is almost exclusively limited to bacteriophages (Harstad, 1965; Harstad, Decker, Buchanan, & Filler, 1967). It is therefore important to extend this research to other viruses, especially given the increasing interest among researchers and industry in low-cost filtration methods to recover or remove virus aerosols. In addition, the glass fiber filter was a good counterpart to the gelatin filter for the experiments described in this paper.

The collection efficiency of each sampler is critical for the reliability of laboratory and field measurements. This is determined by examining two critical parameters: the physical collection efficiency of the sampler, and the recovery rate of infectious particles. The physical collection efficiency describes how many particles can be sustained on the filter or in the collection vessel, regardless of whether these particles are still infectious. This can be determined with microorganisms or small pellets, such as polystyrene latex (PSL) particles or sodium chloride particles. For the SKC BioSampler, the evaporation of the liquid may increase particle bounce or lead to reaerosolization of the collected microorganisms, which decreases the collection efficiency of the device (Grinshpun et al., 1997; Lin, Willeke, Ulevicius, & Grinshpun, 1997). The sampling devices and collection process itself can also have negative effects on the recovery rate of collected microorganisms, for example, desiccation of the microorganism may occur in a filter medium (Dabisch et al., 2012). Dramatic changes to a microorganism's surroundings may also shock and kill them (Lindsley et al., 2010). Therefore, the ability to recover infectious particles, which is measured by the ratio of viable viruses to the total viruses sent to the sampler, is also used to estimate the portion of microorganism that remains infectious after sampling.

Existing research has evaluated and characterized different samplers according to different standards. Fabian et al. (2009) compared the T/I value (total virus concentration / infectious concentration) of the SKC BioSampler, cascade impactor, Teflon filters and gelatin filters with nebulized virus particles whose size is above 1 μm. Turgeon et al. (2014) compared the collection efficiency of the NIOSH sampler and the SKC BioSampler for five different bacteriophages. Despite theses studies that incorporate different samplers in their sampling portfolio, uncertainty remains regarding the percentage of the total aerosolized viruses, which are subsequently recovered. This percentage has been reported for the 20 mL SKC BioSampler with MS2 virus (Hogan et al., 2005; J. Lednicky et al., 2016); however, this percentage is still unknown for 5 mL SKC BioSampler with the real influenza virus.

The objective of this study was to estimate the amount of influenza virus that each sampler was able to recover compared to the total aerosolized particles. The size of interest was 10 – 400 nm, which is closer to the size of the airborne influenza virus when comparing with the size range (above 1 μm) reported by Fabian et al. (2009). The performance of the glass fiber filter and the gelatin filter as for viral recovery was further evaluated. Room sampling was also simulated by comparing direct sampling with indirect chamber sampling.

2. Materials and Methods

2.1 Test virus

The H1N1 influenza A virus A/Puerto Rico/8/1934 (IAV-PR8) was used as the test virus in this study and obtained from St. Jude Children's Research Hospital. It was propagated in the allantoic cavities of 10-day-old embryonic chicken eggs (Boon et al., 2010). The allantoic fluid containing IAV-PR8 was diluted in sterile phosphate buffered saline (PBS) at the indicated doses of 10^5 – 10 tissue culture infectious doses per ml ($TCID_{50}$/ml).

2.2 Test samplers

Three samplers were compared: the SKC BioSampler (5 mL, SKC Inc., Eighty-Four, PA, USA), the gelatin filter (3.0-μm pore size, Sartorius AG, Göttingen, Germany), and the glass fiber filter (Grade EPM 2000, 47 mm, Whatman®, USA) (Fig. A2.S1). Each of these collection samplers possess different structures, working principles, and recovery methodologies. The SKC BioSampler uses inertial impaction to collect and subsequently entrain particles in its sampling media. It consists of three parts: an inlet, a critical orifice section, and a 5 mL collection vessel. These parts were autoclaved separately under a 30-minute sterilization cycle and a 30-minute dry cycle before sampling to minimize potential cross-contamination. The temperature for the autoclave was approximately 122 °C, and it was maintained at a pressure of 1.24 pbar. The critical orifice section contains three 0.63 mm tangential critical orifices (Hogan et al., 2005). Connecting the outlet to a vacuum pump creates a negative pressure over 0.5 atm (15 in Hg) downstream of the critical orifices. This high-pressure drop across the critical orifices maintains a stable 12.5 L/min flowrate and creates a vortex in the media in the collection vessel into which the particles are subsequently entrained.

The gelatin and glass fiber filters must be placed in a filter holder (Figure A2.S1). When air is drawn through the holder, particles collect on the dry film of the filter through the processes of diffusion, interception, and impaction. Because they trap viruses on a dry film rather than in a liquid, additional extraction processes are required. For the gelatin filter, this poses less of an issue, as the filter can be fully dissolved in a liquid (universal viral transport media, UTM (Becton, Dickson and Company, Sparks, MD), was used in the described experiments). In contrast, the glass fiber filter is insoluble and requires extra processing to extract the captured viruses. Two processing methods, submersion and swab, were tested separately on the glass fiber filters. For the submersion method (Blachere et al., 2007), the glass fiber filter was torn into four pieces before being crumpled into a 3 mL vial of UTM solution. To reduce the mechanical agitation that damaged the viral particles, we shortened the vortex time to thirty seconds and prolonged the submersion time to 15 minutes. Then, the filter was removed and the liquid was centrifuged (1,000 x g, 10 minutes) at 4 °C. For the swab method, the glass fiber filter was brushed with a Copan FLOQ swab (Becton, Dickinson and Company) using both vertical and horizontal strokes. Next, the flocked swab was placed into a 3 mL vial of UTM for further analysis.

2.3 Biological analysis with viral culture and real-time PCR.

Culture and real-time PCR techniques were used to evaluate the amount of virus collected from each sampler. For the culture method, virus titers were determined in Madin-Darby canine kidney (MDCK) cells as described previously (Boon et al., 2010). Briefly, confluent monolayers of MDCK cells were grown overnight in 96 well-plates. The following day, the cells were washed with phosphate buffered saline (PBS) and inoculated with ten-fold serial dilutions (10^{-1} to 10^{-8}) of allantoic fluid or sample in Minimal Essential Medium containing penicillin,

streptomycin, L-glutamine, and vitamins plus 0.1% bovine serum albumin (M0.1B) for one hour at 37°C and 5% CO2. After one hour, the cells were washed once with PBS and 200µl of M0.1B with 1µg/ml TPCK-trypsin was added to each well. After 72 hours at 37°C and 5% CO_2, the presence of influenza A virus was determined by hemagglutination assay using 0.5% turkey red blood cells (Boon et al., 2010; Williams, Pinto, Doll, & Boon, 2016). The 50% Tissue Culture Infectious Dose (TCID50) was determined by the Reed-Muench method and presented as $TCID_{50}$/mL (Reed & Muench, 1938).

For real-time PCR based detection, the BioFire FilmArray Respiratory Panel (bioMerieux, Durham, NC) and the Xpert Flu/RSV Assay (Cepheid, Sunnyvale, CA) were used to detect the virus. It is important to note that neither of these instruments can provide a quantitative assay. While the Biofire presents results as either positive or negative, the Xpert demonstrates decreasing cycle threshold values with increasing viral concentration (Table A2.1). Both tests were performed according to manufacturer recommendations, with 300uL used for Xpert testing and 300uL used for Biofire analysis.

Table A2.1 Correlation between the virus suspension concentration and the cycle value from the Xpert for qualitative assessment.

Virus suspension concentration ($TCID_{50}$/mL)	Cycle value
100	21
100	20.4
1,000	17.6
1,000	17.2
10,000	13.9
10,000	14

2.4 Experimental set-up

Table A2.2 provides details on the experiments that were performed in this study, characterizing both the physical collection efficiency (Experiment I) and the virus sampling efficiencies (Experiments II, III, and IV). Virus concentrations, test sampling times, and flowrate specifications are also presented in the table. Each test was repeated twice. The experimental set-up of each test is shown in Fig. A2.1. For all experiments, a constant output atomizer (TSI 3076), operating at a flowrate of 3 L/min and a pressure of 35 psi, was used to aerosolize particles. The particle number size distributions both upstream (triangle in Fig. A2.1a) and downstream (square in Fig. A2.1a) of the samplers were measured using two scanning mobility particle sizers (SMPS). A HEPA filtered air inlet was included in the setup, to create an open system and allow for the removal of any extra air flow. All tests were conducted in a fume hood and the exhaust air was ventilated directly from the fume hood to a sterilizing exhaust.

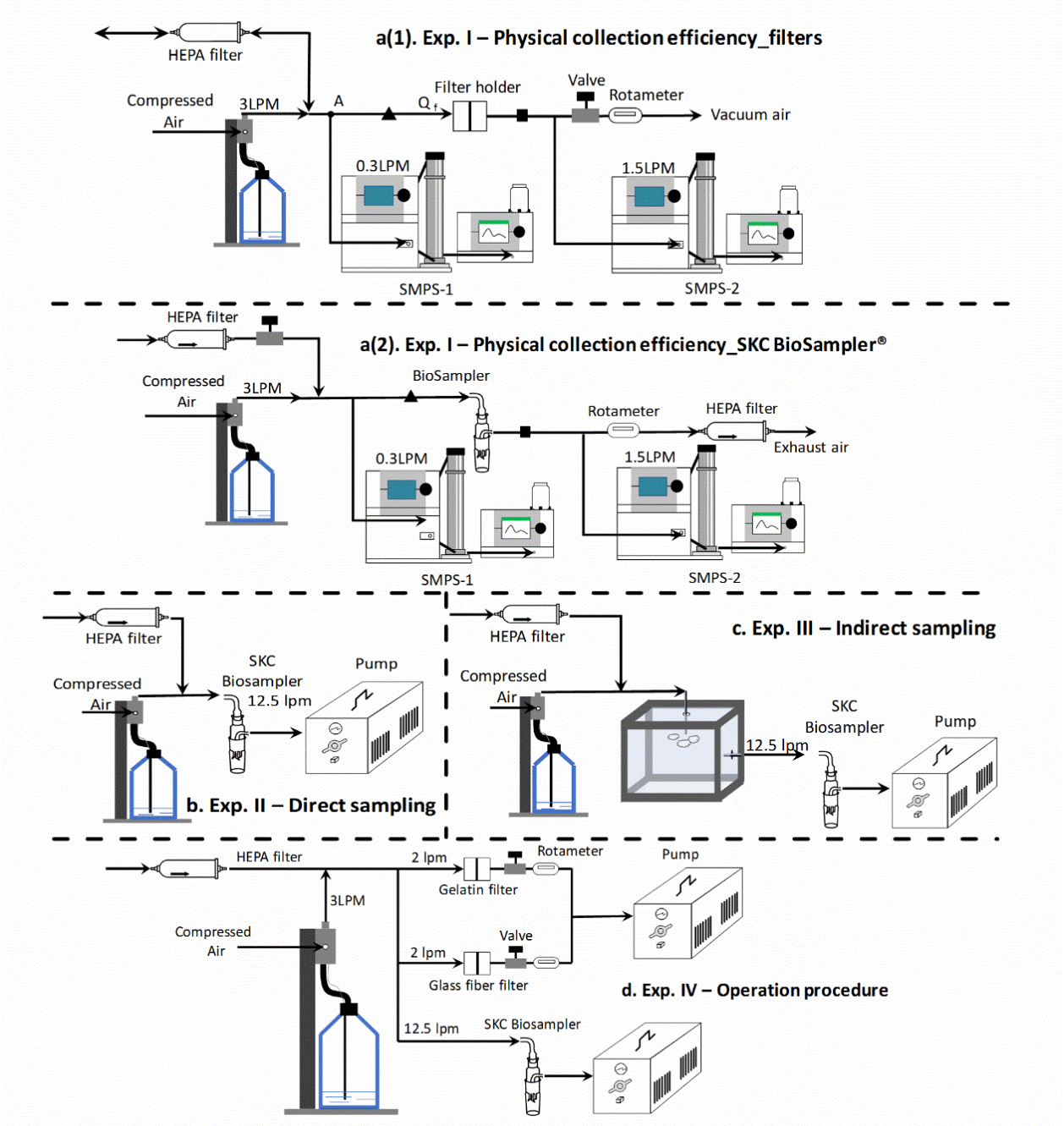

Figure A2.1 Experimental set-up.

*Exp. = experiment; ▲ = the upstream of the sampler; ■ = downstream of the sampler.

Table A2.2 Summary of the experimental plan.

Experiment	Test	Sampler	Atomized solution ($TCID_{50}$/ml)	Run length (minutes)	Specifications	
I. Efficiency	1	Gelatin	PBS	3×3min	Flowrate	2, 3, 4 L/min
	2	Glass		3×3min		2, 3, 4 L/min
	3	SKC		3×3min		12.5 L/min
II. Direct sampling	1	SKC	10	20	SKC solution	5mL UTM
	2		10	5		5mL UTM
	3		10	4		4mL UTM
	4		10	5		4mL PBS
	5		100	10		4mL PBS
	6		1,000	10		4mL PBS
	7		10,000	10		4mL PBS
	8		100,000	10		4mL PBS
III. Indirect sampling	1	SKC	PBS	10	SKC solution	4mL PBS
	2		10	10		4mL PBS
	3		10	10		4mL PBS
	4		100	10		4mL PBS
	5		1,000	10		4mL PBS
	6		10,000	10		4mL PBS
	7		100,000	10		4mL PBS
IV. Operation procedure	1	SKC, Gelatin Glass	1,000	10	Glass retrieve method*	submersion
	2		1,000	10		surface swab
	3		100,000	10		submersion
	4		100,000	10		surface swab

SKC = SKC BioSampler; Gelatin = gelatin filter; Glass = glass filter; Samples from the gelatin filter and SKC were retrieved using the same method. The gelatin filter was dissolved in 3 mm of UTM solution. The SKC solution was manually removed from the collection vessel. *Only the Glass fiber filter had different retrieval methods presented in this table.

2.4.1 Physical collection efficiency

To measure the physical collection efficiency (Experiment I), the atomizer was filled with 200 ml PBS solution and was used to generate nanometer-size particles of PBS, with an average Geometric Mean Diameter (GMD) of 41.71±0.29 nm, ranging from 9.82 to 414.20 nm. The physical collection efficiency (η_{phys}), defined in Eq. A2.1, was determined from Experiment I,

where $d_{p,i}$ is the particle diameter, and $n_{d,neb}(d_{p,i})$ and $n_{d,down}(d_{p,i})$ are the size distributions at the exit of the nebulizer and downstream of the test samplers.

$$\eta_{phys}(d_{p,i}) = \frac{n_{d,neb}(d_{p,i}) - n_{d,down}(d_{p,i})}{n_{d,neb}(d_{p,i})} \quad \text{(A2.1)}$$

Fig. A2.1a(1) depicts the setup for the gelatin and glass fiber filters. The filters were operated at three different flowrates (Q_f =2, 3, and 4 L/min), and controlled using a valve and rotameter. In the SMPS-1 settings, in order to achieve a wide measurement size range, while keeping the particle concentration below the CPC saturation concentration, a sheath flowrate of 6 L/min and a CPC flowrate of 0.3 L/min were used. The SMPS-2 was operated under a high-flow mode (1.5 L/min) to ensure the stability of the flow entering the instrument. When the filter was operated at a flowrate of 2 L/min, the total flowrate before node A was 2.3 L/min (2 L/min from the filter and 0.3 L/min from the SPMS-1). The addition of a HEPA filter permitted the removal of 0.7 L/min of filtered air, which balanced the flowrate in the system. In contrast, when the filter was operated at flowrates of 3 and 4 L/min, the total flowrate before node A was 3.3 and 4.3 L/min, respectively. This time, the HEPA filter was used to supply additional filtered air to the system (0.3 and 1.3 L/min, respectively). During this experiment, the physical collection efficiency of the gelatin and glass fiber filters were averaged over 9 minutes. The SKC BioSampler was operated in much the same way, except for the higher flowrate (12.5 L/min), depicted in Fig. A2.1a(2).

2.4.2. Virus collection efficiency

To evaluate the virus collection efficiency (Experiments II-IV), the different concentrations of viruses, suspended in PBS solution, were atomized, generating particle sizes in similar ranges as

mentioned previously. This time; however, the aerosolized particles were comprised of a mixture of viruses and PBS. Similar to the findings from Hogan et al., (2005), the size distributions did not change with increasing virus concentrations. This is due to the low virus mass to PBS solute mass ratio, and the fact that the PBS concentration was identical for each test. In 1 mL of 10^5 $TCID_{50}$/mL virus suspension, the mass of the total virus is 10^{-9} smaller than the mass of the total solutes from the PBS. However, the concentration of each virus suspension will influence the number of viruses carried in each droplet or particle.

Experiments II, III, and IV evaluated the capability of each sampler to collect viruses within the different experimental parameters. In Experiment II (direct sampling) (Fig. A2.1b), virus suspensions ranging from 10 to 10^5 /mL were aerosolized and sent directly to the SKC BioSampler, which contained either a 4 ml solution of UTM or a 4 ml solution of PBS in its collection vessel. Tests 1-4 compared the performance of the PBS and UTM solution. However, the UTM solution proved an unsuitable collection liquid due to excessive foaming which led to unacceptable evaporation and liquid losses; therefore, the remaining tests only used PBS solution as the collection fluid (Prior testing had demonstrated comparable PCR testing results with viral solutions in PBS and UTM, shown in Table A2.S1). Tests 5-8 examined the sampling capability of the SKC BioSampler at different concentrations of virus suspensions. The test parameters in Experiment III (indirect sampling) (Fig. A2.1c) echoed those of Experiment II, except for the addition of a chamber measuring 15” ×15” ×15” that was placed between the atomizer and the SKC BioSampler. This forced the virus droplets generated by the atomizer to undergo additional evaporation, diffusion, and convection inside the chamber (Wang et al., 2016), before being sampled by the SKC BioSampler, thus simulating more closely the physical changes of aerosols generated in a clinical setting, such as a hospital room. During the sampling

process, the relative humidity levels within the chamber were sustained around 58.3% to 68.1%. Theoretically, the sampling efficiency for the indirect method should be lower than for the direct method due to particle diffusion losses in the chamber. It is also worth noting that the size of the chamber will influence particle loss and the sampling results. For these experiments, the chamber size was dictated by the space inside the fume hood where the tests were being conducted.

Experiment IV (Fig. A2.1d) compared the side-by-side sampling performances of the SKC BioSampler, the gelatin filter, and the glass fiber filter. The aerosolized particles were sent to each sampler simultaneously. The flowrates remained the same for each test: 12.5 L/min for the SKC BioSampler, and 2 L/min for the gelatin and glass fiber filters. The collection vessel of the SKC BioSampler was always filled with 4 mL PBS solution. The liquid from the SKC BioSampler and the UTM solution in which the gelatin filters were dissolved, were stored directly as samples. To retrieve the viruses from the glass fiber filters, Tests 1 and 3 used the submersion method, while Tests 2 and 4 used the swab methods (described previously).

3. Results and discussion

3.1 Experiment I: physical collection efficiency

The physical collection efficiencies were calculated for each sampler using Eq. A2.1 and the particle number size distributions obtained from the 2 SMPSs during Experiment I. Fig. A2.2 and Fig. A2.3 present the results for the SKC BioSampler and gelatin filter respectively. The SKC BioSampler demonstrated a U-shaped collection efficiency curve (Fig. A2.2), lowest for particles around 30 – 50 nm, which is close to the results from previous studies (Hogan et al., 2005; Wei, Rosario, & Montoya, 2010), but higher than the efficiency reported by Hogan et al. (2005). However, while Hogan et al. (2005) tested the 20 mL SKC BioSampler, the 5 mL SKC BioSampler was used in this study. According to Zheng and Yao (2017), SKC BioSamplers with different vessel volumes demonstrated different collection efficiencies in the bacterial size range. Presumably, this would pertain to virus size range also, therefore, differences in physical collection efficiencies may have resulted from the sizes of the collection vessels. In addition, although we suspect that viral particles in the size range of 10-400 nm were not collected, we cannot rule out the mechanism of reaerosolization (Riemenschneider et al., 2010; Grinshpun et al., 1997), given the fierce vortex generated by the high flowrate, and the hydrophobic nature of the test virus. Reaerosolization is determined by multiple factors: sampling time, aerosol flowrate, and the suspension concentrations of the liquid in the collection vessel. Although reaerosolization has not been characterized as a significant limitation of the SKC BioSampler, it may still influence the overall performance (Riemenschneider et al., 2010; Grinshpun et al., 1997). Within the examined size range, the highest efficiencies were also observed at 10 nm (0.9), possibly due to enhanced diffusion inside the collection vessel, and 300-350 nm (~0.7), which has been attributed to enhanced impaction and interception (Hogan et al., 2005). The

strong dependence between collection efficiency and particle size emphasizes the importance of knowing the size range of the pathogen being collected, which in the case of spherical IAV-PR8 virus, is 80-120 nm (Rossman, Leser, & Lamb, 2012).

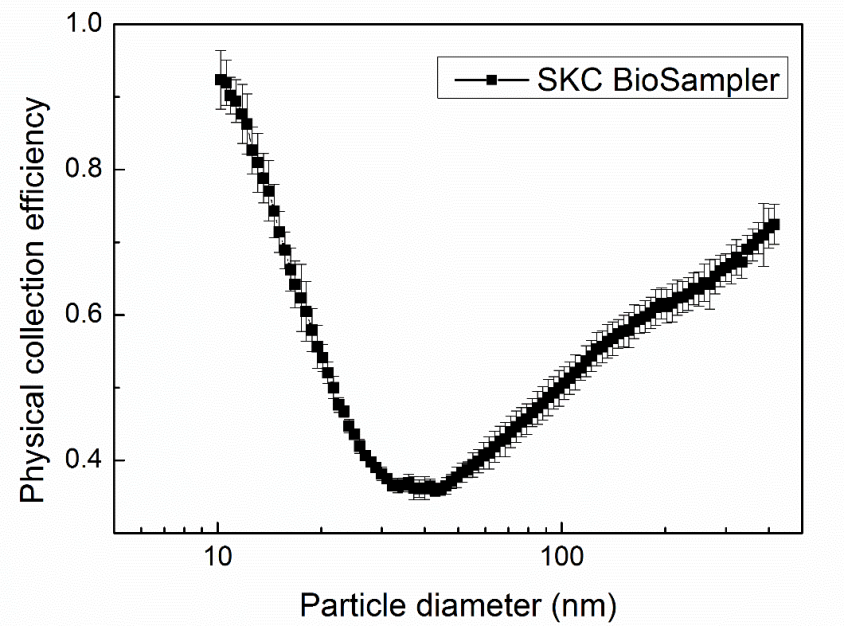

Fig. A2.2 The physical collection efficiency of the SKC BioSampler.
*The flowrate was kept constant at 12.5 L/min. Results are based on the average of 9 test runs.

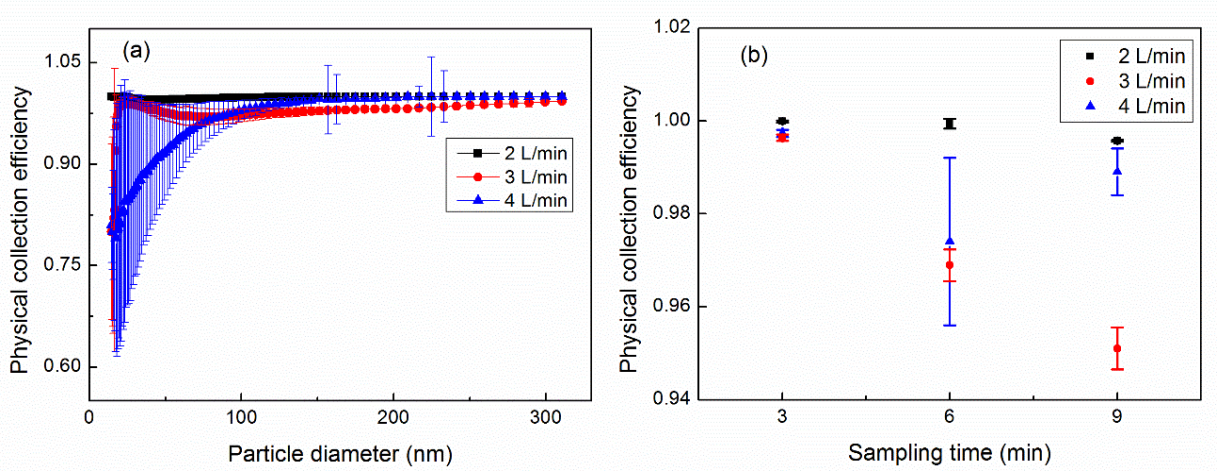

Fig. A2.3 The physical collection efficiency of the gelatin filter with varying flowrates and sampling times.

Fig. A2.3a depicts the influence of particle size and flowrate on the physical collection efficiency of the gelatin filter, which was generally able to capture larger particles more efficiently. However, the sampling flowrate influenced the efficiency curves: a collection efficiency of almost 100% across all particle sizes was observed at the lowest flowrate, while the collection efficiency increased with particle size at the highest flowrate. In addition, the performance of the gelatin filter was unpredictable under higher flowrate. This trend persisted during repeated tests. To show this phenomenon, the total physical collection efficiency ($\eta_{phy,tot}$), defined in Eq. A2.2, where N_{up} and N_{down} represent the upstream and downstream particle number concentrations, was calculated and plotted against time (Fig. A2.3b).

$$\eta_{phys,tot} = \frac{N_{up} - N_{down}}{N_{up}} \tag{A2.2}$$

In general, it is difficult to determine the influence of flowrate on a gelatin filter. In these experiments, the gelatin filter collecting at a flowrate below 2 L/min demonstrated stable performances during three repetitions each lasting 9 minutes. However, the physical collection efficiencies when collecting between 3 and 4 L/min were unpredictable. The texture of the gelatin filter deteriorated during the sampling period, changing from brittle to ductile as the aerosolized particles were continually introduced (Wu, Shen, & Yao, 2010). Fig. A2.S3 is a photo of the gelatin filter dissolving within the filter holder after sampling. The gelatin filter is sensitive to relative humidity, which may impede its performance over extended periods of time (Haig, Mackay, Walker, & Williams, 2016), potentially making it an unpredictable collection medium. Results indicate that a dry flow, and a low flowrate, as well as a short sampling time are the best operating conditions for the gelatin filter, which seems to perform sub-optimally

when these conditions are reversed. In contrast, the glass fiber filter demonstrated a very stable physical collection efficiency (100%) across all measured particle sizes, and during the different flowrates. The efficiency remained stable for the entire test duration (~ 2 hours).

3.2. Experiments II and III: comparison of direct and indirect sampling

Experiments II and III focused on the collection efficiency of viral particles from the SKC BioSampler only. Three methods were used to detect collected viral particles: 1) BioFire Multiplex Respiratory Panel (Biofire), 2) Xpert Flu/RSV assay, and 3) culture. While culture is able to determine viable virus concentration, Biofire and Xpert, which are both real-time PCR methods, are able to detect the presence of viral RNA but are not able to distinguish whether there are viable viruses or not. Tests 5-8 used PBS solution as the virus collection liquid. For the remainder of this section, the term "suspension" will refer to the solution inside the atomizer, and the term "liquid sample" will refer to the solution inside the collection vessel of the SKC BioSampler. The results from the BioFire and Xpert PCRs are presented in Table A2.3 and Fig. A2.4, respectively. In both direct and indirect sampling, the BioFire PCR reported positive influenza A results only from starting suspensions of 10,000 and 100,000 $TCID_{50}$/mL. The Xpert PCR was able to detect virus from starting suspensions of 1,000, 10,000 and 100,000 $TCID_{50}$/mL in direct sampling, and suspensions of 10,000 and 100,000 $TCID_{50}$/mL in indirect sampling. However, the Xpert cycle threshold for 1,000 $TCID_{50}$/mL was 35.4 for the liquid sample from both tests, compared to 34 and 32.3 for 10,000 and 28.2 and 27.3 for 100,000 $TCID_{50}$/mL, respectively, reflecting the relatively lower abundance of virus in the 1000 $TCID_{50}$/mL sample. Although lower numbers of PCR cycles were needed to detect the virus in the more concentrated suspensions, results still indicated that the relative abundance of virus in these samples was low (refer to Table A2.1). The viral culture results were similar (Table A2.4);

a positive well was detected only in the sample liquid for the highest virus suspension (100,000 $TCID_{50}$/mL). The positive well was detected with a 1:10 dilution ratio, which translates to a virus concentration of the liquid sample at approximately 100 $TCID_{50}$/mL.

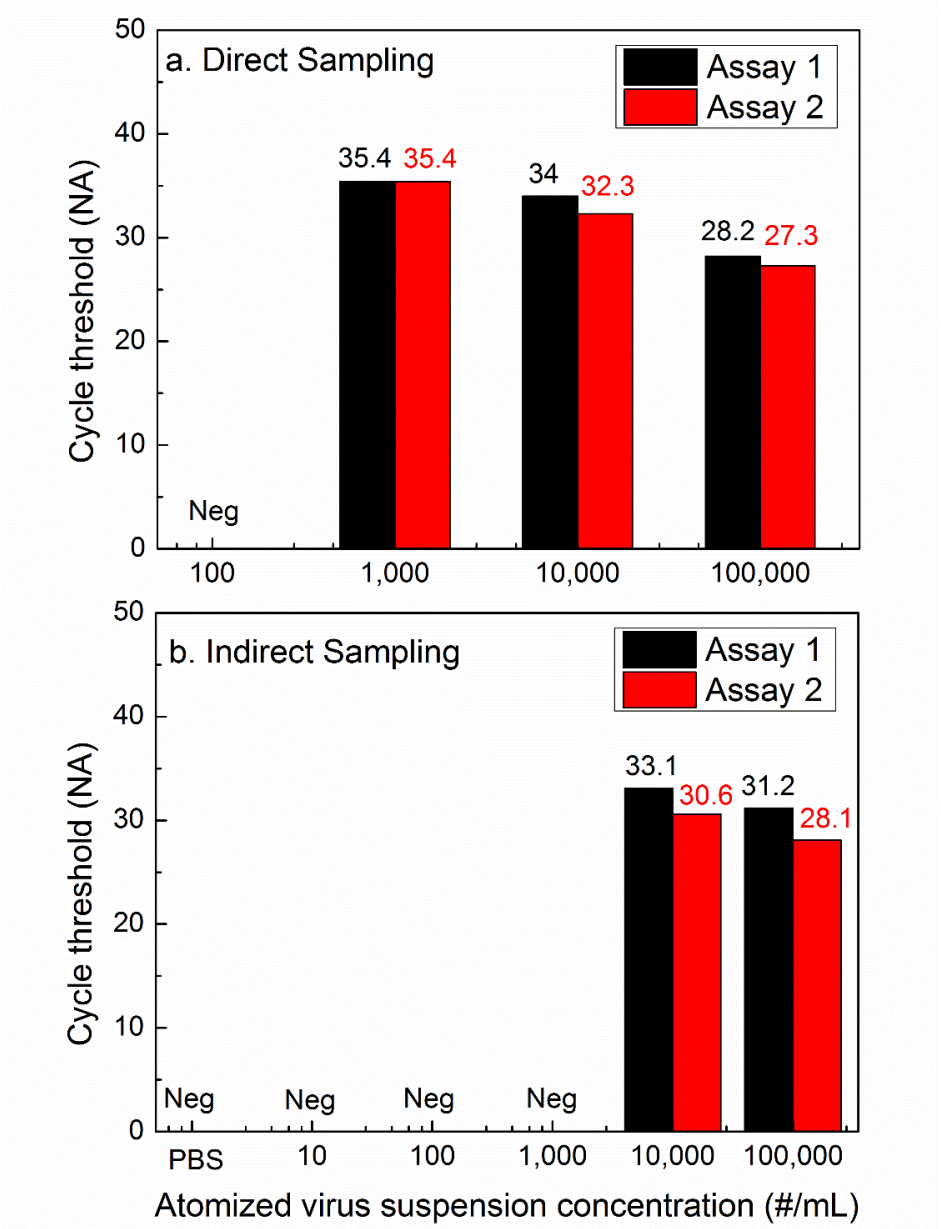

Figure A2.4 Summary of Xpert results from a) direct sampling, and b) indirect sampling using the SKC BioSampler.

*PBS = only PBS was aerosolized for a control; all other experiments used PBS plus different concentrations of virus; Assay 1 = first batch of results; Assay 2 = second batch of results; Neg = negative (no influenza A virus was detected in the sample).

Table A2.3 Summary of BioFire results from the direct and indirect sampling.

Experiment	Atomized virus suspension ($TCID_{50}$/mL)	Interpretation
Direct sampling-Experiment II	100	Negative
	1,000	Negative
	10,000	Influenza A
	100,000	Influenza A
	PBS	Negative
Indirect sampling-Experiment III	10	Negative
	100	Negative
	1,000	Negative
	10,000	Influenza A
	100,000	Influenza A

*Identical results were obtained with all repeated sampling

Table 2.4 Summary of culture results from the Experiment IV

Experiment (Test number)	Atomized virus suspension ($TCID_{50}$/mL)	Sampler	Culture results ($TCID_{50}$/mL)
Experiment IV (1)	1,000	SKC	Negative
		Gelatin	Negative
		Glass (submersion)	Negative
Experiment IV (2)	1,000	SKC	Negative
		Gelatin	Negative
		Glass (swab)	Negative
Experiment IV (3)	100,000	SKC	1,000
		Gelatin	<31
		Glass (submersion)	<31
Experiment IV (4)	100,000	SKC	100
		Gelatin	47
		Glass (swab)	<31

The Biofire PCR results from indirect sampling (with the chamber) were similar to those of direct sampling, with positive influenza A virus detected in the liquid samples of 10,000 and 100,000 $TCID_{50}$/mL suspensions (Table A2.3). However, the Xpert PCR was able to detect virus when the atomized virus suspension concentration was 1,000 $TCID_{50}$/mL or higher during

direct sampling, but was only able to detect virus in the 10,000 and 100,000 $TCID_{50}$/mL suspensions during indirect sampling. Another thing to note is the increased number of Xpert PCR cycles that were required to detect any viral particles for the atomized 100,000 $TCID_{50}$/mL suspension during indirect versus direct sampling, which indicates lower amounts of virus present in the samples collected during indirect sampling. The particle size distributions for direct sampling and indirect sampling are included in the supplementary material (Fig. A2.S2), showing that smaller particles (<50 nm) may be scavenged due to diffusion loss. This may indicate that fewer viral particles were collected during indirect compared to direct sampling and consideration should be paid regarding the type of sampling (direct versus indirect) that is being conducted in order to interpret the results obtained. These findings were reinforced by the culture results.

3.3 Experiment IV: comparison of different samplers and different operation procedures

First, the extraction rate for the gelatin and glass fiber filters were compared with direct inoculation experiments. Two glass fiber filters and one gelatin filter were placed in individual petri dishes. Virus suspension solution, containing approximately 31,000 live viruses, was then injected onto each filter inside of the petri dish. Next, the gelatin filter was dissolved in 3 mL of UTM solution. One of the glass fiber filters was treated with the submersion method using 3 mL of UTM solution, and the other one was treated with the swab method using another 3 mL of UTM solution. Subsequent culture analysis of the liquid samples detected concentrations of approximately 4,700, 470, and <31 $TCID_{50}$/mL for the dissolved gelatin filter, submerged glass fiber filter, and the swabbed glass fiber filter, respectively. After multiplying the detected concentrations by the volume of the UTM solution (3 mL), the total number of viruses detected from the gelatin filter, the submersion method, and the swab method were calculated to be

14100, 1410, and <93, respectively. These results indicate that the gelatin filter outperformed the glass fiber filter ten-fold and was able to retrieve around 45% of the total virus loading that had been injected into the petri dish. It is likely that viruses were killed during the processing, which would explain the moderate virus recovery percentage of the gelatin filter. The glass fiber filter fared even worse, with an extraction rate of only 5% and 0.3% for the submersion and swab methods, respectively. A similar concern, regarding the impact of low extraction rates on qPCR results, was previously expressed by Hospodsky, Yamamoto, & Peccia (2010). Either the glass fiber filters may bind viruses tightly to their surfaces, or the recovery process involving mechanical agitation and vibration may deactivate virus.

After direct inoculation experiments, the liquid samples from the SKC BioSampler, the gelatin filter, and the glass fiber filter collected during atomization of the viral suspension solutions were compared using culture and Xpert PCR; results are reported in Table A2.4 and Fig. A2.5. As previously described, no viable viruses were detected during viral culture of the samples collected for the 1,000 $TCID_{50}$/mL atomized virus suspensions by any of the samplers. For suspensions of 100,000 $TCID_{50}$/mL, only the SKC BioSampler and the gelatin filter produced positive culture results. The SKC BioSampler retrieved approximately 100 – 1000 $TCID_{50}$/mL of 4 mL liquid in the collection vessel using viral culture, which was the highest retrieval rate of all the samplers. This was consistent with the Xpert PCR results, which showed that sample liquid from the SKC BioSampler required the lowest number of cycles to detect (Figure A2.5). The gelatin filter retrieved around 30 – 50 $TCID_{50}$/mL of 3 mL of UTM solution. The number of viral particles captured by the gelatin filter was around 3 – 35% of what was captured by the SKC BioSampler.

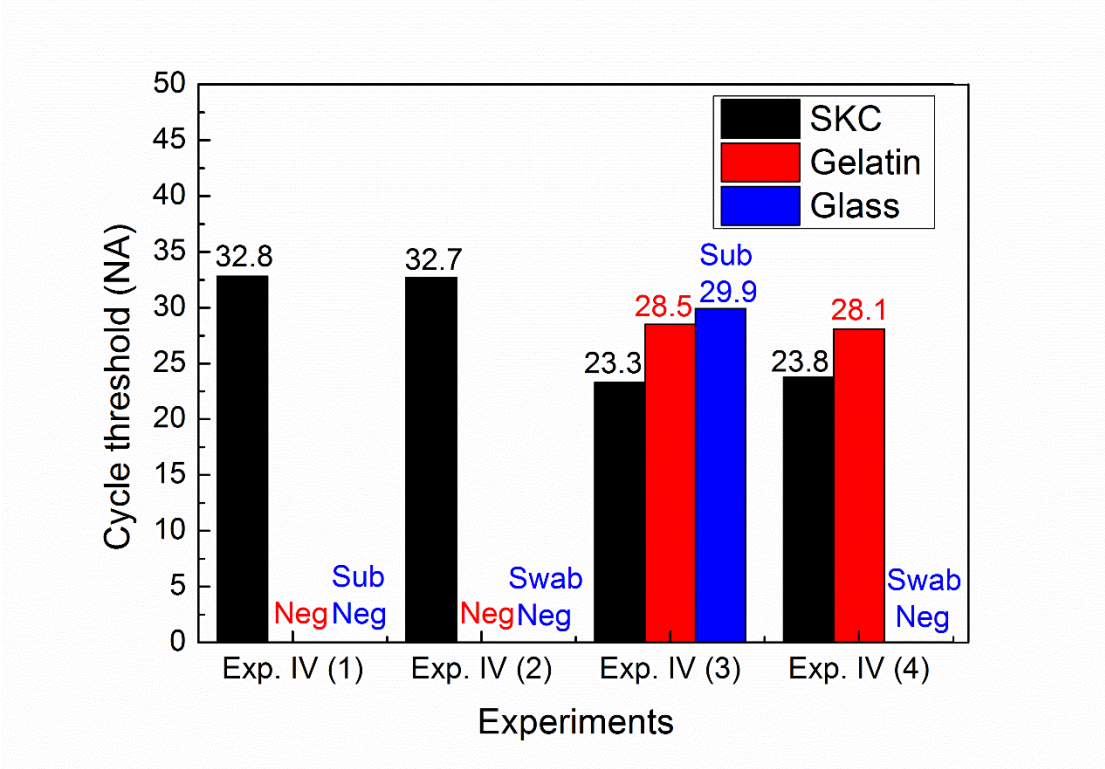

Figure A2.5 Summary of Xpert results from Experiment IV
*SKC = SKC BioSampler; Gelatin = gelatin filter; Glass = glass fiber filter; Exp = experiment; Sub = submersion method; Swab = swab method; Neg = negative (no influenza A virus was detected in the sample).

For the glass fiber filter, the Xpert reported positive results for the submersion method, and negative results for the swab method for the same virus suspension (100,000 $TCID_{50}$/mL). Therefore, the submersion extraction method was more effective than the swab method.

It is also important to compare the number of viral particles retrieved to the total number of viral particles that entered the sampler. To estimate this number, the liquid consumption rate of the atomizer was estimated and compared to the viral culture results. In general, the atomizer consumed 7 mL hourly. This means that an atomized virus suspension of 100,000 $TCID_{50}$/mL would generate a total of 90,000 viral particles in the air flow entering the SKC BioSampler, over a period of 10 minutes (the length of sampling for the current testing). This was calculated

by multiplying the initial virus concentration in the atomizer (100,000 $TCID_{50}$/mL) by the hourly liquid consumption of the atomizer (7 mL/h), multiplied by the duration of the experiment (1/6 h), multiplied by the SKC BioSampler flowrate (12.5 L/min) divided by the total flowrate for all samplers (16.5 L/min). Since there was 4 mL of liquid sample inside the SKC BioSampler, there would be around 400 to 4,000 viable viruses (100 – 1000 $TCID_{50}$/mL * 4 mL) (Table A2.4) captured by the SKC BioSampler. Therefore, the SKC BioSampler was able to collect only 0.5 – 5% of atomized viruses. This percentage is comparable with the percentage reported by Hogan et al. (2005) and Lednicky et al. (2016) for the 20 mL SKC BioSampler. A low collection efficiency will be a concern in the clinical setting, especially for low virus concentrations. This work indicates that if a positive result is obtained using SKC BioSamplers, the virus concentration in the surroundings is likely to be high. However, negative results can not assure a healthy environment. Further work and improvements are required to extrapolate the results in practical use for quantitatively measuring airborne viruses. The recently developed laminar-flow, water-based viable virus aerosol sampler (VIVAS) may be as a promising technology to improve the viable sampling efficiency (J. Lednicky et al., 2016; Pan et al., 2016).

Although the virus collection efficiency for the SKC BioSampler is relatively low, it far outperforms both the gelatin (maximum of 1.5%) and glass fiber filter (too low to quantify). There are several reasons for the overall low collection efficiency reported here. The large pressure drop in the atomizer may have killed and deactivated some of the virus particles. The similar T/I values of the prepared viral suspension and the BioSampler® collected liquid implies that the nebulization process did not overly affect the viability of virus (Fabian et al., 2009). However, the T/I value characterizes the viability of the captured influenza virus, rather than quantitively estimates the proportion of the viruses captured by the samplers. So, it is possible

that particles are destroyed or deactivated during the atomization process. Furthermore, the droplets from the atomizer evaporated gradually during the sampling process, which may lower the portion of viable viruses (Haig et al., 2016). Equally, increasing sampling time will also desiccate or deteriorate the filters, either of which could compromise the viability of the pathogen (Haig et al., 2016, Wu, Shen, & Yao, 2010). This evaporative process may also decrease the risk of viable virus survival in clinical settings. Specific to the SKC BioSampler, the pressure variation at the critical orifice and the shear force due to the violent vortex in the collection vessel could also influence the viability of the viruses (Haig et al., 2016). There may also have been reaerosolization of the particles due to the high sampling flowrate and the low virus concentration of the liquid in the collection vessel (Riemenschneider et al., 2010). Virus particles adhere to the walls of the collection vessel may further decrease the collection efficiency (Haig et al., 2016). Studies have also shown that the volume of the collection liquid can impact viability (Zheng & Yao, 2017). The dry surfaces intrinsic to the filters may not be a suitable environment to sustain virus viability (Dabisch et al., 2012; Lindsley et al., 2010). What is more, the additional extraction processes required for retrieval from the filters could result in even further losses.

4. Conclusions

Results indicated that the gelatin and glass fiber filters demonstrated high physical collection efficiencies. However, concerns over the stability of the gelatin filter were noted. The glass fiber filter maintained high physical collection efficiency across all measured particle sizes, sampling flowrates, and sampling times. The SKC BioSampler demonstrated a slightly lower physical collection efficiency, especially for particles around 30 - 50 nm, but had the highest virus collection efficiency compared to either of the filters. This was most likely due to the

liquid media inside the collection vessel, which provided a more suitable environment for the preservation of viruses. Although the SKC BioSampler demonstrated the highest retrieval rates, it still only managed to recover at most 5% of the total influenza A virus particles. However, the retrieval rate for the gelatin filter (at most 1.5 %) and glass filter (too low to quantify) were still lower. In order to obtain positive results for any of the samplers, the total concentration of viruses entering the sampler must be considered. This poses a challenge when working in the field where there is expected to be substantial variability in viral shedding by a patient depending on a patient's immune status and vaccination status, how long they have been symptomatic and whether they are taking antiviral medications.

References

Bischoff, W. E., Swett, K., Leng, I., & Peters, T. R. (2013). Exposure to influenza virus aerosols during routine patient care. *Journal of Infectious Diseases, 207*(7), 1037-1046.

Belser, J. A., Gustin, K. M., Katz, J. M., Maines, T. R., & Tumpey, T. M. (2014). Influenza virus infectivity and virulence following ocular-only aerosol inoculation of ferrets. *J. Virol.*, 88(17), 9647-9654.

Blachere, F. M., Lindsley, W. G., Slaven, J. E., Green, B. J., Anderson, S. E., Chen, B. T., & Beezhold, D. H. (2007). Bioaerosol sampling for the detection of aerosolized influenza virus. *Influenza Other Respir Viruses., 1*(3), 113-120.

Boon, A. C., Krauss, S., Rubrum, A., Webb, A. D., Webster, R. G., McElhaney, J., & Webby, R. J. (2010). Cross-reactive neutralizing antibodies directed against pandemic H1N1 2009 virus are protective in a highly sensitive DBA/2 mouse influenza model. *Journal of virology, 84*(15), 7662-7667.

Brankston, G., Gitterman, L., Hirji, Z., Lemieux, C., & Gardam, M. (2007). Transmission of influenza A in human beings. *Lancet Infectious Disease, 7*, 257-265.

Burton, N. C., Grinshpun, S. A., & Reponen, T. (2007). Physical collection efficiency of filter materials for bacteria and viruses. *Annals of Occupational Hygiene, 51*(2), 143-151.

Cao, G., Noti, J., Blachere, F., Lindsley, W., & Beezhold, D. (2011). Development of an improved methodology to detect infectious airborne influenza virus using the NIOSH bioaerosol sampler. *Journal of Environmental Monitoring, 13*(12), 3321-3328.

Charu, V., Zeger, S., Gog, J., Bjørnstad, O. N., Kissler, S., Simonsen, L., . . . Viboud, C. (2017). Human mobility and the spatial transmission of influenza in the United States. *PLOS Computational Biology, 13*(2), e1005382. doi: 10.1371/journal.pcbi.1005382

Dabisch, P., Yeager, J., Kline, J., Klinedinst, K., Welsch, A., & Pitt, M. L. (2012). Comparison of the efficiency of sampling devices for aerosolized Burkholderia pseudomallei. *Inhalation Toxicology, 24*(5), 247-254. doi: 10.3109/08958378.2012.666682

Fabian, P., McDevitt, J., Houseman, E., & Milton, D. (2009). Airborne influenza virus detection with four aerosol samplers using molecular and infectivity assays: considerations for a new infectious virus aerosol sampler. *Indoor air, 19*(5), 433-441.

Fidler, D. (2004). *SARS, Governance and the Globalization of Disease*: Springer.

Gao, X., Li, Y., & Leung, G. M. (2009). Ventilation Control of Indoor Transmission of Airborne Diseases in an Urban Community. *Indoor and Built Environment, 18*(3), 205-218. doi: doi:10.1177/1420326X09104141

Grinshpun, S. A., Willeke, K., Ulevicius, V., Juozaitis, A., Terzieva, S., Donnelly, J., . . . Brenner, K. P. (1997). Effect of Impaction, Bounce and Reaerosolization on the

Collection Efficiency of Impingers. *Aerosol Science and Technology, 26*(4), 326-342. doi: 10.1080/02786829708965434

Haig, C., Mackay, W., Walker, J., & Williams, C. (2016). Bioaerosol sampling: sampling mechanisms, bioefficiency and field studies. *Journal of Hospital Infection, 93*(3), 242-255.

Harstad, J. B. (1965). Sampling submicron T1 bacteriophage aerosols. *Appl. Microbiol., 13*(6), 899-908.

Harstad, J. B., Decker, H. M., Buchanan, L., & Filler, M. E. (1967). Air filtration of submicron virus aerosols. *Am J Public Health Nations Health., 57*(12), 2186-2193.

Hospodsky, D., Yamamoto, N., & Peccia, J. (2010). Accuracy, precision, and method detection limits of quantitative PCR for airborne bacteria and fungi. *Appl. Environ. Microbiol., 76*(21), 7004-7012.

Hogan, C., Kettleson, E., Lee, M. H., Ramaswami, B., Angenent, L., & Biswas, P. (2005). Sampling methodologies and dosage assessment techniques for submicrometre and ultrafine virus aerosol particles. *Journal of Applied Microbiology, 99*(6), 1422-1434.

Jena, S., & Singh, G. (2017). Human health risk assessment of airborne trace elements in Dhanbad, India. [Article]. *Atmospheric Pollution Research, 8*(3), 490-502. doi: 10.1016/j.apr.2016.12.003

Lau, J. (2004). SARS Transmission among Hospital Workers in Hong Kong-Volume 10, Number 2—February 2004-Emerging Infectious Disease journal-CDC.

Lednicky, J., Pan, M., Loeb, J., Hsieh, H., Eiguren-Fernandez, A., Hering, S., . . . Wu, C.-Y. (2016). Highly efficient collection of infectious pandemic influenza H1N1 virus (2009) through laminar-flow water based condensation. *Aerosol Sci. Technol., 50*(7), i-iv.

Lednicky, J. A., & Loeb, J. C. (2013). Detection and isolation of airborne influenza A H3N2 virus using a Sioutas Personal Cascade Impactor Sampler. *Influenza Res Treat., 2013*.

Leung, N. H. L., Zhou, J., Chu, D. K. W., Yu, H., Lindsley, W. G., Beezhold, D. H., . . . Cowling, B. J. (2016). Quantification of influenza virus RNA in aerosols in patient rooms. [Article]. *PLoS ONE, 11*(2). doi: 10.1371/journal.pone.0148669

Lewandowski, R., Kozłowska, K., Szpakowska, M., & Trafny, E. A. (2013). Evaluation of applicability of the Sartorius Airport MD8 sampler for detection of Bacillus endospores in indoor air. *Environmental Monitoring and Assessment, 185*(4), 3517-3526. doi: 10.1007/s10661-012-2807-6

Lin, X., Willeke, K., Ulevicius, V., & Grinshpun, S. A. (1997). Effect of Sampling Time on the Collection Efficiency of All-Glass Impingers. *American Industrial Hygiene Association Journal, 58*(7), 480-488. doi: 10.1080/15428119791012577

Lindsley, W. G., Blachere, F. M., Thewlis, R. E., Vishnu, A., Davis, K. A., Cao, G., . . . Khakoo, R. (2010). Measurements of airborne influenza virus in aerosol particles from human coughs. *PloS one, 5*(11), e15100.

Marchand, G., Duchaine, C., Lavoie, J., Veillette, M., & Cloutier, Y. (2016). Bacteria emitted in ambient air during bronchoscopy—a risk to health care workers? *American journal of infection control, 44*(12), 1634-1638.

Nguyen, T. T., Poh, M. K., Low, J., Kalimuddin, S., Thoon, K. C., Ng, W. C., . . . Gray, G. C. (2017). Bioaerosol sampling in clinical settings: A promising, noninvasive approach for detecting respiratory viruses. [Article]. *Open Forum Infectious Diseases, 4*(1). doi: 10.1093/oid/ofw259

Pan, M., Eiguren-Fernandez, A., Hsieh, H., Afshar-Mohajer, N., Hering, S., Lednicky, J., Hugh Fan, Z., Wu, C. Y. (2016). Efficient collection of viable virus aerosol through laminar-flow, water-based condensational particle growth. *J. Appl. Microbiol., 120*(3), 805-815.

Reed, L. J., & Muench, H. (1938). A simple method of estimating fifty per cent endpoints. *American journal of epidemiology, 27*(3), 493-497.

Riemenschneider, L., Woo, M. H., Wu, C. Y., Lundgren, D., Wander, J., Lee, J. H., . . . Heimbuch, B. (2010). Characterization of reaerosolization from impingers in an effort to improve airborne virus sampling. *J. Appl. Microbiol., 108*(1), 315-324.

Rossman, J. S., Leser, G. P., & Lamb, R. A. (2012). Filamentous influenza virus enters cells via macropinocytosis. *J. Virol., 86*(20), 10950-10960.

Teunis, P. F. M., Brienen, N., & Kretzschmar, M. E. E. (2010). High infectivity and pathogenicity of influenza A virus via aerosol and droplet transmission. *Epidemics, 2*, 215-222.

Thorne, P. S., Reynolds, S. J., Milton, D. K., Bloebaum, P. D., Zhang, X., Whitten, P., & Burmeister, L. F. (1997). Field evaluation of endotoxin air sampling assay methods. *Am. Ind. Hyg. Assoc. J., 58*(11), 792-799.

Tian, S., Pan, Y., Wang, J., & Wang, Y. (2016). Concurrent measurements of size-segregated particulate sulfate, nitrate and ammonium using quartz fiber filters, glass fiber filters and cellulose membranes. [Article]. *Atmospheric Environment, 145*, 293-298. doi: 10.1016/j.atmosenv.2016.09.018

Tung-Thompson, G., Libera, D. A., Koch, K. L., Francis III, L., & Jaykus, L.-A. (2015). Aerosolization of a human norovirus surrogate, bacteriophage MS2, during simulated vomiting. *PLoS ONE, 10*(8), e0134277.

Turgeon, N., Toulouse, M.-J., Martel, B., Moineau, S., & Duchaine, C. (2014). Comparison of five bacteriophages as models for viral aerosol studies. *Applied and environmental microbiology, 80*(14), 4242-4250.

VanOsdell, D. W., Liu, B. Y., Rubow, K. L., & Pui, D. Y. (1990). Experimental study of submicrometer and ultrafine particle penetration and pressure drop for high efficiency filters. *Aerosol Science and Technology, 12*(4), 911-925.

Verreault, D., Moineau, S., & Duchaine, C. (2008). Methods for sampling of airborne viruses. *Microbiology and Molecular Biology Reviews, 72*(3), 413-444.

Wang, Y., Li, J., Leavey, A., O'Neil, C., Babcock, H. M., & Biswas, P. (2016). Comparative Study on the Size Distributions, Respiratory Deposition, and Transport of Particles Generated from Commonly Used Medical Nebulizers. *Journal of Aerosol Medicine and Pulmonary Drug Delivery*.

Weber, T. P., & Stilianakis, N. I. (2008). Inactivation of influenza A viruses in the environment and modes of transmission: A critical review. *Journal of Infection, 57*, 361-373.

Wei, Z., Rosario, R. C., & Montoya, L. D. (2010). Collection efficiency of a midget impinger for nanoparticles in the range of 3–100 nm. *Atmospheric Environment, 44*(6), 872-876.

WHO, W. H. O. (2004). WHO guidelines for the global surveillance of severe acute respiratory syndrome (SARS). Updated recommendations, October 2004 Retrieved 03.14.17, from http://www.who.int/csr/resources/publications/WHO_CDS_CSR_ARO_2004_1/en/

WHO, W. H. O. (2009). Weekly epidemiological record Retrieved 03.14.17, from http://www.who.int/wer/2009/wer8421.pdf?ua=1

Williams, G. D., Pinto, A. K., Doll, B., & Boon, A. C. (2016). A North American H7N3 influenza virus supports reassortment with 2009 pandemic H1N1 and induces disease in mice without prior adaptation. *Journal of virology, 90*(9), 4796-4806.

Wu, Y., Shen, F., & Yao, M. (2010). Use of gelatin filter and BioSampler in detecting airborne H5N1 nucleotides, bacteria and allergens. *Journal of Aerosol Science, 41*(9), 869-879.

Zhang, J., Bai, R., Zhou, Z., Liu, X., & Zhou, J. (2017). Simultaneous analysis of nine aromatic amines in mainstream cigarette smoke using online solid-phase extraction combined with liquid chromatography-tandem mass spectrometry. [Article in Press]. *Analytical and Bioanalytical Chemistry*, 1-13. doi: 10.1007/s00216-017-0245-6

Zheng, Y., & Yao, M. (2017). Liquid impinger BioSampler's performance for size-resolved viable bioaerosol particles. *Journal of Aerosol Science, 106*, 34-42.

Table A2.S1 The cycle threshold established for the UTM and the PBS solution containing different concentrations of influenza A.

Virus particle concentration in the suspension (#/mL)	Cycle threshold values for the PBS and the UTM virus suspensions			
	PBS		UTM	
	Assay 1	Assay 2	Assay 1	Assay 2
100	21	21.8	20.4	21.3
1,000	17.6	18.4	17.2	18.1
10,000	13.9	14.7	14	14.7

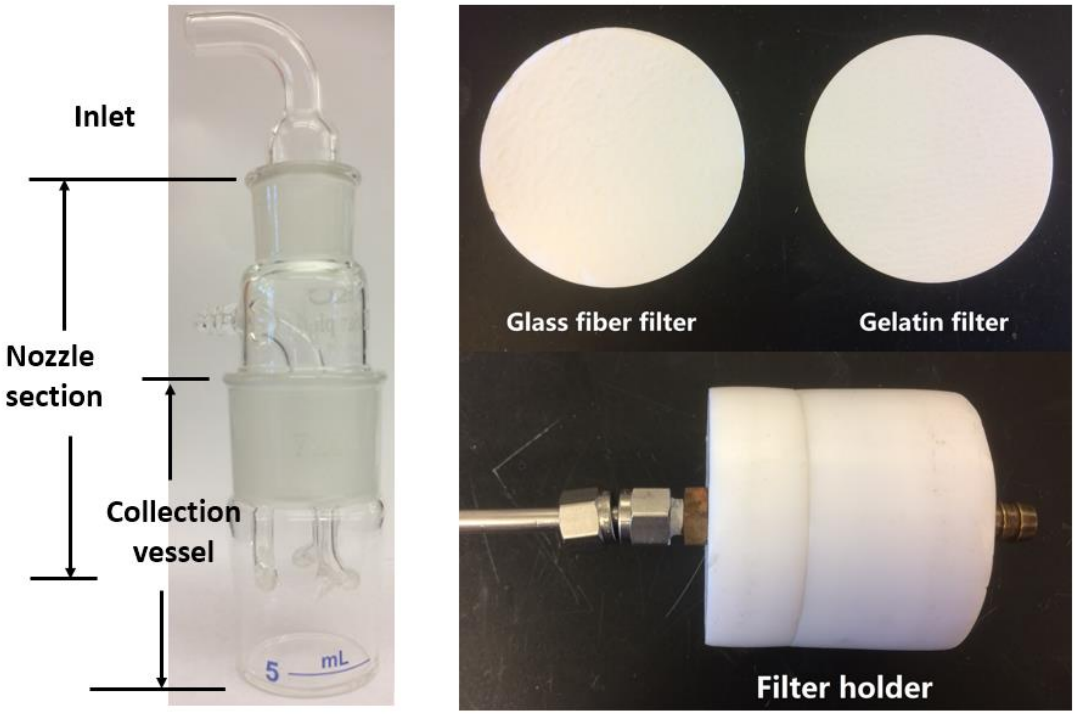

Figure A2.S1 Major components of the SKC BioSampler, the glass fiber filter, and the gelatin filter with the filter holder.

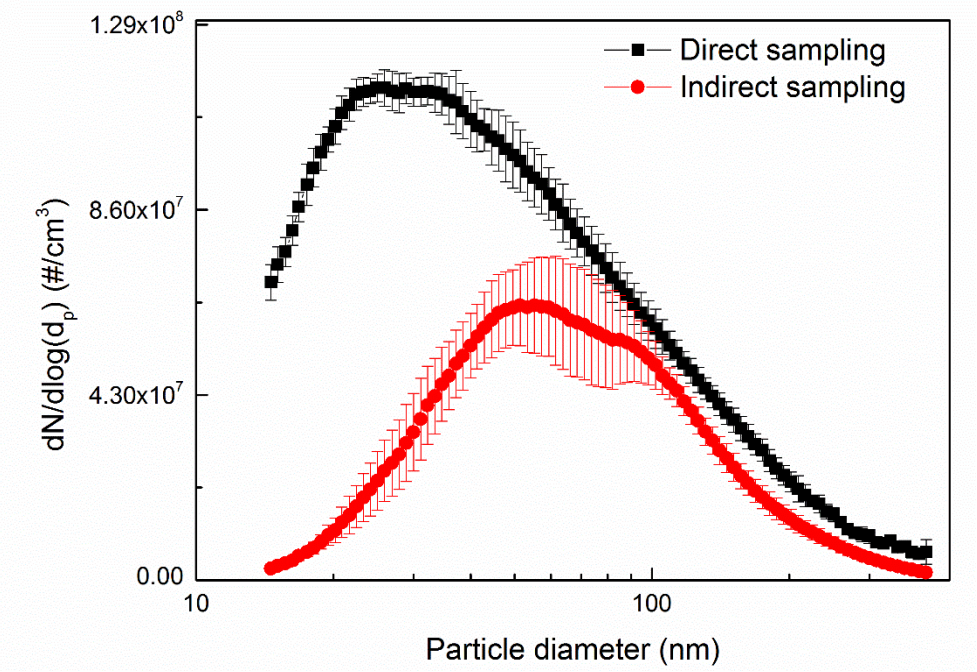

Figure A2.S2 Particle size distributions for direct sampling and indirect sampling.

Figure A2.S3 A photo of the gelatin filter dissolved in the filter holder after sampling for nine minutes.

Appendix III: Comparative study on the size distributions, respiratory deposition, and transport of particles generated from commonly used medical nebulizers

The results of this chapter have been published in Wang, Y., Li, J., Leavey, A., O'Neil, C., Babcock, H. M., & Biswas, P. (2017). Comparative study on the size distributions, respiratory deposition, and transport of particles generated from commonly used medical nebulizers. Journal of aerosol medicine and pulmonary drug delivery, 30(2), 132-140.

Abstract:

Medical nebulizers are widely and conveniently used to deliver medication to the lungs as an inhalable mist; however, the deposition of nebulized particles in the human respiratory system, and the transport of the nebulized particles in the environment have not been studied in detail. Five medical nebulizers of three different types (constant-output, breath-enhanced, and dosimetric) were evaluated. The size distribution functions (SDFs) and respiratory deposition of the particles generated from the nebulizers were characterized. The SDFs were obtained with an Aerodynamic Particle Sizer (APS, TSI Inc., St. Paul) after data correction, and the respiratory deposition was calculated according to the model developed by the International Commission on Radiological Protection. The evaporation, Brownian diffusion, and convective movement are further calculated based on aerosol properties. The SDFs measured by the APS indicated that most of the generated particles were in the size range of 1 to 8 μm. The operating pressure and flow rate affected the number-based SDF of the nebulized particles. Although different values of mean aerodynamic diameter (MAD) were obtained for the nebulizers, the mass median aerodynamic diameter (MMAD) did not differ significantly from each other (between 4 and 5 μm). According to calculation, the deposition of particles in the head airways region accounted for the most of the particle mass collected by the respiratory system. Convective movement was the dominant mechanism for the transport of particles in the size ranges investigated. Relative humidity-dependent evaporation can significantly decrease the size of the emitted particles, resulting in a different respiratory deposition pattern such that the amount of particles deposited in the alveolar region is greatly enhanced. Appropriate protection from these particles should be considered for those persons for whom the medication is not intended (e.g., healthcare workers, family members).

Introduction

Medical nebulizers are widely used in respiratory treatments, where medicine-containing droplets are generated by atomization and delivered to patients through the inhalation gas flow[1]. The nebulized particles deposit in different regions of the respiratory system and deliver the drug to the target area. Three types of commercial medical nebulizers are currently on the market[2]: 1) constant-output; 2) breath-enhanced; and 3) dosimetric. Each type of medical nebulizer has different advantages in terms of cost, reliability, and efficiency. The constant-output nebulizers operate with a T-mouthpiece, where half of the medication is exhausted during exhalation. This waste of medication is eliminated in the breath-enhanced and dosimetric type nebulizers because they have one-way valves that only allow particles to be generated and transported during inhalation. The size of the nebulized particles is one of the most important factors that determine the performance of a medical nebulizer. Other parameters, such as breathing rate and maneuver, lung structure and dimension, also significantly influence the particle deposition in lungs. The mass median aerodynamic diameter (MMAD), often used to evaluate medical nebulizers, is the particle diameter separating the higher half of the particle mass from the lower half. Because particle deposition characteristics are closely related to particle size, MMAD determines where in the respiratory tract, and in what proportion, most of the particles are deposited after they are inhaled[3]. The particle size distribution function (SDF) provides the particle concentration as a function of the particle diameter[4]. By further considering the deposition efficiencies as a function of particle diameter, we can accurately calculate the fraction and location of particles deposited in respiratory systems[5].

Various instruments can measure the size characteristics of nebulized particles. Cascade impactors use a particle's inertia to classify particles according to its aerodynamic size[6, 7]. The drawbacks of this method are the intensive labor required and the low-resolution of the SDF due to the limited number of impactor stages, constrained by their mass and bulk. Laser diffraction determines aerosol SDF based on the Mie theory, which is dependent on the material type and shape of the particles[8]. Time-of-flight (TOF) aerosol analyzers use light detection to measure the aerodynamic diameters of particles during a controlled acceleration in a well-defined flow field, but coincidence effects during sampling limit the accuracy of the measurement above certain particle concentrations[9-11].

Multiple studies have used these methods to compare the performance of medical nebulizers, and concluded that the MMAD of nebulized particles differ significantly depending on the design of the nebulizers[2, 12-15]. Up until now, very few studies have reported the SDFs of the nebulized particles generated by different types of nebulizers. Furthermore, only limited studies have investigated the effects of a nebulizer's operating conditions, such as gas flow rate and pressure, on the SDF of the generated particles[16-18]. The operating pressure affects the shear force applied on the nebulized droplets, which influences the size of the generated particles. The gas flow rate, typically decided by a patient's inhalation flow rate, also determines the size and amount of particles lost in the nebulizer due to inertial impaction. The resulting change in the particle SDF will ultimately change the amount of medicine deposited in the patient's respiratory tract.

Impaction, settling, and Brownian motion are three major mechanisms that cause particles to deposit in the respiratory system. A particle's size determines the relative importance of these mechanisms, and affects the fraction of particles depositing in the three regions of the respiratory system: the head airways (HA) region, tracheobronchial (TB) region, and alveolar (AL) region.

A model developed by the International Commission on Radiological Protection (ICRP[19]) is widely used for predicting total and regional deposition of inhaled particles. It estimates the amount of deposited particles over a wide range of particle sizes and breathing conditions. Hence, by integrating the product of the SDF and the size dependent deposition efficiency, one can calculate the amount and fraction of nebulized particles depositing in different respiratory regions, and hence quantify the dose delivered to a target region.

However, one unintended consequence of using nebulizers for drug delivery to a patient is the potential exposure of healthcare workers, which may be especially concerning if the medication has side effects, given the likelihood that medical staff will be exposed to this medication, or multiple medications, over many years. As particles move through the air, they age and transform, thus their SDF and deposition characteristics may change, leading to different deposition fractions in the respiratory systems of those nearby, than the ones of the intended target. Therefore, it is imperative to study not just the SDF and deposition characteristics of freshly nebulized particles, but also to examine the changing characteristics of these nebulized particles as they transport and transform away from source and are subsequently inhaled by nearby individuals.

In this study, five commonly used medical nebulizers under a range of operating conditions, focusing on the SDF and deposition characteristics of the nebulized particles are evaluated. The transportation and transformation of the nebulized particles in the surrounding environment was also analyzed, and the deposition of the transported particles in the respiratory systems of individuals present in the vicinity is briefly discussed.

Materials and Methods

Experimental Setup

Figure A3.1 shows schematic diagrams of the tested medical nebulizers and the experimental setup. Five nebulizers of three types were tested in this study: the AirLife Misty Max 10 nebulizer (Figure A3.1a, CareFusion, Chicago, IL) and SideStream nebulizer (Figure A3.1b, Philips Respironics, Parsippany, NJ) are the constant-output type; the SideStream Plus nebulizer (Figure A3.1c, Philips Respironics, Parsippany, NJ) and PARI LC Sprint nebulizer (Figure A3.1d, PARI Respiratory Equipment, Inc., Midlothian, VA) are the breath-enhanced type; and the AeroEclipse II Breath Actuated nebulizer (Figure A3.1e, Monaghan Medical Corp., Plattsburgh, NY) is a dosimetric type. For simplicity, these five nebulizers are referred to as the Misty Max 10, SideStream, SideStream Plus, PARI, and AeroEclipse, respectively. The constant-output nebulizers generate particles regardless of the patient's breathing status. During exhalation, the atomized particles can escape from the exit points of the nebulizers due to the convective flow of the exhaled air, resulting in a loss of medication. The breath-enhanced nebulizers use one-way valves that allow generated particles to exit the nebulization chamber only during inhalation, while the exhaled air is released directly into a port near the mouthpiece. The dosimetric nebulizers go even further by connecting the one-way valves with a switch that controls the liquid flow through the nebulizer, so that particles are only generated during inhalation.

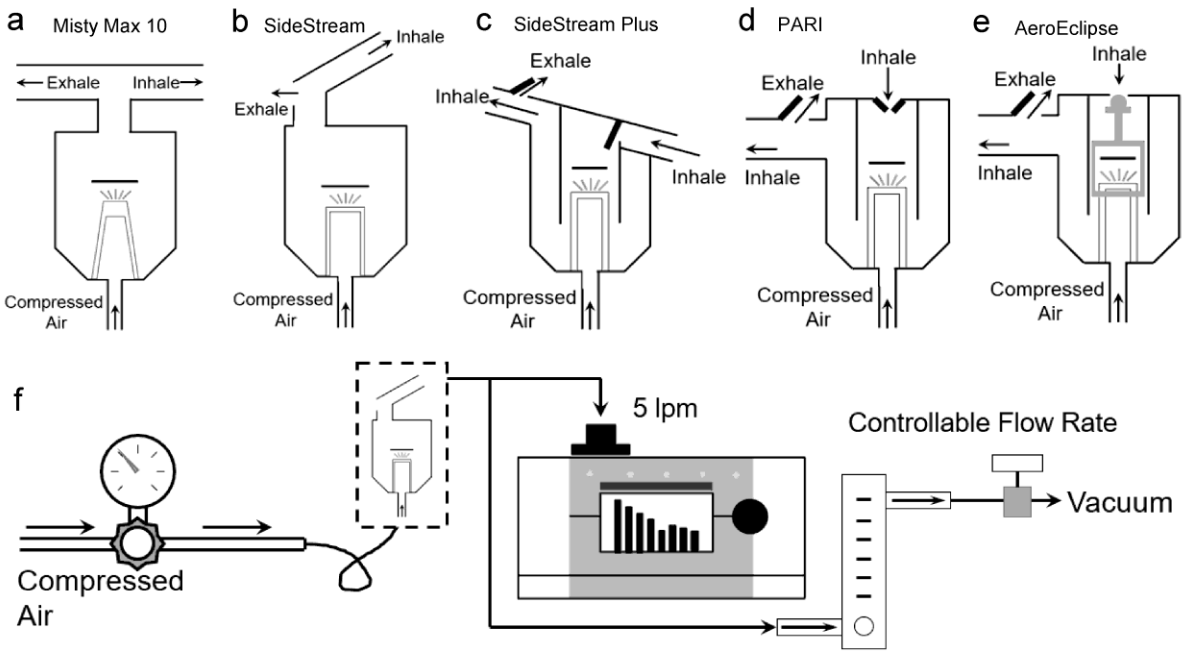

Figure A3.1 Schematic diagrams of the five nebulizers and the experimental setup. a. Misty Max 10 nebulizer; b. SideStream nebulizer; c. SideStream Plus nebulizer; d. PARI nebulizer; e. AeroEclipse nebulizer; f. diagram of the experimental setup.

Figure A3.1f displays the platform for testing the performance of the nebulizers. The experiments were conducted in an open laboratory space where the temperature and relative humidity (RH) were kept at 22.5 ^{o}C and 45%, respectively. Before nebulization, each device was filled with 5 ml of 0.9 % NaCl (>99.0%, Sigma-Aldrich, St. Louis, MO) aqueous solution. Compressed air was used as the high pressure source, and controlled by a pressure regulator (Airgas, Inc., Radnor, PA). The flow through the mouthpiece (outlet) of the nebulizer was split into two streams. One stream was fed into an aerodynamic particle sizer (APS, TSI 3321, St. Paul, MN) through a 10 cm tube at a flow rate of 5 lpm. To achieve a controllable outlet flow rate, the other stream was connected to a rotameter (Dwyer Instruments, Michigan City, IN) and a vacuum source. The RH value of 98±5% at the inlet of the APS was measured with a sensor probe (HMP60, Vaisala Inc., accuracy: ±3% in 0 to 90% RH, ±5% in 90 to 100% RH).

Operating on the time-of-flight theory, the APS measures the aerodynamic size distributions of particles ranging from 0.5 to 20 μm, which is a suitable range for evaluating medical nebulizers whose MMAD values are between 1 and 10 μm. In the APS, the sampled particles flow along the centerline of an accelerating flow created by the sheath air. As they pass through two broadly focused laser beams, each particle scatters light twice, which is collected by the photodetector in the APS. The aerodynamic particle size is then calculated based on the time interval between the pulses of the scattered light. Existing work has shown that shifts in particle size may occur due to the gradual accumulation of particles in the nozzle of the APS. This size shift[20] in μm is quantified by Eq. A3.1 as shown in Table A3.1. Other important equations used in this study are also listed in Table A3.1.

Table A3.1 Equations used for calculating the respiratory deposition, transform, and transport of nebulized particles.

No.	Equation
A3.1	$\Delta = -\frac{2.723\times10^{-4} d_p^2}{\eta^{0.6486}\sigma^{0.3864}}$
A3.2	$DF_{HA} = IF[\frac{1}{1+\exp(6.84+1.183\ln d_p)} + \frac{1}{1+\exp(0.924-1.885\ln d_p)}]$
A3.3	$DF_{TB} = \frac{0.00352}{d_p}\{\exp[-0.234(\ln d_p + 3.40)^2] + 63.9\exp[-0.819(\ln d_p - 1.61)^2]\}$
A3.4	$DF_{AL} = \frac{0.0155}{d_p}\{\exp[-0.416(\ln d_p + 2.84)^2] + 19.11\exp[-0.482(\ln d_p - 1.362)^2]\}$
A3.5	$DF = IF[0.0587 + \frac{0.991}{1+\exp(4.77+1.485\ln d_p)} + \frac{0.943}{1+\exp(0.508-2.58\ln d_p)}]$
A3.6	$\tau = \frac{kTd_p^2}{4D(p_d - p_e)v_m}$
A3.7	$\ln\frac{p_d}{p_s} = \frac{4\sigma v_m}{d_p kT} - \frac{6n_2 v_m N_A}{\pi d_p^3}$
A3.8	$\frac{\partial n}{\partial t} = \frac{D}{r}(\frac{\partial^2 (nr)}{\partial^2 r})$
A3.9	$n = \frac{n_0 R}{r}[1 - erf(\frac{r-R}{\sqrt{2Dt}})]$
A3.10	$\frac{\partial n}{\partial t} + \nabla\cdot(n\vec{v}) = 0$
A3.11	$\tau_s = \frac{\rho_p d_p^2 C}{18\mu}$
A3.12	$v_g = \frac{g\rho_p d_p^2 C}{18\mu}$
A3.13	$v_n \approx \sqrt{\frac{\Delta\rho}{\rho} gL}$

Experimental Plan

The particle size distribution function (SDF) and time for nebulizing the entire solution were experimentally studied. Before directly comparing the five nebulizers, we first investigated the influence of the operating conditions on their performance. In this study, the operating pressure and the flow rate at the nebulizer outlet can change the SDF of the nebulized particles. Pressures of 25, 35, and 45 psi were used, covering the recommended operating pressures of the tested nebulizers. A nebulizer's outlet flow rate is typically determined by a patient's inhalation flow rate, which is strongly dependent on the age, gender, and exercise level of the patient[21]. Based on the age and activity of a person, the average inhalation flow rate may range from 10 to 40 lpm [3]. In this study, nebulizer outlet flow rates of 10, 20, and 30 lpm were used, resulting in flow rates through the bypass stream of 5, 15, and 25 lpm, respectively. The results and discussion highlight the influence of operating conditions on the Misty Max 10 nebulizer only, since similar influences were also observed for the other nebulizers. The direct comparisons among the five nebulizers were conducted at a pressure of 35 psi and an outlet flow rate of 20 lpm. Each test was conducted at least three times to ensure repeatability. With the obtained SDF, we could further calculate the respiratory deposition and transport of nebulized particles.

Respiratory deposition of nebulized particles

The deposition of particles in the human respiratory system is strongly dependent on the SDF of the particles[22]. Smaller particles have larger diffusivity and smaller inertia, making it easier for them to diffuse to the deeper alveolar (AL) region, where the particle residence time is the highest and the airway is the narrowest. With higher mass and inertia, the larger particles are predominantly collected in the head airways (HA) and tracheobronchial (TB) regions due to

impaction. Settling by gravity further affects particle deposition in the TB regions. Apart from particle SDF, the deposition of particles is also affected by breathing conditions. There is large inter-subject variability among adults and children, and individuals may have different deposition patterns. The ICRP model uses empirical equations based on experimental data and theory to characterize deposition by different mechanisms. Averaging the data for males and females at three exercise levels yields a set of simplified equations which estimates the deposition fractions of d_p -sized (aerodynamic size) particles in different respiratory regions.

The deposition fraction for the HA region (DF_{HA}) is calculated by Eq. A3.2, where IF is the inhalable fraction and satisfies $IF = 1 - 0.5(1 - \frac{1}{1 + 0.00076 d_p^{2.8}})$. The deposition fractions for the TB region (DF_{TB}), AL region (DF_{AL}), and the whole respiratory system are calculated by Eqs. A3.3, A3.4, and A3.5, respectively. Since the APS measures the aerodynamic particle size, the mass-based SDF can be calculated by multiplying the size-based SDF with the mass of particles at each size, where particles were assumed to be spherical. The regional and total deposition of particle mass are then calculated by integrating the product of *DF*s (DF_{HA}, DF_{TB}, and DF_{AL}) and the mass-based particle SDF, and the total particle mass concentration is calculated by integrating the mass-based particle SDF only. Further, we can obtain the mass fraction of particles deposited in different regions of the respiratory system by taking the ratio of the deposited mass over the total particle mass.

Transport of nebulized particles

Medical nebulizers may release some of the generated particles into the surrounding environment. These particles can then transport to the respiratory systems of nearby healthcare workers. Hence, it is important to examine how particle properties change during their transportation through the surrounding environment, for example, the medicine-containing droplets may lose solvent due to evaporation, leading to a change in the aerodynamic particle size. The movement of the nebulized particles are governed by Brownian diffusion, as well as the convective flow of the surrounding air. Theoretically, these mechanisms should be solved simultaneously to accurately predict the transform and transport of particles. However, the combined equation is a complex non-linear second order partial differential equation which cannot be solved analytically. To simplify this analysis, the three processes that alter particles' properties: evaporation, Brownian diffusion, and convective flow, are considered separately.

Evaporation occurs when the pressure of the solvent at the surface of the particle is higher than the pressure of the environment. With water as the solvent, the characteristic evaporation time of a particle with a diameter of d_p can be calculated with Eq. A3.6, where D is the diffusion coefficient of water vapor molecules, p_d and p_e are the water vapor pressure at the surface of the droplet and the environment, v_m is the volume of the water molecule, k is Boltzmann's constant, and T is the temperature. p_e is dependent on the RH and the water saturation vapor pressure (p_s), where $p_e = RHp_s$, and a value of 3173 Pa was used for p_s according to the property of water vapor at 25 ^{o}C. Hospitals typically maintain an RH of at least 30 % in different types of rooms[23], meaning that the nebulized particles will evaporate quickly due to the vapor pressure difference. This reduction in size means that now any nearby healthcare workers are potentially being exposed to a higher fraction of smaller particles with high diffusivity and low

inertia, which if inhaled, may deposit further down in the AL region. Thus, the particle respiratory deposition patterns may differ between the patient for whom the medicine is targeted, and nearby healthcare workers.

It should be noted that nebulization also generates highly concentrated water vapors; hence the RH around the nebulized particles continuously changes, from around 100% at the outlet of the nebulizer to the RH in the surrounding air. In this study, characteristic evaporation times were calculated with various RH values to determine the effect of evaporation. Due to the Kelvin effect and solute interaction[24], the water vapor pressure at the surface of the droplet is determined by Eq. A3.7. In this equation, σ is the surface tension of water, n_2 is the number of moles of solute in the droplet, and N_A is Avogadro's number. In this studied case (0.9 % saline solution), $n_2 v_m N_A << \pi d_p^3 / 6$, resulting in a relationship of $p_d = p_s \exp(\frac{4\sigma v_m}{d_p kT})$. According to Eqs. A3.6 and A3.7, the characteristic evaporation time is strongly dependent on the diameter of the droplet.

Particle diffusion occurs when there is a concentration gradient of particles in space. Neglecting the convective air flow around the medical nebulizer and considering the nebulizer as a spherical source releasing particles, we derived a second-order partial differential equation (Eq. A3.8) describing the concentration distribution of particles as a function of time. In this equation, n is the concentration of particles, t is time, r is the radial distance between the point of interest and the particle source, and D is the diffusion coefficient of the particle. D is calculated by $D = kTC / 3\pi\mu d_p$, where C is the Cunningham correction factor. For particles larger than 1 μm, C has a value close to 1. The boundary conditions of Eq. A3.8 are $n(t = 0, r) = 0$,

$n(t, r = R) = n_0$, and $n(t, r = \infty) = 0$, where R is the radius of the particle-emitting source and n_0 is the particle concentration at the surface of the source. This partial differential equation has an analytical solution as shown in Eq. A3.9.

Due to ventilation and gravitational force, particles may move through convection, as described by Eq. A3.10, where $\vec{v}$ is the velocity of particles. Eq. A3.10 has boundary conditions of $n(t = 0, \forall x, y, z) = 0$, $n(x, y, z = 0, \forall t) = n_0$. For particles generated from medical nebulizers, $\vec{v}$ evolves from an initial velocity to a final constant velocity. The characteristic time that determines this evolution is calculated by Eq. A3.11, where ρ_p is the density of the particle. After the particle reaches a constant velocity, Eq. A3.10 can be further simplified by taking $\vec{v}$ out of the divergence operator. The solution for Eq. A3.10 is a wave that travels with a speed $\vec{v}$, while the shape of the solution does not change as a function of time and location. In the case of particles generated from nebulizers, this solution means that the particle concentration of a location remains 0 until the flow of particles passes by, which changes the particle concentration to n_0. Particle transport in the case of convective movement is determined by the final particle velocity. This final particle velocity is affected by the external air velocity and the particle settling velocity due to gravitational force. So, it is necessary to compare the magnitudes of these two velocities. The particle settling velocity is calculated by Eq. A3.12, where g is the gravitational acceleration. The external air velocity (v_e) is dependent on the air exchange rate of the environment and is strongly location-dependent. The air velocity due to natural convection can be estimated by Eq. A3.13. In this equation, ρ is the air density, $\Delta\rho$ is the difference in the air densities between the two locations, and L is the distance between the two locations.

Results

Figures A3.2 and A3.3 show the influence of the operating flow rate and pressure on the number-based and mass-based SDF of particles generated from the Misty Max 10 nebulizer. As the operating flow rate increased, especially from 20 to 30 lpm, the size of the particles decreased (Figure A3.2a), possibly caused by the enhanced impaction loss of larger particles as they were transported from the nebulization chamber to the mouthpiece of the nebulizer. Due to their smaller inertia, the smaller particles could follow the streamline well. At the same time, the reduced diffusion loss due to the decrease of residence time helped preserve the smaller particles. Because of this effect, the mass-based SDFs are significantly reduced at high flow rates (Figure A3.2b). Since particle mass is proportional to the cube of particle diameter, the high number concentration at around 1 μm is less important than for particles of around 4 μm. It should be noted that the change in flow rate did not significantly affect the lognormal shape of the mass-based SDF. This result implies that the regionally deposited fraction of the total deposited particle mass does not change as a function of the outlet flow rate. As the operating pressure increased, the number concentration of particles at around 1 μm dropped (Figure A3.3a). The geometric standard deviation of particle size distribution at the lower pressure condition was higher, possibly caused by the instability of the nebulization process. This instability also resulted in generating smaller particles. As the pressure further increased, the concentration of particles at around 4 μm also decreased. This change was caused by the stronger shear force, which broke up the larger particles, and the higher particle velocity, which resulted in a larger impaction loss. This effect led to a lower mass-based SDF in this size range, as indicated in Figure A3.3b.

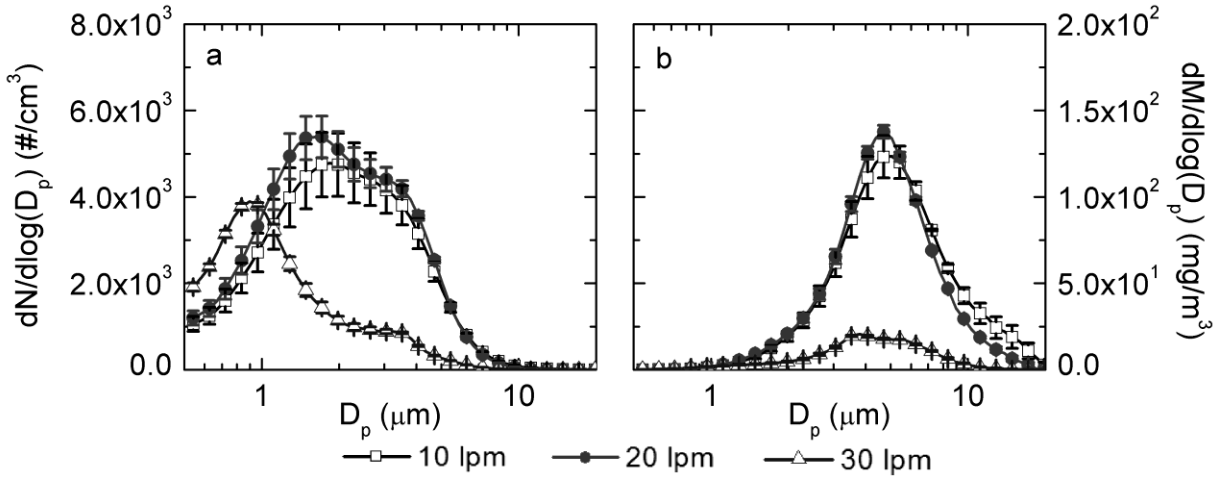

Figure A3.2 Influence of operating flow rate on the (a) number-based and (b) mass-based SDF of particles generated from the Misty Max 10 nebulizer.

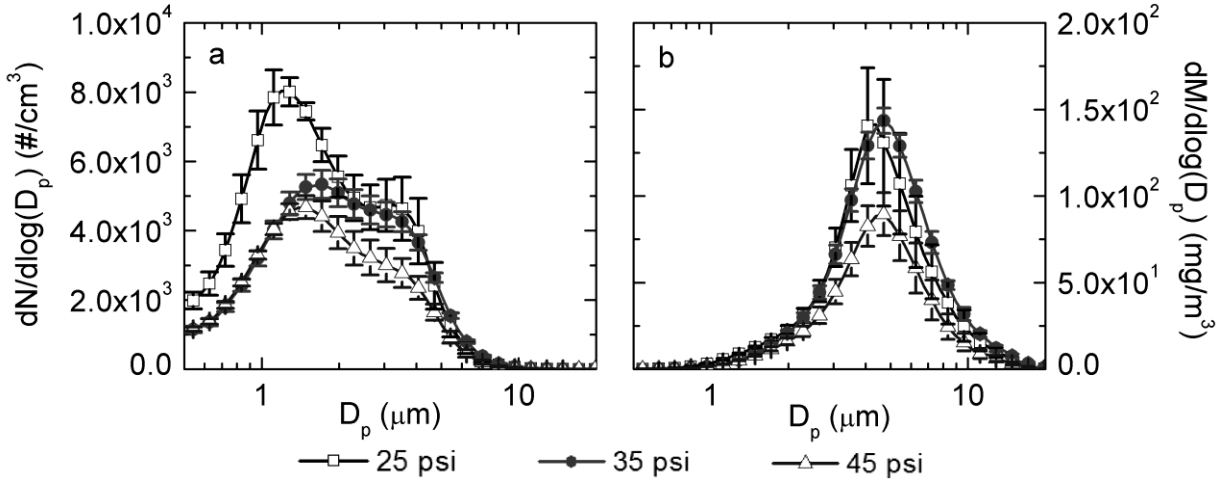

Figure A3.3 Influence of operating pressure on the (a) number-based and (b) mass-based SDF of particles generated from the Misty Max 10 nebulizer.

Table A3.2 lists the mean aerodynamic diameter (MAD), mass median aerodynamic diameter (MMAD), time for nebulizing 5 ml of saline solution, and their standard deviations (SD) for the Misty Max 10 nebulizer under different operating conditions (Tests 1 through 5). The MMAD values remained around 4.5 μm under a broad range of operating conditions, although the MAD values differ greatly among the tests. The stabilized MMAD values ensure uniform deposition

characteristics of particles generated from nebulizers. Similar time periods (~ 15 min) were required to completely nebulize 5 ml of saline solution under different operating conditions. The test with the highest operating pressure had the shortest nebulizing time, 12.78 min, probably a result of the higher nebulization rate, while the loss of larger particles during their transport in the nebulizer produced a lower mass-based SDF (Figure A3.3b).

Table A3.2 Mean aerodynamic diameter (MAD), mass median aerodynamic diameter (MMAD), time for nebulizing 5 ml of saline solution, and the standard deviations (SD) of different nebulizers at various operating conditions.

Test #	Brand	Flow (lpm)	Pressure (psi)	MAD (μm)	SD (μm)	MMAD (μm)	SD (μm)	Time (min)	SD (min)
1	Misty Max 10	10	35	2.157	0.056	5.048	0.312	13.67	1.33
2	Misty Max 10	20	35	2.119	0.054	4.698	0.598	14.50	0.50
3	Misty Max 10	30	35	1.258	0.021	4.068	0.487	15.00	1.19
4	Misty Max 10	20	25	1.889	0.139	4.371	0.697	15.89	1.34
5	Misty Max 10	20	45	1.901	0.06	4.371	0.030	12.78	0.68
6	SideStream	20	35	1.636	0.097	4.068	0.038	10.00	1.00
7	SideStream Plus	20	35	1.969	0.054	4.371	0.323	6.83	0.17
8	PARI	20	35	1.806	0.032	4.068	0.754	7.00	1.00
9	AeroEclipse	20	35	1.212	0.003	4.698	0.063	24.44	0.96

Figure A3.4 presents the (a) number-based and (b) mass-based SDF of particles generated from the five tested nebulizers at an operating pressure of 35 psi and a flow rate of 20 lpm. With the exception of the AeroEclipse nebulizer, all nebulizers produced particles predominantly in the size range of 2 to 4 μm (Figure A3.4a). A major peak at 1 μm was observed in the number-based SDF of particles generated by the AeroEclipse nebulizer. This peak was mainly due to the presence of a plate near the outlet of the nebulization chamber, which collected the larger particles through impaction. These accumulated droplets then flowed back to the liquid reservoir, which resulted in a longer time before the solution was completely nebulized (Table A3.2 Test 9). However, in the mass-based SDFs (Figure A3.4b), the AeroEclipse nebulizer also generated

particles with the largest sizes, around 5 μm, which demonstrated the strong dependence of mass concentration on the size of the nebulized particles. Although the SideStream Plus and AeroEclipse nebulizers were the quickest and slowest to nebulize the 5 ml of saline solution, respectively, the MMAD values of the particles generated from the five nebulizers were distributed quite narrowly between 4 to 5 μm, despite the widely varied MAD values. The wide variation in the number-based SDFs and the consumption rate of the nebulized solution suggest that each nebulizer should be calibrated under multiple operating conditions by the manufacturers, as indicated in existing studies [12].

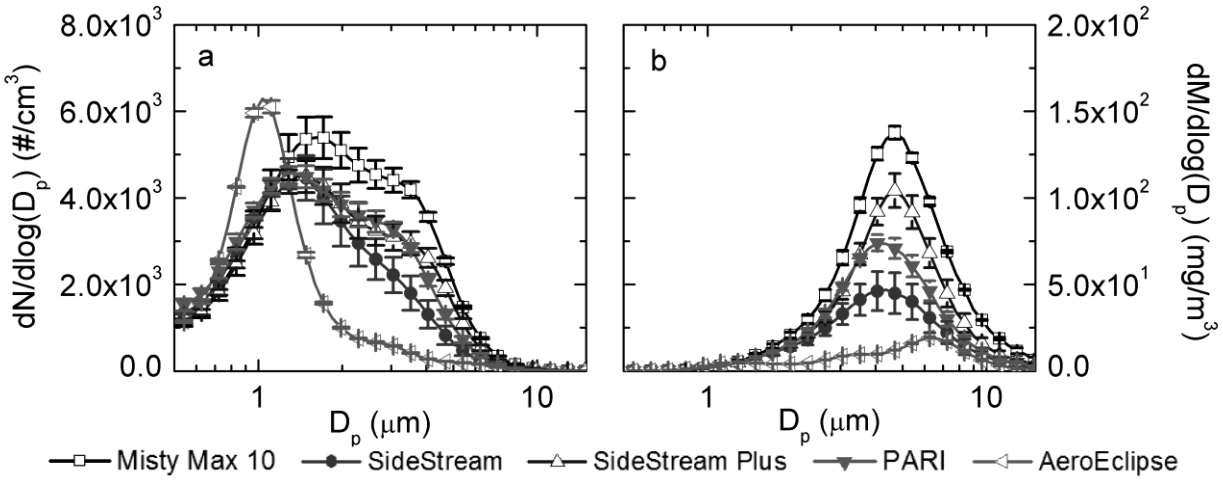

Figure A3.4 (a) Number-based and (b) mass-based SDF of particles generated from five commercially available nebulizers.

Discussion

Table A3.3 (Tests 1 to 9) lists the mass fractions of particles deposited in different regions of the respiratory system and the mass fractions of particles exiting the respiratory system calculated with the measured particle size distributions. Particles deposited in the HA region dominated the total mass of particles generated from nebulization. It is also interesting to observe that the different nebulizers demonstrated similar mass distributions even under a wide range of operating conditions. This could be attributed to the similar mass-based SDFs (Figs A3.2b, A3.3b, A3.4b) which were mainly distributed above 3 μm, where the deposition efficiency of particles in the HA region is the highest [19]. The airway surfaces of the HA and TB regions are covered with a layer of mucus which enhances the collection of deposited particles. The mucus is slowly propelled by ciliary action to the pharynx, where it is subconsciously swallowed into the gastrointestinal tract[3, 25]. This transport process can remove the deposited particles in the airways from the respiratory system in a matter of hours. Therefore, any medication administered specifically to this region should release fairly quickly, and such a method may not be optimal when extended-release medications are required. Under these circumstances, a shorter time for finishing the nebulization is needed to reduce the waste of medication. The treatment of pulmonary diseases using aerosolized medications may require that medicine-containing particles reach deeper into the TB or AL regions of the respiratory system. For this to be optimally achieved, the size of the generated particles should be reduced efficiently (< 0.2 μm) so that they can reach these regions through diffusion. This method may not be adequate since the mass-based SDF is very sensitive to the proportion of particles with large sizes, as indicated by the case of the AeroEclipse nebulizer. Therefore, installing multiple impactors that efficiently collect particles above 1 μm may be a viable method to alter the deposition characteristics of the

nebulized particles. In the end, the decision as to which medical nebulizer will best administer a given medication to a given lung region will not just be based on the particle size distribution, but many other factors including nebulization time, staff working time, availability and cost effectiveness.

Table A3.3 Respiratory deposition fractions of particles generated by different nebulizers at various operating conditions. The mass fractions of particles deposited in the head airways (HA) region, tracheobronchial (TB) region, alveolar (AL) region, and the mass fraction of particles exiting the respiratory system are listed. Test 10 shows the deposition fractions of particles generated by the Misty Max 10 nebulizer after complete drying.

Test #	Brand	Flow (lpm)	Pressure (psi)	HA (%)	TB (%)	AL (%)	Escape (%)
1	Misty Max 10	10	35	82.3	3.5	4.7	9.6
2	Misty Max 10	20	35	83.2	3.9	5.3	7.6
3	Misty Max 10	30	35	82.1	4.0	5.6	8.3
4	Misty Max 10	20	25	83.0	4.1	5.7	7.1
5	Misty Max 10	20	45	83.1	4.0	5.5	7.3
6	SideStream	20	35	81.6	4.0	5.7	8.7
7	SideStream Plus	20	35	83.5	4.0	5.5	6.9
8	PARI	20	35	82.4	4.2	5.9	7.5
9	AeroEclipse	20	35	81.7	3.1	4.2	10.9
10	Misty Max 10 (dried)	20	35	46.8	4.2	11.5	37.5

Figure A3.5 shows the characteristic evaporation times of particles ranging from 0.01 to 10 μm at different RH values. It can be observed that RH indeed has a strong effect on the evaporation of droplets. When the particle size is larger than 1 μm, the characteristic evaporation times differ by several orders of magnitude when RH drops from 100 % to 30 %. Given the fact that hospital rooms normally maintain a low RH, this information may be important for the design of medical nebulizers, since the generated particles are mainly concentrated in the size range from 1 to 8 μm (Figures A3.2 to A3.4), where the evaporation time is very sensitive to particle size. Take the 4 μm particles as an example: after they are emitted from the nebulizer, they may conserve their size for several seconds, since the nebulizer also produces highly concentrated water vapor,

which leads to an RH value close to 100 %. But as the particles mix with the surrounding air, the significantly reduced characteristic evaporation time (below 1 ms) quickly shrinks the droplet, and eventually leaves solute particles which may be in nanometer range, depending on the concentration of the nebulized solution. This process was observed during the experiments: the nebulizer generated a cloud of white mist directly at the outlet, which quickly disappeared, in a matter of seconds. For saline solution, the final solute particle size is around 0.21 μm when the original droplet size is 1 μm. Therefore, the deposition characteristics of the transported particles may be greatly different from the original particles. For example, 0.21 μm solid particles have deposition efficiencies of 2.7%, 0.8%, and 6.0% in the HA, TB, and AL region, respectively, meaning that the alveoli become the major region for the deposition of particles in the respiratory tract. This large alteration to the respiratory deposition pattern can change the effects on nearby healthcare workers because of the potential for chronic exposure to these transformed particles. According to the size distribution of particles generated from the Misty Max 10 nebulizer, the dried particle size distribution can be calculated by assuming particles keep spherical. Similar method can be used to derive the deposition fractions of the dried particles, which are shown in the Test 10 of Table A3.3. Although the dried particles still mainly deposit in the HA region, the fraction dropped, due to the increased mass deposition in the AL region (11.5%) and the escape of particles (37.5%).

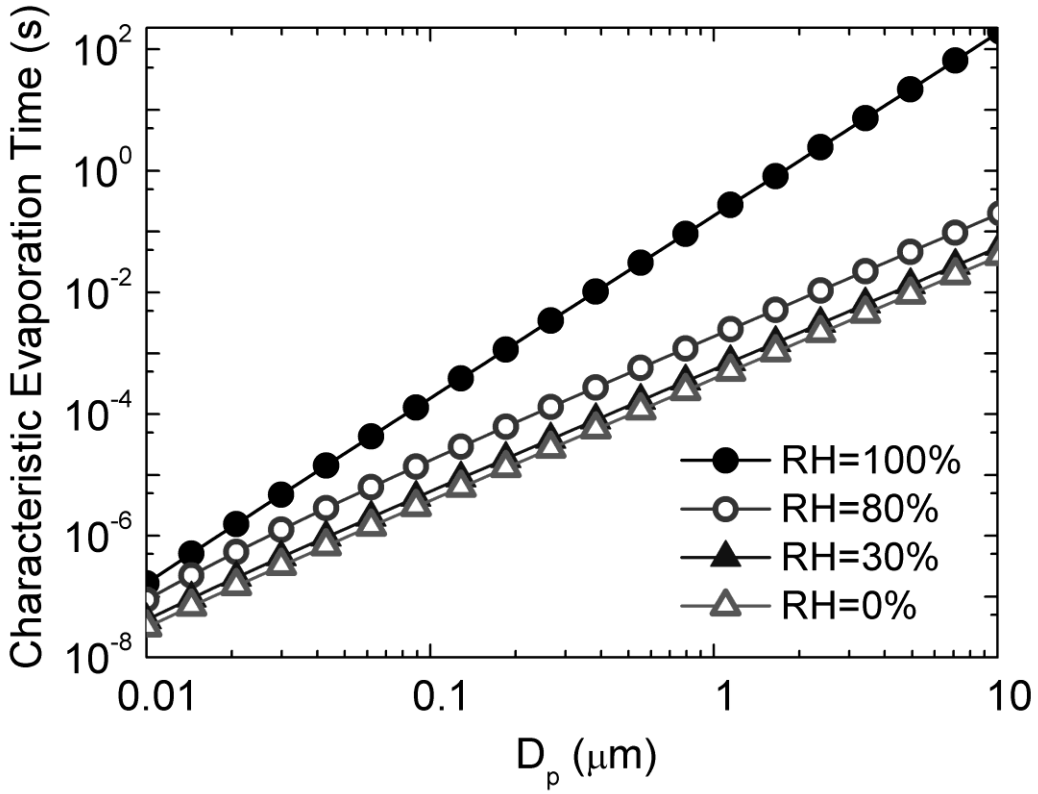

Figure A3.5 Influence of RH on the characteristic evaporation times of particles with sizes ranging from 0.01 to 10 μm.

In a diffusion-only scenario, the concentration profile around the source of particles is closely related to time and the distance from the point of interest and the particle source, as shown in Eq. A3.9. In the case of nebulized particles, we use $1-erf(\frac{r-R}{\sqrt{2Dt}})=0.03$ to quantitatively represent that particles have diffused through a distance of r. By further using $R=0.01$ m, which is the radius of the nebulizer mouthpiece, we obtained the required time for particles to diffuse to the locations of r = 0.02, 0.1, and 1 m as a function of particle size (Figure A3.6). It takes at least 150 s even for particles with a size of 0.01 μm to diffuse 0.01 m (to r = 0.02 m), mainly because of the low diffusion coefficients of the particles. Hence, it is not possible to observe the

movement of nebulized particles due to diffusion only, and the effect of diffusion in transporting the nebulized particles is minimal, even if they are dried due to the low RH in the environment. Figure A3.7 plots both the characteristic time for particles to follow the external air velocity and the settling velocity of particles as a function of particle size. The time needed for particles to reach the external flow velocity is very short (below 1 ms for a particle with a size of 10 μm) due to their small inertia. Hence, we can conclude that particles generated from medical nebulizers are transported mainly through convective movement. Calculations show that the settling velocity of particles between 0.01 and 10 μm in size is smaller than 0.01 m/s. This velocity is very small, since the natural convection of air between two locations with a distance of 1 m and a temperature difference of 0.1 ^{o}C can cause a flow velocity of 0.06 m/s, according Eq. A3.13. Hence, healthcare workers are recommended to avoid pathways through which the nebulized particles move, and major air outlets in patient rooms where nebulized medication is administered.

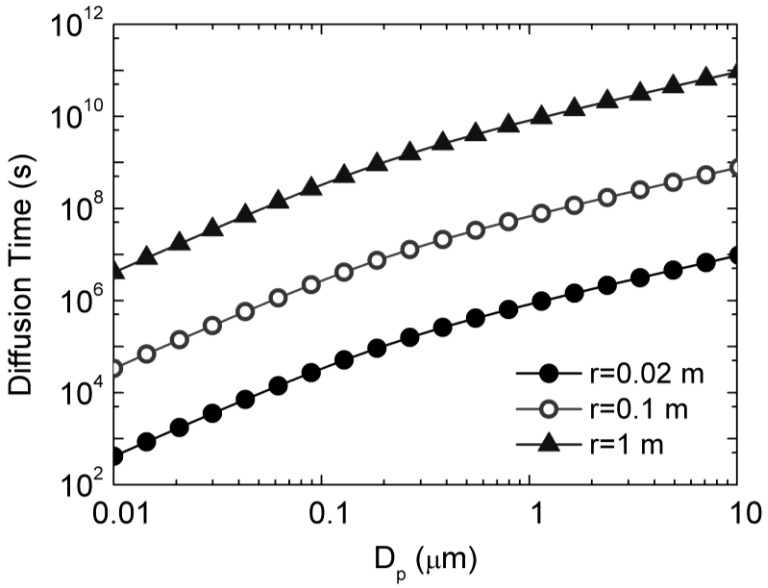

Figure A3.6 Times needed for particles in the size range of 0.01 to 1 μm to diffuse to the location at r=0.02, 0.1, and 1 m.

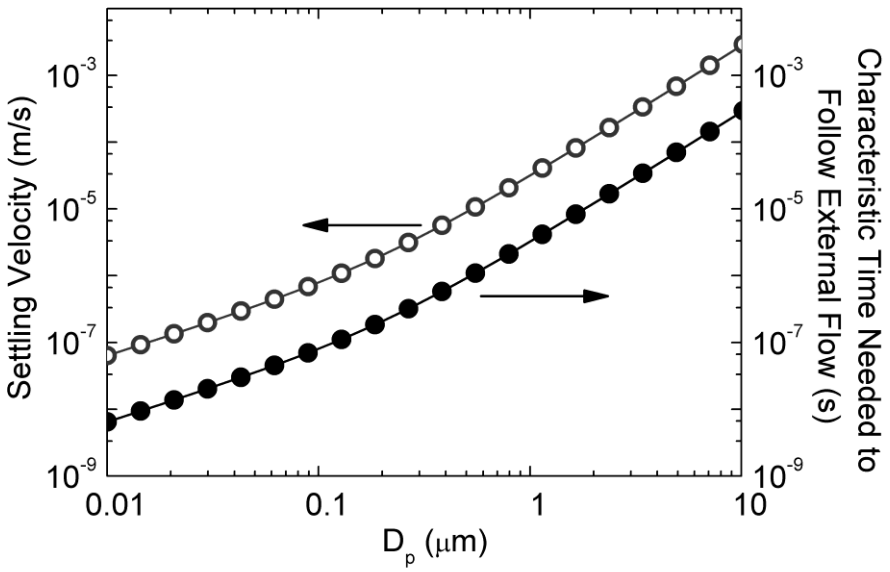

Figure A3.7 Settling velocity (open circle line) and the characteristic time for particles to follow the external flow (closed circle line) as a function of particle size.

From the analysis above, we can make several generalizations about the transport of particles released from medical nebulizers. After particles are emitted, the high water vapor concentration at the outlet of the nebulizer conserves the size of the particles for several seconds; however, as soon as the external (dry) air mixes with the plume of particles, the particles shrink within milliseconds, leaving a particle composed of solute materials. Particle diffusion plays a minimal role in the transport of nebulized and dried particles, due to the small diffusion coefficient of the particles. Convection (both forced and natural) is the dominant mechanism for transporting the particles generated from medical nebulizers, and any settling due to gravitational force can be neglected. Notably, the convective movement of particles promotes the mixing of the surrounding air with the particles, which accelerates particle evaporation. Hence, the respiratory

deposition of the transported particles may be significantly different from that of the original particles, since submicron particles mainly composed of solute materials can easily penetrate deeper into the respiratory systems. Considering the potential side effects of, and long-term exposure to, the nebulized medication, more consideration should be given on how to remove those particles released from medical nebulizers from the environment, perhaps through specialized ventilation or filtration equipment, before they are able to transport into the breathing zones of nearby healthcare workers, or at least to equip healthcare workers with personal protective equipment (PPE) that will prevent these small particles from being inhaled. The impact of repeated inhalation of nebulized medications on healthcare workers such as respiratory therapists has not been well studied. The importance of prevention is especially important considering the potential side effects of, and long exposure times to, these medications.

References:

1. Clark A: Medical aerosol inhalers: past, present, and future. *Aerosol Sci Technol*. 1995;22:374-391.

2. Rau JL, Ari A, and Restrepo RD: Performance comparison of nebulizer designs: constant-output, breath-enhanced, and dosimetric. *Respir Care*. 2004;49:174-179.

3. Hinds WC: *Aerosol technology: properties, behavior, and measurement of airborne particles*. John Wiley & Sons, 2012.

4. Chadha TS, Chattopadhyay S, Venkataraman C, and Biswas P: Study of the charge distribution on liposome particles aerosolized by air-jet atomization. *J Aerosol Med Pulm Drug Deliv*. 2012;25:355-364.

5. Leavey A, Fang J, Sahu M, and Biswas P: Comparison of measured particle lung-deposited surface area concentrations by an Aerotrak 9000 using size distribution measurements for a range of combustion aerosols. *Aerosol Sci Technol*. 2013;47:966-978.

6. Biswas P: Impactors for aerosol measurements: developments and sampling biases. Vol Ph.D. California Inst. of Tech., Pasadena (USA), 1985.

7. Berg E, Svensson JO, and Asking L: Determination of nebulizer droplet size distribution: a method based on impactor refrigeration. *J Aerosol Med*. 2007;20:97-104.

8. Clark AR: The use of laser diffraction for the evaluation of the aerosol clouds generated by medical nebulizers. *Int J Pharm*. 1995;115:69-78.

9. Mitchell JP and Nagel MW: Time-of-flight aerodynamic particle size analyzers: their use and limitations for the evaluation of medical aerosols. *J Aerosol Med Pulm Drug Deliv*. 1999;12:217-240.

10. Mitchell JP, Nagel MW, Wiersema KJ, and Doyle CC: Aerodynamic particle size analysis of aerosols from pressurized metered-dose inhalers: comparison of Andersen 8-stage cascade impactor, next generation pharmaceutical impactor, and model 3321 aerodynamic particle sizer aerosol spectrometer. *AAPS PharmSciTech*. 2003;4:425-433.

11. De Boer A, Gjaltema D, Hagedoorn P, and Frijlink H: Characterization of inhalation aerosols: a critical evaluation of cascade impactor analysis and laser diffraction technique. *Int J Pharm*. 2002;249:219-231.

12. Smith E, Denyer J, and Kendrick A: Comparison of twenty three nebulizer/compressor combinations for domiciliary use. *Eur Respir J*. 1995;8:1214-1221.

13. Weber A, Morlin G, Cohen M, Williams-Warren J, Ramsey B, and Smith A: Effect of nebulizer type and antibiotic concentration on device performance. *Pediatr Pulmonol*. 1997;23:249-260.

14. Harvey C, O'doherty M, Page C, Thomas S, Nunan T, and Treacher D: Comparison of jet and ultrasonic nebulizer pulmonary aerosol deposition during mechanical ventilation. *Eur Respir J*. 1997;10:905-909.

15. Zhou Y, Ahuja A, Irvin C, Kracko D, McDonald J, and Cheng Y: Evaluation of nebulizer performance under various humidity conditions. *J Aerosol Med*. 2005;18:283-293.

16. Phipps PR and Gonda I: Droplets produced by medical nebulizers. Some factors affecting their size and solute concentration. *CHEST J*. 1990;97:1327-1332.

17. Corcoran T, Dauber J, Chigier N, and Iacono A: Improving drug delivery from medical nebulizers: the effects of increased nebulizer flow rates and reservoirs. *J Aerosol Med*. 2002;15:271-282.

18. Hess D, Fisher D, Williams P, Pooler S, and Kacmarek RM: Medication nebulizer performance: effects of diluent volume, nebulizer flow, and nebulizer brand. *CHEST J*. 1996;110:498-505.
19. ICRP: Human Respiratory Tract Model for Radiological Protection. In: H Smith, (ed). *Annals of the ICRP*. Vol 1: Tarrytown, NY, 1994.
20. Baron P, Deye GJ, Martinez AB, Jones EN, and Bennett JS: Size shifts in measurements of droplets with the aerodynamic particle sizer and the aerosizer. *Aerosol Sci Technol*. 2008;42:201-209.
21. Daigle CC, Chalupa DC, Gibb FR, Morrow PE, Oberdörster G, Utell MJ, and Frampton MW: Ultrafine particle deposition in humans during rest and exercise. *Inhalation Toxicol*. 2003;15:539-552.
22. Sahu M, Peipert J, Singhal V, Yadama GN, and Biswas P: Evaluation of mass and surface area concentration of particle emissions and development of emissions indices for cookstoves in rural India. *Environ Sci Tech*. 2011;45:2428-2434.
23. Woods J, Braymen D, Rasmussen R, Reynolds G, and Montag G: Ventilation requirements in hospital operating rooms. I: Control of airborne particles. *ASHRAE Trans*. 1986;92:396-426.
24. Friedlander SK: *Smoke, dust, and haze: fundamentals of aerosol behavior*. Vol 198. Oxford University Press New York, USA, 2000.
25. Hilding A: Phagocytosis, mucous flow, and ciliary action. *Arch Environ Health*. 1963;6:61-73.

Appendix IV: Characterization of Aerosols Generated During Patient Care Activities

The results of this chapter have been published in O'neil, C. A., Li, J., Leavey, A., Wang, Y., Hink, M., Wallace, M., ... & Babcock, H. M. (2017). Characterization of Aerosols Generated During Patient Care Activities. Clinical Infectious Diseases.

ABSTRACT

Background. Questions remain about the degree to which aerosols are generated during routine patient care activities and whether such aerosols could transmit viable pathogens to healthcare personnel. The objective of this study was to measure aerosol production during multiple patient care activities and to examine the samples for bacterial pathogens.

Methods. Five aerosol characterization instruments were used to measure aerosols during seven patient care activities: patient bathing, changing bed linens, pouring and flushing liquid waste, bronchoscopy, non-invasive ventilation, and nebulized medication administration (NMA). Each procedure was sampled 5 times. A SKC BioSampler was used for pathogen recovery. Bacterial cultures were performed on the sampling solution. Patients on contact precautions for drug resistant organisms were selected for most activity sampling. Any patient undergoing bronchoscopy was eligible.

Results. Out of 35 sampling episodes, only two procedures showed significant increase in particle concentrations over baseline: NMA and bronchoscopy with NMA. Bronchoscopy without NMA and non-invasive ventilation did not generate significant aerosols. Of 78 cultures from the impinger samples, 6/28 baseline samples (21.4%) and 14/50 procedure samples (28.0%) were positive.

Conclusions. In this study, significant aerosol generation was only observed during NMA, both alone and during bronchoscopy. Minimal viable bacteria were recovered, mostly common environmental organisms. Although more research is needed, these data suggest that some of the procedures considered to be aerosol-generating may pose little infection risk to healthcare personnel.

BACKGROUND

The majority of pathogens are spread person to person under normal circumstances through contact or droplet transmission, with a small number known to be transmitted by small particle aerosols. For pathogens spread by contact or droplet, additional respiratory protection with a respirator is not considered necessary to protect healthcare personnel (HCP) from exposure [1]. However, concerns have been raised that some infections usually spread by contact or droplet routes could also be transmitted through aerosols generated during certain medical procedures. These concerns have been heightened during outbreaks of emerging infections such as Ebola, Severe Acute Respiratory Syndrome (SARS), Middle East Respiratory Syndrome (MERS), and pandemic influenza. Some infection prevention guidelines therefore recommend that HCP use additional respiratory protection (e.g., a fitted particulate respirator) when performing "aerosol-generating procedures" to protect themselves from exposure to infectious agents [1-8].

Concerns about disease transmission to HCP during aerosol-generating procedures were raised during the 2003 SARS outbreak [9], when there were multiple reports of disease transmission to HCP who were wearing appropriate personal protective equipment [10-12]. Aerosol transmission during medical procedures was the suspected source of infection, based largely on observational and anecdotal evidence [11, 13, 14]. Air sampling conducted in the rooms of SARs patients at a hospital in Toronto provided experimental confirmation of the possibility of airborne transmission of SARs, but did not correlate this with the performance of medical procedures [15].

Aerosol-generating procedures have also been suspected as a source of HCP infection in other outbreaks, such as 2009 H1N1 Influenza [2, 4, 16], seasonal influenza [3, 17, 18], and MERS

[19, 20]. Some have also raised concerns that filoviruses, including Ebola, may be transmitted through aerosols, though this remains controversial [21]. Other infections that may occasionally be transmitted via aerosols include Norovirus [8, 22] and methicillin resistant *Staphylococcus aureus* [22].

Routine healthcare procedures most often identified as potentially "aerosol-generating" include: intubation and extubation, cardiopulmonary resuscitation, bronchoscopy, non-invasive ventilation, tracheotomy, sputum induction, airway suctioning, manual ventilation, and administering oxygen or nebulized medication [2, 4, 8, 13, 22-24]. For most of these procedures, evidence for the generation of infectious aerosols is based mostly on case reports and anecdotal evidence rather than on epidemiological studies or environmental air sampling. A 2009 review by Davies et al. concluded that, although there are a number of procedures considered to be aerosol-generating, few have sufficient evidence to confirm that they actually do produce aerosols [23].

In absence of clear evidence, questions remain about the degree to which aerosols are generated during "aerosol-generating" medical procedures, the size and concentration of medically-aerosolized particles, and whether such aerosols could transmit viable pathogens to HCP or to other patients [1, 7, 25]. Uncertainty about which procedures are associated with increased risk makes it difficult for hospitals to develop effective preventive measures [7, 23, 25]. The objective of this investigation was to characterize any aerosols generated during several common medical procedures, and to determine whether bacterial pathogens could be isolated from these aerosols.

METHODS

Sampling Strategy

Aerosol production was measured during seven routine patient care activities: changing bed linens, patient bathing, pouring liquids into a hopper, flushing liquid waste, non-invasive ventilation using Bilevel Positive Airway Pressure (BiPAP), nebulized medication administration (NMA), and bronchoscopy with and without NMA, including both intubation (laryngeal mask) and extubation during the procedure. Prior to sampling, both the patient and the HCP performing the procedure were informed about the aerosol sampling and asked to provide verbal assent. For patients who were unconscious or sedated, a family member or surrogate was asked to provide assent, if they were present.

Each type of procedure was sampled five separate times. All samples were collected in patient and procedure rooms at a large tertiary care medical center. Most samples were collected in the Medical ICU, although some NMA samples were collected in the cystic fibrosis ward. These rooms all had routine air handling. Bronchoscopy samples were collected in both the Interventional Pulmonology suite (routine air handling) and the ICU bronchoscopy suite (negative pressure ventilation). During some of the bronchoscopies, nebulized medication was administered to the patient before and after the procedure.

Subjects

For all procedures except bronchoscopy, patients were selected from among inpatients on contact precautions for drug resistant organisms, including methicillin-resistant *Staphylococcus aureus* (MRSA), vancomycin-resistant *Enterococcus* (VRE), multi-drug resistant gram negative

organisms (MDRO), and *Clostridium difficile*. Bronchoscopy patients were not pre-screened for colonization or infection with specific organisms.

Aerosol Sampling

Whenever possible, baseline samples were collected in the room before the procedure began. It was not possible to collect baseline samples for mechanical ventilation or non-invasive ventilation, which were continuous. For pouring/flushing of patient waste in a hopper, a single baseline sample was collected for two procedure samples (one pouring, one flushing). For bronchoscopies, one baseline and two procedure samples were collected (one including intubation and one including extubation).

During each procedure, five real-time aerosol characterization instruments were used to detect and characterize any generated aerosols. These included: a P-Trak Ultrafine Particle Counter (TSI Inc.), which measures particle number concentration (#/cm^3); a SidePak AM510 Personal Aerosol Mobility Spectrometer (TSI Inc.), which measures particle mass concentration (mg/cm^3); a Portable Aerosol Mobility Spectrometer (PAMS, Kanomax Inc.), which measures the particle number size distribution of sub-micrometer aerosols (14 - 862 nm); an Aerodynamic Particle Sizer (APS) Spectrometer (TSI Inc.), which measures the particle number size distribution of larger aerosols (0.5 - 20 µm); and a Nanoparticle Surface Area Monitor (NSAM,TSI Inc.), which measures lung-deposited surface area, providing an estimate of the total surface area of particles that would deposit in the alveolar regions of the human lung ($\mu m^2/cm^3$). All samples were collected using two sets of conductive silicone tubing that were hung at a single point three feet from the patient's head at approximately HCP head level. One set of tubing was connected to the impinger inlet and the other was connected to the real time aerosol

sampling instruments. The tubing was inspected prior to sampling to ensure that it had no sharp bends or kinks. All instruments were calibrated prior to each use to ensure accurate measurements.

Testing of Biological Samples

To determine whether the aerosols generated during the various procedures included any potentially infectious particles, a BioSampler (SKC Inc.) was used to collect samples for bacterial pathogen recovery. The sterile BioSampler was filled with 15 ml of phosphate buffered saline with Tween-80. Tubing attached to the impinger inlet was hung alongside the collection tubing for the aerosol characterization instruments. After sampling, the collection liquid was decanted and centrifuged, and the pellet re-suspended. A Gram stain and culture was performed, and the sample was inoculated on several culture plates: 5% sheep's blood agar (Hardy Diagnostics); Spectra MRSA agar (Remel); chromID VRE (bioMerieux); CCMB-TAL broth for *Clostridium difficile* detection (Anaerobe Systems); and a 6.5% NaCl broth (Hardy), which was incubated for 18-26 hours and then plated to the blood, MRSA, and VRE agars. Bacterial colonies were identified using the VITEK MS MALDI-TOF MS system [26-29]. Following each procedure, the collection tubing was rinsed with ethanol and the BioSamplers were rinsed and autoclaved to reduce the potential for cross-contamination.

Analysis

Averages and standard deviations were calculated for all aerosol characterization data (particle counts, mass, size, lung-deposited surface area) for each procedure and associated baseline (when available), so the contribution of each procedure to overall measured particle concentrations could be compared.

The study protocol was reviewed by the Washington University Human Research Protection Office, which determined that it did not require Institutional Review Board oversight because no personally identifiable information was collected.

RESULTS

A Total of 35 procedures were sampled (5 samples for each of 7 types of procedure) over a four month period from June through October, 2015.

Particle Concentration

Differences between baseline and procedure particle number and mass for the different types of procedure samples are presented in Figure 1. Data from the mechanical ventilation and non-invasive ventilation samples are not included in this figure because no baseline samples were collected for these procedures. No significant differences between the baseline and procedure measurements were observed for bathing, changing linens, pouring liquids into the hopper, flushing the hopper, and bronchoscopy without NMA. However, there was an increase in particle concentrations during NMA, and during bronchoscopy procedures that started and ended with NMA. Bronchoscopy with NMA was associated with up to a 30,000 #/cm^3 increase in particle counts and a 1.5 mg/m^3 increase in particle mass, while NMA alone was associated with up to a 70,000 #/cm^3 increase in particle count and a 0.8 mg/m^3 increase in particle mass. However, as indicated by the error bars in Figure 1, there was a high amount of variation in particle concentration among the NMA samples.

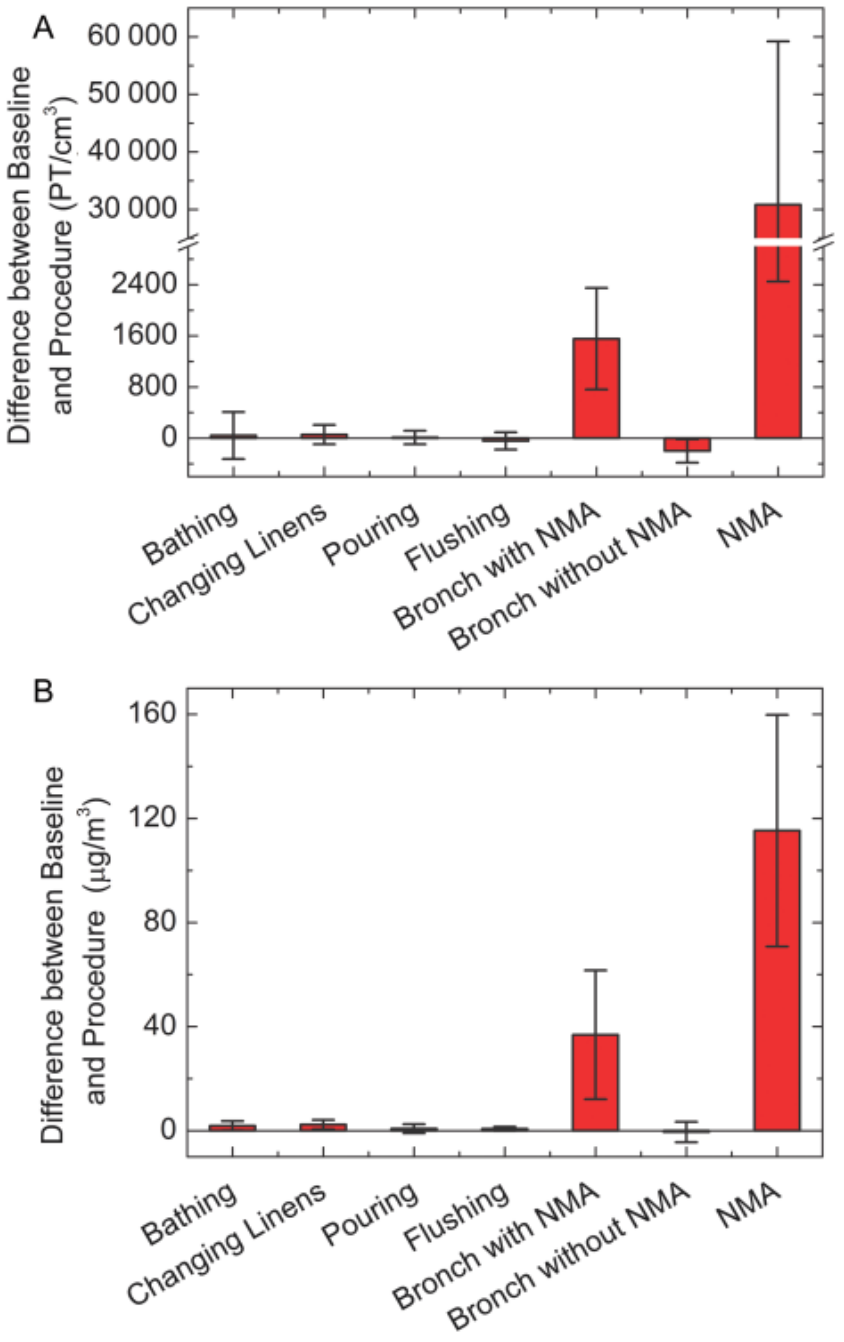

Figure 1: Change from pre-procedure baseline in particle number (a) and mass (b) concentrations during the sampled procedures. Mechanical ventilation and non-invasive ventilation are not included in this figure because no baseline samples could be collected for these procedures. Bronch = bronchoscopy. NMA = nebulized medication administration. Error bars = standard deviation.

Figure 2 presents particle number and mass concentration time-series data comparing baseline and procedure samples collected during bronchoscopy with NMA (a & c) and NMA alone (b & d). For samples collected during bronchoscopy with NMA, two narrow concentration peaks are observed, which correspond with the nebulized medication administration before and after the procedure. The samples collected during NMA alone demonstrate wider concentration peaks (when adjusted for the different time scales), as the nebulizer was running throughout the entire procedure, and higher particle counts but lower mass concentrations, indicative of smaller particle sizes. For the NMA alone procedures, baseline aerosol concentration levels were not re-established until 10 to 20 minutes after the procedure had ended.

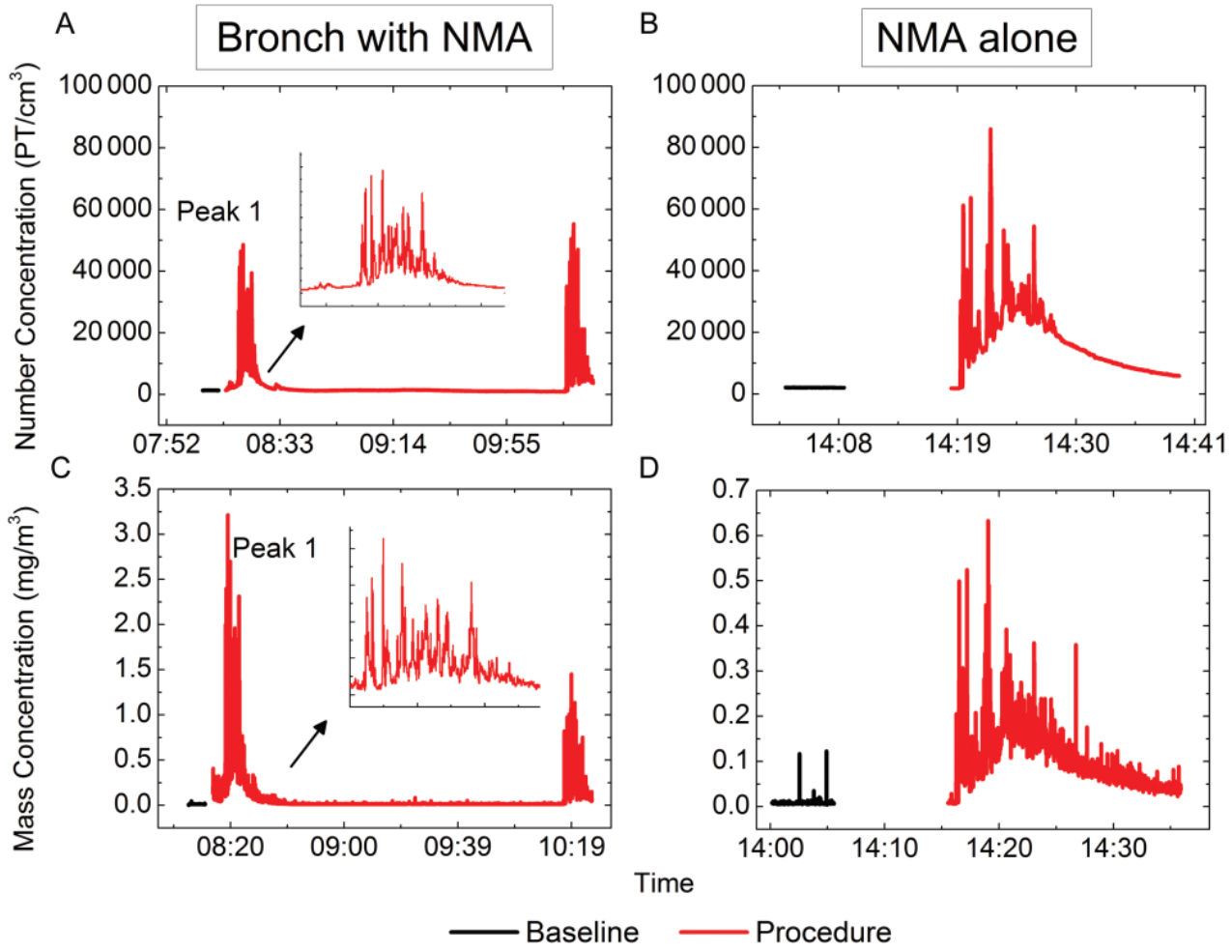

Figure 2: Particle number and mass concentrations for bronchoscopy with nebulized medication administration (NMA) (a & c), and for NMA alone (b & d). Please note the different y-axis scales for the two mass concentration graphs (c & d). The insert shows an enlarged view of the first peak of the bronchoscopy with NMA graph (a & d) to make the time scale comparable to the NMA alone graphs (b & d).

Particle Size Distribution

Particle number size distribution data (Figure 3) indicates that the particles generated during bronchoscopy with NMA (a,c) were generally larger (geometric mean diameter (GMD) 44 nm, SD 2.75) than those generated during NMA alone (b, d; GMD 33 nm, SD 2.61). This is consistent with the results presented in Figure 2, which showed higher mass concentrations for

bronchoscopy with NMA, as larger particles contribute more to mass concentration than smaller particles. Since the nebulized particles are composed mainly of water, their sizes are largely affected by the nebulizing conditions (such as pressure and air flow rate) and time allowed for evaporation after they are emitted from the nebulizer [30]. It is therefore possible that the different particle sizes observed during the two types of procedures may be due to different air flow patterns in the rooms where the procedures were performed (some bronchoscopies were performed in negative pressure ventilation rooms, unlike those used for NMA). The particle size observations may also be influenced by different locations of the patient relative to air intake/outlet in the rooms, different NMA administration techniques (mask versus mouth piece), and whether albuterol was co-administered with another medication. Particle size distribution data for the other procedures evaluated in this study showed that pouring and flushing liquid waste in the hopper did produce a few aerosolized particles of around 1 μm (less than 0.5 #/cm^3); however, this peak was no longer discernable after 20 seconds, as particles most likely drifted, settled, or were carried away by convection. Changing linens also produced small amounts of particles of around 40 nm in size. Bathing patients produced a low concentration of 0.5-1.5 μm particles, possibly caused by the evaporation of chlorhexidine gluconate in the soap used for bathing.

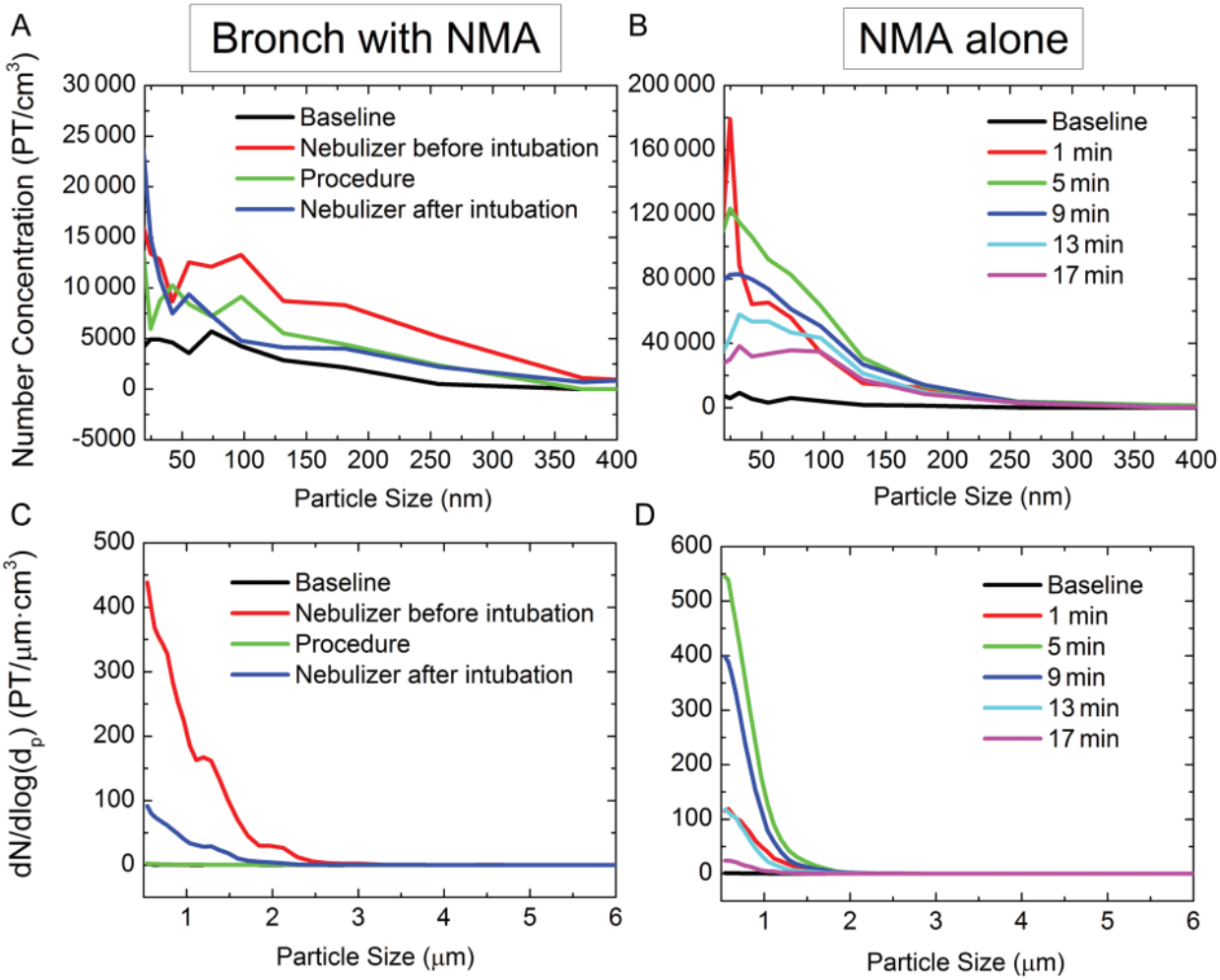

Figure 3: Particle number size distribution curves for (a) bronchoscopy with NMA as measured by portable aerosol mobility spectrometer (PAMS), (b) NMA alone as measured by PAMS, (c) bronchoscopy with NMA as measured by aerodynamic particle sizer spectrometer (APS), and (d) NMA alone as measured by APS. Please note the different y-axis scales for the two number concentration graphs (a & b). NMA = nebulized medication administration.

Lung-Deposited Surface Area

Figure 4 shows the difference between the average baseline and procedure measurements of the particle surface area that would deposit in the alveoli of the lung if inhaled. Bronchoscopy with NMA showed only a small elevation from baseline, while concentrations during NMA alone were much higher. No substantial elevation from baseline was observed during any of the other patient care activities that were sampled.

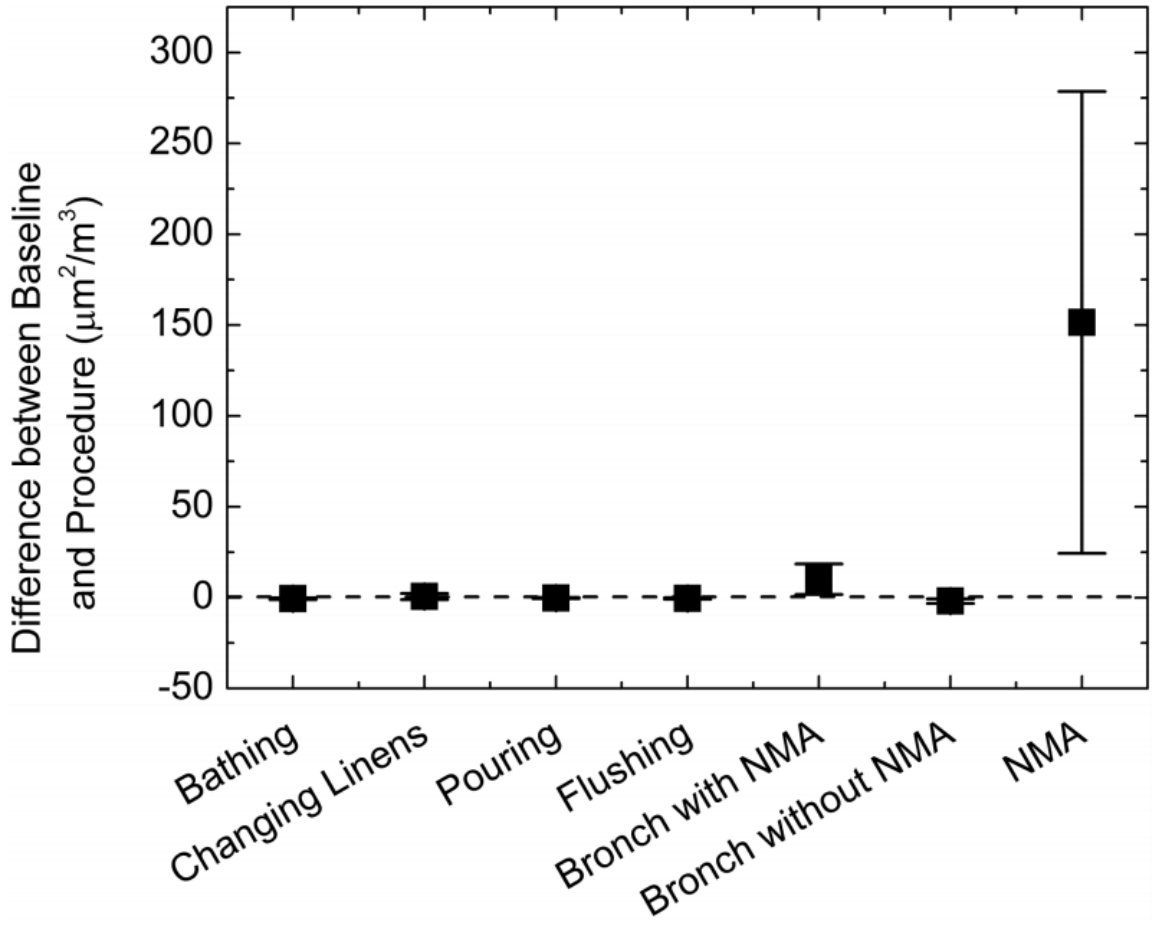

Figure 4: Change from pre-procedure baseline in lung-deposited surface area concentrations (alveolar region) during the sampled procedures. Mechanical ventilation and non-invasive ventilation are not included in this figure because no baseline samples could be collected for these procedures. Bronch = bronchoscopy. NMA = nebulized medication administration. Error bars = standard deviations.

Microbiology

Of 78 baseline and procedure BioSampler collection liquid samples that were cultured, bacteria were isolated from 6 of the 28 baseline samples (21.4%), as compared to 14 of 50 procedure samples (28.0%). In all cases, the bacterial burden was low (rare growth on solid medium or growth only upon broth enrichment). The most common culture result was mixed Gram-positive flora, with the most frequently isolated organisms being coagulase-negative

Staphylococcus spp. (n=12) and *Micrococcus* spp. (n=6). Other organisms identified included viridans group *Streptococcus, Bacillus* spp., *Paenibacillus spp.*, *Corynebacterium* spp., and a non-meningitidis species of *Neisseria*. Twenty five samples were collected during procedures involving patients who were on contact precautions for drug resistant organisms (18 patients with VRE; 3 with *C. difficile*; 8 with MRSA; and 5 with MDRO). None of the drug-resistant organisms were recovered from any of these samples.

DISCUSSION

The protection of HCP from disease transmission during potentially aerosol generating procedures is a priority. Effective recommendations require a clear understanding of the physical characteristics of any aerosols produced during these procedures and whether they carry viable pathogens that could pose an infection risk. In this study, multiple air sampling instruments were used to collect detailed real-time measurements of the aerosols generated during seven common medical procedures, including several that are generally considered to be "aerosol-generating." Microbiological analysis was used to determine the presence and viability of any bacterial organisms in these aerosols.

Significant aerosol generation was only observed during two types of procedures: NMA and bronchoscopy with NMA. The NMA findings are not surprising because nebulized medications are designed to be administered in aerosol form. Changing bed linens, patient bathing, pouring liquids into a hopper, flushing liquid waste, non-invasive ventilation, and bronchoscopy without NMA were not associated with significantly greater aerosols than at baseline. In addition,

minimal amounts of viable bacteria were recovered during the sampled procedures, and what was recovered represented mainly common environmental or skin contaminants. These comprehensive aerosol assessment results, while from only a small number of sampled procedures, are reassuring about the potential risk to HCP.

Other studies have indicated that the risks posed by potentially aerosol-generating procedures may be overestimated [31-33]. Two reviews evaluating evidence for whether noninvasive ventilation should be considered a high-risk procedure found little epidemiologic data to support the theory that noninvasive ventilation increases occupational exposure [9, 34]. A 2013 review of evidence for whether flushing toilets is associated with infectious disease transmission found that no studies have clearly demonstrated toilet plume-related disease transmission [35]. Although bronchoscopy is frequently cited as a possible aerosol-generating procedure, a 2012 systematic review found no evidence of a significant association between bronchoscopy and increased risk of SARS transmission to HCP [24].

The most consistent clinical evidence for the transmission of infections via aerosols generated during medical procedures is during patient intubation [7, 24]. Although no increase in aerosol production over baseline was observed during patient intubations in this study, most captured intubations were laryngeal mask intubations on sedated patients for the purpose of bronchoscopy and may not be representative of emergent or less controlled settings.

Only NMA and bronchoscopy with NMA were found to generate a significant increase in particle concentrations (number, mass, and lung-deposited surface area) over baseline levels. The high particle concentrations are likely related to the use of a nebulizer during these procedures, and the particles are most likely aerosolized medication that escaped from the nebulizer device. This conclusion is supported by the results of a previous study, which evaluated droplet dispersion during nebulizer treatment and

found an aerosol output profile consistent with nebulizer characteristics, rather than with dissemination of droplets from patients [36]. The extent of particle generation during NMA is probably related to the type of nebulizer used, treatment length, and patient characteristics, as a high amount of variability in particle concentration was observed during the different NMA sampling episodes. Although there was no significant bacterial pathogen recovery during NMA, the high concentrations of small aerosolized particles (median of 1 μm) could potentially affect HCP who administer the treatments.

Limitations of this study include small sample numbers (five samples for each procedure), lack of clinical data, having only one sampling location for each sample, non-continuous air sampling, and lack of viral pathogen recovery. In addition, the study focused on only seven of the many medical procedures that may be considered "aerosol-generating." The SKC BioSamplers used to capture aerosolized particles in this study also have limited sampling efficiency for particles <1 μm or ≥9μm in diameter, though most bacterial particles are expected to fall within the 1 – 9 μm range [37].

Strengths of this study include the use of multiple real-time aerosol measurement instruments, use of culture to determine the presence of viable microbes as a metric to assess the infection risk posed by medically-generated aerosols, and sampling during seven types of medical procedures in a real-world healthcare setting.

Studies documenting the frequency and type of aerosols generated during common medical procedures in healthcare settings provide critical information needed to inform infection prevention strategies and guidelines. Evidence-based guidelines are necessary to help protect HCP from infection, especially in outbreak situations. Current guidelines for HCP participating in suspected aerosol-generating procedures have had to rely on minimal or low-quality evidence [6, 7]. Though additional research is needed, the results of this study suggest that some of the

procedures that are widely considered to be high risk for the generation of infectious aerosols may actually pose little infection risk to HCP.

While this study has provided some information on aerosol generating procedures that could potentially be used to inform infection prevention protocols, further research is needed to confirm these findings. Additional studies are also needed to describe aerosol generation during other procedures suspected to be aerosol-generating, to investigate whether viruses can be isolated from medically-generated aerosols, and to examine the impact of patient clinical characteristics on aerosol production and pathogen recovery. Such studies would provide a more solid base of evidence on which to base infection prevention guidelines, and would provide information that could be used to develop methods that reduce aerosol generation during medical procedures, thereby reducing the risk of environmental contamination and infection transmission.

References

1. Coia JE, Ritchie L, Adisesh A, et al. Guidance on the use of respiratory and facial protection equipment. J Hosp Infect **2013**; 85(3): 170-82.
2. CDC. Interim Guidance on Infection Control Measures for 2009 H1N1 Influenza in Healthcare Settings, Including Protection of Healthcare Personnel. Available at: http://www.cdc.gov/h1n1flu/guidelines_infection_control.htm. Accessed 8/10/2016.
3. CDC. Prevention Strategies for Seasonal Influenza in Healthcare Settings. Available at: http://www.cdc.gov/flu/professionals/infectioncontrol/healthcaresettings.htm. Accessed June.
4. WHO. Infection prevention and control in health care for confirmed or suspected cases of pandemic (H1N1) 2009 and influenza-like illnesses. Available at: http://www.who.int/csr/resources/publications/cp150_2009_1612_ipc_interim_guidance_h1n1.pdf?ua=1. Accessed August 8.
5. Chughtai AA, Seale H, MacIntyre CR. Availability, consistency and evidence-base of policies and guidelines on the use of mask and respirator to protect hospital health care workers: a global analysis. BMC Res Notes **2013**; 6: 216.
6. Gralton J, McLaws ML. Protecting healthcare workers from pandemic influenza: N95 or surgical masks? Critical care medicine **2010**; 38(2): 657-67.
7. WHO. Infection prevention and control of epidemic-and pandemic-prone acute respiratory infections in health care: WHO Guidelines. Geneva, Switzerland: World Health Organization, **2014**.
8. Siegel JD, Rhinehart E, Jackson M, Chiarello L, Health Care Infection Control Practices Advisory C. 2007 Guideline for Isolation Precautions: Preventing Transmission of Infectious Agents in Health Care Settings. Am J Infect Control **2007**; 35(10 Suppl 2): S65-164.
9. McCracken J. Should noninvasive ventilation be considered a high-risk procedure during an epidemic? Cmaj **2009**; 181(10): 663-4.
10. Christian MD, Loutfy M, McDonald LC, et al. Possible SARS coronavirus transmission during cardiopulmonary resuscitation. Emerg Infect Dis **2004**; 10(2): 287-93.
11. Fowler RA, Lapinsky SE, Hallett D, et al. Critically ill patients with severe acute respiratory syndrome. Jama **2003**; 290(3): 367-73.
12. Ofner M, Lem M, Sarwal S, Vearncombe M, Simor A. Cluster of severe acute respiratory syndrome cases among protected health care workers-Toronto, April 2003. Can Commun Dis Rep **2003**; 29(11): 93-7.
13. CDC. Infection control precautions for aerosol-generating procedures on patients who have suspected severe acute respiratory syndrome (SARS). Atlanta: US Centers for Disease Control, **2013**.
14. Hui DS. Severe acute respiratory syndrome (SARS): lessons learnt in Hong Kong. Journal of thoracic disease **2013**; 5 Suppl 2: S122-6.
15. Booth TF, Kournikakis B, Bastien N, et al. Detection of airborne severe acute respiratory syndrome (SARS) coronavirus and environmental contamination in SARS outbreak units. J Infect Dis **2005**; 191(9): 1472-7.
16. Kuster SP, Coleman BL, Raboud J, et al. Risk factors for influenza among health care workers during 2009 pandemic, Toronto, Ontario, Canada. Emerg Infect Dis **2013**; 19(4): 606-15.

17. Tellier R. Aerosol transmission of influenza A virus: a review of new studies. J R Soc Interface **2009**; 6 Suppl 6: S783-90.

18. Lindsley WG, Blachere FM, Davis KA, et al. Distribution of airborne influenza virus and respiratory syncytial virus in an urgent care medical clinic. Clin Infect Dis **2010**; 50(5): 693-8.

19. Al-Dorzi HM, Alsolamy S, Arabi YM. Critically ill patients with Middle East respiratory syndrome coronavirus infection. Crit Care **2016**; 20: 65.

20. Al-Tawfiq JA, Perl TM. Middle East respiratory syndrome coronavirus in healthcare settings. Current opinion in infectious diseases **2015**; 28(4): 392-6.

21. Mekibib B, Arien KK. Aerosol Transmission of Filoviruses. Viruses **2016**; 8(5).

22. Eames I, Tang JW, Li Y, Wilson P. Airborne transmission of disease in hospitals. J R Soc Interface **2009**; 6 Suppl 6: S697-702.

23. Davies A, Thompson G, Walker J, Bennett A. A review of the risks and disease transmisison associated with aerosol generating medical procedures. Journal of Infection Prevention **2009**; 10: 122-6.

24. Tran K, Cimon K, Severn M, Pessoa-Silva CL, Conly J. Aerosol generating procedures and risk of transmission of acute respiratory infections to healthcare workers: a systematic review. PLoS One **2012**; 7(4): e35797.

25. Gamage B, Moore D, Copes R, Yassi A, Bryce E. Protecting health care workers from SARS and other respiratory pathogens: a review of the infection control literature. Am J Infect Control **2005**; 33(2): 114-21.

26. Branda JA, Rychert J, Burnham CA, et al. Multicenter validation of the VITEK MS v2.0 MALDI-TOF mass spectrometry system for the identification of fastidious gram-negative bacteria. Diagn Microbiol Infect Dis **2014**; 78(2): 129-31.

27. Manji R, Bythrow M, Branda JA, et al. Multi-center evaluation of the VITEK(R) MS system for mass spectrometric identification of non-Enterobacteriaceae Gram-negative bacilli. Eur J Clin Microbiol Infect Dis **2014**; 33(3): 337-46.

28. Richter SS, Sercia L, Branda JA, et al. Identification of Enterobacteriaceae by matrix-assisted laser desorption/ionization time-of-flight mass spectrometry using the VITEK MS system. Eur J Clin Microbiol Infect Dis **2013**; 32(12): 1571-8.

29. McElvania TeKippe E, Burnham CA. Evaluation of the Bruker Biotyper and VITEK MS MALDI-TOF MS systems for the identification of unusual and/or difficult-to-identify microorganisms isolated from clinical specimens. Eur J Clin Microbiol Infect Dis **2014**; 33(12): 2163-71.

30. Wang Y, Li J, Leavey A, O'Neil C, Babcock HM, Biswas P. Comparative Study on the Size Distributions, Respiratory Deposition, and Transport of Particles Generated from Commonly Used Medical Nebulizers. J Aerosol Med Pulm Drug Deliv **2016**.

31. Zhang Y, Seale H, Yang P, et al. Factors associated with the transmission of pandemic (H1N1) 2009 among hospital healthcare workers in Beijing, China. Influenza Other Respir Viruses **2013**; 7(3): 466-71.

32. Seto WH. Airborne transmission and precautions: facts and myths. J Hosp Infect **2015**; 89(4): 225-8.

33. Thompson KA, Pappachan JV, Bennett AM, et al. Influenza aerosols in UK hospitals during the H1N1 (2009) pandemic--the risk of aerosol generation during medical procedures. PLoS One **2013**; 8(2): e56278.

34. Esquinas AM, Egbert Pravinkumar S, Scala R, et al. Noninvasive mechanical ventilation in high-risk pulmonary infections: a clinical review. European respiratory review : an official journal of the European Respiratory Society **2014**; 23(134): 427-38.

35. Johnson DL, Mead KR, Lynch RA, Hirst DV. Lifting the lid on toilet plume aerosol: a literature review with suggestions for future research. Am J Infect Control **2013**; 41(3): 254-8.

36. Simonds AK, Hanak A, Chatwin M, et al. Evaluation of droplet dispersion during non-invasive ventilation, oxygen therapy, nebuliser treatment and chest physiotherapy in clinical practice: implications for management of pandemic influenza and other airborne infections. Health Technol Assess **2010**; 14(46): 131-72.

37. Kesavan J, Schepers D, McFarland AR. Sampling and Retention Efficiencies of Batch-Type Liquid-Based Bioaerosol Samplers. Aerosol Sci Tech **2010**; 44(10): 817-29.

Appendix V: Curriculum vitae

Jiayu Li

EDUCATION

Fellow of the McDonnell International Scholars Academy Aug 2014 – now
Ph. D. Candidate, Washington University in St. Louis Aug 2014 – now
Energy, Environmental, and Chemical Engineering Cumulative GPA: 3.99/4.0
Aerosol and Air Quality Research Laboratory
B. S. Tsinghua University
Environmental Engineering Aug 2010 – July 2014

AWARDS

Fellow of the McDonnell International Scholars Academy Aug 2014 – now
NASA Earth and Space Air Prize 2018

RESEARCH EXPERIENCE

2014 – Now **Graduate Research Assistant**
Supervisors: Professors **Pratim Biswas**, Brent Williams, Rajan Chakrabarty, Chenyang Lu, and Pramod Kulkarni,

Low-cost sensor calibration and application
Bioaerosol measurements during clinical procedures

2012 – 2014 **Undergraduate Research Assistant**
Supervisor: Professor **Jingkun Jiang**

DEG degradation mechanism as the working fluid of condensed particle counter (CPC)

PUBLICATIONS (# first author)

Peer-Reviewed Publications

10#. **Jiayu Li**, Huang Zhang, Chun-Ying Chao, Ling-Jyh Chen, Pratim Biswas. "Combining Ground Measurement, Low-cost Sensor, and Aerosol Optical Depth for high-resolution pollution mapping" (submit soon).

9#. **Jiayu Li**, Simar K. Mattewal, Sameer Patel, Pratim Biswas. "Evaluation of Nine Low-cost Sensor Based Personal PM Monitors". ***Aerosol Air Qual. Res.*** (submitted)

8. Abhay Cashikar, **Jiayu Li**, Pratim Biswas. "Combining a Low-Cost Particulate Matter Sensor with a Robot for Field Measurements". ***J Environ Eng.*** (Accepted)

7#. **Jiayu Li**, Haoran Li, Yehan Ma, Yang Wang, Ahmed Abokifa, Chenyang Lu, and Pratim Biswas (2018). "Spatiotemporal 3D Measurements of Particle Mass Concentrations with a Distributed Sensor Network Platform". ***Build. Environ.*** doi.org/10.1016/j.buildenv.2017.11.001.

6#. **Jiayu Li** and Pratim Biswas (2017). "Optical Characterization Studies of a Low-Cost Particle Sensor". ***Aerosol Air Qual. Res.*** doi.org/10.4209/aaqr.2017.02.0085.

5. Sameer Patel, **Jiayu Li**, Apoorva Pandey, Shamsh Perves, Rajan K. Chakrabarty, and Pratim Biswas (2017). "Spatio-temporal measurement of indoor particulate matter concentrations using a wireless network of low-cost sensors in households using solid fuels". ***Environ. Res***. doi.org/10.1016/j.envres.2016.10.001.

4#. **Jiayu Li**, Anna Leavey, Yang Wang, Caroline O'Neil, Meghan A. Wallace, Carey-Ann D. Burnham, Adrianus CM Boon, Hilary Babcock, and Pratim Biswas (2017). "Comparing the Performance of 3 Airborne Virus Samplers for Influenza Virus". ***J. Aerosol Sci.*** doi.org/10.1016/j.jaerosci.2017.08.007.

3. Carrie O'Neil, **Jiayu Li**, Anna Leavey, Yang Wang, Meghan Wallace, Carey-Ann D. Burnham, Pratim Biswas, and Hilary Babcock, (2017). "Characterization of Aerosols Generated During Patient Care Activities". ***Clin. Infect. Dis.*** doi.org/10.1093/cid/cix535.
2. Yang Wang, **Jiayu Li**, Anna Leavey, Hilary Babcock, and Pratim Biswas (2016). "Comparative Study on the Size Distributions and Respiratory Deposition of Particles Generated from Commonly Used Medical Nebulizers". ***J. Aerosol Med. Pulm. Drug Deliv.*** doi.org/10.1089/jamp.2016.1340.
1. Yang Wang, **Jiayu Li**, He Jing, Qiang Zhang, Jingkun Jiang, and Pratim Biswas (2015). "Laboratory Evaluation of Three Low-Cost Particle Sensors for Particulate Matter Measurement". ***Aerosol Sci. Technol.*** doi.org/10.1080/02786826.2015.1100710. (**Editor's selection of notable 2015 papers in *Aerosol Sci. Technol.*** Featured in AAAR 2015 Winter Newsletter).

Manuscripts under preparation

3#. **Jiayu Li**, Pratim Biswas. "Low-cost sensor: from principle to application: A review".
2#. **Jiayu Li**, Tandeep Chadha, Jiaxi Fang, Su Huang, Pratim Biswas. "Coupling single particle counter with a low-cost spectrometer to retrieve refractive index for aerosol classification".
1. Carrie O'Neil, **Jiayu Li**, Ramesh Raliya, Anna Leavey, Yang Wang, Meghan Wallace, Carey-Ann D. Burnham, Pratim Biswas, and Hilary Babcock. "Characterization of Aerosols Generated from clinical sample during flu season in St. Louis"

SELECTED PRESENTATIONS (Presenter with *)

6. Jiayu Li, Carrie O'neil, Ramesh Raliya, Yang Wang, Anna Leavey, Meghan Wallace, Carey-Ann, Burnham, Adrianus Boon, **Hillary Babcock***, and Pratim Biswas. September 2018. "Defining Pathogen Transmission Risks during Aerosol Generating Procedures in Healthcare Settings" St. Louis, MO. IAC 10th Conference.5. **Jiayu Li***, Jiaxi Fang, Fandeep Chadha, Benjamin Sumlin, Rajan K. Chakrabarty, and Pratim Biswas. September 2018. "Low-cost Sensor Calibration, Application, and Modification for Size Distribution and Refractive Index Measurement" St. Louis, MO. IAC 10th Conference.
4. **Jiayu Li***, Haoran Li, Yehan Ma, Yang Wang, Ahmed, Abokifa, Chenyang Lu and Pratim Biswas. August 2017. "Optical Characterization of the Low-Cost Sensor and Its Application with Robots" Raleigh, NC. AAAR 36th Annual Conference.
3. **Jiayu Li*** and Pratim Biswas. August 2016. "Distributed Low-cost Wireless Particle Sensors: Optical Characterization" Portland, OR. AAAR 35th Annual Conference.
2. **Jiayu Li**, Yang Wang, and Pratim Biswas*. August 2016. "Optical Characterization and Deployment of a Distributed Low-Cost Wireless Particle Sensor Network." Tours, France. 22nd European Aerosol Conference.
1. Yang Wang, **Jiayu Li***, He Jing, Qiang Zhang, Jingkun Jiang, and Pratim Biswas. October 2015. "Laboratory Evaluation of Three Low-cost Particle Sensors for Particulate Matter Measurement." Minneapolis, MN. AAAR 34th Annual Conference.

TEACHING EXPERIENCES

Teaching Assistant
Transport Phenomena (Fall 2015), Thermodynamics (Spring 2016), Environmental Nanochemistry (Spring 2018)

JOURNAL REVIEW ACTIVITY

Environmental Science and Technology Letters; Building and Environment; Journal of Aerosol Science; Aerosol and Air Quality Research; Sensors; Aerosol Science and Technology

Appendix VI: Transcript

Jiayu Li

Department	Course	Units	Final	Title
E33 EECE	501	3.0	A+	Transport Phenomena in Energy, Environmental, and Chemical Engineering
E37 MEMS	5610	3.0	A	Quantitative Materials Science & Engineering
E63 ChE	518	3.0	A-	Aerosol Science and Technology
E33 EECE	503	3.0	A	Kinetics and Reaction Engineering Principles
E33 EECE	511	3.0	A	Advanced Thermodynamics
E44 EECE	503	3.0	A	Mathematical Methods in EECE
E44 EECE	512	3.0	A+	Combustion Phenomena
E44 EECE	531	3.0	A	Environmental Organic Chemistry
E44 EECE	510	3.0	A	Advanced Topics in Aerosol Science & Engineering
E44 EECE	514	3.0	A	Atmospheric Science and Climate